# Polarization and Fiber Nonlinearities

by

**Qiang Lin**

Submitted in Partial Fulfillment
of the
Requirements for the Degree

Doctor of Philosophy

Supervised by

**Professor Govind P. Agrawal**

**The Institute of Optics**

The College
School of Engineering and Applied Sciences

**University of Rochester**
Rochester, New York

2006

# Curriculum Vitae

The author was born in Gutian, Fujian, China, in 1973. He began his undergraduate studies in 1991 at Physics Department of Tsinghua University, Beijing, China, and received his Bachelor of Science in Applied Physics in 1996. At the same university, he received his Master of Science in Optics in 1999. He then started his graduate studies at the Institute of Optics in the Fall of 1999, and obtained another Master of Science in Optics in 2003. He has carried out his doctoral research under the supervision of Professor Govind P. Agrawal since the summer of 2000. His research interest covers broad areas, including nonlinear optics, quantum optics, ultrafast optics, fiber and waveguide optics, and optical communication.

# Acknowledgements

Seven years of my graduate studies in Rochester were very enjoyable, although sometimes challenging. Looking back to this whole period, I find that every moment there was someone who stood behind me providing strong support, either for my research or for my life. Without them, I would not have been able to finish even a small piece of this thesis. Therefore, I would like to take this chance to express my sincere acknowledgements to all of them.

First and foremost, I am deeply grateful to my thesis advisor, Professor Govind P. Agrawal, for his invaluable support, guidance, and mentoring of my rewarding doctoral studies. It is he who lead me into this exciting field, guided me for coherent thinking, taught me with excellent technical writing, and provided me with invaluable advice about academic careers. I am deeply indebted to him for the freedom, flexibility, and encouragement he provided throughout my doctoral research. I am deeply indebted to him for his tremendous time and patience he spent in every aspect of my doctoral research.

I am very grateful to Professor Stojan Radic for his invaluable training of my experimental skills and for his generous financial and technical support with my experiments in his lab at UCSD. I am deeply indebted to Professor Joseph H. Eberly for his numerous helps with my research and for his wonderful course of Quantum Optics. His excellent physical interpretation and insight have inspired me to think about complex problems with simple physical pictures, which has benefited me significantly with all of my research. I am very grateful to Professor Wayne H. Knox for his invaluable advice about academic careers, for his inspiring discussions about research, and for the use of his lab equipments. I am very grateful to Professor Robert W. Boyd for his help with nonlinear optics, for his invaluable advice about academic careers, and for the use of his lab equipments. I am very grateful to Professor Chunlei Guo for his numerous supports with my experiments in his lab and for his inspiring discussions about many aspects of research and academic lives. I am also indebted to all these professors for serving as my references during my search for a postdoctoral position. I am very grateful to Professor Nicholas George for the use of his lab equipments and for his enlightening discussions about academic lives.

I thank my colleagues in Prof. Agrawal's group for continuous and inspiring discussions on a variety of research topics and on academic lives. In particular, I thank Fatih Yaman for continuous collaborations in many research topics about applications of fiber nonlinearities. I thank Nick Usechak for his numerous help with lab equipments, experiments, and programming. I thank Lianghong Yin for wonderful collaborations on the topics related to silicon photonics.

I thank Wanli Chi for numerous help with my research, particularly in numerous mathematical problems I encountered in my research. I thank Yujun Deng for wonderful collaborations on fiber-optic parametric oscillators and for numerous inspiring discussions about research and academic lives. I thank Jidong Zhang for wonderful collaborations on topics related to silicon photonics, and for his help with broadening my knowledge about nano-fabrication technology. I thank Fei Lu for wonderful collaborations on vector soliton fission.

I thank Colin O'Sullivan-Hale and Irfan A. Khan for helpful discussions about quantum problems related to parametric downconversion and coincidence counting experiments. I thank Rui Jiang and Jian Ren for numerous help with my experiments in Professor Stojan Radic's lab. I thank Giovanni Piredda for his help with Z-scan experiments and with the use of OPA. I thank Yufeng Li for helpful discussions about many aspects of research and academic lives. I thank Jorge Zurita-Sanchez, Alberto Marino, and Michael Beversluis for many helpful discussions about various research topics.

I greatly appreciate the help that the staffs in the Institute of Optics have provided during my graduate studies. I thank Joan Christian, Noelene Votens, Betsy Benedict, Brian McIntyre, Gayle Thompson, and Gina Kern for their helps. In particular, I would like to thank Per Adamson for his tremendous support with many lab equipments.

I would like to express my deep gratitude to Changmeng Liu, Xi Chen, and Wanli Chi for their continuous and invaluable support and help with many aspects of my life in Rochester. In particular, I am very grateful to Yujun Deng and his wife Huimin Ouyang, Changmeng Liu and his wife Xi Chen for their invaluable help with me to pass a challenging stage of my life in Rochester.

I thank Changmeng Liu and Jidong Zhang for their enthusiasm about skiing, snowboarding, and rock climbing, which has inspired me with great interest and has helped make my life in Rochester more enjoyable.

Finally, I would like to dedicate this thesis to my parents, sisters, and brothers, who have endowed me with their continuous and unconditional support and encouragement.

# Publications

## *Journal Articles*

1. **Q. Lin**, F. Yaman, and G. P. Agrawal, "Photon pair generation in optical fibers through four-wave mixing: Role of Raman scattering and pump polarization", submitted to Phys. Rev. A.
2. L. Yin, **Q. Lin**, and G. P. Agrawal, "Soliton fission and supercontinuum generation in silicon waveguides", accepted for publication in Opt. Lett.
3. F. Yaman, **Q. Lin**, and G. P. Agrawal, "A novel design for polarization-independent single-pump fiber-optic parametric amplifiers", IEEE Photon. Technol. Lett. **18**, 2335 (2006).
4. **Q. Lin** and G. P. Agrawal, "Raman response function for silica fibers", Opt. Lett. **31**, 3086 (2006).
5. **Q. Lin** and G. P. Agrawal, "Silicon waveguides for creating quantum-correlated photon pairs", Opt. Lett. **31**, 3140 (2006).
6. F. Yaman, **Q. Lin**, S. Radic, and G. P. Agrawal,"Fiber-optic parametric amplifiers in the presence of polarization-mode dispersion and polarization-dependent loss", J. Lightwave Technol **24**, 3088 (2006).
7. **Q. Lin**, J. Zhang, P. M. Fauchet, and G. P. Agrawal, "Ultrabroadband parametric generation and wavelength conversion in silicon waveguides", Opt. Exp. **14**, 4786 (2006).
8. L. Yin, **Q. Lin**, and G. P. Agrawal, "Dispersion tailoring and soliton propagation in silicon waveguides", Opt. Lett. **31**, 1295 (2006).
9. **Q. Lin**, F. Yaman, and G. P. Agrawal,"Photon-pair generation by four-wave mixing inside optical fibers", Opt. Lett. **31**, 1286 (2006).
10. **Q. Lin**, F. Yaman, and G. P. Agrawal, "Raman-induced polarization-dependent gain in parametric amplifiers pumped with orthogonally polarized lasers", IEEE Photon. Technol. Lett. **18**, 397 (2006).
11. A. N. Pinto, J. F. de Rocha, **Q. Lin**, and G. P. Agrawal, "Optical versus electrical dispersion compensation: Role of timing jitter", J. Lightwave Technol. **24**, 387 (2006).

12. **Q. Lin**, R. Jiang, C. F. Marki, C. J. McKinstrie, R. M. Jopson, J. Ford, G. P. Agrawal, and S. Radic, "40-Gb/s Optical Switching and Wavelength Multicasting in A Two-Pump Parametric Device", IEEE Photon. Technol. Lett. **17**, 2376 (2005).
13. Y. Deng, **Q. Lin**, F. Lu, G. P. Agrawal, and W. H. Knox, "Broadly tunable femtosecond parametric oscillator using a photonic crystal fiber", Opt. Lett. **30**, 1234 (2005).
14. F. Yaman, **Q. Lin**, G. P. Agrawal, and S. Radic, "Pump noise transfer in dual-pump fiber-optic parametric amplifiers: walk-off effects", Opt. Lett. **30**, 1048 (2005).
15. **Q. Lin** and G. P. Agrawal, "Intrapulse depolarization in optical fibers: A classical analog of spin decoherence", Opt. Lett. **30**, 821 (2005).
16. F. Yaman, **Q. Lin**, S. Radic, and G. P. Agrawal, "Impact of pump-phase modulation on dual-pump fiber-optic parametric amplifiers and wavelength converters", IEEE Photon. Technol. Lett. **17**, 2053 (2005).
17. **Q. Lin**, K. Wright, G. P. Agrawal, and C. Guo, "Spectral responsitivity and efficiency of metal-based femtosecond autocorrelation technique", Opt. Comm. **242**, 279 (2004).
18. F. Lu, **Q. Lin**, W. H. Knox, and G. P. Agrawal, "Vector soliton fission", Phys. Rev. Lett. **93**, 183901 (2004).
19. **Q. Lin** and G. P. Agrawal, "Impact of fiber birefringence on optical switching with nonlinear optical loop mirrors", IEEE J. Sel. Top. Quan. Electron. **10**, 1107 (2004).
20. **Q. Lin** and G. P. Agrawal, "Effects of polarization mode dispersion on fiber-based parametric amplification and wavelength conversion", Opt. Lett. **29**, 1114 (2004).
21. **Q. Lin** and G. P. Agrawal, "Vector Theory of cross-phase modulation: role of nonlinear polarization rotation", IEEE J. Quan. Electron. **40**, 958 (2004).
22. **Q. Lin** and G. P. Agrawal, "Vector theory of four-wave mixing: polarization effects in fiber-optic parametric amplifiers", J. Opt. Soc. Am. B **21**, 1216 (2004).
23. F. Yaman, **Q. Lin**, S. Radic, And G. P. Agrawal, "Impact of dispersion fluctuations on dual-pump fiber-optic parametric amplifiers", IEEE Photonic Technol. Lett. **16**, 1292 (2004).
24. **Q. Lin** and G. P. Agrawal, "Effects of polarization mode dispersion on cross-phase modulation in dispersion-managed WDM systems", (invited paper), J. Lightwave Technol. **22**, 977 (2004).
25. F. Yaman, **Q. Lin**, and G. P. Agrawal, "Effects of polarization mode dispersion in dual-pump fiber-optic parametric amplifiers", IEEE Photon. Technol. Lett. **16**, 431 (2004).
26. **Q. Lin** and G. P. Agrawal, "Vector Theory of stimulated Raman scattering and its application to fiber-based Raman amplifiers", J. Opt. Soc. Am. B **20**, 1616 (2003).

27. **Q. Lin** and G. P. Agrawal, "Impact of polarization-mode dispersion on measurement of zero-dispersion wavelength through four-wave mixing", IEEE Photon. Technol. Lett. **15**, 1719 (2003).
28. S. Radic, C. J. McKinstrie, R. M. Jopson, J. C. Centanni, **Q. Lin** and G. P. Agrawal, "Record performance of parametric amplifier constructed with highly nonlinear fiber", Electron. Lett. **39**, 838 (2003).
29. **Q. Lin** and G. P. Agrawal," Statistics of polarization dependent gain in fiber-based Raman amplifiers", Opt. Lett. **28**, 227 (2003).
30. **Q. Lin** and G. P. Agrawal, "Correlation theory of polarization mode dispersion in optical fibers", J. Opt. Soc. Am. B. **20**, 292 (2003).
31. **Q. Lin** and G. P. Agrawal, "Polarization mode dispersion induced fluctuations during Raman amplification in optical fibers", Opt. Lett. **27**, 2194 (2002).
32. **Q. Lin** and G. P. Agrawal, "Pulse broadening induced by dispersion fluctuations in optical fibers", Opt. Comm. **206**, 313 (2002).

## *Book Chapters*

1. F. Yaman, **Q. Lin**, and G. P. Agrawal, "Fiber-optic parametric amplifiers for lightwave systems", (review book chapter), *Guided Wave Optical Components and Devices*, B. P. Pal Ed. (Academic Press, San Diego, CA, 2005).

## *Conference Presentations*

1. **Q. Lin** and G. P. Agrawal, "Correlated photon pairs using silicon waveguides", OSA annual meeting, FThI4, Rochester, NY (2006).
2. L. Yin, **Q. Lin**, and G. P. Agrawal, "Soliton fission and continuum generation in silicon waveguides", OSA annual meeting, FWM5, Rochester, NY (2006).
3. **Q. Lin** and G. P. Agrawal, "An accurate model for the Raman response function in silica fibers", CLEO06, CMW5, Long Beach, CA (2006).
4. L. Yin, **Q. Lin**, and G. P. Agrawal, "Dispersion tailoring and soliton propagation in Si waveguides", CLEO06, CMEE7, Long Beach, CA (2006).
5. F. Yaman, **Q. Lin**, and G. P. Agrawal, "A novel design for polarization-independent single-pump fiber-optic parametric amplifiers", CLEO06, JWB59, Long Beach, CA (2006).

6. **Q. Lin**, F. Yaman, S. Radic, and G. P. Agrawal, "Fundamental noise limits in dual-pump fiber-optic parametric amplifiers and wavelength converters", CLEO05, CTuT4, Baltimore, MD (2005).
7. F. Yaman, **Q. Lin**, S. Radic, and G. P. Agrawal, "Impact of pump-phase modulation on fiber-optic parametric amplifiers and wavelength converters", CLEO05, CTuJ6, Baltimore, MD (2005).
8. F. Yaman, **Q. Lin**, S. Radic, and G. P. Agrawal, "Impact of pump-phase modulation on the performance of dual-pump fiber-optic parametric amplifiers", OFC05, OWN3, p.3, Anaheim, CA (2005).
9. F. Yaman, **Q. Lin**, and G. P. Agrawal, "Walk-off effects in dual-pump parametric amplifiers", OSA annual meeting, FMB2, Rochester, NY (2004).
10. **Q. Lin** and G. P. Agrawal, "Optical switching in a nonlinear fiber-loop mirror: Effects of polarization-mode dispersion", OSA annual meeting, FWI3, Rochester, NY (2004).
11. **Q. Lin** and G. P. Agrawal, "Intrapulse depolarization in optical fibers", OSA annual meeting, FThM6, Rochester, NY (2004).
12. **Q. Lin**, F. Yaman, and G. P. Agrawal, "Impact of randomly varying fiber dispersion on dual-pump fiber optic parametric amplifiers", NLGW04, MC36, Toronto, Ontario, CA (2004).
13. F. Yaman, **Q. Lin**, and G. P. Agrawal, "Impact of polarization mode dispersion on dual-pump fiber optic parametric amplifiers", NLGW04, MC31, Toronto, Ontario, CA (2004).
14. **Q. Lin** and G. P. Agrawal, "PMD effects in fiber-based Raman amplifiers", OFC03, TuC4, p.159, Atlanta, GA (2003).
15. **Q. Lin** and G. P. Agrawal, "Effects of PMD on fiber-based parametric amplification and wavelength conversion", OSA annual meeting'03, TuP3, Tucson, AZ (2003).

# Abstract

This thesis is devoted to a thorough investigation of various nonlinear phenomena in optical fibers over a variety of length, time, and power scales. It presents a unified theoretical description of fiber nonlinearities, their applications, existing problems, and possible solutions, particularly focusing on the polarization dependence of nonlinearities. The thesis begins with an investigation of quantum-correlated photon pair generation in the extremely low-power regime, and fundamental quantum noise properties of dual-pump parametric amplfiers in the very high gain regime. It then focuses on two experimental demonstrations of applications based on four-wave mixing: an ultrafast all-optical switching scheme with the capability of multi-band wavelength casting, and a subpicosecond parametric oscillator with broadband tunability. The thesis next deals with the theoretical and experimental investigation of a novel phenomenon of vector soliton fission during supercontinuum generation in a tapered fiber in the femtosecond regime. The vectorial nature of Raman scattering is discussed next. In particular, I propose a vector form of the Raman response function to descibe accurately the Raman-related phenomena during ultrashort pulse propagation inside optical fibers. The thesis also presents a unified theory to describe nonlinearities in long fibers with random birefringence and polarization-mode dispersion. It focuses on the statistical nature of the interactions between random polarizaiton-mode disperion and various nonlinear effects like stimulated Raman scattering, cross-phase modulation, four-wave mixing, and self-phase modulation. In particular, I quantify their impacts on various nonlinear photonic functionalities such as Raman amplification, nonlinear optical switching, parametric amplfication, wavelength conversion, soliton stability, etc.

# Table of Contents

# List of Tables

# List of Figures

# 1 Introduction

## 1.1 Important Nonlinear Effects in Optical Fibers

Optical fibers are circular dielectric waveguides designed to confine optical waves inside a narrow core. They are ideal for the delivery of an optical wave over considerable distances and have found applications ranging from quantum optics [1]-[4], atomic and molecular physics [5]-[7], medical optics [8]-[10], to optical telecommunications [11]. Because of a high degree of mode confinement, optical intensity can become quite high inside fibers even for a moderate input power. Such intense optical fields can cause anharmonic motion of bound electrons of silica and thus induce polarization that depends on the magnitude of the optical intensity. As the secondary waves emitted by the driven bound electrons are directly proportional to the induced polarization, the total optical field experiences an extra phase retardation manifested as an intensity-dependent change in the refractive index. This phenomenon is referred to as the optical Kerr effect and is the dominant nonlinear effect inside optical fibers [12]. As the electron mass is tiny, bound electrons can follow oscillations of the optical field nearly instantly, and the response time of Kerr nonlinearity is within an optical cycle ($\sim$ 1 fs) [13]. Such nearly instantaneous nature of the Kerr nonlinearity underlies many phenomena in optical fibers and enables numerous applications requiring ultrafast response, as discussed in detail in this thesis.

When an intense wave propagates inside a fiber, it introduces changes in the refractive index through the Kerr nonlinearity, which imposes a nonlinear phase shift on the wave itself. This phenomenon is referred to as self-phase modulation (SPM) [12, 14]. SPM together with the group-velocity dispersion (GVD) underlies the formation of optical solitons [12, 15, 16]. Similarly, Such induced nonlinear refractive-index changes can also be experienced by other waves co-existing inside the fiber, a phenomenon referred to as cross-phase modulation (XPM) [12, 17]. If three or four waves co-propagate along a fiber, the Kerr nonlinearity can be induced by their beatings. When the wave fronts of two waves catch those of the other two (the so-called phase matching condition), in-phase anharmonic motion of electrons can transfer energy from two photons to the other two. This phenomenon is referred to as four-wave mixing (more accurately, four-photon scattering) [12],[18]-[21]. If optical frequencies of interacting waves are far below the resonant frequencies of bound electrons (in the ultra-violet region for silica fibers), electrons return to their original equilibrium states after interactions and do not take away energy, resulting in an elastic scattering process in which total energy is conserved among the four interacting photons [13].

Apart from the off-resonant interaction with bound electrons, optical waves can also interact with molecules inside silica fibers. In particular, when the beating between two optical waves resonates with a vibration mode of molecules, a high-frequency photon can be scattered into a low-frequency photon and an optical phonon. This phenomenon is referred to as stimulated Raman scattering (SRS) [12, 22] whose response time is related to the phonon lifetime. As fused silica is a glass, it exhibits a rich variety of vibration modes, dominated by the symmetric stretching motion of the bridging oxygen atom in the Si-O-Si bond [23]. Unlike a crystal, random Si-O-Si bond networks inside silica glass inhomogeneously broaden vibration modes, resulting in an effective phonon lifetime of $\sim$ 30 fs [24, 25]. As a result, SRS inside silica fibers exhibits a spectrum peaked at 13.2 THz with a FWHM of about 5 THz [22]-[26]. Moreover, the complex Raman spectrum extends from 0 to more than 40 THz [26]. Such broadband SRS can transfer energy of high-frequency components of an ultrashort pulse to its low-frequency components, leading to a red shift of pulse carrier frequency, the so-called Raman-induced frequency shift (RIFS) [27, 28] that is one of the dominant nonlinear effect during short-pulse propagation inside optical fibers. Similarly, optical waves can also resonantly interact with acoustic phonons and lead to stimulated Brillioun scattering (SBS) [12, 29]. As acoustic phonons have a low energy and a long lifetime, SBS has a narrow bandwidth ($\sim$ 13 MHz) and a $\sim$ 10–11 GHz frequency shift at wavelength near 1.55 $\mu$m.

All these nonlinear phenomena, SPM, XPM, FWM, SRS, and SBS, form a family of the third-order nonlinear effects in optical fibers.[1] They have been studied extensively and applied to realize many practical applications [12, 30], since the invention of low-loss optical fibers in 1970s [31]-[33]. Their potential for realizing high-speed, all-optical, classical and quantum information processing devices have been pursued during the past two decades. In particular, the advent of high-power fiber amplifiers [34]-[38], femtosecond short pulse sources [39]-[41], and new kinds of fibers (*i.e.*, high-nonlinearity fibers [42] and microstructured fibers [43, 44]) in recent years provides the opportunity to investigate new physics and new applications of fiber nonlinearities. These advances have moved current studies into

[1] Third-order nonlinearity also includes processes like third-harmonic generation. However, this process has very low efficiency in general because of the difficulty in satisfying the phase-matching condition, unless higher-order fiber modes are used [45].

new regimes such as photon-pair generation at extremely low power level, broadband optical signal processing in the very high gain regime, octave-spanned supercontinuum generation in femtosecond time scale, and so on. Exploration of nonlinear optical phenomena in these new regimes requires a new theoretical insight. One of the goals of this thesis is to develop a unified theoretical framework for investigating various nonlinear processes. The second goal of this thesis is to take advantage of fiber nonlinearities in these new regimes to develop experimental techniques and explore new practical applications.

An important issue related to fiber nonlinearities is their polarization dependence originating from the vectorial nature of optical waves. Photons have intrinsic spins manifested through their states of polarization (SOP) that can vary from linear to circular to elliptical. In isotropic media like silica glass, spin conservation is required among the interacting photons and phonons, a feature that makes nonlinear processes to depend strongly on polarization. On the one hand, such polarization dependence leads to new phenomena such as vectorial modulation instability [46]-[55], formation of vectorial solitary waves [56]-[60], polarization instability [61]-[66], etc. On the other hand, it also introduces strong polarization dependence on the performance of nonlinear photonic devices based on fiber nonlinearities, which becomes an obstacle to practical implementations.

Note that fiber nonlinearities are relatively weak compared with other materials. As a result, most fiber-based nonlinear photonic devices often require long fiber length and high power levels. In practice, fiber birefringence generally varies both in magnitude and orientation randomly along the length on a length scale of $\sim$10 meters (birefringence correlation length $l_c$) [67] because of imperfections in both the manufacturing process and handling conditions. Moreover, it also changes randomly with time on a time scale associated with external environmental perturbations (such as temperature and stress variations). Owing to its frequency-dependent nature, fiber birefringence not only introduces random differential group delay (DGD) between the two polarization modes of one pulse, but also depolarizes relative SOPs among optical waves of different frequencies. This phenomenon is known as polarization-mode dispersion (PMD) and has been extensively studied in recent years in the context of optical communications [68, 69] and turns out to be an ultimate limiting factor for high-bit rate communication systems.

Clearly, such random PMD-induced depolarization of interacting waves would significantly affect polarization-dependent nonlinear interactions, resulting in quite different behavior of nonlinear effects in long fibers. On the one hand, it would exhibit new features that are absent in short fibers. On the other hand, it would affect significantly the performance of nonlinear photonic devices. It is thus important to investigate the interactions between PMD and various fiber nonlinearities. This is the third goal of this thesis. The aim is to develop a unified theoretical framework to quantitatively analyze such interactions and to provide practical guidance for improving performance of nonlinear photonic devices.

## 1.2 Thesis Objective

This thesis is intended to provide a comprehensive study of fiber nonlinearities, their polarization dependence, and their applications on both short- and long-length scales, and in both continuous-wave and ultrashort-time regimes. More specifically, we study four-wave mixing in both the low-level pumping regime for creating quantum-correlated photon pairs, and in the high-level pumping regime for parametric amplification and wavelength conversion. We use four-wave mixing inside optical fibers to develop techniques for ultrafast all-optical switching with capability of multi-band wavelength casting. Its capability for simultaneous pulse reamplification, reshaping, retiming, provides great potential for future all-optical signal processing. We also use four-wave mixing to experimentally demonstrate a subpicosecond parametric oscillator with broadband tunability. We study the nonlinear effects and their polarization dependence on a femtosecond time scale in the case of vector soliton propagation. We study the physical origin of polarization dependence of Raman response in silica fibers. We provide a comprehensive investigation on the interaction of PMD with various nonlinear effects, such as self-phase modulation, cross-phase modulation, stimulated Raman scattering, and four-wave mixing, in fibers with length much longer than birefringence correlation length. We also investigate their impacts on various nonlinear photonic devices like Raman amplifiers, nonlinear optical switches, parametric amplifiers, and telecommunication systems.

## 1.3 Thesis Outline

The thesis is organized as follows. Chapters 2−6 deal with the nonlinear effects on a short length scale when the intrinsic polarization dependence dominates. In particular, Chapter 2 provides a derivation of the general formalism used throughout this thesis: both the classical and quantum version of generalized nonlinear Schrödinger equation. Chapter 3 considers the generation of quantum-correlated photon pairs inside optical fibers, with focus on the role of spontaneous Raman scattering and pump polarization. Chapter 4 discusses fundamental quantum noise and its polarization dependence in dual-pump fiber-optic parametric amplifiers. Chapter 5 presents the experimental results related to applications based on four-wave mixing. We demonstrate all-optical ultrafast switching and multi-band wavelength translation at a rate of 40 Gb/s. Such a scheme can be used for packet switching as well as bit-level switching with high conversion efficiency, high extinction ratio, and with the capability of subrate pump control. We also demonstrate a subpicosecond fiber-optic parametric oscillator with 200-nm tunability around 1 $\mu$m, by use of modulation instability pumped in the normal-dispersion regime. Chapter 6 investigates the phenomena of vector soliton fission and supercontinuum generation inside tapered fibers. Chapter

7 presents a vector form of the Raman response function of silica fibers which can provide a correct quantitative description of Raman-related optical phenomena.

Chapter 8−12 focus on the nonlinear effects on a long length scale where random birefringence and PMD become significant. In particular, Chapter 8 provides a derivation of the general formalism of generalized nonlinear Schrödinger equation in the presence of random birefringence. This equation is used in Chapter 9−12 for discussing various nonlinear effects. Chapter 8 deals with the interplay between stimulated Raman scattering and PMD inside Raman amplifiers. Chapter 10 focuses on the interaction between cross-phase modulation and PMD, which leads to a novel phenomenon that has its significance in nonlinear optical switching. Chapter 11 discusses the interplay between PMD and four-wave mixing and its impact on fiber-based optical parametric amplification and wavelength conversion. Chapter 12 discusses the soliton propagation under the random perturbation of PMD.

## References


[1] P. D. Drummond, R. M. shelby, S. R. Friberg, and Y. Yamamoto, Nature **365**, 307 (1993).

[2] G. Leuchs and N. Korolkova, Opt. Photon. News **13**, Feburary, 64 (2002).

[3] X. Li, P. L. Voss, J. E. Sharping, and P. Kumar, Phys. Rev. Lett. **94**, 053601 (2005).

[4] H. Takesue and K. Inoue, Phys. Rev. A **72**, 041804(R) (2005).

[5] F. Benabid, J. C. Knight, G. Antonopoulos, and P. St. J. Russell, Science **298** 399 (2002).

[6] S. Ghosh, J. E. Sharping, D. G. Ouzounov, and A. L. Gaeta, Phys. Rev. Lett. **94** 093902 (2005).

[7] S. Ghosh, A. R. Bhagwat, C. K. Renshaw, S. Goh, A. L. Gaeta, and B. J. Kirby, Phys. Rev. Lett. **97**, 023603 (2006).

[8] D. Bird and Min Gu, Opt. Lett. **27**, 1031 (2002).

[9] P. Matousek, E. R. C. Draper, A. E. Goodship, I. P. Clark, K. L. Ronayne, and A. W. Parker, Appl. Spect. **60**, 758 (2006).

[10] M. Yamanari, S. Makita, V. D. Madjarova, T. Yatagai, and Y. Yasuno, Opt. Exp. **14**, 6502 (2006).

[11] I. P. Kaminow and T. L. Koch, eds., *Optical Fiber Telecommunications IV A, B* (Academic, San Diego, Calif., 2002).

[12] G. P. Agrawal, *Nonlinear Fiber Optics*, $3^{rd}$ ed. (Academic, San Diego, CA, 2001).

[13] R. W. Boyd, *Nonlinear Optics*, $2^{nd}$ ed. (Academic, San Diego, CA, 2003).

[14] R. H. Stolen and C. Lin, Phys. Rev. A **17**, 1448 (1978).

[15] A. Hasegawa and F. Tappert, Appl. Phys. Lett. **23**, 142 (1973).

[16] L. F. Mollenauer, R. H. Stolen, and J. P. Gordon, Phys. Rev. Lett. **45**, 1095 (1980).

[17] M. N. Islam, L. F. Mollenauer, R. H. Stolen, J. R. Simpson, and H. T. Shang, Opt. Lett. **12**, 625 (1987).

[18] R. H. Stolen, J. E. Bjorkholm, and A. Ashkin, Appl. Phys. Lett. **24**, 308 (1974).

[19] K. O. Hill, D. C. Johnson, B. S. Kawaski, and R. I. MacDonald, J. Appl. Phys. **49**, 5098 (1974).

[20] R. H. Stolen, IEEE J. Quantum Electron. **11**, 100 (1975).

[21] R. H. Stolen and J. E. Bjorkholm, IEEE J. Quantum Electron. **18**, 1062 (1982).

[22] R. H. Stolen and E. P. Ippen, Appl. Phys. Lett. **22**, 276 (1973).

[23] F. L. Galeener, A. J. Leadbetter, and M. W. Stringfello, Phys. Rev. B **27**, 1052 (1983); see also references therein.

[24] R. H. Stolen, J. P. Gordon, W. J. Tomlinson, and H. A. Haus, J. Opt. Soc. Am. B **6**, 1159 (1989).

[25] K. J. Blow and D. Wood, IEEE J. Quantum Electron. **25**, 2665 (1989).

[26] R. H. Stolen, in *Raman Amplifiers for Telecommunications 1*, M. N. Islam Ed. (Springer, New York 2003).

[27] F. M. Mitschke and L. F. Mollenauer, Opt. Lett. **11**, 659 (1987).

[28] J. P. Gordon, Opt. Lett. **11**, 662 (1986).

[29] E. P. Ippen and R. H. Stolen, Appl. Phys. Lett. **21**, 539 (1972).

[30] G. P. Agrawal, *Application of Nonlinear Fiber Optics* (Academic Press, San Diego, 2001).

[31] F. P. Kapron, D. B. Keck, and R. D. Maurer, Appl. Phys. Lett. **17**, 423 (1970).

[32] W. G. French, J. B. MacChesney, P. B. O'Connor, and G. W. Tasker, Bell. Syst. Tech. J. **53**, 951 (1974).

[33] T. Miya, Y. Terunuma, T. Hosaka, and T. Miyashita, Electron. Lett. **15**, 106 (1979).

[34] R. J. Mears, L. Reekie, I. M. Jauncey, D. N. Payne, Electron. Lett. **23**, 1026 (1987).

[35] E. Desurvire, J. R. Simpson, and P. C. Becker, Opt. Lett. **12**, 888 (1987).

[36] E. Desurvire, *Erbium-Doped Fiber Amplifiers* (Wiley, New York, 1994).

[37] R. Paschotta, J. Nilsson, A. C. Tropper, D. C. Hanna, IEEE J. Quantum Electron. **33**, 1049 (1997).

[38] A. K. Srivastava and Y. Sun, *Optical Fiber Telecommunications IV A*, I. P. Kaminow and T. L. Koch, eds. (Academic, San Diego, Calif., 2002), Chap. 4.

[39] M. T. Asaki, C. P. Huang, D. Garvey, J. P. Zhou, H. C. Kapteyn, and M. M. Murnane, Opt. Lett. **18**, 977 (1993).

[40] L. E. Nelson, D. J. Jones, K. Tamura, H. A. Haus, and E. P. Ippen, Appl. Phys. B **65**, 277 (1997).

[41] U. Keller, Nature **424**, 831 (2003).

[42] M. Takahashi, R. Sugizaki, J. Hiroishi, M. Tadakuma, Y. Taniguchi, and T. Yagi, J. Lightwave Technol. **23**, 3615 (2005).

[43] P. Russell, Science **299**, 358 (2003).

[44] J. C. Knight, Nature **424**, 847 (2003).

[45] A. Efimov, A. Taylor, F. Omenetto, J. Knight, W. Wadsworth, and P. St. J. Russell, Opt. Exp. **11**, 2567 (2003).

[46] S. Wabnitz, Phys. Rev. A **38**, 2018 (1988).

[47] S. Trillo and S. Wabnitz, J. Opt. Soc. Am. B **6**, 238 (1989).

[48] J. E. Rothenberg, Phys. Rev. A **42**, 682 (1990).

[49] S. Trillo and S. Wabnitz, J. Opt. Soc. Am. B **9**, 1061 (1992).

[50] E. A. Golovchenko and A. N. Pilipetskii, J. Opt. Soc. Am. B **11**, 92 (1994).

[51] S. G. Murdoch, R. Leonhardt, and J. D. Harvey, Opt. Lett. **20**, 866 (1995).

[52] G. Millot, M. Seve, and S. Wabnitz, Phys. Rev. Lett. **79**, 661 (1997).

[53] P. T. Dinda, G. Millot, and S. Wabnitz, J. Opt. Soc. Am. B **15**, 1433 (1998).

[54] G. Millot, P. T. Dinda, E. Seve, and S. Wabnitz, Opt. Fiber Technol. **7**, 170 (2001).

[55] R. J. Kruhlak, G. K. L. Wong, J. S. Y. Chen, S. G. Murdoch, R. Leonhardt, J. D. Harvey, N. Y. Joly, J. C. Knight, Opt. Lett. **31**, 1379 (2006).

[56] K. J. Blow, N. J. Doran, and D. Wood, Opt. Lett. **12**, 202 (1987).

[57] C. R. Menyuk, IEEE J. Quantum Electron. **23**, 174 (1987); Opt. Lett. **12**, 614 (1987); J. Opt. Soc. Am. B **5**, 392 (1988).

[58] T. Ueda and W. L. Kath, Phys. Rev. A **42**, 563 (1990).

[59] S. Pitois, G. Millot, and S. Wabnitz, Phys. Rev. Lett. **81**, 1409 (1998).

[60] E. Seve, G. Millot, S. Wabnitz, T. Sylvestre, and H. Maillotte, J. Opt. Soc. Am. B **16**, 1642 (1999).

[61] H. G. Winful, Appl. Phys. Lett. **47**, 213 (1985).

[62] B. Daino, G. Gregori, and S. Wabnitz, Opt. Lett. **11**, 42 (1986).

[63] S. Trillo, S. Wabnitz, R. H. Stolen, G. Assanto, C. T. Seaton, and G. I. Stegeman, Appl. Phys. Lett. **49**, 1224 (1986).

[64] S. Wabnitz, E. M. Wright, and G. I. Stegeman, Phys. Rev. A **41**, 6415 (1990).

[65] S. Wabnitz and B. Daino, Phys. Lett. A **182**, 289 (1993).

[66] S. Pitois, G. Millot, and S. Wabnitz, J. Opt. Soc. Am. B **18**, 432 (2001).

[67] A. Galtarossa, L. Palmieri, M. Schiano, and T. Tambosso, Opt. Lett. **25**, 384 (2000); **26**, 962 (2001).

[68] C. D. Poole, in *Optical Fiber Telecommunications III A*, I. P. Kaminow and T. L. Koch, eds. (Academic, San Diego, Calif., 1997), Chap. 6 and references therein.

[69] H. Kogelnik, R. Jopson, and L. Nelson, in *Optical Fiber Telecommunications IV B*, I. P. Kaminow and T. L. Koch, eds. (Academic, San Diego, Calif., 2002), Chap. 15 and references therein.

# 2 Nonlinear Wave Interactions in Optical Fibers: General Formalism

Before we start to discuss various nonlinear effects in fibers, it is important to have a theoretical platform on which we can conveniently perform investigations. In this chapter, I will provide such a general formalism to obtain the dynamic equation which underlies all the topics covered in this thesis.

## 2.1 Third-Order Nonlinear Polarization

In the field of nonlinear optics, the polarization induced in a dielectric medium is expanded in powers of the optical field $\boldsymbol{E}_r(\boldsymbol{r},t)$ as

$$\boldsymbol{P}_r(\boldsymbol{r},t) = \boldsymbol{P}_r^{(1)}(\boldsymbol{r},t) + \boldsymbol{P}_r^{(2)}(\boldsymbol{r},t) + \boldsymbol{P}_r^{(3)}(\boldsymbol{r},t) + \cdots, \tag{2.1}$$

where the subscript $r$ denotes a real field, $\boldsymbol{P}_r^{(1)}(\boldsymbol{r},t)$ represents the linear contribution and the other terms account for the second, third, and higher order nonlinear effects. As fused silica exhibits an inversion symmetry, all the even-order nonlinear effects vanish ($\boldsymbol{P}_r^{(2n)} = 0$), and the lowest-order nonlinear effect is of third order. The third-order nonlinear polarization in a medium such as silica glass can be written in its most general form as [1, 2]

$$\begin{aligned}\boldsymbol{P}_r^{(3)}(\boldsymbol{r},t) = {} & \frac{\varepsilon_0}{2}\sigma\left[\boldsymbol{E}_r(\boldsymbol{r},t)\cdot\boldsymbol{E}_r(\boldsymbol{r},t)\right]\boldsymbol{E}_r(\boldsymbol{r},t) + \varepsilon_0\boldsymbol{E}_r(\boldsymbol{r},t)\int_0^\infty a(\tau)\left[\boldsymbol{E}_r(\boldsymbol{r},t-\tau)\cdot\boldsymbol{E}_r(\boldsymbol{r},t-\tau)\right]d\tau \\ & + \varepsilon_0\boldsymbol{E}_r(\boldsymbol{r},t)\cdot\int_0^\infty b(\tau)\boldsymbol{E}_r(\boldsymbol{r},t-\tau)\,\boldsymbol{E}_r(\boldsymbol{r},t-\tau)\,d\tau,\end{aligned} \tag{2.2}$$

where $a(\tau)$ and $b(\tau)$ govern the delayed Raman response (related to nuclear motion) while $\sigma$ accounts for the instantaneous electronic response of the nonlinear medium.

In general, it is convenient to represent a real electromagnetic field in the form of a complex analytic signal whose spectrum consists of only positive frequency components [3]. Optical waves in the visible and infrared spectral regions generally have a spectral width much narrower than their carrier frequency $\omega_0$. Thus, without loss of generality, we can decompose the field and the induced polarization as

$$\boldsymbol{E}_r(\boldsymbol{r},t) = \frac{1}{2}[\boldsymbol{E}(\boldsymbol{r},t)e^{-i\omega_0 t} + c.c.], \qquad \boldsymbol{P}_r(\boldsymbol{r},t) = \frac{1}{2}[\boldsymbol{P}(\boldsymbol{r},t)e^{-i\omega_0 t} + c.c.], \tag{2.3}$$

where $\boldsymbol{E}$ and $\boldsymbol{P}$ denotes slowly varying amplitudes and $c.c.$ stands for complex conjugate. Substituting Eq. (2.3) into Eq. (2.2), the third-order nonlinear polarization becomes

$$\begin{aligned}
\boldsymbol{P}^{(3)}(\boldsymbol{r},t) =& \frac{\varepsilon_0\sigma}{8}\{2[\boldsymbol{E}^*(\boldsymbol{r},t)\cdot\boldsymbol{E}(\boldsymbol{r},t)]\boldsymbol{E}(\boldsymbol{r},t) + [\boldsymbol{E}(\boldsymbol{r},t)\cdot\boldsymbol{E}(\boldsymbol{r},t)]\boldsymbol{E}^*(\boldsymbol{r},t)\} \\
&+ \frac{\varepsilon_0}{2}\boldsymbol{E}(\boldsymbol{r},t)\int_{-\infty}^{+\infty} a(\tau)[\boldsymbol{E}^*(\boldsymbol{r},t-\tau)\cdot\boldsymbol{E}(\boldsymbol{r},t-\tau)]d\tau \\
&+ \frac{\varepsilon_0}{4}\boldsymbol{E}(\boldsymbol{r},t)\cdot\int_{-\infty}^{+\infty} b(\tau)[\boldsymbol{E}(\boldsymbol{r},t-\tau)\boldsymbol{E}^*(\boldsymbol{r},t-\tau) + \boldsymbol{E}^*(\boldsymbol{r},t-\tau)\boldsymbol{E}(\boldsymbol{r},t-\tau)]d\tau \\
&+ \frac{\varepsilon_0}{4}\boldsymbol{E}^*(\boldsymbol{r},t)\int_{-\infty}^{+\infty} a(\tau)e^{2i\omega_0\tau}[\boldsymbol{E}(\boldsymbol{r},t-\tau)\cdot\boldsymbol{E}(\boldsymbol{r},t-\tau)]d\tau \\
&+ \frac{\varepsilon_0}{4}\boldsymbol{E}^*(\boldsymbol{r},t)\cdot\int_{-\infty}^{+\infty} b(\tau)e^{2i\omega_0\tau}\boldsymbol{E}(\boldsymbol{r},t-\tau)\boldsymbol{E}(\boldsymbol{r},t-\tau)d\tau.
\end{aligned} \tag{2.4}$$

As $a(\tau)$ and $b(\tau)$ are both slow Raman responses that cannot respond on a time scale of an optical cycle or less [2, 4, 5], the last two terms in Eq. (2.4) are negligible, and Eq. (2.4) can be written in a compact form of

$$P_i^{(3)}(\boldsymbol{r},t) = \varepsilon_0\chi_0 E_j(\boldsymbol{r},t)\int_{-\infty}^{+\infty} R_{ijkl}^{(3)}(t-\tau)E_k^*(\boldsymbol{r},\tau)E_l(\boldsymbol{r},\tau)d\tau, \tag{2.5}$$

where $i,j,k,l = x,y,z$, $\chi_0$ is the magnitude of third-order susceptibility, and the third-order nonlinear response is given by

$$R_{ijkl}^{(3)}(\tau) = \frac{f_E}{3}\delta(\tau)\left(\delta_{ij}\delta_{kl} + \delta_{ik}\delta_{jl} + \delta_{il}\delta_{jk}\right) + f_R R_a(\tau)\delta_{ij}\delta_{kl} + \frac{f_R}{2}R_b(\tau)\left(\delta_{ik}\delta_{jl} + \delta_{il}\delta_{jk}\right), \tag{2.6}$$

where $R_a(\tau)$ and $R_b(\tau)$ are normalized isotropic and anisotropic Raman response, and $f_R$ represents their fractional contribution to the nonlinear refractive index (whose magnitude is related to $\chi_0$). $f_E = 1 - f_R$ represents the fraction of electronic contribution. All these parameters and functions are given by

$$\chi_0 \equiv \frac{3\sigma}{8} + \frac{1}{2}\int_{-\infty}^{+\infty}[a(\tau)+b(\tau)]d\tau, \qquad f_R \equiv \frac{1}{2\chi_0}\int_{-\infty}^{+\infty}[a(\tau)+b(\tau)]d\tau, \tag{2.7}$$

$$R_a(\tau) \equiv \frac{a(\tau)}{2f_R\chi_0}, \qquad R_b(\tau) \equiv \frac{b(\tau)}{2f_R\chi_0} \tag{2.8}$$

with $\int_{-\infty}^{+\infty}[R_a(\tau)+R_b(\tau)]d\tau = 1$. Note that $a(\tau) = 0$ and $b(\tau) = 0$ when $\tau < 0$ because of causality.

In the frequency domain, the third-order nonlinear polarization given in Eq. (2.5) becomes

$$\widetilde{P}_i^{(3)}(\boldsymbol{r},\omega) = \frac{\varepsilon_0\chi_0}{(2\pi)^2}\iint_{-\infty}^{+\infty}\widetilde{R}_{ijkl}^{(3)}(\omega_2-\omega_1)\widetilde{E}_k^*(\boldsymbol{r},\omega_1)\widetilde{E}_l(\boldsymbol{r},\omega_2)\widetilde{E}_j(\boldsymbol{r},\omega+\omega_1-\omega_2)d\omega_1 d\omega_2. \tag{2.9}$$

## 2.2 General Wave Equation

The propagation of optical waves inside silica fibers is described by a dynamic equation called generalized nonlinear Schrödinger equation (GNLSE). Different versions of the derivation of such equation can be found in Refs. [6]-[8]. Here I provide a slightly different but more complete approach.

The propagation of an optical wave in a dielectric medium is governed by the wave equation

$$\nabla^2 \boldsymbol{E}_r - \frac{1}{c^2}\frac{\partial^2 \boldsymbol{E}_r}{\partial t^2} = \mu \frac{\partial^2 \boldsymbol{P}_r}{\partial t^2}. \tag{2.10}$$

Using the analytical representation in Eq. (2.3) and transferring Eq. (2.10) into the frequency domain, We obtain the nonlinear Helmholtz equation as

$$\nabla^2 \widetilde{\boldsymbol{E}}(\boldsymbol{r}, \omega - \omega_0) + \frac{\omega^2}{c^2}\overleftrightarrow{\epsilon}(\omega) \cdot \widetilde{\boldsymbol{E}}(\boldsymbol{r}, \omega - \omega_0) = -\mu\omega^2 \widetilde{\boldsymbol{P}}^{(3)}(\boldsymbol{r}, \omega - \omega_0), \tag{2.11}$$

where $\overleftrightarrow{\epsilon}$ accounts for the linear dispersive and material birefringent properties of the medium, and a tilde denotes a Fourier transform defined as $\widetilde{\boldsymbol{A}}(\boldsymbol{r}, \omega) = \int_{-\infty}^{+\infty} \boldsymbol{A}(\boldsymbol{r}, t)\exp(i\omega t)dt$ ($\boldsymbol{A} = \boldsymbol{E}$ or $\boldsymbol{P}$).

In optical fibers, the longitudinal component of the optical field is generally much smaller than the transverse one and the latter dominates the nonlinear effects. Thus, the electric field can be approximated as $\widetilde{\boldsymbol{E}} = [\widetilde{E}_x; \widetilde{E}_y]$, where we have assumed the propagation direction is the $z$ axis along the fiber length. Moreover, the eigenmodes of optical fibers can be decomposed as the product of transversely and longitudinally distributed components, *i.e.*,

$$\widetilde{E}_i(\boldsymbol{r}, \omega - \omega_0) = F_i(x, y, \omega)\widetilde{A}_i(z, \omega - \omega_0), \tag{2.12}$$

where $i = x, y$. Equation (2.12) together with the neglect of the longitudinal component $\widetilde{E}_z$ amounts to assuming negligible self-focusing inside fiber. This approximation is reasonable in most cases of wave propagation and interaction in silica fibers. Substituting Eq. (2.12) into Eq. (2.11), multiplying by $F_i^*$, and integrating over the transverse plane, we obtain the wave equation in the form

$$\frac{\partial^2 \widetilde{A}_i}{\partial z^2} + \left[\frac{\omega^2}{c^2}\overleftrightarrow{\epsilon}_{ij}(\omega) - \overleftrightarrow{\boldsymbol{k}}_{ij}(\omega)\right]\widetilde{A}_j = -\mu\omega^2 \frac{\iint F_i^* \widetilde{P}_i^{(3)} dxdy}{\iint |F_i|^2 dxdy}, \tag{2.13}$$

where $\overleftrightarrow{\boldsymbol{k}}(\omega)$ is a diagonal matrix with the elements $\overleftrightarrow{\boldsymbol{k}}_{ii}(\omega) = k_{ii}^2(\omega)$ defined as

$$k_{ii}^2(\omega) = -\frac{\iint F_i^* \nabla_T^2 F_i dxdy}{\iint |F_i|^2 dxdy}, \tag{2.14}$$

and the subscript $T$ denotes derivation operation over the transverse coordinates $x$ and $y$. Equation (2.14) can be solved for a specific fiber geometry and boundary conditions to obtain the tensor $\overleftrightarrow{\boldsymbol{k}}$ associated with a specific eigenmode[1], in particular, the fundamental mode. Different boundary conditions experienced by the $x$ and $y$ polarization components introduce geometric birefringence manifested as different

[1]This amounts to assuming that the coordinate $x$ and $y$ are along the symmetric axes of the fiber geometric configuration

magnitudes of the two diagonal elements of $\overleftrightarrow{\boldsymbol{k}}$. In general, the birefringence of optical fibers is very small (the modal index difference between the two polarization modes are at least three orders of magnitude smaller than the modal indices themselves [6]), and we can write

$$\frac{\omega^2}{c^2}\overleftrightarrow{\epsilon}(\omega) - \overleftrightarrow{\boldsymbol{k}}(\omega) = \beta^2(\omega)\overleftrightarrow{I} - \beta(\omega)\omega\overleftrightarrow{\boldsymbol{B}}, \tag{2.15}$$

where $\overleftrightarrow{\boldsymbol{B}}$ represents the birefringence properties of a fiber with the magnitude $\left|\det|\overleftrightarrow{\boldsymbol{B}}|\right| \ll [\beta(\omega)/\omega]^2$. Because of its small magnitude, we have neglected the frequency dependence of birefringence tensor.

In general, the third-order nonlinear effects are small and act as only perturbations to the linear wave propagation with a phase factor $e^{\pm i\beta(\omega)z}$ varying on a length scale of optical wavelength [see Eqs. (2.13) and (2.15)] (the sign depends on propagation direction: $+$ for forward propagation). This indicates that $\widetilde{\boldsymbol{A}}' \equiv \widetilde{\boldsymbol{A}}(z,\omega-\omega_0)e^{\mp i\beta(\omega)z}$ should be a slowly varying amplitude compared with the rapidly varying phase factor:

$$\left|\frac{\partial^2 \widetilde{\boldsymbol{A}}'}{\partial z^2}\right| \ll 2\left|\beta(\omega)\frac{\partial \widetilde{\boldsymbol{A}}'}{\partial z}\right|. \tag{2.16}$$

As a result, we can make the so-called slowly varying envelope approximation (SVEA) as follows[2]:

$$\frac{\partial^2 \widetilde{\boldsymbol{A}}}{\partial z^2} + \beta^2(\omega)\widetilde{\boldsymbol{A}} = \left[\frac{\partial^2 \widetilde{\boldsymbol{A}}'}{\partial z^2} + 2i\beta(\omega)\frac{\partial \widetilde{\boldsymbol{A}}'}{\partial z}\right] e^{i\beta(\omega)z} \approx 2i\beta(\omega)\left[\frac{\partial \widetilde{\boldsymbol{A}}}{\partial z} - i\beta(\omega)\widetilde{\boldsymbol{A}}\right]. \tag{2.17}$$

This approximation corresponds to assuming a forward-propagating wave (for backward propagation, change $\partial\widetilde{\boldsymbol{A}}/\partial z$ to $-\partial\widetilde{\boldsymbol{A}}/\partial z$). Under the SVEA, the wave equation (2.13) is simplified and takes the form

$$\frac{\partial \widetilde{A}_i}{\partial z} = i\beta(\omega)\widetilde{A}_i - \frac{i\omega}{2}\overleftrightarrow{\boldsymbol{B}}_{ij}\widetilde{A}_j + \frac{i\mu\omega^2}{2\beta(\omega)}\frac{\iint F_i^* \widetilde{P}_i^{(3)} dxdy}{\iint |F_i|^2 dxdy}. \tag{2.18}$$

Although different boundary conditions for the two polarization components introduce birefringence, $F_i(x,y,\omega)$ in general exhibits only a slight dependence on both the frequency and polarization for the two fundamental polarization modes (as indicated by a relatively small magnitude of birefringence compared with the model indices themselves). We can thus assume that, over a relatively broad bandwidth, $F_x(x,y,\omega_1) \approx F_y(x,y,\omega_2) \equiv F(x,y,\omega)$. As a result, the nonlinear polarization in Eq. (2.9) becomes

$$\widetilde{\boldsymbol{P}}^{(3)}(\boldsymbol{r},\omega) \approx \varepsilon_0\chi_0|F(x,y,\omega)|^2 F(x,y,\omega)\widetilde{\boldsymbol{P}}^{NL}(z,\omega), \tag{2.19}$$

where the normalized nonlinear polarization is given by

$$\widetilde{P}_i^{NL}(z,\omega) = \frac{1}{(2\pi)^2}\iint_{-\infty}^{+\infty} \widetilde{R}_{ijkl}^{(3)}(\omega_2-\omega_1)\widetilde{A}_k^*(z,\omega_1)\widetilde{A}_l(z,\omega_2)\widetilde{A}_j(z,\omega+\omega_1-\omega_2)d\omega_1 d\omega_2. \tag{2.20}$$

---

[2] The SVEA can be seen even more clearly by noticing that $\frac{\partial^2}{\partial z^2}+\beta^2 = \left(\frac{\partial}{\partial z}+i\beta\right)\left(\frac{\partial}{\partial z}-i\beta\right)$. SVEA means that $\left|\frac{\partial \widetilde{\boldsymbol{A}}'}{\partial z}\right| \ll 2\left|\beta(\omega)\widetilde{\boldsymbol{A}}'\right|$, which is the same as Eq. (2.16). As $\frac{\partial \boldsymbol{A}}{\partial z} = e^{\pm i\beta z}\frac{\partial \boldsymbol{A}'}{\partial z} \pm i\beta\boldsymbol{A}$, $\left(\frac{\partial}{\partial z}+i\beta\right)\boldsymbol{A} \approx 2i\beta\boldsymbol{A}$ for a forward-propagating wave and $\left(\frac{\partial}{\partial z}-i\beta\right)\boldsymbol{A} \approx -2i\beta\boldsymbol{A}$ for a backward-propagating one. As a result, $\left(\frac{\partial^2}{\partial z^2}+\beta^2\right)\boldsymbol{A} \approx \pm 2i\beta\left(\frac{\partial \boldsymbol{A}}{\partial z} \mp i\beta\boldsymbol{A}\right)$.

Substituting Eq. (2.19) into Eq. (2.18) and normalizing the field amplitude such that $|\boldsymbol{A}(z,t)|^2$ represents optical power, we find that the field amplitude vector $\widetilde{\boldsymbol{A}}(z,\omega-\omega_0)$ satisfies

$$\frac{\partial \widetilde{\boldsymbol{A}}}{\partial z} = i\beta(\omega)\widetilde{\boldsymbol{A}} - \frac{i\omega}{2}\overleftrightarrow{\boldsymbol{B}}\cdot\widetilde{\boldsymbol{A}} + \frac{i\omega}{\varepsilon_0 c^2 n(\omega_0) n(\omega) a_{\text{eff}}(\omega)}\widetilde{\boldsymbol{P}}^{NL}, \tag{2.21}$$

where we have used $\beta(\omega) = \omega n(\omega)/c$, and $n(\omega)$ is the modal index. $a_{\text{eff}}$ is the effective mode area defined as

$$a_{\text{eff}}(\omega) \equiv \frac{\left[\iint |F(x,y,\omega)|^2 dxdy\right]^2}{\iint |F(x,y,\omega)|^4 dxdy}. \tag{2.22}$$

Note that the optical field amplitude in Eq. (2.20) is now also normalized to the square root of optical power.

In the last term of Eq. (2.21), both the modal index and effective mode area depends on frequency and we can taylor-expand them to the first order of $\omega-\omega_0$. Equation (2.21) then reduces to a simple form of GNLSE in the frequency domain as

$$\frac{\partial \widetilde{\boldsymbol{A}}}{\partial z} = i\beta(\omega)\widetilde{\boldsymbol{A}} - \frac{i\omega}{2}\overleftrightarrow{\boldsymbol{B}}\cdot\widetilde{\boldsymbol{A}} + i\gamma\left[1+(\omega-\omega_0)\eta\right]\widetilde{\boldsymbol{P}}^{NL}, \tag{2.23}$$

where $\gamma$ is the nonlinear parameter defined as

$$\gamma(\omega_0) \equiv \frac{\chi_0\omega_0}{\varepsilon_0 c^2 n^2(\omega_0) a_{\text{eff}}(\omega_0)}. \tag{2.24}$$

Conventionally, the nonlinear parameter $\gamma(\omega_0)$ is defined through a nonlinear-index coefficient $n_2$ as $\gamma = n_2\omega_0/(c a_{\text{eff}})$ [6]. Compare it with Eq. (2.24), we find that $n_2(\omega_0) = \chi_0/[\varepsilon_0 c n^2(\omega_0)]$ in our notation. In Eq. (2.23), $\eta$ is related to the dispersion in the magnitude of fiber nonlinearity and is given by

$$\eta \equiv \frac{1}{\omega_0} + \frac{1}{n_2(\omega_0)}\left.\frac{dn_2}{d\omega}\right|_{\omega_0} - \frac{1}{a_{\text{eff}}(\omega_0)}\left.\frac{da_{\text{eff}}}{d\omega}\right|_{\omega_0}. \tag{2.25}$$

As the group index only slightly differs from the modal index in fibers, $\frac{\omega_0}{n(\omega_0)}\frac{dn}{d\omega} \approx 0.02$, the first term of Eq. (2.25) is much larger than the second term in general. The effective mode area also depends on frequency only slightly, unless the mode field diameter becomes much less than the optical wavelength [9, 10]. Therefore, Eq. (2.25) is dominated by the first term in most cases.

The first term on the right side of Eq. (2.23) governs the dispersive effect, one of the dominant effect in optical fibers. It can also include fiber losses and their dispersion if $\beta(\omega)$ is treated as complex, say, $\beta(\omega) \to \beta(\omega) + i\alpha(\omega)/2$. By Taylor-expanding the propagation constant $\beta(\omega)$ around the carrier frequency $\omega_0$ and transferring Eq. (2.23) into time domain, we obtain the GNLSE for the field amplitude $\boldsymbol{A}(z,t)$ in the time domain as

$$\frac{\partial \boldsymbol{A}}{\partial z} = \sum_{m=0}^{+\infty}\frac{i^{m+1}\beta_m}{m!}\frac{\partial^m \boldsymbol{A}}{\partial t^m} - \frac{i}{2}\overleftrightarrow{\boldsymbol{B}}\cdot\left(\omega_0 + i\frac{\partial}{\partial t}\right)\boldsymbol{A} + i\gamma\left[1+i\eta\frac{\partial}{\partial t}\right]\boldsymbol{P}^{NL}, \tag{2.26}$$

where $\beta_m$ is the $m^{th}$-order fiber dispersion given by $\beta_m = (d^m\beta/d\omega^m)|_{\omega_0}$, and the nonlinear polarization in time domain $\boldsymbol{P}^{NL}(z,t)$ can be obtained from Eq. (2.20) as:

$$P_i^{NL}(z,t) = A_j(z,t)\int_{-\infty}^{+\infty} R_{ijkl}^{(3)}(t-\tau)A_k^*(z,\tau)A_l(z,\tau)d\tau. \tag{2.27}$$

In Eq. (2.26), the first term describes the linear dispersive and loss effects; the second term represents birefringent effects and associated polarization-mode dispersion (PMD); the third term governs the Kerr nonlinearity and its dispersion. Equations (2.23) and (2.26) provide the theoretical basis for nonlinear effects in optical fibers and will be widely used in other chapters to discuss different nonlinear effects.

## 2.3 Wave Propagation: Quantum Case

In the last section, we have assumed an intense optical wave so that it can be treated as a classical field. In some cases, we need to investigate the fundamental noise properties associated with low-power electromagnetic fields in optical fibers. In these cases, the optical field needs to be quantized to account for the particle nature of photons. A general quantum theory of nonlinear optical phenomenon in optical fibers has been developed before in the context of soliton squeezing [11]–[13], starting from a Hamiltonian that includes the third-order nonlinear polarization and the background photon/phonon reservoirs. Here we only provide the final equations that will be used in this thesis. These equations can be obtained from the classical equations in the last section by simple physical arguments, although such a derivation may not be rigorous in the mathematical sense.

To deal with the photon interaction and photon statistics, it is generally convenient to work in the Heisenberg picture and normalize the optical field such that $\hat{A}_j^\dagger(z,\tau)\hat{A}_j(z,\tau)$ represents the operator for the photon flux for the $j^{th}$ polarization component, leading to the following communication relations for the field operator

$$[\hat{A}_j(z,\tau), \hat{A}_k^\dagger(z,\tau')] = \delta_{jk}\delta(\tau-\tau'), \tag{2.28}$$

$$[\hat{A}_j(z,\omega_u), \hat{A}_k^\dagger(z,\omega_v)] = 2\pi\delta_{jk}\delta(\omega_u-\omega_v), \tag{2.29}$$

in the time and spectral domain, respectively ($j,k = x,y$).

It turns out that the quantum version of wave equation exhibits a form quite similar to that presented in the last section, except for some minor changes related to a correct description of the quantum effects. First, the field operators in all the interaction terms need to be placed in a normal order to correctly count the quantum effects. Second, the Raman response of optical fibers results from the resonant interaction between photons and optical phonons. The participation of broadband thermal phonons in the interaction introduces noise. It is small and negligible when optical waves themselves are intense (as in the last section), but becomes important when we consider wave interactions at a level of only a few photons. Therefore, we need to introduce a noise operator into the GNLSE to correctly describe such Raman-induced noise. With these considerations and with the field normalization in Eq. (2.29), we obtain the quantum version of GNLSE in the spectral domain as [13]

$$\begin{aligned}\frac{\partial \hat{A}_i}{\partial z} &= i\sum_j \widetilde{R}^{(1)}_{ij}(\omega)\hat{A}_j(z,\omega) + \frac{i\sqrt{\hbar\omega_0}}{2\pi}\sum_j \int d\omega_1 \hat{m}_{ij}(z,\omega-\omega_1)\hat{A}_j(z,\omega_1) \\ &+ \frac{i\hbar\omega_0\gamma}{(2\pi)^2}\sum_{jkl}\iint d\omega_1 d\omega_2 \widetilde{R}^{(3)}_{ijkl}(\omega_2-\omega_1)\hat{A}^\dagger_k(z,\omega_1)\hat{A}_l(z,\omega_2)\hat{A}_j(z,\omega+\omega_1-\omega_2),\end{aligned} \tag{2.30}$$

where $\widetilde{R}^{(1)}_{ij}(\omega) \equiv \beta(\omega) - \omega\overleftrightarrow{B}_{ij}/2$ accounts for both the dispersive and birefringence effects and $\hat{m}_{ij}(z,\Omega)$ represents noise operator at phonon frequency $\Omega$, resulting from the presence of a phonon reservoir. Conservation of the commutation relation for the optical field in Eq. (2.29) at any point $z$ inside the optical fiber requires that $\hat{m}_{ij}(\Omega)$ satisfy the following commutation relation:

$$[\hat{m}_{ij}(z,\Omega_u),\hat{m}^\dagger_{kl}(z',\Omega_v)] = 2\pi\delta(z-z')\delta(\Omega_u-\Omega_v)\{g_a(\Omega_u)\delta_{ij}\delta_{kl} + \tfrac{1}{2}g_b(\Omega_u)(\delta_{ik}\delta_{jl}+\delta_{il}\delta_{jk})\}, \tag{2.31}$$

where $g_a$ and $g_b$ are Raman gain/loss coefficients corresponding to the isotropic and anisotropic Raman response functions $R_a$ and $R_b$, respectively, defined as $g_a(\Omega) = 2\gamma f_R \mathrm{Im}[\widetilde{R}_a(\Omega)]$ and $g_b(\Omega) = 2\gamma f_R \mathrm{Im}[\widetilde{R}_b(\Omega)]$. They are related to the Raman gain measured for linearly copolarized and orthogonally polarized pumps as [2] $g_\parallel = g_a + g_b$ and $g_\perp = g_b/2$.

Accordingly, by taking the Fourier transform of Eq. (2.30), we can obtain the quantum version of the GNLSE in the time domain as

$$\begin{aligned}\frac{\partial \hat{A}_i}{\partial z} &= i\sum_j \int_{-\infty}^{\tau} d\tau' R^{(1)}_{ij}(\tau-\tau')\hat{A}_j(z,\tau') + i\sqrt{\hbar\omega_0}\sum_j \hat{m}_{ij}(z,\tau)\hat{A}_j(z,\tau) \\ &+ i\hbar\omega_0\gamma\sum_{jkl}\int_{-\infty}^{\tau} d\tau' R^{(3)}_{ijkl}(\tau-\tau')\hat{A}^\dagger_k(z,\tau')\hat{A}_l(z,\tau')\hat{A}_j(z,\tau),\end{aligned} \tag{2.32}$$

where $R^{(1)}_{ij}$ is the Fourier transform of $\widetilde{R}^{(1)}_{ij}(\omega)$ and the time-dependent noise operator $\hat{m}_{ij}(\tau)$ now satisfies the commutation relation

$$[\hat{m}_{ij}(z,\tau),\hat{m}_{kl}(z',\tau')] = i\gamma\delta(z-z')\{R^{(3)}_{klij}(\tau'-\tau) - R^{(3)}_{ijkl}(\tau-\tau')\}. \tag{2.33}$$

Equations (2.30)-(2.33) represent the main results of this section. In the following chapters, we use them to investigate photon statistics of quantum-correlated photon pair generation in optical fibers, and to study the quantum noise properties of fiber-based parametric amplifiers.

## References


[1] R. Hellwarth, J. Cherlow, and T. Yang, Phys. Rev. B **11**, 964 (1975).

[2] R. W. Hellwarth, Prog. Quantum Electron. **5**, 1-68 (1977).

[3] L. Mandel and E. Wolf, *Optical coherence and quantum optics* (Cambridge, New York, 1995), Chap. 3.

[4] R. H. Stolen, J. P. Gordon, W. J. Tomlinson, and H. A. Haus, J. Osa. Soc. Am. B **6**, 1159 (1989).

[5] R. H. Stolen, in *Raman Amplifiers for Telecommunications 1*, M. N. Islam Ed. (Springer, New York 2003).

[6] G. P. Agrawal, *Nonlinear Fiber Optics*, $3^{rd}$ ed. (Academic, San Diego, CA, 2001).

[7] K. J. Blow and D. Wood, IEEE J. Quantum Electron. **25**, 2665 (1989).

[8] P. V. Mamyshev and S. V. Chernikov, Opt. Lett. **15**, 1076 (1990).

[9] N. A. Mortensen, Opt. Exp. **10**, 341 (2002).

[10] M. A. Foster, K. D. Moll, and A. L. Gaeta, Opt. Exp. **12**, 2880 (2004).

[11] L. Boivin, F. X. Kartner, and H. A. Haus, Phys. Rev. Lett. **73**, 240 (1994).

[12] F. X. Kartner, D. J. Dougherty, H. A. Haus, and E. P. Ippen, J. Opt. Soc. Am. B **11**, 1267 (1994).

[13] P. D. Drummond, in *Coherence and Quantum Optics VII*, J. H. Eberly, L. Mandel, and E. Wolf (Eds.) (Plenum Press, New York), 323 (1996).

# 3 Photon-Pair Generation In Optical Fibers

In this chapter, we present a general quantum theory [1, 2] capable of describing photon statistics under the combined effects of four-wave mixing (FWM) and Raman scattering inside optical fibers. As our theory is vectorial in nature and includes all polarization effects, it can be used for a wide variety of pumping configurations. The analysis shows that spontaneous Raman scattering degrades the pair correlation in all cases but the extent of degradation depends on the pumping configuration employed. We also present a theory to quantify the impact of such pair correlation on the degree of energy-time and polarization entanglement. This work is done in collaboration with Fatih Yaman in Prof. Agrawal's group.

## 3.1 Introduction

Entangled photon pairs are essential for quantum technologies requiring delivery of quantum information over significant distances [3]. Conventionally, such photon pairs are generated by spontaneous parametric downconversion in the visible region [4, 5]. However, practical implementation of quantum communication relies on its compatibility with fiber-optic networks operating around 1.55 $\mu$m [6]. Availability of correlated photon pairs in this wavelength regime thus becomes a key step towards practical applications of quantum technologies. Several techniques based on periodically poled lithium niobate crystals or waveguides [7, 8] have been used to realize such photon-pair sources. However, sources based on bulk media or rectangular waveguides often suffer from relatively large losses that occur from coupling their light into optical fibers [9].

The phenomenon of four-wave mixing (FWM) occurring inside optical fibers provides a natural way to generate correlated photon pairs in a single spatial mode directly inside fibers [10]–[20]. Indeed, FWM has been used to realize polarization entanglement [21, 22] as well as time-bin [23] entanglement.

Although FWM in principle should generate correlated photon pairs with an efficiency higher than other techniques [24]-[26], in practice, the performance of fiber-based photon-pair sources is severely deteriorated by the phenomenon of spontaneous Raman scattering (SpRS) that accompanies FWM inevitably [27]. SpRS originates from the retarded molecular response to the underlying third-order nonlinearity [28, 29], and it leads to a serious limitation on the available range of photon-pair frequencies and the degree of quantum correlation [10]–[20].

Existing theories cannot describe the impact of SpRS on photon-pair correlation because of a complete neglect of the Raman contribution [24]-[26]. For this reason, empirical fitting is widely used for the experimental data [10]–[20]. As FWM becomes a promising way towards creating fiber-based correlated photon sources, it is important to develop a general theory that can explain the experimental data and provide guidance for improving the performance of such sources. In this chapter, we develop a general quantum theory capable of describing photon statistics under the combined effects of FWM and Raman scattering inside optical fibers, including both the spontaneous and stimulated contributions. Moreover, our theory is vectorial in nature and includes all polarization effects. It can be used for a wide variety of pumping configurations.

In the following sections, we use the general equations (2.30) and (2.31) to investigate photon statistics under different pumping configurations. Same equations, or their simpler scalar form, has been successfully used to describe quantum squeezing in optical fibers [31, 35, 36], timing jitter in communication systems [37], and Raman noise in fiber-optic parametric amplifiers [27]. Here we use it to investigate the impact of SpRS on photon-pair generation through FWM inside optical fibers. The analysis can be simplified considerably if we notice that there are usually only three or four waves interacting with each other, depending on the pumping configuration. In the case of a photon-pair source, the pumps are always much more intense than the signal and the idler fields. Hence, they can be treated classically and assumed to remain undepleted. Moreover, in most experimental situations, the pump pulses are wide enough and fibers are short enough that the dispersion-induced pulse broadening is negligible. As a result, the pumps can be assumed to be quasi-continuous such that $A_j(z,\omega) = A_{pj}(z)2\pi\delta(\omega-\omega_p)$, where $\omega_p$ is the pump frequency. For convenience, we renormalize the pump field amplitude such that $|A_{pj}|^2$ provides the pump power of the $j^{th}$ polarization component at $\omega_p$. As short fibers are generally used for photon generation, we neglect fiber losses in the following analysis.

## 3.2 Single-Pump Configuration

In this section, we focus on the case in which FWM is induced by a single pump wave launched at $\omega_p$. Energy conservation requires $2\omega_p = \omega_s + \omega_i$, where $\omega_s$ and $\omega_i$ are frequencies of signal and idler

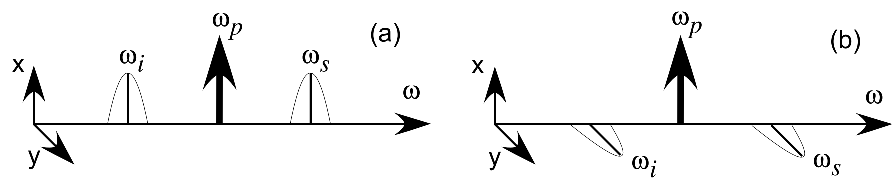


Figure 3.1: Illustration of the frequency and polarization relationship among the pump, signal and idler, in the single-pump configuration.

photons, respectively. We assume that the pump is linearly polarized along a principal axis of the fiber, say, the $x$ axis. It is easy to show [34] that the Kerr nonlinearity only imposes a phase modulation on the pump wave such that $A_{px}(z) = A_p\Phi(z)$, where $\Phi(z) = \exp\{i[k_x(\omega_p) + \gamma P_0]z\}$, $A_p$ is the input pump field amplitude, $P_0 = |A_p|^2$ is the pump power, and $k_x(\omega_p) \equiv \widetilde{R}^{(1)}_{xx}(\omega_p)$ is the propagation constant.

### 3.2.1 Signal and Idler Evolution

It turns out that the FWM process can be decoupled into two independent "eigen" processes shown in Fig. 3.1 such that the created photon pairs are polarized either (a) parallel or (b) orthogonal to the pump. Of course, the phase-matching condition for these two processes is not the same. The process (a) is phase-matched in practice by use of fiber dispersion through appropriately locating the pump wavelength. In contrast, the process (b) is affected considerably by fiber birefringence [34]. In the following analysis, we compare the two cases assuming that the phase-matched condition is individually satisfied for them.

If we use $\omega = \omega_s$ in Eq. (2.30) and retain only the first order terms at this frequency and at its conjugate frequency $\omega_i = 2\omega_p - \omega_s$, we obtain the Heisenberg equations for the two polarization components of the signal in the form

$$\frac{\partial \hat{A}_j(z,\omega_s)}{\partial z} = i[k_j(\omega_s) + \gamma\xi_j(\Omega_{sp})P_0]\hat{A}_j(z,\omega_s) + i\gamma\eta_j(\Omega_{sp})A_{px}^2\hat{A}_j^\dagger(z,\omega_i) + iA_{px}\hat{m}_{jx}(z,\Omega_{sp}), \quad (3.1)$$

where $j = x, y$, $k_j(\omega_s) = \widetilde{R}^{(1)}_{jj}(\omega_s)$ is the propagation constant at frequency $\omega_s$, and $\Omega_{sp} = \omega_s - \omega_p$ is the signal-pump frequency separation. The idler equation can be obtained by exchanging the subscripts $s$ and $i$.

The complex quantities $\xi_x$ and $\xi_y$ take into account the nonlinear phase shift produced by the pump through cross-phase modulation as well as the effects of Raman scattering. They are given by

$$\xi_x(\Omega_{sp}) = 2 - f_R + f_R\widetilde{R}_a(\Omega_{sp}) + f_R\widetilde{R}_b(\Omega_{sp}), \quad (3.2)$$

$$\xi_y(\Omega_{sp}) = 2(1 - f_R)/3 + f_R\widetilde{R}_a(0) + f_R\widetilde{R}_b(\Omega_{sp})/2. \quad (3.3)$$

The Raman effects enter through $\widetilde{R}_a$ and $\widetilde{R}_b$, as discussed in the previous chapter. In the absence of Raman contribution ($f_R = 0$), $\xi_x = 2$ and $\xi_y = 2/3$, as expected from the standard theory of cross-phase modulation [34]. Also note that $\xi_x(0) = 2$ even when Raman contribution is included because $\widetilde{R}_a(0) + \widetilde{R}_b(0) = 1$.

The FWM efficiency is related to $\eta_j$ and is different for the two eigen processes. More specifically,

$$\eta_x(\Omega_{sp}) = (1 - f_R) + f_R\widetilde{R}_a(\Omega_{sp}) + f_R\widetilde{R}_b(\Omega_{sp}), \tag{3.4}$$

$$\eta_y(\Omega_{sp}) = (1 - f_R)/3 + f_R\widetilde{R}_b(\Omega_{sp})/2. \tag{3.5}$$

In practice, the first term dominates, indicating that copolarized FWM is roughly three times more efficient than the orthogonally polarized one. For this reason, most recent experiments have focused on the copolarized configuration [21]–[19]. However, this approach has a serious drawback because SpRS is also maximized when the signal and idler are copolarized with the pump. Moreover, the Raman process also changes the refractive index through the Kramers–Kronig relation and thus affects the FWM efficiency [29]. The magnitude of $\eta_x$ decreases by about 20% when the signal is detuned far beyond Raman gain peak.

Equation (3.1) in combination with the corresponsing idler equation can be solved analytically because of their linear nature. The resulting solution for the signal amplitude at the end of a fiber of length $L$ is given by:

$$\hat{A}_j(L,\omega_s) = [\alpha_j(L,\omega_s)\hat{A}_j(0,\omega_s) + \beta_j(L,\omega_s)\hat{A}_j^{\dagger}(0,\omega_i) + \hat{N}_j(L,\omega_s)]\Phi(L), \tag{3.6}$$

where the first two terms are due to FWM but the last one describes the impact of Raman scattering. The coefficients appearing in this equation are given by [34]

$$\alpha_j(L,\omega_s) = [\cosh(g_jL) + (i\kappa_j/2g_j)\sinh(g_jL)]e^{iK_jL}, \tag{3.7}$$

$$\beta_j(L,\omega_s) = (i\gamma\eta_j/g_j)A_p^2\sinh(g_jL)e^{iK_jL}, \tag{3.8}$$

$$\hat{N}_j(L,\omega_s) = i\int_0^L \hat{m}_{jx}(z,\Omega_{sp})[A_p\alpha_j(L-z,\omega_s) - A_p^*\beta_j(L-z,\omega_s)]dz, \tag{3.9}$$

where the parametric gain coefficient $g_j$ is given by $g_j^2 = (\gamma\eta_jP_0)^2 - (\kappa_j/2)^2$ and $K_j = [k_j(\omega_s) - k_j(\omega_i)]/2$. Further, the extent of phase mismatch is governed by

$$\kappa_j = k_j(\omega_s) + k_j(\omega_i) - 2k_x(\omega_p) + 2\gamma P_0(\xi_j - 1). \tag{3.10}$$

In practice, the signal and idler fields are filtered spectrally to limit their bandwidth using an optical filter. The filtered field can be written as

$$\hat{A}_{uj}(z,\tau) = \frac{1}{2\pi}\int_{-\infty}^{\infty} H_u(\omega - \bar{\omega}_u)\hat{A}_j(z,\omega)\exp(-i\omega\tau)d\omega, \tag{3.11}$$

where $H_u(\omega - \bar{\omega}_u)$ is the filter transmission function centered at $\bar{\omega}_u$ ($u = s, i$) and assumed to be polarization independent. In the following discussion, we denote the signal as the anti-Stokes wave and assume $\bar{\omega}_s > \omega_p$. The idler field then lies, by definition, on the Stokes side of the pump.

### 3.2.2 Photon-Pair Generation rate

As the two FWM processes in Fig. 3.1 have the same form of solution, we simplify the following analysis by dropping the polarization subscript $j$ in Eqs. (3.6)–(3.11). The two cases shown in Fig. 3.1 can be compared by choosing the appropriate form of $\xi_j$, $\eta_j$, $\kappa_j$, and $g_j$ with $j = x$ or $y$. The generation rate of photon pairs is related to the photon flux $I_u$, defined as $I_u \equiv \langle \hat{A}_u^\dagger(L,\tau)\hat{A}_u(L,\tau)\rangle$, where $u = s$ for signal photons, $u = i$ for idler photons, and the angle brackets denote average with respect to the vacuum input state and a thermally populated phonon reservoir. Such an average can be performed analytically and results in the following expression:

$$I_u = \frac{1}{2\pi}\int_{-\infty}^{\infty} |H_u|^2 \ \{ \ |\beta_u|^2 + \mathscr{N}(\Omega_{up})\mathrm{sgn}(\Omega_{up})[1 + |\beta_u|^2 - |\alpha_u|^2]\} d\omega_u, \tag{3.12}$$

where $H_u \equiv H_u(\omega_u - \bar{\omega}_u)$, $\alpha_u \equiv \alpha(L, \omega_u)$, $\beta_u \equiv \beta(L, \omega_u)$, $\mathrm{sgn}(\Omega_{uv}) = \pm 1$ depending on the sign of $\Omega_{uv}$, and

$$\mathscr{N}(\Omega_{uv}) = \begin{cases} n(\Omega_{uv}) & \text{when } \Omega_{uv} > 0, \\ n(\Omega_{uv}) + 1 & \text{when } \Omega_{uv} < 0. \end{cases} \tag{3.13}$$

Here $n(\Omega_{uv}) = [\exp(\hbar|\Omega_{uv}|/k_BT) - 1]^{-1}$ is the phonon population at frequency $\Omega_{uv} = \omega_u - \omega_v$ and at temperature $T$. As the magnitude of $\beta$ in Eq. (3.8) is determined by the phase-matching condition, photon flux peaks at the location where this condition is satisfied.

Equation (3.12) is quite general as it includes both the spontaneous and stimulated processes. For correlated photon-pair generation, the pump power is kept low enough that $\gamma P_0 L \ll 1$ to prevent stimulated scattering. Moreover, the filters have a bandwidth much narrower than the phase-matching bandwidth and are positioned at the center of phase-matching window where $\mathrm{Re}(\kappa) \approx 0$. In this case, Eq. (3.12) reduces to

$$I_u = \Delta\nu_u(|\gamma P_0 \eta_u L|^2 + P_0 L|g_R|\mathscr{N}_{up}), \tag{3.14}$$

where $\eta_u$, $g_R$, and $\mathscr{N}_{up}$ are calculated at the frequency $\bar{\Omega}_{up} = \bar{\omega}_u - \omega_p$ ($u = s, i$) and the filter bandwidth $\Delta\nu_u$ is defined as $\Delta\nu_u = \int |H_u(\omega - \bar{\omega}_u)|^2 d\omega/2\pi$. $g_R = g_\parallel$ and $g_\perp$ for the processes shown in Fig. 3.1(a) and (b), respectively.

When pump pulses of duration of $\tau_p$ at a repetition rate of $B$ are used (for a continuous pump, $\tau_p B = 1$), the photon counting rate is related to $I_u$ as $\mathscr{R}_u = (\zeta_u \tau_p B) I_u$ [24], where $\zeta_u$ is the detection

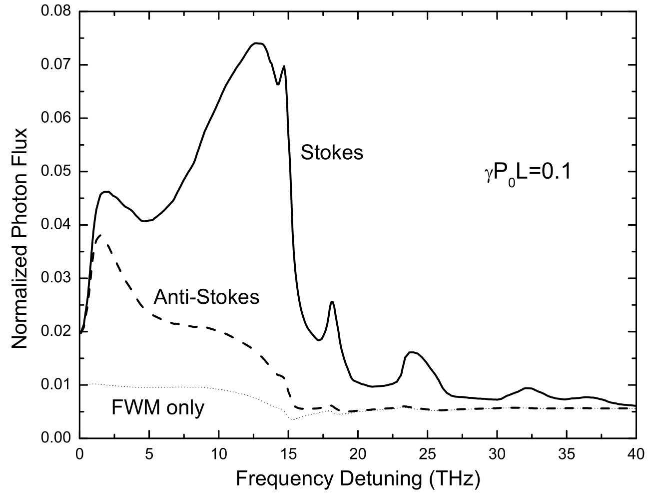


Figure 3.2: Normalized photon flux as a function of pump-signal detuning. The solid and dashed curves show photon flux for idler (Stokes) and signal (anti-Stokes), respectively. The thin dotted curve show for comparison that created by FWM only [the first term of Eq. (3.14)].

efficiency. As expected, the photon counting rate consists of two terms: one originates from FWM and grows quadratically with both pump power $P_0$ and fiber length $L$; the other is due to SpRS and grows only linearly with the product $P_0L$.

Figure 3.2 shows the normalized photon flux defined as $I_\mu/\Delta\nu_\mu$ at a typical pumping level of $\gamma P_0 L = 0.1$, which corresponds to a 1.25-GHz photon flux created by FWM with a 1-nm filter at 1550 nm and with a continuous-wave pump. The fiber parameters used in the 1550-nm regime are $n_2 = 2.6 \times 10^{-20}\mathrm{m}^2/\mathrm{W}$, a peak Raman gain of $0.62 \times 10^{-13}\mathrm{m/W}$ [34, 39, 40], and a temperature of $T = 300$ K. The Raman spectra are taken from Ref. [28]. The photon pair is assumed to be created copolarized with the pump. When $|\bar{\Omega}_{up}|/2\pi < 2$ THz, the phonon population $n(\bar{\Omega}_{up}) \gg 1$ and SpRS generates similar amount of signal and idler photons. When $|\bar{\Omega}_{up}|/2\pi > 2$ THz, $n(\bar{\Omega}_{up}) \ll 1$ and SpRS creates much more noise photons on the idler (Stokes) than the signal (anti-Stokes). Moreover, below 15-THz frequency detuning, SpRS noise photon flux is significantly larger than that created by FWM in both signal and idler, especially in the low-frequency regime. It is negligible for the signal beyond 15 THz, but still contributes considerable amount to the idler at the Stokes side. Although such dominance of SpRS can be reduced by increasing pump power, it also significantly reduces the photon-pair quality because of an increased stimulated scattering (see next section). As a result, SpRS remains as a dominant degradation source for the correlated photon-pair generation.

### 3.2.3 Self- and Cross-Correlation Coefficients

An important way to characterize the quality of a photon-pair source is the degree of quantum correlation, given by the ratio between the true coincidence counting and the accidental one. Consider first the self-correlation coefficient of the signal (or idler) photons defined as [41]

$$\rho_u(\tau) = \langle \hat{A}_u^\dagger(L,t)\hat{A}_u^\dagger(L,t+\tau)\hat{A}_u(L,t+\tau)\hat{A}_u(L,t)\rangle / I_u^2 - 1, \tag{3.15}$$

where $u = s$ and $i$ for the signal and idler photons, respectively. As before, the average can be calculated analytically using Eqs. (3.6)–(3.11) to yield

$$\rho_u(\tau) = \frac{1}{(2\pi I_u)^2}\left|\int_{-\infty}^{\infty} |H_u|^2[|\beta_u|^2 + \mathscr{N}(\Omega_{up})\text{sgn}(\Omega_{up})(1+|\beta_u|^2 - |\alpha_u|^2)]e^{-i\omega_u\tau}d\omega_u\right|^2. \tag{3.16}$$

For optical filters with a bandwidth much narrower than the phase-matching bandwidth, $\alpha_u$ and $\beta_u$ can be treated as constant. In this case, the self-correlation coefficient reduces to a remarkably simple expression $\rho_u(\tau) = |\varphi_u(\tau)|^2$, where $\varphi_u(\tau)$ is the autocorrelation function of the filter response defined as

$$\varphi_u(\tau) = \frac{1}{2\pi\Delta\nu_u}\int_{-\infty}^{\infty} |H_u(\omega_u - \bar{\omega}_u)|^2 e^{-i\omega_u\tau}d\omega_u. \tag{3.17}$$

It is easy to show that $\rho_u(\tau) \le \rho_u(0) = 1$. Thus, the signal as well as the idler photons exhibit bunching effect, irrespective of whether they are created through FWM or SpRS. This is expected as the state of spontaneously generated photons is a thermal state [62]. Indeed, such thermal nature is directly reflected in the general expression Eq. (3.16), as it can be written in a simple form of $\rho_u(\tau) = |\langle \hat{A}_u^\dagger(L,t+\tau)\hat{A}_u(L,t)\rangle|^2/I_u^2$.

Because of the thermal nature of spontaneous scattering (both FMW and SpRS), a Hanbury-Brown–Twiss type experiment measuring photon self-correlation cannot be used to test the dominance of single photons or to show the existence of SpRS. Note that the self-correlation is also independent of pump power when narrowband filters are used. The decrease in the experimentally recorded values at low pump powers observed in Ref. [19] is likely due to dark counting.

Although photons generated by FWM as well as SpRS follow a thermal distribution, FWM-generated signal photons are strongly correlated with the idler photons but SpRS-generated ones are not. This quantum correlation between the signal and idler photons is quantified by the cross-correlation coefficient defined as [41]

$$\rho_c(\tau) = \langle \hat{A}_i^\dagger(L,t)\hat{A}_s^\dagger(L,t+\tau)\hat{A}_s(L,t+\tau)\hat{A}_i(L,t)\rangle / (I_sI_i) - 1, \tag{3.18}$$

where $\langle \hat{A}_i^\dagger(L,t)\hat{A}_s^\dagger(L,t+\tau)\hat{A}_s(L,t+\tau)\hat{A}_i(L,t)\rangle$ is the biphoton probability of signal-idler pair. By using Eqs. (3.6)–(3.9), the pair correlation in its most general form is given by

$$\rho_c(\tau) = \frac{1}{(2\pi)^2 I_sI_i}\left|\int_{-\infty}^{\infty} \mathscr{H}(\omega_s)[\alpha_i\beta_s + \mathscr{N}(\Omega_{sp})\text{sgn}(\Omega_{sp})(\alpha_i\beta_s - \alpha_s\beta_i)]e^{-i\omega_s\tau}d\omega_s\right|^2, \tag{3.19}$$

where $\mathscr{H}(\omega_s) \equiv H_s(\omega_s - \bar{\omega}_s)H_i(\omega_i - \bar{\omega}_i)$ with $\omega_i = 2\omega_p - \omega_s$. As the magnitudes of $\alpha$ and $\beta$ are maximized when the FWM efficiency is maximum, $\rho_c$ peaks when the center frequencies of the two filters are tuned to the centers of phase-matched spectral window with $\bar{\omega}_s + \bar{\omega}_i = 2\omega_p$. The magnitude of $\rho_c$ decreases when either filter is detuned away from this condition, as also observed experimentally in Refs. [18] and [19]. It turns out that Eq. (3.19) can be written in a simple form of $\rho_c(\tau) = |\langle \hat{A}_s(L,t+\tau)\hat{A}_i(L,t)\rangle|^2/(I_sI_i)$. This is a direct result of the thermal nature of spontaneous scattering.

The general expression in Eq. (3.19) can be used to find the quantum correlation under low-power conditions such that $\gamma P_0 L \ll 1$. Far from the phase-matching condition ($|\Delta kL| \gg 1$), FWM becomes negligible, and SpRS dominates. In this case, Eq. (3.19) reduces to

$$\rho_c(\tau) = |\varphi_c(\tau)|^2 \left[\frac{\sin(\Delta kL/2)}{\Delta kL/2}\right]^2 \frac{\gamma^2|\mathrm{Re}(\eta_s)/g_R|^2 + (n+1/2)^2}{n(n+1)}, \tag{3.20}$$

where $\Delta k = k(\omega_s) + k(\omega_i) - 2k(\omega_p)$ is the linear phase mismatch and $\varphi_c(\tau)$ is the cross-correlation of the two filter responses defined as

$$\varphi_c(\tau) = \frac{1}{2\pi\sqrt{\Delta\nu_s\Delta\nu_i}} \int_{-\infty}^{\infty} H_s(\omega - \bar{\omega}_s)H_i(\bar{\omega}_s - \omega)e^{-i\omega\tau}d\omega. \tag{3.21}$$

Clearly, $\rho_c \to 0$ for $|\Delta kL| \gg 1$, indicating independent creation of the signal and idler photons. This is expected in view that they are generated from thermal phonon states.

To generate correlated photon pairs, the signal and idler are tuned to the phase-matching peak. Equation (3.19) in this case reduces to

$$\rho_c(\tau) = \frac{|\varphi_c(\tau)|^2\{[\gamma\mathrm{Re}(\eta_s)]^2 + |g_R(n+1/2)|^2\}}{[|\gamma\eta_s|^2P_0L + |g_R|(n+1)][|\gamma\eta_s|^2P_0L + |g_R|n]}. \tag{3.22}$$

The pair correlation decreases with increased pump power because of an increased probability of multiphoton generation, as observed experimentally [13, 18, 19]. SpRS introduces considerable accidental coincidence counting and thus reduces the correlation magnitude. For a pure FWM process without SpRS, $\eta_s$ is real and the pair correlation reduces to $\rho_c(\tau) = |\varphi_c(\tau)|^2/|\gamma\eta_s P_0 L|^2$.

### 3.2.4 Two Polarization Configurations

Figure 3.3 shows $\rho_c(0)$ as a function of pump-signal detuning for the two polarization configurations of Fig. 1 at a typical pumping level of $\gamma P_0 L = 0.1$, assuming an identical shape for the two optical filters so that $|\varphi_c(0)|^2 = 1$. As mentioned earlier in previous section, the FWM efficiency is reduced roughly by a factor of 3 in the case of orthogonal configuration. For a fair comparison of the two configurations, we increase the input pump power $P_0$ by a factor of 3 in the orthogonal case to ensure that FWM creates nearly the same number of photons in the two cases.

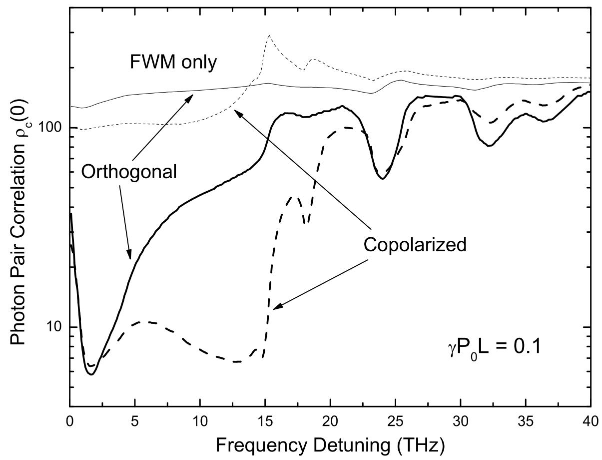


Figure 3.3: Pair correlation $\rho_c(0)$ versus pump-signal detuning, assuming perfect phase matching in a fiber same as Fig. 3.2. The dashed and solid curves show the copolarized and orthogonally polarized cases, respectively. The thin dotted and dash-dotted curves show for comparison the pair correlation of FWM-created photons only, in the configuration of Fig. 3.1(a) and (b), respectively. A slight difference between them is due to different Raman-induced nonlinearity dispersion.

Several conclusions can be drawn from Fig. 3.3. In general, SpRS degrades photon pair correlation over very broad spectrum extending from 0 to 40 THz, if the photon-pair is created copolarized to the pump. When the signal is close to the pump (frequency detuning $<1$ THz), pair correlation is reduced by more than 50%, compared with a pure FWM process (thin dashed curve). For example, Eq. (3.22) shows that pair correlation is about 12 at a frequency detuning of 0.5 THz for a typical value of $\gamma P_0 L = 0.15$, but it reduces to 3.5 when $\gamma P_0 L$ increases to 0.4, indicating that the recent experiments operating in this regime are close to the fundamental limit set by SpRS [12, 13, 18]. For frequency detunings $>2$ THz, the magnitude of copolarized Raman gain grows rapidly and leads to more SpRS-created idler photons, even though SpRS creates less signal photons because of a reduction in the phonon population (see Fig. 3.2). As a result, the accidental counting rate becomes large in the copolarized case (dashed curves), and the correlation drops to a rather low value over a broad spectral range extending from 2 to 15 THz. This degradation is a direct consequence of enhanced SpRS in the copolarized configuration of Fig. 3.1.

As seen in Fig. 3.3, $\rho_c(0)$ increases to high values when the signal is detuned far beyond the Raman-gain peak (but with a $\sim$40% reduction in the FWM-generated photons because of a Raman-induced decrease in the FWM efficiency, see Fig. 3.2). SpRS only has a minor effect at this spectral region. For example, near 30 THz, $\rho_c(0)$ varies from 39 to 138 for $\gamma P_0 L$ in the range of 0.1–0.2; it can be increases to 450 when $\gamma P_0 L$ is decreased to 0.05. For this reason, several experiments have been designed to operate in this regime [14, 19, 15]. As an example, consider the data of Ref. [19]. With a pump-signal detuning of 28 THz near 735 nm, Eq. (3.22) shows that $\rho(0) = 2105$, 42 and 17 for $\gamma P_0 L = 0.0155$, 0.19 and 0.31, respectively (corresponding to average power levels of 0.05, 0.6 and 1 mW in Ref. [19], respectively). These values are higher than the experimentally measured correlation of 300, 23 and 10 at these power levels, implying the possibility of further experimental improvement in this spectral regime.

A relatively large difference between the theoretical and experimental values of $\rho_c(0)$ at the lowest power level can be attributed to dark counting that tends to dominate at low photon-detection rates [23]. In practice, the photon counting rate is given by $\mathscr{R}'_u = \mathscr{R}_u + \mathscr{R}_{du}$ $(u = s, i)$, where $\mathscr{R}_{du}$ is the dark count rate. The presence of dark counts increases the accidental coincidence counting rate given by $\mathscr{R}_{ac}(\tau_0) = \int_{\tau_0}^{\tau_0+\tau_c} \mathscr{R}'_s \mathscr{R}'_i d\tau$, where $\tau_c$ is the coincidence time window. However, it does not affect the true coincidence counting rate provided by $\mathscr{R}_{tc}(\tau_0) = \zeta_s \zeta_i \tau_p B \int_{\tau_0}^{\tau_0+\tau_c} I_s I_i \rho_c(\tau) d\tau$. The experimental recorded value $\rho'_c(\tau)$ is the ratio $\mathscr{R}_{tc}/\mathscr{R}_{ac}$. If the real photon detection rate dominates ($\mathscr{R}_u \gg \mathscr{R}_{du}$), $\rho'_c$ would be close to $\rho_c$ given in Eqs. (3.19) and (3.22). However, if $\mathscr{R}_u < \mathscr{R}_{du}$ at low pump levels, $\rho'_c$ would be significantly lower than $\rho_c$.

Figure 3.3 shows that high-quality photon pairs can be generated with copolarized FWM only when signal is far from the pump (detuning >20 THz). However, the quality of photon pairs can be maintained at a high level over a broad spectral region below 20 THz when they are generated with polarization orthogonal to the pump (solid curves). This improvement is due to the fact that the Raman gain is almost negligible in the orthogonal configuration [28], a feature that improves $\rho_c(0)$ considerably. The most improvement occurs in the detuning range of 5 to 15 THz, the same range where the copolarized configuration is the worst. Near the copolarized Raman-gain peak close to 13 THz, the quantum correlation can be increased from a value of 7 to more than 60 for $\gamma P_0 L = 0.1$.

In practice, phase matching in the orthogonal configuration of FWM can be realized using low-birefringence fibers [42, 43]. Detailed analysis of Eq. (3.10) shows that the phase mismatch is determined by both the birefringence and even-order dispersion at the pump frequency given as

$$\begin{aligned}\kappa_y &= k_y(\omega_s) + k_y(\omega_i) - 2k_x(\omega_p) + 2\gamma P_0(\xi_y - 1) \\ &= 2\gamma P_0(\xi_y - 1) + 2\frac{\omega_p}{c}\delta n + 2\sum_{m=1}^{+\infty} \frac{\beta_{2m}\Omega_{sp}^{2m}}{(2m)!},\end{aligned} \tag{3.23}$$

where $\delta n = n_y(\omega_p) - n_x(\omega_p)$ is the birefringence and $\beta_{2m}$ is the $(2m)^{th}$-order dispersion at $\omega_p$ for the $y$ principal axis. In the low power regime for photon-pair generation, nonlinear phase shift has negligible effect on the phase matching condition which is dominated by fiber birefringence and dispersion. Figure 3.4 shows examples of phase-matched pump-signal detuning as a function of pump wavelength inside a fiber with different magnitude of birefringence using $\beta_3 = 0.06541$ ps$^2$/km, $\beta_4 = -1.0383 \times 10^{-4}$ ps$^4$/km, $\beta_5 = 3.3756 \times 10^{-7}$ ps$^5$/km, $\beta_6 = -1.1407 \times 10^{-10}$ ps$^6$/km, and $\gamma = 23$ W$^{-1}$/km at the

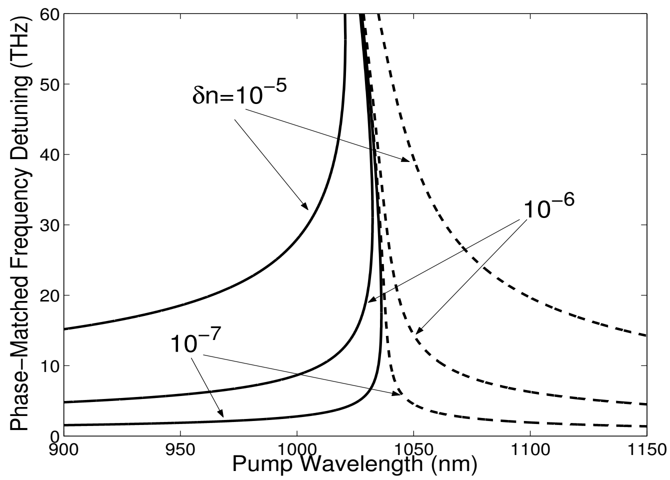


Figure 3.4: Phase matching curves as a function of pump wavelength. The pump is launched at the slow-axis ($\delta n < 0$) for solid curves and at the fast-axis ($\delta n > 0$) for dashed curves. Fiber dispersion is assumed to be same for both axes.

zero-dispersion wavelength of 1038 nm [44]. Clearly, phase-matching condition can be satisfied at a variety of pump-signal detunings by tuning the pump wavelength and polarization. Note that conventional standard or dispersion-shifted fibers with random birefringence cannot be used for realizing the orthogonal configuration studied here because the relative polarization orientation of the pump, signal, and idler changes in a random manner when a long fiber is employed [45, 46]. In practice, a fiber with random birefringence can be used only if its length is shorter than the birefringence correlation length.

In this case of orthogonal polarized FWM, SpRS still creates noise photons that are copolarized with the pump, but this noise background can be removed by simply placing polarizers oriented orthogonal to the pump before the signal and idler photons reach the two detectors. It is important to stress that, although the signal and idler fields are polarized orthogonal to the pump polarization, their spectra remain symmetric, as dictated by the fiber dispersion [34] [see Eq. (3.23)]. Thus, the proposed scheme does not suffer from the distinguishability induced by spectral asymmetry in the type-II phase matching used for $\chi^{(2)}$-based devices [47, 48]. One issue that needs to be addressed is the amount of walk off between the pump and signal/idler; it can be controlled in practice by using longer pump pulses.

### 3.2.5 Effect of Fiber Temperature

Equation (3.14) and (3.22) show that SpRS-created noise photon and its impact on pair correlation are both related to the phonon population, which strongly depends on fiber temperature. Hence, SpRS can be significantly reduced by cooling the fiber, as recently demonstrated in experiments [16, 17]. Figure 3.5

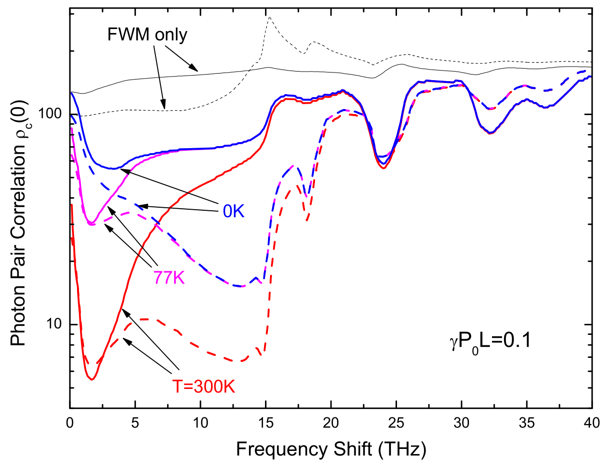


Figure 3.5: Pari correlation $\rho_c(0)$ versus pump-signal detuning, assuming perfect phase matching in a fiber same as Fig. 3.2. The dashed and solid curves show the copolarized and orthogonally polarized cases, respectively. The thin dotted curve shows for comparison of pair correlation of FWM-created photons only, in the copolarized configuration.

shows pair correlation at three temperatures. As phonon population inversely exponentially depends on pump-signal frequency detuning, it has most effect at low frequency detuning, leading to strong temperature dependence below 5 THz. By reducing the fiber temperature to that of liquid nitrogen at 77K, pair correlation can be enhanced by up to 5 times around this regime. However, it has negligible effect when frequency detuning is large. Moreover, SpRS can not be completely eliminated by reducing the temperature. This can be seen by the curves at zero temperature, where SpRS still remains a significant effect over a broad spectral region. This is because SpRS for the idler at the Stokes side is dominantly coupled to the ground state of phonon, which always introduces noise photons irrespective of fiber temperature, although SpRS can be nearly eliminated for the signal at the anti-Stokes side.

## 3.3 Dual-Pump Configuration

One advantage of the FWM in optical fibers compared with a $\chi^{(2)}$-based process is that it allows for the use of two pumps with different frequencies and polarization states. In fact, a dual-pump configuration is used routinely for classical, fiber-based parametric amplification and wavelength conversion [49]-[52]. Even when the pumps are copolarized, the dual-pump configurations shown schematically in Fig. 3.6 may offer some advantages. For example, unlike the single-pump configuration in which the signal and idler photons are always created on opposite sides of pump frequency, and are thus distinguishable on the basis of their frequencies, two photons at the same frequency can be obtained by placing a filter

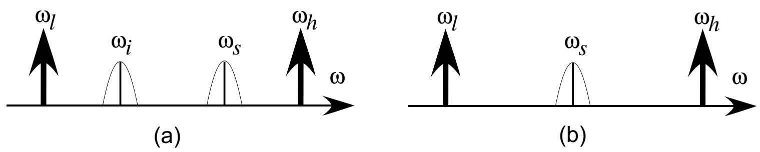


Figure 3.6: Illustration of the frequency relationship in the two copolarized pumping configuration.

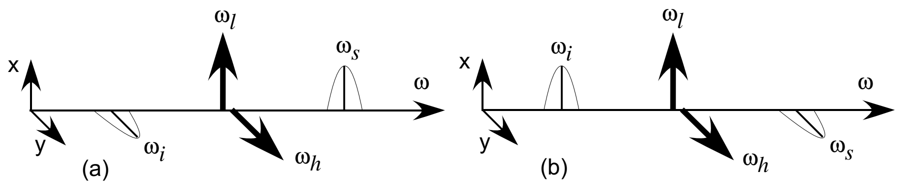


Figure 3.7: (a) and (b) Illustration of the frequency and polarization relationship among the pumps, signal and idler, in the orthogonal pumping configuration.

at the center frequency of the two pumps [18], as shown schematically in Fig. 3.6(b). On the other hand, when two separate pump beams are used, it becomes possible to align the polarizations of two pumps orthogonal to each other (see Fig. 3.7). This scheme is often used for polarization-independent operation of a classical parametric amplifier [49, 51]. Because of a spin-conservation requirement for the four interacting photons, the signal and idler photons must also be orthogonally polarized, although their individual state of polarizations (SOPs) can be arbitrary [53]. This feature provides a simple way to realize polarization entanglement automatically. In this section, we investigate the general case in which two pumps are launched into an optical fiber for creating correlated photon pairs.

### 3.3.1 Signal and Idler Equations

We assume that the two pumps at frequencies $\omega_l$ and $\omega_h$ are launched either along a principal axis of a birefringent fiber (say, the $x$ axis) for copolarized pumping or along two principal axes for orthogonal pumping. In the latter case, we assume the low-frequency pump is polarized along the $x$ axis, as shown in Fig. 3.7. In both cases, the two pumps maintain their SOPs along the fiber. Unlike the case of a single pump discussed in the last section, the two pumps can interact with each other through the fiber nonlinearity. From Eq. (2.30), the pump fields, $A_{lx}(z)$ and $A_{hx}(z)$ [or $A_{hy}(z)$, depending on pumping configuration] are found to satisfy

$$\frac{\partial A_{uj}}{\partial z} = i\,[k_j(\omega_u) + \gamma P_u + \gamma \xi_q(\Omega_{uv}) P_v] A_{uj}, \tag{3.24}$$

where $u \neq v$ and $\Omega_{uv} = \omega_u - \omega_v$. $j = q = x$ for copolarized pumping, but for orthogonal pumping, $q = y$, while $j = x$ when $u = l$ but $j = y$ when $u = h$. Eq. (3.24) can be easily solved to obtain the solution for the pump power in the form

$$P_u(z) = \frac{P_0 P_u(0)}{P_u(0) + P_v(0)\exp[g_\varepsilon(\Omega_{uv})P_0 z]}, \tag{3.25}$$

where $P_0 = P_l(z) + P_h(z)$ is the total input pump power that remains constant along the fiber, and $\varepsilon$ denotes $\parallel$ and $\perp$ for copolarized and orthogonal pumping, respectively.

As seen from Eq. (3.25), the two pumps transfer powers between them through stimulated Raman scattering (SRS). However, in a realistic experiment on photon-pair generation, the pump powers are maintained at a low level to prevent stimulated contribution. Under such conditions, $|g_\varepsilon(\Omega_{hl})P_0 L| \ll 1$, and the extent of SRS-induced pump power transfer is small. For an example of copolarized pumping, SRS only transfers 12% of the high-frequency pump power to the other one even when $\gamma P_0 L$ has a relatively large value of 0.5 and the second pump is located at the Raman gain peak ($|\Omega_{hl}|/2\pi = 13.2$ THz). In most cases, $\gamma P_0 L$ is smaller and pump frequency spacing is far from being 13.2 THz, resulting in negligible SRS-induced power transfer between the two pumps. For the case of orthogonal pumping, such Raman-induced power transfer is even much smaller [28]. Under such conditions, $\xi_q(\Omega_{uv}) \approx \xi_q(0)$, and $P_u(z) \approx P_u(0)$. The pump fields then evolve along the fiber as

$$A_{uj}(z) \approx A_u \exp\{iz[k_j(\omega_u) + \gamma P_u + \gamma \xi_q(0) P_v]\}, \tag{3.26}$$

where $A_u$ is the input pump amplitude at $\omega_u$.

Energy conservation during non-degenerate FWM requires $\omega_s + \omega_i = \omega_l + \omega_h$. From Eq. (2.30), the two polarization components of the signal wave are found to satisfy the following Heisenberg equation:

$$\begin{aligned}\frac{\partial \hat{A}_j(z,\omega_s)}{\partial z} &= i[k_j(\omega_s) + \gamma \xi_j(\Omega_{sl})P_l + \gamma \xi_q(\Omega_{sh})P_h]\hat{A}_j(z,\omega_s) + i\gamma \eta_j(\omega_s) A_{lx} A_{h\sigma} \hat{A}_q^\dagger(z,\omega_i) \\ &+ iA_{lx}\hat{m}_{jx}(z,\Omega_{sl}) + iA_{h\sigma}\hat{m}_{j\sigma}(z,\Omega_{sh}),\end{aligned} \tag{3.27}$$

where $j,q = x,y$, $q = j$ for copolarized pumping and $q \neq j$ for orthogonal pumping. $\sigma$ denotes the SOP of the high-frequency pump: $\sigma = x$ and $y$ for copolarized and orthogonal pumping, respectively. As before, the idler equation is obtained from Equation (3.27) by interchanging subscripts $s$ and $i$. In Eq. (3.27), $\eta_j(\omega_s) \equiv \eta_j(\Omega_{sl}) + \eta_j(\Omega_{sh})$ for copolarized pumping, where both $\eta_j(\Omega_{sl})$ and $\eta_j(\Omega_{sh})$ are given by either Eq. (3.4) or (3.5), depending on signal polarization. However, in the orthogonal pumping configuration, $\eta_j(\omega_s)$ becomes

$$\eta_x(\omega_s) = 2(1-f_R)/3 + f_R\widetilde{R}_a(\Omega_{sl}) + f_R\widetilde{R}_b(\Omega_{sh})/2, \tag{3.28}$$

$$\eta_y(\omega_s) = 2(1-f_R)/3 + f_R\widetilde{R}_a(\Omega_{sh}) + f_R\widetilde{R}_b(\Omega_{sl})/2. \tag{3.29}$$

In the case of orthogonal pumping, it turns out that the FWM process can be decomposed into two indistinguishable "eigen" processes shown in Fig. 3.7. Equation (3.27) shows that $x$-polarized signal only couples to $y$-polarized idler and vice versa. Clearly, the two processes shown in Fig. 3.7 are independent of each other. In both cases of pumping configurations, the linear Equation (3.27) provides an analytic solution similar to Eq. (3.6). It has the form

$$\hat{A}_j(L,\omega_s) = \left[\alpha_j(L,\omega_s)\hat{A}_j(0,\omega_s) + \beta_j(L,\omega_s)\hat{A}_q^\dagger(0,\omega_i) + \hat{N}_{lj}(L,\omega_s) + \hat{N}_{hj}(L,\omega_s)\right]\Phi(L), \quad (3.30)$$

where $q = j$ for copolarized pumping but $q \neq j$ for orthogonal one. The detailed expressions of the coefficients $\alpha_j$ and $\beta_j$, $\Phi$, and the accumulated noise operators $\hat{N}_{lj}$ and $\hat{N}_{hj}$ are all given in Appendix A and B for copolarized and orthogonal pumping, respectively. A new feature of the dual-pump configuration is that the two pumps introduce SpRS independently, as represented by the two noise operators in Eq. (3.30). In the following subsections, we use Eq. (3.30) to investigate the photon statistics in both copolarized and orthogonal pumping configurations. Detailed expressions of photon flux and pair correlation, including both contributions of spontaneous and stimulated scattering, are given in Appendix A and B. In the following subsections, we focus on the case when pump powers are low so that spontaneous effect dominates. To simplify the analysis, we also assume that narrowband signal and idler filters are located within the phase-matched spectral window such that $\bar{\omega}_s + \bar{\omega}_i = \omega_l + \omega_h$.

### 3.3.2 Photon Flux and Pair Correlation: Copolarized Pumping

One advantage of copolarized pumping is that the phase-matching condition can be satisfied over a broad spectral range when the two pumps are located on opposite sides of the zero-dispersion wavelength of the fiber and are separated far apart [50, 53]. This configuration results in a broad frequency range of available signal/idler photons with a nearly uniform photon-generation efficiency. In the general case shown in Fig. 3.6, the signal and idler frequencies are sandwiched between the two pumps because the phase-matching condition is easy to satisfy there. Thus, the signal and idler act simultaneously as the Stokes for the $\omega_h$ pump and the anti-Stokes for the $\omega_l$ pump. This situation leads to a significant effect on the photon-pair correlation, as discussed next.

Note that in copolarized pumping, the photon pairs can also be created with polarization orthogonal to the pumps, similar to the single-pump case discussed in the previous section. Comparing Eq. (3.30) with Eq. (3.6), we note that the two polarization cases are quite similar. As a result, the discussion of Section 3.2 related to the polarization issues applies to the copolarized dual-pump configuration as well. In the following, we focus on the photon pairs that are created copolarized with the pumps, and drop the polarization indices $x$ and $y$ for simplicity of notation.

Consider first the photon flux. In the low-power regime where $\gamma P_0 L \ll 1$, it is given by

$$I_u = \Delta\nu_u[|\gamma\eta_u L|^2 P_l P_h + P_l L|g_R(\bar{\Omega}_{ul})|\mathcal{N}_{ul} + P_h L|g_R(\bar{\Omega}_{uh})|\mathcal{N}_{uh}], \quad (3.31)$$

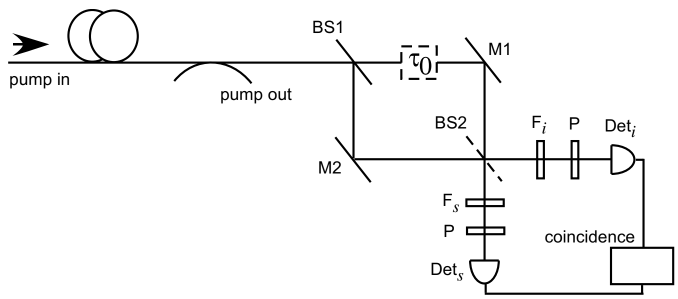


Figure 3.8: Illustration the unbalanced Mach-Zhendre interferometer used for coincidence counting and for constructing time-bin entanglement. BS: 50-50 beam splitter. M: mirror. P: polarizer. $F_s$ and $F_i$: signal and idler filters centering at $\bar{\omega}_s$ and $\bar{\omega}_i$, respectively. Det: photon counting detector.

where $\eta_u = \eta(\bar{\Omega}_{ul}) + \eta(\bar{\Omega}_{uh})$, $\mathscr{N}_{uv} = \mathscr{N}(\bar{\Omega}_{uv})$, and $\bar{\Omega}_{uv} = \bar{\omega}_u - \omega_v$ with $v = l$ and $h$ for the two pumps.

Different from the single-pump case, the FWM-created photon flux now depends on the product $P_l P_h$ of two pump powers, a quantity that is maximized when the two pumps have equal powers (for a constant total power). Moreover, both pumps introduce SpRS photons independently. In general, as the signal and idler have similar frequency relationship with each pump, SpRS generates comparable number of noise photons for both waves. When the pump-signal frequency detuning is small (below 2 THz), the two pumps would create similar amounts of SpRS photons for the signal as well as idler. When the frequency detuning increases, phonon population decreases and the contribution of the high-frequency pump dominates for both of them. This would increase the accidental coincidence counting and thus degrade the pair correlation.

The degree of quantum correlation between the signal and idler photons can be obtained in a way similar to the case of single-pump configuration. Detailed expressions including both spontaneous and stimulated scattering are given in Appendix A. When the signal and idler are distinguishable with each other [$\bar{\omega}_s \neq \bar{\omega}_i$, Fig. 3.6(a)], the pair correlation at a low pump level is given by

$$\rho_c(\tau) = |\varphi_c(\tau)|^2 P_l P_h (Y_1/Y_2), \tag{3.32}$$

where $Y_1$ and $Y_2$ are defined as

$$Y_1 = [\gamma \mathrm{Re}(\eta_s)]^2 + [|g_{Rl}|(n_l + \tfrac{1}{2}) + |g_{Rh}|(n_h + \tfrac{1}{2})]^2, \tag{3.33}$$

$$Y_2 = [|\gamma\eta_s|^2 P_l P_h L + P_l|g_{Rl}|n_l + P_h|g_{Rh}|(n_h+1)][|\gamma\eta_s|^2 P_l P_h L + P_l|g_{Rh}|n_h + P_h|g_{Rl}|(n_l+1)], \tag{3.34}$$

where $g_{Ru} = g_R(\bar{\Omega}_{su})$ and $n_u = n(\bar{\Omega}_{su})$ with $u = l,h$. In the absence of SpRS, Eq. (3.32) reduces to a simple expression, $\rho_c(\tau) = |\varphi_c(\tau)|^2/(|\gamma\eta_s L|^2 P_l P_h)$. When the two pumps have equal powers, $\rho_c$ has the same value as the single-pump configuration for a given total pump power, because $\eta_s = 2$ in the absence of SpRS.

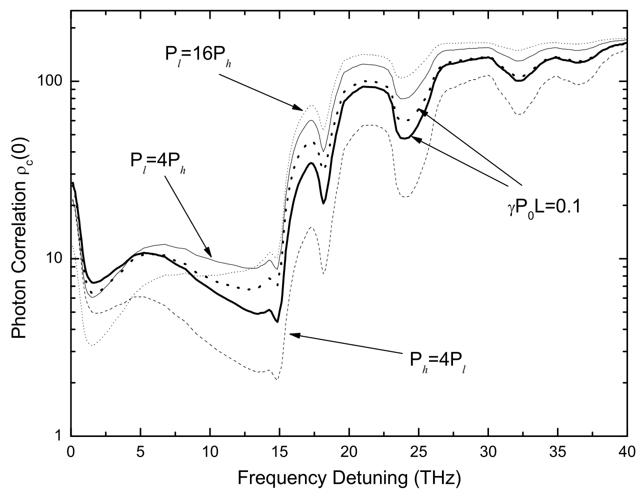


Figure 3.9: Photon correlation $\rho_c(0)$ for the degenerate case of Fig. 5 (b) compared with the single-pump configuration. In all the curves, the pump power is set as $P_l P_h$ equal to the pump power $P_0^2/4$ in single-pump configuration to maintain a same FWM-generated photon rates.

When the signal and idler photons are indistinguishable with each other [$\bar{\omega}_s = \bar{\omega}_i$, Fig. 3.6(b)], coincidence counting can be realized through the experimental setup in Fig. 3.8 by removing the beam splitter 2 and using identical filters for the two detectors [18]. As the two arms are identical, the pair correlation has a same form of Eq. (3.15). In the case of low pump powers with $\gamma P_0 L \ll 1$, pair correlation is found to be

$$\rho_c(\tau) = |\varphi_s(\tau)|^2 + |\varphi_c(\tau)|^2 \frac{P_l P_h \{[\gamma \mathrm{Re}(\eta_s)]^2 + [|g_R|(2n+1)]^2\}}{[|\gamma\eta_s|^2 P_l P_h L + |g_R|(nP_0 + P_h)]^2}, \tag{3.35}$$

where $g_R = g_R(\bar{\Omega}_{sl})$, $n = n(\bar{\Omega}_{sl})$, and we used $\Omega_{sl} = \Omega_{hs}$. Comparing Eq. (3.35) with Eq. (3.32), we find that the second term in Eq. (3.35) provides the cross-correlation between the signal-idler pair. The first term reflects the self-correlation of signal photons as the thermal nature of spontaneous scattering enables creating multiple pairs (although the probability is very small) which can go through either arm and can be detected by either of the two detectors (see Fig. 3.8).

Note that the FWM process in this degenerate configuration [Fig. 3.6(b)] is the reverse process of one shown in Fig. 3.1(a) [18]. Figure 3.9 compares the pair correlation in these two cases under the same FWM-generated photon rates by setting $P_l P_h$ in Eq. (3.35) equal to $P_0^2/4$ at a total pump level of $\gamma P_0 L = 0.1$. In general, the two configurations exhibit a qualitatively similar behavior, especially at small frequency detunings (<4 THz) for which two pumps contribute almost equally to SpRS photons, and at very large frequency detunings (>27 THz) for which SpRS becomes negligible. However, the situation changes in the intermediate spectral range in which noise photons are dominantly introduced by the high-frequency pump. When the two pumps have equal powers (thick solid curves), $\rho_c(0)$ can be lower than the single-pump case (thick dotted curve) by 10 to 40% over a frequency range of 5–27 THz. Even though these two FWM processes are exactly the reverse of each other, they do not exhibit the same degree of correlation because of different SpRS processes involved. This difference is enhanced at low pump powers but decreases at high pump power levels for which FWM dominates.

As SpRS is dominated by the high-frequency pump over a quite broad spectral range, photon-pair correlation would strongly depend on the power imbalance between the two pumps. This is shown clearly in Fig. 3.9 where FWM-generated photon rate is maintained constant. If $P_h$ is four time larger than $P_l$ (thin dashed curve), corresponding to a 1.25-times increase in total pump power, correlation magnitude drops significantly (by 25 to 60%) over most of the detuning range, except in a small region below 1 THz. In contrast, the correlation can be enhanced by 20 to 100% if the pump powers are flipped such that $P_l = 4P_h$ (thin solid curve). If we unbalance the pump powers further such that $P_l = 16P_h$ (thin dotted curves), the correlation can be improved even more (by up to 140% compared with the equal-pump-power case) for detunings larger than 10 THz. However, it is degraded by a similar factor in the low-detuning region because of SpRS enhancement induced by an increase in the total pump power. These results show that the power imbalance between the two pumps may be used to advantage when a dual-pump configuration is adopted.

### 3.3.3 Photon Flux and Pair Correlation: Orthogonal Pumping

In this subsection, we look into the case of orthogonal pumping, by which, in principle, it is possible to automatically generate a polarization-entangled state. However, fiber birefringence usually introduces different phase-matching conditions for the two eigen processes shown in Fig. 3.7, leading to partial distinguishability between them and degrading the degree of polarization entanglement. This situation is quite similar to the birefringence-induced distinguishability in a Type-II $\chi^{(2)}$-based process [47]. Thus, similar techniques can be used to engineer the indistinguishability [54]. Moreover, unlike nonlinear crystals, which generally exhibit a high intrinsic birefringence, silica glass is isotropic, and fiber birefringence mainly results from geometrical asymmetry or internal stress. Both of these, in principle, can be reduced to realize a low-birefringence fiber with a beat length longer than 10 m. As a result, birefringence effects can be mitigated to a negligible level if a high-nonlinearity fiber of length $\sim$1 m is employed for photon-pair generation [18, 19]. In the following discussion, we assume that the fiber is isotropic (no birefringence) and focus on the polarization effects of FWM and SpRS.

Although the two eigen processes have similar FWM efficiencies, they exhibit quite different polarization-dependent Raman scattering. In the process of Fig. 3.7(a), the signal and idler are copolarized with the low-frequency and high-frequency pumps, respectively. As a result, the signal is mainly coupled with the low-frequency pump, while the idler is mainly coupled with the high-frequency pump. The situation is reverse in Fig. 3.7(b). Such different Raman couplings are reflected through the polarization-dependent noise operators in Eq. (3.27) (see Appendix B for the detailed expression).

In general, a polarizer is placed in front of the detector to a select a specific polarization state of the incoming signal or idler photons. Assuming that the polarizer is aligned at an angle of $\theta_u$ ($u = s, i$) with respect to the $x$-axis of fiber, the optical field falling on the detector is given by

$$\hat{A}_u(t, \theta_u) = \cos\theta_u \hat{A}_{ux}(L,t) + \sin\theta_u \hat{A}_{uy}(L,t), \tag{3.36}$$

where $\hat{A}_{ux}(L,t)$ and $\hat{A}_{uy}(L,t)$ are $x$- and $y$-polarized signal/idler fields, respectively. As the two eigen processes shown in Fig. 3.7 are independent of each other, the photon flux is given by

$$I_u(\theta_u) = I_{ux}\cos^2\theta_u + I_{uy}\sin^2\theta_u, \tag{3.37}$$

where $I_{uj} \equiv \langle \hat{A}^\dagger_{uj}(L,t)\hat{A}_{uj}(L,t)\rangle$ is the photon flux for the $j$th polarization component ($j = x, y$). Their general expressions are given in Appendix B. When the pump powers are low enough that $\gamma P_0 L \ll 1$, they have simple forms as

$$I_{ux} = \Delta\nu_u[|\gamma\eta_{ux}L|^2 P_l P_h + P_l L|g_\parallel(\bar{\Omega}_{ul})|\mathscr{N}_{ul} + P_h L|g_\perp(\bar{\Omega}_{uh})|\mathscr{N}_{uh}], \tag{3.38}$$

$$I_{uy} = \Delta\nu_u[|\gamma\eta_{uy}L|^2 P_l P_h + P_l L|g_\perp(\bar{\Omega}_{ul})|\mathscr{N}_{ul} + P_h L|g_\parallel(\bar{\Omega}_{uh})|\mathscr{N}_{uh}], \tag{3.39}$$

where $\eta_{uj} = \eta_j(\bar{\omega}_u)$ ($u = s, i$ and $j = x, y$) is given by Eqs. (3.28) and (3.29). If we compare the preceding equations with Eq. (3.31), we find that, for the same pump power, the number of FWM-generated photons is about 1/9 of that in the copolarized-pump case, since $\eta_{ux}$ and $\eta_{uy}$ here are roughly 1/3 of $\eta_u$ in Eq. (3.31). Moreover, these two equations show that, because of polarization dependence of Raman scattering, the two pumps provide different SpRS contributions to the two polarization components of the signal or idler. In general, SpRS photons are dominated by the copolarized pump, which is roughly half of the total pump power. Compared with the single-pump copolarized configuration, SpRS is reduced by a factor of 1/2, but FWM is reduced by 1/9. Clearly, at the same pump level, SpRS has a higher impact for this scheme than the single-pump one. As a result, pair correlation is expected to be degraded for the orthogonal-pump configuration.

For arbitrary polarization angles of the signal and idler waves, the pair correlation is found to have the form

$$\rho_c(\tau, \theta_s, \theta_i) = \left|\mathscr{P}_{xy}(\tau)\cos\theta_s\sin\theta_i + \mathscr{P}_{yx}(\tau)\sin\theta_s\cos\theta_i\right|^2 / I_s(\theta_s) I_i(\theta_i), \tag{3.40}$$

where the quantities $\mathscr{P}_{xy}(\tau) \equiv \langle \hat{A}_{sx}(L,t+\tau)\hat{A}_{iy}(L,t)\rangle$ and $\mathscr{P}_{yx}(\tau) \equiv \langle \hat{A}_{sy}(L,t+\tau)\hat{A}_{ix}(L,t)\rangle$ are related to pair correlations in the two configurations shown in Figs. 3.7(a) and 5(b), respectively; they are given by (see Appendix B for general expressions)

$$\mathscr{P}_{xy}(\tau) = \sqrt{\Delta\nu_s\Delta\nu_i}\varphi_c(\tau)A_lA_hL[i\gamma\mathrm{Re}(\eta_{sx}) - |g_{al}|(n_l + \tfrac{1}{2}) - |g_{\perp h}|(n_h + \tfrac{1}{2})], \tag{3.41}$$

$$\mathscr{P}_{yx}(\tau) = \sqrt{\Delta\nu_s\Delta\nu_i}\varphi_c(\tau)A_lA_hL[i\gamma\mathrm{Re}(\eta_{sy}) - |g_{ah}|(n_h + \tfrac{1}{2}) - |g_{\perp l}|(n_l + \tfrac{1}{2})], \tag{3.42}$$

where $g_{av} = g_a(\bar{\Omega}_{sv})$ and $g_{\perp v} = g_{\perp}(\bar{\Omega}_{sv})$ $(v = l,h)$. If we substitute Eqs. (3.41) and (3.42) into Eq. (3.40) and use Eqs. (3.38) and (3.39), we can obtain the pair correlation for arbitrary combinations of signal and idler polarization angles.

In the absence of SpRS, $\eta_{sx} = \eta_{sy} = 2/3$ and the preceding equations reduce to

$$\mathscr{P}_{xy}(\tau) = \mathscr{P}_{yx}(\tau) = 2i(\Delta\nu_s\Delta\nu_i)^{1/2}\varphi_c(\tau)\gamma A_lA_hL/3. \tag{3.43}$$

The two processes in Fig. 3.7 become completely indistinguishable with each other. The pair correlation in this specific case is given by

$$\rho_c(\tau,\theta_s,\theta_i) = \frac{9|\varphi_c(\tau)|^2\sin^2(\theta_s+\theta_i)}{4\gamma^2L^2P_lP_h}. \tag{3.44}$$

It has the maximal value for the two eigen-processes of Fig. 3.7, $\rho_c(\tau,0,\pi/2) = 9|\varphi_c(\tau)|^2/(4\gamma^2L^2P_lP_h)$. As the biphoton probability of the signal-idler pair is given by $I_s(\theta_s)I_i(\theta_i)[1+\rho_c(\tau,\theta_s,\theta_i)]$, it varies with signal and idler polarization angles periodically. The resulting "fringe pattern" has a visibility of

$$V_f(\tau) = \frac{\rho_c(\tau,0,\pi/2)}{2+\rho_c(\tau,0,\pi/2)}. \tag{3.45}$$

Note that $V_f(0)$ is close to 1 when $\gamma P_0L \ll 1$, indicating that orthogonal-pumped FWM can provide automatic polarization entanglement.

If the pump frequencies are close to each other, the two eigen-processes in Fig. 3.7 would have almost the same values of pair correlation since the signal and idler have similar frequency detunings from the two pumps. The visibility of biphoton probability is still given by Eq. (3.45) except that $\rho_c(\tau,0,\pi/2)$ is now provided by the general form of Eq. (3.40). Figure 3.10 compares the pair correlation for Fig. 3.7(a) (solid curve) with the single-pump configuration of Fig. 3.1(a) (dotted curve). The two pumps are assumed to have equal powers and their total power is three times larger than the single-pump case to maintain the same FWM efficiency. Clearly, the pair correlation is significantly lower over the whole spectrum for the orthogonal-pumping configuration than that in the single-pump one because the FWM efficiency is reduced more compared with SpRS.

The situation is different when the two pumps are separated far apart with the signal and idler sandwiched in between. The signal (idler) is anti-Stokes (Stokes) of the low-frequency (high-frequency) pump with a frequency separation of $|\Omega_{sl}|$ in Fig. 3.11(a) but it is the Stokes (anti-Stokes) of the high-frequency (low-frequency) pump with a different frequency separation of $|\Omega_{sh}|$ in Fig. 3.11(b). As a

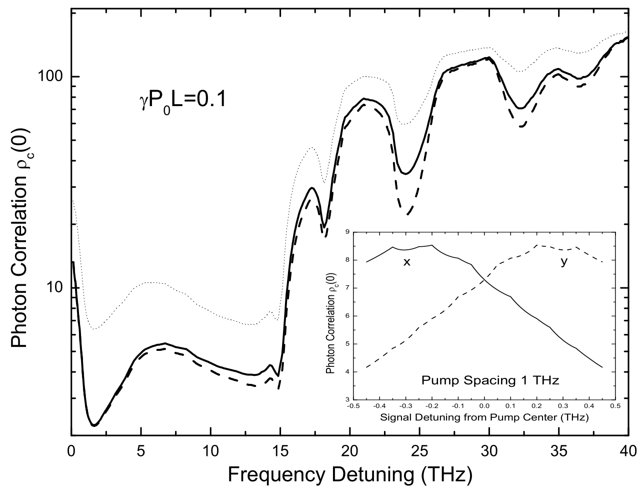


Figure 3.10: Comparison of pair correlation $\rho_c(0)$ in different pumping configurations. The dotted, solid, and dashed curves show the cases of Fig. 3.1(a), Fig. 3.7(a), and Fig. 3.11(c), respectively. In the case of Fig. 3.11(c), frequency detuning means the pump frequency spacing. The inset shows the pair correlation for the two eigen-processes of Fig. 3.11(a) and (b) with a fixed pump spacing of 1 THz at the same pump level.

result, the $x$-polarized signal/idler has fewer SpRS photons than the $y$-polarized one, leading to quite different pair correlations in the two processes of Fig. 3.11(a) and (b). The inset of Fig. 3.10 shows an example with a pump spacing of 1 THz. Clearly, photon pair correlation is strongly polarization dependent. This polarization dependence increases with increased pump spacing.

Such polarization dependence vanishes when the signal and idler frequencies are identically located at the pump center ($\bar{\omega}_s = \bar{\omega}_i$) [Fig. 9 (c)]. In this case, photon self-correlation would generally contribute to coincidence counting, similar to the copolarized dual-pump case discussed in the last subsection. Equation (3.40) then changes to be

$$\rho_c'(\tau,\theta_s,\theta_i) \;= \rho_c(\tau,\theta_s,\theta_i) + \frac{|\varphi_s(\tau)|^2}{I_s(\theta_s)I_s(\theta_i)}\left|I_{sx}\cos\theta_s\cos\theta_i + I_{sy}\sin\theta_s\sin\theta_i\right|^2, \tag{3.46}$$

where $\rho_c$ is given by Eq. (3.40). In general, the magnitude of the self-correlation term is less than 1. It is interesting to note that self-correlation vanishes for the two eigen-processes with $\theta_s = 0$ and $\theta_i = \pi/2$, or $\theta_s = \pi/2$ and $\theta_i = 0$, since the two polarizers are orthogonal to each other. The dashed curve of Fig. 3.10 shows this case, which is close to the case of Fig. 3.7. A slight lower value of correlation is because of SpRS enhanced by the high-frequency pump, similar to the case of copolarized pumping.

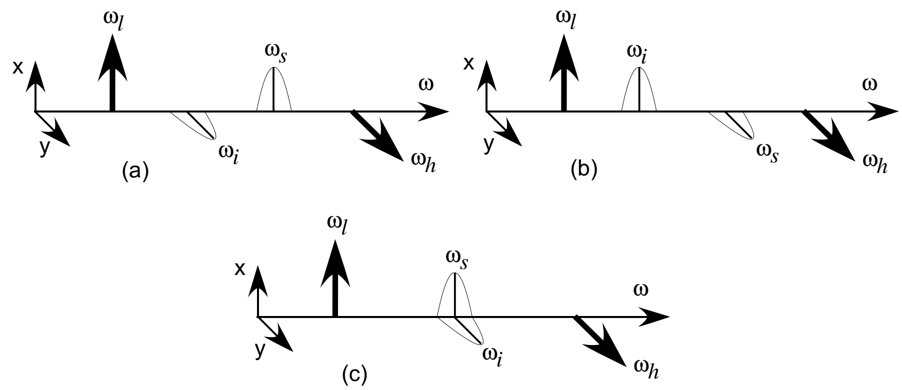


Figure 3.11: Illustration of the frequency and polarization relationship among the four waves in the orthogonal pumping configuration when the two pumps are separated far apart.

## 3.4 Impact on Quantum Entanglement

The degradation of photon correlation induced by SpRS would directly impact specific quantum entanglement constructed from the created photon pairs. Here we consider two typical examples and study how SpRS affects the energy-time and polarization entanglement.

### 3.4.1 Energy-Time Entanglement

The energy-time entanglement [3] can be realized with an unbalanced Mach-Zehnder interferometer [55]-[57] shown in Fig. 5 with an inserted beam splitter 2, when the relative time delay in the two arms is made much larger than the coherence time of signal and idler photons but much shorter than the pump coherence time (to prevent first-order interference) [58]. The equal-time biphoton probability between the two outputs, $p_{12} \equiv \langle \hat{A}_1^\dagger(t)\hat{A}_2^\dagger(t)\hat{A}_2(t)\hat{A}_1(t)\rangle$, is found to be

$$p_{12} = \frac{I_s I_i}{4}\left\{1+\frac{1}{2}\rho_c(0)[1-\cos(2\omega_p\tau_0+2\phi_0)]\right\}, \tag{3.47}$$

where $\tau_0$ and $\phi_0$ are time and phase delay between the two arms, and the subscripts 1 and 2 denote the two output ports of the Mach-Zehnder interferometer. The fringe visibility of two-photon quantum interference is given by $V_f = \rho_c(0)/[2+\rho_c(0)]$. Quantum entanglement requires $\rho_c(0) \gg 2$ so that it can be clearly distinguished from the classical visibility of 50% [59, 60]. A higher value of pair correlation translates into a higher degree of entanglement. Any reduction in correlation induced by SpRS would directly deteriorate the degree of entanglement. For example, the typical correlation value obtained experimentally of 10 would result in a fringe visibility of only 83%.

### 3.4.2 Polarization Entanglement

A polarization-entangled state can be constructed either by degenerate FWM with specific techniques, or automatically generated by non-degenerate FWM with orthogonal pumping. The degree of quantum entanglement can be tested by the extent of its violation to the Clauser-Horne-Shimony-Holt (CHSH) inequality $|S(\tau)| \leq 2$, where the CHSH parameter $S(\tau)$ is given by [61, 62]

$$S(\tau) = E(\tau, \theta_s, \theta_i) - E(\tau, \theta_s, \theta_i') + E(\tau, \theta_s', \theta_i) + E(\tau, \theta_s', \theta_i'), \tag{3.48}$$

and $E(\tau, \theta_s, \theta_i)$ is a correlation function defined as $E(\tau, \theta_s, \theta_i) = \mathscr{E}_-(\tau)/\mathscr{E}_+(\tau)$, where $\mathscr{E}_\pm(\tau) \equiv \langle \mathscr{T} : \hat{I}_{s\pm}(t+\tau)\hat{I}_{i\pm}(t) : \rangle$, :: denotes normal ordering, and $\mathscr{T}$ denotes time ordering. $\hat{I}_{u\pm}(t)$ is the sum and differential photon-flux operator for two orthogonal polarization angles of $\theta_u$ $(u = s, i)$ and $\theta_{u\perp} = \theta_u + \pi/2$. It is defined as

$$\hat{I}_{u\pm}(t) \equiv \hat{A}_u^\dagger(t, \theta_u)\hat{A}_u(t, \theta_u) \pm \hat{A}_u^\dagger(t, \theta_{u\perp})\hat{A}_u(t, \theta_{u\perp}), \tag{3.49}$$

where $\hat{A}_u(t, \theta_u)$ and $\hat{A}_u(t, \theta_{u\perp})$ are given by Eq. (3.36) with polarization angle $\theta_u$ and $\theta_{u\perp}$, respectively. It is easy to show that $\hat{I}_{u+}(t)$ is invariant with the polarization angle because it represents the total photon flux.

In practice, the CHSH parameter requires sixteen measurement of coincidence counting between signal and idler at polarization angles of $\theta_s$, $\theta_s'$, $\theta_i$, $\theta_i'$, and their orthogonal angles [5]. Although Eq. (3.48) looks complicated, it turns out that the CHSH parameter can be written in a compact form in a circular-polarization basis as

$$S(\tau) = \frac{1}{\mathscr{E}_+(\tau)}\left[\Gamma_1(\tau)\Theta_1 + \Gamma_2(\tau)\Theta_2 + c.c.\right], \tag{3.50}$$

where $c.c.$ denotes complex conjugate, and $\Gamma_1(\tau)$ and $\Gamma_2(\tau)$ are given by

$$\Gamma_1(\tau) = \langle \hat{A}_{i\uparrow}^\dagger(t)\hat{A}_{s\uparrow}^\dagger(t+\tau)\hat{A}_{s\downarrow}(t+\tau)\hat{A}_{i\downarrow}(t)\rangle, \tag{3.51}$$

$$\Gamma_2(\tau) = \langle \hat{A}_{i\downarrow}^\dagger(t)\hat{A}_{s\uparrow}^\dagger(t+\tau)\hat{A}_{s\downarrow}(t+\tau)\hat{A}_{i\uparrow}(t)\rangle. \tag{3.52}$$

$\hat{A}_{u\uparrow}$ and $\hat{A}_{u\downarrow}$ $(u = s, i)$ denotes the field operators for left- (spin-up) and right-circular (spin-down) polarizations, respectively, related to linear polarization as $\hat{A}_{u\uparrow} = (\hat{A}_{ux} + i\hat{A}_{uy})/\sqrt{2}$ and $\hat{A}_{u\downarrow} = (\hat{A}_{ux} - i\hat{A}_{uy})/\sqrt{2}$. In Eq. (3.50), the two scalar factors $\Theta_1$ and $\Theta_2$ are related to the relative polarization angles as

$$\Theta_1 = e^{2i(\theta_s+\theta_i)} - e^{2i(\theta_s+\theta_i')} + e^{2i(\theta_s'+\theta_i)} + e^{2i(\theta_s'+\theta_i')}, \tag{3.53}$$

$$\Theta_2 = e^{2i(\theta_s-\theta_i)} - e^{2i(\theta_s-\theta_i')} + e^{2i(\theta_s'-\theta_i)} + e^{2i(\theta_s'-\theta_i')}. \tag{3.54}$$

In the following, we use Eqs. (3.50)-(3.54) to find $S(\tau)$ for the polarization-entangled states constructed from different FWM processes, and use it to discuss the impact of SpRS.

### Degenerate FWM

Although each photon pair created by degenerate FWM is copolarized, a polarization-entangled state can be constructed by employing a time-multiplexing technique [22] or a polarization-diversity loop [21]. The pump is split into two parts of equal powers with orthogonal polarizations, each part generating independent photon pairs with half probability. After combining them together and erasing the time or path information between them, a polarization-entangled state is constructed.

For such polarization-entangled states constructed from degenerate FWM, we are able to find (see Appendix C) that the CHSH parameter with the maximal magnitude, $S_m(\tau)$, takes a simple form of

$$S_m(\tau) = \frac{2\sqrt{2}\rho_c(\tau)}{2+\rho_c(\tau)}. \tag{3.55}$$

This equation shows that violation of the CHSH inequality requires the pair correlation to be $\rho_c(\tau) > 2/(\sqrt{2}-1) \approx 4.8$. If the photon pair generation is dominated by FWM with $\rho_c(0) \gg 5$, $S_m(0) \to 2\sqrt{2}$ shows a clear violation of CHSH inequality. A typical experimental value of $\rho_c(0) = 10$ corresponds to $S_m(0) = 2.36$. Same conclusions apply to the case of copolarized dual pumping, as the two cases are quite similar. In the case of Fig. 3.6(b), photon self-correlation would contribute to coincidence counting and $\rho_c(\tau)$ in Eq. (3.55) should be given by Eq. (3.35).

In general, the pump not only creates correlated copolarized signal-idler pairs, but also generates extra orthogonally polarized noise background through anisotropic Raman scattering. If such orthogonally polarized noise is not filtered out, it would contribute to photon fluxes of signal and idler and introduce extra accidental coincidence counting. In this case, (3.55) is still valid if $\rho_c(\tau)$ is given as the realistic ratio between the true coincidence counting and accidental one. It is interesting to note that the polarization diversity loop can automatically remove such orthogonally polarized noise background.

### Non-Degenerate FWM with Orthogonal Pumping

In the case of orthogonal pumping, when the signal and idler are distinguishable ($\bar{\omega}_s \neq \bar{\omega}_i$), the maximum CHSH parameter is found to be (see Appendix C)

$$S_m(\tau) = \frac{\sqrt{2}\left[|\mathscr{P}_{xy}(\tau)+\mathscr{P}_{yx}(\tau)|^2 - (I_{sx}-I_{sy})(I_{ix}-I_{iy})\right]}{(I_{sx}+I_{sy})(I_{ix}+I_{iy}) + |\mathscr{P}_{xy}(\tau)|^2 + |\mathscr{P}_{yx}(\tau)|^2}. \tag{3.56}$$

As the magnitudes of $\mathscr{P}_{xy}(\tau)$ and $\mathscr{P}_{yx}(\tau)$ are directly related to the magnitude of pair correlation, a higher correlation value implies a larger value of $|S_m(\tau)|$. In the absence of SpRS, Eq. (3.56) reduces to Eq. (3.55) where $\rho_c(\tau) = \rho_c(\tau, 0, \pi/2) = 9|\varphi_c(\tau)|^2/(4\gamma^2 L^2 P_l P_h)$. Clearly, $|S_m(\tau)| \to 2\sqrt{2}$ when $\gamma L\sqrt{P_l P_h} \ll 1$. In the orthogonal pumping configuration, pure FWM-generated photon pairs at low power level exhibit a high degree of polarization entanglement.

SpRS reduces the magnitude of $\mathscr{P}_x$ and $\mathscr{P}_y$ and increases the accidental counting rate indicated by the first term in the denominator of Eq. (3.56), and thus reduces the magnitude of $|S_m(\tau)|$. In particular, when the two pump frequencies are close to each other, the two processes of Fig. 3.7 experience similar SpRS and Eq. (3.56) also reduces to Eq. (3.55) except that $\rho_c(\tau) = \rho_c(\tau, 0, \pi/2)$ is now provided by the general form of Eq. (3.40).

When the signal and idler are identical with each other [$\bar{\omega}_s = \bar{\omega}_i$, Fig. 3.11(c)], photon self-correlation starts to involve because the polarization-angle settings for coincidence counting are generally not orthogonal to each other. In this case, the CHSH parameter is found to be (see Appendix C)

$$S_m(\tau) = \frac{\sqrt{2}\left[4I_{sx}I_{sy}\rho_c(\tau) - (I_{sx} - I_{sy})^2(1 + |\varphi_s(\tau)|^2)\right]}{(I_{sx} + I_{sy})^2 + |\varphi_s(\tau)|^2(I_{sx}^2 + I_{sy}^2) + 2I_{sx}I_{sy}\rho_c(\tau)}, \tag{3.57}$$

where $\rho_c(\tau) = \rho_c(\tau, 0, \pi/2)$ is given by Eq. (3.40). For a pure FWM process without SpRS, indistinguishability between the two eigen-processes reduces Eq. (3.57) to a simple form of

$$S_m(\tau) = \frac{2\sqrt{2}\rho_c(\tau)}{2 + |\varphi_s(\tau)|^2 + \rho_c(\tau)}, \tag{3.58}$$

where $\rho_c(\tau) = 9|\varphi_c(\tau)|^2/(4\gamma^2L^2P_lP_h)$. The involvement of photon self-correlation is the result of collinear nature of FWM in optical fibers. Equations (3.57) and (3.58) show that, unlike the reverse degenerate FWM discussed previously, photon self-correlation would increases the requirement of pair-correlation for violation of CHSH inequality. For example, Eq. (3.58) shows that $|S_m(0)| > 2$ requires $\rho_c(0) > 7.2$. Moreover, Eq. (3.57) shows that polarization-dependent SpRS introduces difference noise photons to the $x$- and $y$-polarized signal and thus degrade the magnitude of $S_m(\tau)$ even more. However, if the generated photon pairs have high quality with large pair correlation, photon self-correlation would have negligible effect in testing CHSH inequality.

Figure 3.12 compares $S_m(0)$ in different pumping configurations, at a same level of FWM-generated photon flux. In general, the single-pump configuration has a larger $S_m(0)$ value, indicating a better polarization entanglement. In particular, orthogonally polarized FWM in the single-pump configuration exhibits a $S_m(0)$ values close to the maximum value of $2\sqrt{2}$ over most region of frequency detuning. In the copolarized FWM, SpRS significantly degrades the value of $S_m(0)$ over a broad spectrum from $2-15$ THz. In the dual-pump configuration, polarization entanglement can only be realized with a frequency detuning either very small ($<$ 1 THz) or very large ($>$ 16 THz). SpRS has most severe effect in the orthogonal pumping configuration with the two pumps separated apart.

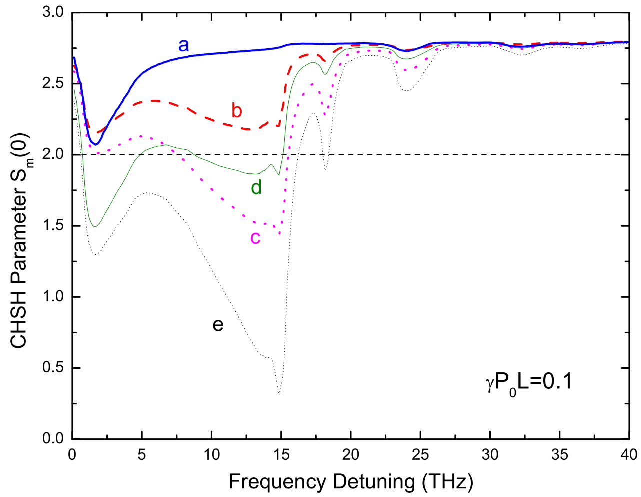


Figure 3.12: Comparison of CHSH parameter in different pumping configurations at a pump level of $\gamma P_0 L = 0.1$. The two pumps have an equal power in the dual pump cases. The total pump power is increased by three times in the orthogonal pumping configurations to maintain nearly same amount of FWM-generated photon flux. (a) Fig. 3.1(b); (b) Fig. 3.1(a); (c) Fig. 3.6(b); (d) Fig. 3.10 (a) and (b); (e) Fig. 3.11(c). In the cases of (a), (b), (c), the orthogonally polarized noise background is assumed to be removed, say, by use of a polarization diversity loop.

## 3.5 Summary

FWM occurring inside optical fibers provides a natural way to generate correlated photon pairs in a single spatial mode. However, in practice, the performance of fiber-based photon-pair sources is severely deteriorated by SpRS that accompanies FWM inevitably. In this chapter, we have developed a general quantum theory capable of describing photon statistics under the combined effects of FWM and Raman scattering inside optical fibers. Since our theory is vectorial in nature and includes all polarization effects, it can be used for a wide variety of pumping configurations.

We have applied our general formalism to several different pumping configurations. When a single pump beam is launched into a birefringent fiber, it is possible to satisfy the FWM phase-matching condition such that the the signal and idler photons are polarized either parallel or orthogonal to the pump. Our results show that, under conditions in which frequency of the signal or idler photons lies close to the Raman gain peak, the orthogonal configuration can improve the magnitude of pair correlation. The reason for then improvement is related to the fact that Raman gain almost vanishes for an orthogonally polarized pump. Although the FWM efficiency is also reduced by a factor of three in this configuration, one can maintain nearly the same photon flux by increasing the pump power by a factor of three.

In the case of a dual-pump configuration, the two pumps may be polarized parallel or orthogonal to each other. When two pumps are copolarized, it is possible to create photon pairs that are indistinguishable on the basis of their frequencies. This is desirable for some applications. Our results show that the quality of correlated photon pairs can be improved by using two pumps with different powers such that the lower-frequency pump has a larger power. The case of two orthogonally polarized pumps leads to a situation in which the signal and idler photons generated through FWM are also orthogonally polarized. However, each photon pair can be generated through two eigen processes in which signal photons are copolarized either with the low-frequency pump or with the high-frequency pump. Because the two processes can occur simultaneously, this configurations makes it possible to create photon pairs that are polarization entangled. The extent of quantum correlation is however reduced in this configuration when compared with the case of a single pump.

Our analysis shows that SpRS remains a serious degradation source for correlated photon-pair generation inside optical fibers over a broad spectral range. Although some techniques, such as using specific polarization configuration or cooling the fiber, can mitigate the impact of SpRS, it cannot be eliminated completely. Another approach for creating high-quality photon pairs would be to search for new materials which have a high nonlinearity, are free from Raman scattering, and are easy for waveguide fabrication. It turns out that silicon is such a kind of material. Detailed discussion is beyond the scope of this thesis and can be found elsewhere [63].

# Appendix A

In the field solution of copolarized dual-pump configuration in Eq. (3.30), the coefficient $\alpha_j$ and $\beta_j$ ($j = x, y$) are given by Eqs. (3.7) and (3.8) except that $A_p^2$ and $\eta_j$ in Eq. (3.8) are replaced with $A_l A_h$ and $\eta_j(\omega_s) \equiv \eta_j(\Omega_{sl}) + \eta_j(\Omega_{sh})$, respectively. The other quantities are defined as

$$g_j^2 = (\gamma\eta_j)^2 P_l P_h - (\kappa_j/2)^2, \tag{A3.1}$$

$$\kappa_j = k_j(\omega_s) + k_j(\omega_i) - k_x(\omega_l) - k_x(\omega_h) + \gamma P_0[\xi_j(\Omega_{sl}) + \xi_j(\Omega_{sh}) - 3], \tag{A3.2}$$

$$K_j = \{k_j(\omega_s) - k_j(\omega_i) + \gamma(P_l - P_h)[\xi_j(\Omega_{sl}) - \xi_j(\Omega_{sh})]\}/2, \tag{A3.3}$$

$$\Phi(L) = \exp\{i[k_x(\omega_l) + k_x(\omega_h) + 3\gamma P_0]L/2\}. \tag{A3.4}$$

The two noise operators in Eq. (3.30) are given by

$$\hat{N}_{uj}(L, \omega_s) = i\int_0^L \hat{m}_{jx}(z, \Omega_{su}) f_{uj}(z, \omega_s) e^{i\Delta_{uv}z} dz, \tag{A3.5}$$

where $\Delta_{uv} = [k_x(\omega_u) - k_x(\omega_v) + \gamma(P_v - P_u)]/2$ with $u, v = l, h$ ($v \neq u$), and

$$f_{uj}(z, \omega_s) = A_u \alpha_j(L - z, \omega_s) - A_v^* \beta_j(L - z, \omega_s). \tag{A3.6}$$

Equations (3.30), (A3.1)-(A3.5) can be used to find the following general expression of photon flux:

$$I_u = \frac{1}{2\pi} \int_{-\infty}^{+\infty} |H_u|^2 [|\beta_u|^2 + \mathscr{N}(\Omega_{ul})|g_R(\Omega_{ul})|F_l(\omega_u) + \mathscr{N}(\Omega_{uh})|g_R(\Omega_{uh})|F_h(\omega_u)] d\omega_u, \tag{A3.7}$$

where $u = s$ or $i$ for signal and idler photons. The quantity $F_v(\omega) \equiv \int_0^L |f_v(z, \omega)|^2 dz$ ($v = l, h$) describes the magnitude of amplified SpRS; its analytical expression can be obtained from Eq. (A3.6).

The degree of quantum correlation between the signal and idler photons is obtained from Eqs. (3.30) and (A3.1)-(A3.5) using the definition given in Eq. (3.18). When the signal and idler are distinguishable with each other [$\bar{\omega}_s \neq \bar{\omega}_i$, Fig. 3.6(a)], the correlation is given by:

$$\begin{aligned}\rho_c(\tau) = \frac{1}{(2\pi)^2 I_s I_i} \Big| \int_{-\infty}^{\infty} & \mathscr{H}(\omega_s)[\alpha_i \beta_s - \mathscr{N}(\Omega_{sl})|g_R(\Omega_{sl})|\mathscr{F}_l(\omega_s) \\ & - \mathscr{N}(\Omega_{sh})|g_R(\Omega_{sh})|\mathscr{F}_h(\omega_s)] e^{-i\omega_s \tau} d\omega_s \Big|^2,\end{aligned} \tag{A3.8}$$

where $\mathscr{F}_u(\omega_s) = \int_0^L f_u(z, \omega_s) f_v(z, \omega_i) dz$ with $u,\ v = l$ or $h$ ($u \neq v$) and $\omega_i = \omega_l + \omega_h - \omega_s$; its analytical form can be obtained from Eq. (A3.6).

When the signal and idler photons are indistinguishable on the basis of their frequencies [$\bar{\omega}_s = \bar{\omega}_i$, Fig. 3.6(b)], the pair correlation for the experimental configuration in Fig. 3.8 can be obtained by use of the definition in Eq. (3.15). Its general form is given by

$$\begin{aligned}\rho_c(\tau) = \frac{I_s^{-2}}{(2\pi)^2} \Big| \int_{-\infty}^{\infty} & \mathscr{H}(\omega_s)[\alpha_i \beta_s - \mathscr{N}(\Omega_{sl})|g_R(\Omega_{sl})|\mathscr{F}_l(\omega_s) \\ & - \mathscr{N}(\Omega_{sh})|g_R(\Omega_{sh})|\mathscr{F}_h(\omega_s)] e^{-i\omega_s \tau} d\omega_s \Big|^2, \\ + \frac{I_s^{-2}}{(2\pi)^2} \Big| \int_{-\infty}^{\infty} & |H_s|^2 [|\beta_s|^2 + \mathscr{N}(\Omega_{sl})|g_R(\Omega_{sl})|F_l(\omega_s) \\ & + \mathscr{N}(\Omega_{sh})|g_R(\Omega_{sh})|F_h(\omega_s)] e^{-i\omega_s \tau} d\omega_s \Big|^2,\end{aligned} \tag{A3.9}$$

where the first term in Eq. (A3.9) is close to Eq. (A3.8) and provides the cross-correlation between the signal-idler pair. The second term is very similar to Eq. (3.16), and it reflects the self-correlation of signal photons.

# Appendix B

In the case of orthogonal pumping, the coefficients $\alpha_j$ and $\beta_j$ ($j = x, y$) in Eq. (3.30) are still given by Eqs. (3.7) and (3.8) except that $A_p^2$ is replaced by $A_l A_h$ and $\eta_j$ is used from Eqs. (3.28) and (3.29). The parametric gain coefficient is found to have the form of Eq. (A3.1) but the other parameters are given by

$$\kappa_j = k_j(\omega_s) + k_q(\omega_i) - k_x(\omega_l) - k_y(\omega_h) + \gamma P_0[\xi_j(\Omega_{sl}) + \xi_q(\Omega_{sh}) - \xi_y(0) - 1]. \tag{B3.10}$$

$$K_j = \tfrac{1}{2}\{k_j(\omega_s) - k_q(\omega_i) + \gamma(P_l - P_h)[\xi_j(\Omega_{sl}) - \xi_q(\Omega_{sh})]\}. \tag{B3.11}$$

$$\Phi(L) = \exp\{\tfrac{i}{2}L\{k_x(\omega_l) + k_y(\omega_h) + \gamma P_0[1 + \xi_y(0)]\}\}. \tag{B3.12}$$

The accumulated noise operators in Eq. (3.30) are found to be

$$\hat{N}_{lj}(L,\omega_s) = i\int_0^L \{A_l\alpha_j(L-z,\omega_s)\hat{m}_{jx}(z,\Omega_{sl}) - A_h^*\beta_j(L-z,\omega_s)\hat{m}_{qy}(z,\Omega_{sl})\}e^{i\Delta z}dz, \tag{B3.13}$$

$$\hat{N}_{hj}(L,\omega_s) = i\int_0^L \{A_h\alpha_j(L-z,\omega_s)\hat{m}_{jy}(z,\Omega_{sh}) - A_l^*\beta_j(L-z,\omega_s)\hat{m}_{qx}(z,\Omega_{sh})\}e^{-i\Delta z}dz, \tag{B3.14}$$

where $\Delta$ is given by

$$\Delta = \tfrac{1}{2}\{k_x(\omega_l) - k_y(\omega_h) + \gamma(P_l - P_h)[1 - \xi_y(0)]\}. \tag{B3.15}$$

By use of Eqs. (3.30), (B3.13), and (B3.14), the photon flux $I_{uj}$ for the $j$th polarization component is found to have the following general expressions:

$$\begin{aligned} I_{ux} &= \frac{1}{2\pi}\int_{-\infty}^{\infty} d\omega_u |H_u|^2\{|\beta_{ux}|^2 + \mathscr{N}(\Omega_{uh})|g_\perp(\Omega_{uh})|F_{hx}(\omega_u) \\ &\quad + \mathscr{N}(\Omega_{ul})[|g_a(\Omega_{ul})|F_{lx}(\omega_u) + |g_b(\Omega_{ul})|F'_{lx}(\omega_u)]\}, \end{aligned} \tag{B3.16}$$

$$\begin{aligned} I_{uy} &= \frac{1}{2\pi}\int_{-\infty}^{\infty} d\omega_u |H_u|^2\{|\beta_{uy}|^2 + \mathscr{N}(\Omega_{ul})|g_\perp(\Omega_{ul})|F_{ly}(\omega_u) \\ &\quad + \mathscr{N}(\Omega_{uh})[|g_a(\Omega_{uh})|F_{hy}(\omega_u) + |g_b(\Omega_{uh})|F'_{hy}(\omega_u)]\}, \end{aligned} \tag{B3.17}$$

where $F_{uj}(\omega) = \int_0^L |f_{uj}(z,\omega)|^2 dz$, $f_{uj}$ is given by Eq. (A3.6), and $F'_{uj}$ is defined as

$$F'_{uj}(\omega) = \int_0^L [P_u|\alpha_j(z,\omega)|^2 + P_v|\beta_j(z,\omega)|^2]dz, \tag{B3.18}$$

with $j = x, y$ and $u, v = l, h$ but $v \neq u$.

Similarly, $\mathscr{P}_{xy}$ and $\mathscr{P}_{yx}(\tau)$ in Eq. (3.40) are given by

$$\begin{aligned} \mathscr{P}_{xy}(\tau) &= \frac{1}{2\pi}\int_{-\infty}^{\infty} \mathscr{H}(\omega_s)\{\alpha_{iy}\beta_{sx} - \mathscr{N}(\Omega_{sh})|g_\perp(\Omega_{sh})|\mathscr{F}_{hx}(\omega_s) \\ &\quad - \mathscr{N}(\Omega_{sl})[|g_a(\Omega_{sl})|\mathscr{F}_{lx}(\omega_s) + |g_b(\Omega_{sl})|\mathscr{F}_{lx}(\omega_s)]\}e^{-i\omega_s\tau}d\omega_s, \end{aligned} \tag{B3.19}$$

$$\begin{aligned} \mathscr{P}_{yx}(\tau) &= \frac{1}{2\pi}\int_{-\infty}^{\infty} \mathscr{H}(\omega_s)\{\alpha_{ix}\beta_{sy} - \mathscr{N}(\Omega_{sl})|g_\perp(\Omega_{sl})|\mathscr{F}_{ly}(\omega_s) \\ &\quad - \mathscr{N}(\Omega_{sh})[|g_a(\Omega_{sh})|\mathscr{F}_{hy}(\omega_s) + |g_b(\Omega_{sh})|\mathscr{F}_{hy}(\omega_s)]\}e^{-i\omega_s\tau}d\omega_s, \end{aligned} \tag{B3.20}$$

where $\mathscr{F}_{uj}(\omega_s) = \int_0^L f_{uj}(z,\omega_s)f_{vq}(z,\omega_i)dz$ with $\omega_i = \omega_l + \omega_h - \omega_s$, and $\mathscr{F}_{uj}(\omega_s)$ is defined as

$$\mathscr{F}_{uj}(\omega_s) = -\int_0^L dz[P_u\alpha_j(z,\omega_s)\beta_q(z,\omega_i) + P_v\beta_j(z,\omega_s)\alpha_q(z,\omega_i)], \tag{B3.21}$$

where $u, v = l, h$ with $v \neq u$ and $j, q = x, y$ with $q \neq j$.

# Appendix C

In this appendix, we provide the derivation of the CHSH parameter [61, 62] for polarization-entangled states constructed using some typical FWM processes inside fibers.

## Degenerate FWM: single pump configuration

In the degenerate FWM discussed in Section 3, a time-multiplexing technique [22] or a polarization diversity loop [21] can be used to construct a polarization-entangled state. In this approach, the signal photon is coupled to the copolarized idler but the two processes at different polarizations are independent of each other.

By using Eqs. (3.6)-(3.9), we find that $\Gamma_1$, $\Gamma_2$, and $\mathscr{E}_+(\tau)$ become

$$\Gamma_1(\tau) = \frac{1}{4}\left[(I_{sx}-I_{sy})(I_{ix}-I_{iy}) + |\mathscr{P}_{xx}(\tau) - \mathscr{P}_{yy}(\tau)|^2\right], \tag{C3.22}$$

$$\Gamma_2(\tau) = \frac{1}{4}\left[(I_{sx}-I_{sy})(I_{ix}-I_{iy}) + |\mathscr{P}_{xx}(\tau) + \mathscr{P}_{yy}(\tau)|^2\right], \tag{C3.23}$$

$$\mathscr{E}_+(\tau) = (I_{sx}+I_{sy})(I_{ix}+I_{iy}) + |\mathscr{P}_{xx}(\tau)|^2 + |\mathscr{P}_{yy}(\tau)|^2, \tag{C3.24}$$

where $\mathscr{P}_{qq}(\tau) \equiv \langle \hat{A}_{sq}(t+\tau)\hat{A}_{iq}(t)\rangle$ $(q = x, y)$ is related to the signal-idler pair correlation, as discussed in Section 3.

In general, birefringent components are used to constructed four EPR-Bell states [5, 22]. Here we consider one of them, assuming that the two FWM paths have an identical phase. As the two FWM paths are nearly identical to each other, $\Gamma_1(\tau) \approx 0$. It is easy to show that the magnitude of $S(\tau)$ is maximized by setting, for example, $\theta_s = \pi/8$, $\theta_s' = -\pi/8$, $\theta_i = 0$, $\theta_i' = -\pi/4$, resulting in

$$S_m(\tau) = \frac{4\sqrt{2}\Gamma_2(\tau)}{\mathscr{E}_+(\tau)} = \frac{\sqrt{2}[(I_{sx}-I_{sy})(I_{ix}-I_{iy}) + |\mathscr{P}_{xx}(\tau) + \mathscr{P}_{yy}(\tau)|^2]}{(I_{sx}+I_{sy})(I_{ix}+I_{iy}) + |\mathscr{P}_{xx}(\tau)|^2 + |\mathscr{P}_{yy}(\tau)|^2}. \tag{C3.25}$$

In the optimal case, the pump power is split equally to create equal probability of signal-idler pairs. In this case, $I_{ux} = I_{uy}$, $\mathscr{P}_{xx}(\tau) = \mathscr{P}_{yy}(\tau)$, and Eq. (C3.25) reduces to the simple form of Eq. (3.55).

Eqs. (C3.25) and (3.55) are still valid even when orthogonally polarized noise background is present. In this case, the photon fluxes $I_{uq}$ in Eq. (C3.25) should include such contribution. Hence, $\rho_c(\tau)$ in Eq. (3.55) should be given as the realistic ratio between the true coincidence counting and accidental one.

## Non-degenerate FWM: copolarized pumping

The situation is quite similar in the case of copolarized pumping shown in Fig. 3.6. If the signal and idler are identical to each other [$\bar{\omega}_s = \bar{\omega}_i$, Fig. 3.6(b)], photon self-correlation would contribute to coincidence counting measurement. However, it turns out that the CHSH parameter with the maximum magnitude is still given by $S_m(\tau) = 4\sqrt{2}\Gamma_2(\tau)/\mathscr{E}_+(\tau)$, except that $\Gamma_2$ and $\mathscr{E}_+(\tau)$ now become

$$\Gamma_2(\tau) = \frac{1}{4}\left[(I_{sx} - I_{sy})^2 + |\mathscr{P}_{xx}(\tau) + \mathscr{P}_{yy}(\tau)|^2 + |\mathscr{P}'_{xx}(\tau) + \mathscr{P}'_{yy}(\tau)|^2\right], \tag{C3.26}$$

$$\mathscr{E}_+(\tau) = (I_{sx} + I_{sy})^2 + |\mathscr{P}_{xx}(\tau)|^2 + |\mathscr{P}_{yy}(\tau)|^2 + |\mathscr{P}'_{xx}(\tau)|^2 + |\mathscr{P}'_{yy}(\tau)|^2, \tag{C3.27}$$

where $\mathscr{P}'_{qq}(\tau) \equiv \langle \hat{A}^\dagger_{sq}(L, t+\tau)\hat{A}_{sq}(L,t)\rangle$ $(q = x, y)$ is related to the self-correlation of the $x$-polarized and $y$-polarized signal photons, respectively. In the optimal case when the pump power is equally split in two polarizations, $S_m(\tau)$ is still given by the simple form of Eq. (3.55) but where $\rho_c(\tau)$ is now given by Eq. (3.35).

## Non-degenerate FWM: orthogonal pumping

In the case of orthogonal pumping shown in Figs. 3.7 and 3.11, the $x$-polarized signal is coupled to the $y$-polarized idler, and vice versa. The two eigen processes are independent of each other.

When the signal and idler are distinguishable from each other ($\bar{\omega}_s \neq \bar{\omega}_i$), by use of Eqs. (3.30), (B3.13), and (B3.14), we can find that $\Gamma_1(\tau)$, $\Gamma_2(\tau)$, and $\mathscr{E}_+(\tau)$ are given by

$$\Gamma_1(\tau) = \frac{1}{4}\left[(I_{sx} - I_{sy})(I_{ix} - I_{iy}) - |\mathscr{P}_{xy}(\tau) + \mathscr{P}_{yx}(\tau)|^2\right], \tag{C3.28}$$

$$\Gamma_2(\tau) = \frac{1}{4}\left[(I_{sx} - I_{sy})(I_{ix} - I_{iy}) - |\mathscr{P}_{xy}(\tau) - \mathscr{P}_{yx}(\tau)|^2\right], \tag{C3.29}$$

$$\mathscr{E}_+(\tau) = (I_{sx} + I_{sy})(I_{ix} + I_{iy}) + |\mathscr{P}_{xy}(\tau)|^2 + |\mathscr{P}_{yx}(\tau)|^2. \tag{C3.30}$$

Note that $\mathscr{P}_{xy}(\tau)$ and $\mathscr{P}_{yx}(\tau)$ are now given by Eqs. (B3.19) and (B3.20) [or by Eqs. (3.41) and (3.42) at low pump power levels], respectively. As the two eigen-processes are nearly identical to each other, $\Gamma_2(\tau) \approx 0$. It is easy to show that the magnitude of the CHSH parameter is maximized by setting, for example, $\theta_s = \pi/8$, $\theta'_s = -\pi/8$, $\theta_i = \pi/2$, $\theta'_i = 3\pi/4$, resulting in

$$S_m(\tau) = \frac{-4\sqrt{2}\Gamma_1(\tau)}{\mathscr{E}_+(\tau)}. \tag{C3.31}$$

By use of Eqs. (C3.30) and (C3.28), we find Eq. (C3.31) becomes Eq. (3.56).

If the signal and idler are identical ($\bar{\omega}_s = \bar{\omega}_i$) [Fig. 3.11(c)], self-correlation would contribute to coincidence counting. $S_m(\tau)$ is still given by Eq. (C3.31) under the same angle setting, but $\Gamma_1(\tau)$ and $\mathscr{E}_+(\tau)$ are now modified to be

$$\Gamma_1(\tau) = \frac{1}{4}\left[(I_{sx} - I_{sy})^2 - |\mathscr{P}_{xy}(\tau) + \mathscr{P}_{yx}(\tau)|^2 + |\mathscr{P}'_{xx}(\tau) - \mathscr{P}'_{yy}(\tau)|^2\right], \tag{C3.32}$$

$$\mathscr{E}_+(\tau) = (I_{sx} + I_{sy})^2 + |\mathscr{P}_{xy}(\tau)|^2 + |\mathscr{P}_{yx}(\tau)|^2 + |\mathscr{P}'_{xx}(\tau)|^2 + |\mathscr{P}'_{yy}(\tau)|^2. \tag{C3.33}$$

If narrowband filters are used for the signal, Eqs. (C3.32) and (C3.33) reduce to

$$\Gamma_1(\tau) = \frac{1}{4}\left[(I_{sx}-I_{sy})^2(1+|\varphi_s(\tau)|^2) - |\mathscr{P}_{xy}(\tau)+\mathscr{P}_{yx}(\tau)|^2\right], \tag{C3.34}$$

$$\mathscr{E}_+(\tau) = (I_{sx}+I_{sy})^2 + |\varphi_s(\tau)|^2(I_{sx}^2+I_{sy}^2) + |\mathscr{P}_{xy}(\tau)|^2 + |\mathscr{P}_{yx}(\tau)|^2, \tag{C3.35}$$

where $\varphi_s(\tau)$ is given by Eq. (3.17). Because of the symmetry of the two eigen processes, their pair correlations are same and Eq. (C3.31) reduces to Eq. (3.57).

## References


[1] Q. Lin, F. Yaman, and G. P. Agrawal, Opt. Lett. **31**, 1286 (2006).

[2] Q. Lin, F. Yaman, and G. P. Agrawal, "Photon pair generation in optical fibers through four-wave mixing: Role of Raman scattering and pump polarization," submitted to Phys. Rev. A.

[3] N. Gisin, G. Ribordy, W. Tittel, and H. Zbinden, Rev. Mod. Phys. **74**, 145 (2002).

[4] D. C. Burnham and D. L. Weinberg, Phys. Rev. Lett. **25**, 84 (1970).

[5] P. G. Kwiat, K. Mattle, H. Weinfurter, and A. Zeilinger, Phys. Rev. Lett. **75**, 4337 (1995).

[6] S. Tanzilli, W. Tittel, M Halder, O. Alibart, P. Baldi, N. Gisin, and H. Zbinden, Nature **437**, 116 (2005).

[7] S. Tanzilli, H. De Riedmatten, W. Tittel, H. Zbinden, P. Baldi, M. De Micheli, D. B. Ostrowsky, N. Gisin, Electron. Lett. **37**, 26 (2001).

[8] H. Takesue, K. Inoue, O. Tadanaga, Y. Nishida, and M. Asobe, Opt. Lett. **30**, 293 (2005).

[9] C. Kurtsiefer, M. Oberparleiter, and H. Weinfurter, Phys. Rev. A **64**, 023802 (2001).

[10] M. Fiorentino, P. L. Voss, J. E. Sharping, and P. Kumar, IEEE Photon. Technol. Lett. **14**, 983 (2002).

[11] J. E. Sharping, J. Chen, X. Li, P. Kumar, and R. S. Windeler, Opt. Exp. **12**, 3086 (2004).

[12] X. Li, J. Chen, P. Voss, J. Sharping, and P. Kumar, Opt. Exp. **12**, 3737 (2004).

[13] K. Inoue and K. Shimizu, Jap. J. Appl. Phys. **43**, 8048 (2004).

[14] J. G. Rarity, J. Fulconis, J. Duligall, W. J. Wadsworth, and P. St. J. Russell, Opt. Exp. **13**, 534 (2005).

[15] J. Fulconis, O. Alibart, W. J. Wadsworth, P. St. J. Russell, and J. G. Rarity, Opt. Exp. **13**, 7572 (2005).

[16] H. Takesue and K. Inoue, Opt. Exp. **13**, 7832 (2005).

[17] K. F. Lee, J. Chen, C. Liang, X. Li, P. L. Voss, and P. Kumar, Opt. Lett. **31**, 1905 (2006).

[18] J. Fan, A. Dogariu, and L. J. Wang, Opt. Lett. **30**, 1530 (2005).

[19] J. Fan, A. Migdall, and L. J. Wang, Opt. Lett. **30**, 3368 (2005).

[20] J. Fan and A. Migdall, Opt. Exp. **13**, 5777 (2005).

[21] H. Takesue and K. Inoue, Phys. Rev. A **70**, 031802(R) (2004).

[22] X. Li, P. L. Voss, J. E. Sharping, and P. Kumar, Phys. Rev. Lett. **94**, 053601 (2005).

[23] H. Takesue and K. Inoue, Phys. Rev. A **72**, 041804(R) (2005).

[24] L. J. Wang, C. K. Hong, and S. R. Friberg, J. Opt. B **3**, 346 (2001).

[25] J. Chen, X. Li, and P. Kumar, Phys. Rev. A **72**, 033801 (2005).

[26] O. Alibart, J. Fulconis, G. K. L. Wong, S. G. Murdoch, W. J. Wadsworth, and J. G. Rarity, New J. Phys. **8**, 67 (2006).

[27] P. L. Voss and P. Kumar, Opt. Lett. **29**, 445 (2004); J. Opt. B **6**, S762 (2004).

[28] R. H. Stolen, in *Raman Amplifiers for Telecommunications 1*, M. N. Islam Ed. (Springer, New York, 2003), Chap. 2. The Raman spectrum data used in this chapter were provided by R. H. Stolen.

[29] R. H. Stolen, J. P. Gordon, W. J. Tomlinson, and H. A. Haus, J. Opt. Soc. Am. B **6**, 1159 (1989).

[30] L. Boivin, F. X. Kartner, and H. A. Haus, Phys. Rev. Lett. **73**, 240-243 (1994).

[31] F. X. Kartner, D. J. Dougherty, H. A. Haus, and E. P. Ippen, J. Opt. Soc. Am. B **11**, 1267 (1994).

[32] P. D. Drummond, in *Coherence and Quantum Optics VII*, J. H. Eberly, L. Mandel, and E. Wolf (Eds.) (Plenum Press, New York), 323 (1996).

[33] R. W. Hellwarth, Progress in Quantum Electronics **5**, 1 (1977).

[34] G. P. Agrawal, *Nonlinear Fiber Optics*, 3*rd* ed. (Academic, Boston, 2001).

[35] S. J. Carter and P. D. Drummond, Phys. Rev. Lett. **67**, 3757 (1991).

[36] J. H. Shapiro and L. Boivin, Opt. Lett. **20**, 925 (1995).

[37] P. D. Drummond and J. F. Corney, J. Opt. Soc. Am. B **18**, 139 (2001); 153 (2001).

[38] P. L. Voss, K. G. Köprülü, and P. Kumar, J. Opt. Soc. Am B **23**, 598 (2006).

[39] D. J. Dougherty, F. X. Karnter, H. A. Haus, and E. P. Ippen, Opt. Lett. **20**, 31-33 (1995).

[40] D. Mahgerefteh, D. L. Butler, J. Goldhar, B. Rosenberg, and G. L. Burdge, Opt. Lett. **21**, 2026 (1996).

[41] L. Mandel and E. Wolf, *Optical Coherence and Quantum Optics* (Cambridge Univeristy Press, 1995), Chap. 14.

[42] S. G. Murdoch, R. Leonhardt, and J. D. Harvey, Opt. Lett. **20**, 866 (1995).

[43] R. J. Kruhlak, G. K. L. Wong, J. S. Y. Chen, S. G. Murdoch, R. Leonhardt, J. D. Harvey, N. Y. Joly, and J. C. Knight, Opt. Lett. **31**, 1379 (2006).

[44] Y. Deng, Q. Lin, F. Lu, G. P. Agrawal, and W. H. Knox, Opt. Lett. **30**, 1234 (2005).

[45] Q. Lin and G. P. Agrawal, Opt. Lett. **29**, 1114 (2004).

[46] C. J. McKinstrie, H. Kogelnik, R. M. Jopson, S. Radic, and A. V. Kanaev, Opt. Exp. **12**, 2033 (2004).

[47] W. P. Grice and I. A. Walmsley, Phys. Rev. A **56**, 1627 (1997).

[48] T. E. Keller and M. H. Rubin, PHys. Rev. A **56**, 1534 (1997).

[49] K. K. Y. Wong, M. E. Marhic, K. Uesaka, and L. G. Kazovsky, IEEE Photon. Technol. Lett. **14**, 911 (2002).

[50] S. Radic, C. J. McKinstrie, R. M. Jopson, J.C.Centanni, Q. Lin and G. P. Agrawal, IEE Electron. Lett. **39**, 838 (2003).

[51] T. Tanemura and K. Kikuchi, IEEE Photon. Technol. Lett. **15**, 1573 (2003).

[52] Q. Lin, R. Jiang, C. F. Marki, C. J. McKinstrie, R. Jopson, J. Ford, G. P. Agrawal, and S. Radic, IEEE Photon. Technol. Lett. **17**, 2376 (2005).

[53] Q. Lin and G. P. Agrawal, J. Opt. Soc. Am. B **21**, 1216 (2004).

[54] D. Branning, W. P. Grice, R. Erdmann, and I. A. Walmsley, Phys. Rev. Lett. **83**, 955 (1999).

[55] P. G. Kwiat, W. A. Vareka, C. K. Hong, H. Nathel, and R. Y. Chiao, Phys. Rev. A. **41**, 2910 (1990).

[56] Y. H. Shih, A. V. Sergienko, M. H. Rubin, T. E. Kiess, and C. O. Alley, Phys. Rev. A **49**, 4243 (1994).

[57] K. Sanaka, K. Kawahara, and T. Kuga, Phys. Rev. Lett. **86**, 5620 (2001).

[58] J. D. Franson, Phys. Rev. Lett. **62**, 2205 (1989).

[59] Z. Y. Ou, X. Y. Zou, L. J. Wang, and L. Mandel, Phys. Rev. Lett. **65**, 321 (1990).

[60] M. H. Rubin and Y. H. Shih, Phys. Rev. A **45**, 8138 (1990).

[61] J. F. Clauser, M. A. Horne, A. Shimony, and R. A. Holt, Phys. Rev. Lett. **23**, 880 (1969).

[62] D. F. Walls and G. J. Milburn, *Quantum Optics* (Springer-Verlag, 1994), Chap. 5.

[63] Q. Lin and G. P. Agrawal, “Silicon waveguides for creating quantum-correlated photon pairs”, Opt. Lett. **31**, November (2006).

# 4 Four-Wave Mixing in Dual-Pump Configuration: Quantum Noise and Polarization Dependence

In this chapter, we use the general theory presented in Chapter 2 to investigate the quantum noise properties and intrinsic polarization-dependent gain in dual-pump fiber-optic parametric amplifiers (FOPAs). In this case, the situation becomes much more complicated compared with last chapter, because high pump powers, required for a large gain and high conversion efficiency, simultaneously excite multiple FWM processes, including degenerate and non-degenerate ones, which couple with each other. Here we develop a complete vector theory which fully incorporates the contributions of both the spontaneous and stimulated Raman scattering. We show that Raman scattering adds considerably to the noise figure of dual-pump parametric amplifiers [1].

We provide a simple physical picture to explain the polarization properties of complicated FWM process [2]. We also show that, contrary to a common belief, the orthogonal-pumping configuration exhibits polarization-dependent gain (PDG) because of the contribution of Raman scattering to the underlying four-wave mixing (FWM) process [3]. We also extend the theory to describe the quantum noise in such orthogonal pumping configuration and show that the amplified spontaneous emission (ASE) becomes polarization dependent.

This work is done in collaboration with Fatih Yaman in Prof. Agrawal's group.

## 4.1 Introduction

Modern fiber-optic parametric amplifiers (FOPAs) employ four-wave mixing (FWM) inside highly nonlinear fibers (HNLF) or microstructured fibers and are useful for applications such as signal amplification, wavelength conversion, and ultrafast signal processing [4]. Dual-pump FOPAs are often preferred as they provide more flexibility through individual control of pumps [5, 6]. It is believed that phase-insensitive FOPAs can operate close to the 3-dB quantum-noise limit [7]. However, dual-pump FOPAs involve multiple FWM processes [8], whose presence can degrade the FOPA performance. Moreover, the third-order fiber nonlinearity contains Raman contribution with a retarded molecular response, which involves thermal phonons and is likely to introduce additional noise [9, 10]. Because of the inherent complexity of the problem, the fundamental quantum-noise limit of dual-pump FOPAs still remains unknown. In Section 3 of this chapter, we develop a complete theory to investigate this aspect and show that the noise figure of dual-pump FOPAs not only oscillates with signal wavelength, but it also exhibits a noise floor far above the 3-dB quantum limit. Such a noise floor exists for any separation of pump wavelengths.

The polarization-independent operation is essential for practical FOPAs to ensure that the same performance is realized for signals with any input state of polarization (SOP). It is commonly accepted that the non-degenerate FWM process implemented with two orthogonal linearly polarized pumps is intrinsically polarization independent and it can provide a relatively uniform gain over a broad bandwidth [2],[11]-[14]. Polarization-dependent gain (PDG) observed experimentally [14, 15] in such a configuration is attributed to the impact of fiber birefringence [16, 17]. The absence of PDG for orthogonally polarized pumps holds when the underlying FWM results from the instantaneous electronic response. However, the third-order nonlinear response of optical fibers also depends on the retarded molecular response. Because of the latter, the FWM process is inevitably accompanied with Raman scattering [18] that is known to exhibit a strong polarization dependence [19]. In Section 4 of this chapter, we develop a vector theory of FWM that includes the Raman contribution and show that the orthogonally polarized pumping configuration exhibits considerable PDG because of retarded Raman response.

Although orthogonal pumping configuration is widely used, little is known about the noise properties of such a pumping configuration. In Section 5 of this chapter, we extend the theory to find the ASE and associated noise figure (NF) for this configuration, and show that the NF is strongly polarization dependent because of polarization-dependent SRS.

## 4.2 General Theory

Dual-pump FOPAs operate such that multiple FWM interactions among the four sidebands shown in Fig. 4.1 occur simultaneously [5]. More specifically, if $\omega_l$ and $\omega_h$ are frequencies of the two pumps and $\omega_1$ is the signal frequency, three idlers are generated through the frequency combinations $\omega_l + \omega_h \rightarrow \omega_1 + \omega_2$, $2\omega_l \rightarrow \omega_1 + \omega_3$, $2\omega_h \rightarrow \omega_2 + \omega_4$, $\omega_l + \omega_2 \rightarrow \omega_h + \omega_3$, and $\omega_h + \omega_1 \rightarrow \omega_l + \omega_4$. In our analysis, we include all six fields but assume that they are in the form of CW waves. Substituting the total field, $\hat{\boldsymbol{A}} = \sum_j \hat{\boldsymbol{A}}_j \exp[-i(\omega_j - \omega_0)\tau]$, into Eq. (2.32), decomposing it into different frequency components, we

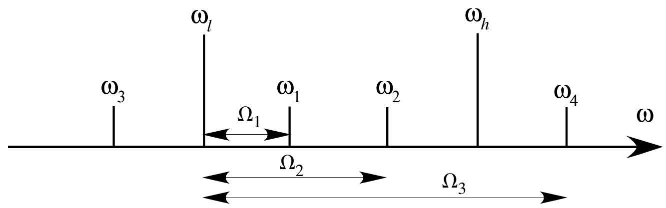


Figure 4.1: Illustration of the frequency relationship among the two pumps and the four sidebands. $\omega_h$ and $\omega_l$ are the pump frequencies and $\omega_1$ to $\omega_4$ are those of four sidebands.

can obtain evolution equations for each wave. In general, the two pumps are much more intense than the four sidebands. As a result, they can be treated classically and assumed to be non-depleted. The pump equation is given by:

$$\begin{aligned}\frac{d\boldsymbol{A}_l}{dz} = &\; i\overleftrightarrow{\boldsymbol{k}}_l \cdot \boldsymbol{A}_l + i\frac{\gamma}{3}(2+f_R)P_0\boldsymbol{A}_l + i\gamma\eta_{lh}(2)(\boldsymbol{A}_h^* \cdot \boldsymbol{A}_l)\boldsymbol{A}_h \\ &+ i\frac{\gamma f_E}{3}[\boldsymbol{A}_l^*(\boldsymbol{A}_l \cdot \boldsymbol{A}_l) + 2\boldsymbol{A}_h^*(\boldsymbol{A}_l \cdot \boldsymbol{A}_h)],\end{aligned} \tag{4.1}$$

where $\eta_{jk}(n) = nf_E/3 + f_R\widetilde{R}_a(\omega_j - \omega_k)$ and $P_0 = |\boldsymbol{A}_l|^2 + |\boldsymbol{A}_h|^2$ is the total pump power. The tensor $\overleftrightarrow{\boldsymbol{k}}_l$ is the propagation vector related to a Fourier component of $\chi_{ij}^{(1)}$, which may include birefringence at the pump frequency $\omega_l$. The equation for $\boldsymbol{A}_h$ can be obtained from Eq. (4.1) by exchanging the subscripts $l$ and $h$. It is easy to show from Eq. (4.1) that the total pump power remains constant along the fiber. Fiber losses are neglected since short fibers ($\sim$1 km) are generally used for making FOPAs.

The four sidebands are treated quantum mechanically to include the effects of vacuum fluctuations. The wave at $\omega_1$ is found to satisfy

$$\begin{aligned}\frac{d\hat{\boldsymbol{A}}_1}{dz} = &\; i\overleftrightarrow{\boldsymbol{k}}_1 \cdot \hat{\boldsymbol{A}}_1 + i\frac{\gamma}{3}(2+f_R)P_0\hat{\boldsymbol{A}}_1 + i\gamma\eta_{1l}(2)(\boldsymbol{A}_l^* \cdot \boldsymbol{A}_1)\hat{\boldsymbol{A}}_l + i\gamma\eta_{1h}(2)(\boldsymbol{A}_h^* \cdot \hat{\boldsymbol{A}}_1)\boldsymbol{A}_h \\ &+ i\frac{2\gamma f_E}{3}[\boldsymbol{A}_l^*(\boldsymbol{A}_l \cdot \hat{\boldsymbol{A}}_1) + \boldsymbol{A}_h^*(\boldsymbol{A}_h \cdot \hat{\boldsymbol{A}}_1)] + i\gamma\eta_{l2}(2)(\hat{\boldsymbol{A}}_2^\dagger \cdot \boldsymbol{A}_l)\boldsymbol{A}_h + i\gamma\eta_{h2}(2)(\hat{\boldsymbol{A}}_2^\dagger \cdot \boldsymbol{A}_h)\boldsymbol{A}_l \\ &+ i\frac{2\gamma f_E}{3}\hat{\boldsymbol{A}}_2^\dagger(\boldsymbol{A}_l \cdot \boldsymbol{A}_h) + i\gamma\eta_{l3}(2)(\hat{\boldsymbol{A}}_3^\dagger \cdot \boldsymbol{A}_l)\boldsymbol{A}_l + i\frac{\gamma f_E}{3}\hat{\boldsymbol{A}}_3^\dagger(\boldsymbol{A}_l \cdot \boldsymbol{A}_l) + i\gamma\eta_{lh}(2)(\boldsymbol{A}_h^* \cdot \boldsymbol{A}_l)\hat{\boldsymbol{A}}_4 \\ &+ i\gamma\eta_{4h}(2)(\boldsymbol{A}_h^* \cdot \hat{\boldsymbol{A}}_4)\boldsymbol{A}_l + i\frac{2\gamma f_E}{3}\boldsymbol{A}_h^*(\boldsymbol{A}_l \cdot \hat{\boldsymbol{A}}_4) + i\hat{m}_{1l}\boldsymbol{A}_l + i\hat{m}_{1h}\boldsymbol{A}_h,\end{aligned} \tag{4.2}$$

where $\hat{m}_{jk} = \hat{m}(z, \omega_j - \omega_k)$ is the noise operator for a specific phonon mode of frequency $|\omega_j - \omega_k|$ related to a Fourier component of the noise operator $\hat{m}(z,\tau)$. It satisfies the commutation relation [9, 20] of $[\hat{m}(z_1,\Omega_j), \hat{m}^\dagger(z_2,\Omega_k)] = g_R(\Omega_j)\delta_{jk}\delta(z_1 - z_2)$, where $g_R(\Omega_j) \equiv 2\gamma f_R \mathrm{Im}[\widetilde{R}_a(\Omega_j)]$ is the Raman gain/loss coefficient at $\Omega_j$. At the thermal equilibrium with a fiber temperature of $\mathscr{T}$, the phonon mode at $|\Omega_j|$ has a population of $n_j^{th} = [\exp(\hbar|\Omega_j|/k_B\mathscr{T}) - 1]^{-1}$. Note that we have dropped in Eqs. (4.1) and (4.2) the anisotropic part of Raman scattering because of its negligible magnitude [19].

In Eq. (4.2), the fields of four sidebands have been normalized such that $\hat{A}^{\dagger}_{j\mu}\hat{A}_{j\mu}$ represents the photon number at $\omega_j$ ($j = 1-4$) and $\mu$ ($\mu = x, y$) polarization so that $[\hat{A}_{j\mu}(z), \hat{A}^{\dagger}_{k\nu}(z)] = \delta_{jk}\delta_{\mu\nu}$. Equations for other three waves can be obtained by considering the symmetry among the four sidebands. For $\hat{\boldsymbol{A}}_2$, we exchange subscripts $l$, 1, 3 with $h$, 2, 4, respectively. For $\hat{\boldsymbol{A}}_3$, we exchange subscripts 1 and 2 with 3 and 4, respectively. For $\hat{\boldsymbol{A}}_4$, we exchange subscripts $l$, 1, 2 with $h$, 4, 3, respectively. Eqs. (4.1) and (4.2) are quite general as they count in both polarizations. In experiments, only specific polarization configuration is used for parametric generation. In the following sections, we will use these equations to discuss FWM in different polarization configurations and its impact on parametric amplification.

## 4.3 Quantum Noise in Copolarized Pumping Configuration

Dual-pump parametric amplifiers commonly employ a polarization configuration in which two pumps are copolarized to maximize the FWM efficiency. In this section, we investigate the quantum noise properties of this configuration. To simplify the analysis, we assume all the fields are linearly polarized along a principal axis of the fiber. As a result, all waves would maintain their polarizations along the fiber, and thus can be treated as scalar fields. In this section, we suppress the polarization subscripts $x$ and $y$. After making a transformation for all the fields, $\hat{A}_j \to \hat{A}_j \exp[-i\gamma P_0 z]$, to remove a common phase factor, the pump equation (4.1) reduces to

$$\frac{dA_j}{dz} = ik_j A_j + i\widetilde{R}_{jk} P_k A_j \quad (j,k = h,l \text{ with } j \neq k), \tag{4.3}$$

where $k_j$ is the propagation constant, $P_j = |A_j|^2$ is the pump power, $\widetilde{R}_{jk} = \gamma\eta_{jk}(3) = \gamma[f_E + f_R\widetilde{R}_a(\omega_j - \omega_k)]$. Equation (4.3) is easy to solve and provides an analytical solution for the pump waves. The fiber nonlinearity not only imposes phase modulation on two pumps but also induces power transfer between them through stimulated Raman scattering. However, the total pump power $P_0 = P_h + P_l$ remains constant along the fiber.

Equation (4.2) for the wave at $\omega_1$ reduces to

$$\begin{aligned}\frac{d\hat{A}_1}{dz} &= i\big(\beta_1 + \widetilde{R}_{1l}P_l + \widetilde{R}_{1h}P_h\big)\hat{A}_1 + i\big(\widetilde{R}_{l2} + \widetilde{R}_{h2}\big)A_l A_h \hat{A}_2^{\dagger} \\ &+ i\widetilde{R}_{l3}A_l^2\hat{A}_3^{\dagger} + i\big(\widetilde{R}_{4h} + \widetilde{R}_{lh}\big)A_h^* A_l \hat{A}_4 + iA_l\hat{\eta}_{1l} + iA_h\hat{\eta}_{1h}.\end{aligned} \tag{4.4}$$

If one pump is absent, say $A_h = 0$, Eq. (4.2) reduces to the case of degenerate FWM [10].

To simplify the analysis, we define a column vector $\hat{\boldsymbol{F}} = [\hat{A}_1; \hat{A}_2^{\dagger}; \hat{A}_3^{\dagger}; \hat{A}_4]$ and write Eq. (4.2) together with those for three other waves in a vector form as:

$$d\hat{\boldsymbol{F}}/dz = \boldsymbol{M}\hat{\boldsymbol{F}} + \hat{\boldsymbol{u}}, \tag{4.5}$$

where $\boldsymbol{M}$ is a $4\times 4$ matrix describing FWM couplings among the four sidebands and its elements can be obtained from Eq. (4.4). $\hat{\boldsymbol{u}} = [\hat{u}_1; \hat{u}_2^\dagger; \hat{u}_3^\dagger; \hat{u}_4]$ represents spontaneous Raman scattering along the fiber, where $\hat{u}_j = iA_l\hat{\eta}_{jl} + iA_h\hat{\eta}_{jh}$ $(j = 1-4)$. When the two pumps remain undepleted, Eq. (4.5) is a set of linear equations with the following formal solution:

$$\hat{\boldsymbol{F}}(L) = \boldsymbol{T}(L)\hat{\boldsymbol{F}}(0) + \hat{\boldsymbol{N}}, \tag{4.6}$$

where the transfer matrix $\boldsymbol{T}$ is the solution of $d\boldsymbol{T}/dz = \boldsymbol{MT}$ and $\hat{\boldsymbol{N}}$ is the amplified spontaneous Raman scattering (ASRS) accumulated along the fiber and defined as $\hat{\boldsymbol{N}} = \int_0^L \boldsymbol{T}(L-z)\hat{\boldsymbol{u}}(z)dz$.

In the following, we consider phase-insensitive amplification in which only one signal wave at $\omega_m$ $(m = 1-4)$, with a mean photon number of $\langle n_m(0)\rangle = n_0$, is launched into a FOPA to generate three idlers. Equation (4.6) shows that the mean photon number at $\omega_j$, $\langle \hat{n}_j\rangle \equiv \langle \hat{A}_j^\dagger \hat{A}_j\rangle$, is given by

$$\langle \hat{n}_j(L)\rangle = \langle \hat{\boldsymbol{F}}_j^\dagger(L)\hat{\boldsymbol{F}}_j(L)\rangle = |\boldsymbol{T}_{jm}|^2 n_0 + |\boldsymbol{T}_{j2}|^2 + |\boldsymbol{T}_{j3}|^2 + \langle \hat{\boldsymbol{N}}_j^\dagger \hat{\boldsymbol{N}}_j\rangle, \qquad (j = 1,4), \tag{4.7}$$

$$\langle \hat{n}_j(L)\rangle = \langle \hat{\boldsymbol{F}}_j(L)\hat{\boldsymbol{F}}_j^\dagger(L)\rangle = |\boldsymbol{T}_{jm}|^2 n_0 + |\boldsymbol{T}_{j1}|^2 + |\boldsymbol{T}_{j4}|^2 + \langle \hat{\boldsymbol{N}}_j \hat{\boldsymbol{N}}_j^\dagger\rangle, \qquad (j = 2,3), \tag{4.8}$$

where the angle brackets denote an average over the quantum state. Clearly, the average output consists of three contributions: (i) amplification or wavelength conversion of the input signal with an efficiency $|T_{jm}|^2$, (ii) amplified spontaneous FWM, equivalent to adding one photon to conjugated waves at the input end, and (iii) ASRS given by the last term. Similarly, we can find the variances of photon number fluctuations, $\langle(\Delta n_j)^2\rangle \equiv \langle n_j^2\rangle - \langle n_j\rangle^2$, to be

$$\begin{aligned}\langle[\Delta n_j(L)]^2\rangle &= n_0|\boldsymbol{T}_{jm}|^2\Big[\sum_{k=1}^{4}|\boldsymbol{T}_{jk}|^2 + \langle \hat{\boldsymbol{N}}_j\hat{\boldsymbol{N}}_j^\dagger + \hat{\boldsymbol{N}}_j^\dagger\hat{\boldsymbol{N}}_j\rangle\Big] \\ &\quad + W_{j14}W_{j23} + W_{j14}\langle \boldsymbol{N}_j^\dagger\boldsymbol{N}_j\rangle + W_{j23}\langle \boldsymbol{N}_j\boldsymbol{N}_j^\dagger\rangle + \sigma_j^2,\end{aligned} \tag{4.9}$$

where $W_{j14} \equiv |\boldsymbol{T}_{j1}|^2 + |\boldsymbol{T}_{j4}|^2$, $W_{j23} \equiv |\boldsymbol{T}_{j2}|^2 + |\boldsymbol{T}_{j3}|^2$, and $\sigma_j^2 \equiv \langle(\boldsymbol{N}_j^\dagger\boldsymbol{N}_j)^2\rangle - \langle\boldsymbol{N}_j^\dagger\boldsymbol{N}_j\rangle^2$. In practice, the photon number of the input signal is generally much larger than 1 ($n_0 \gg 1$), resulting in

$$\langle n_j(L)\rangle \approx n_0|\boldsymbol{T}_{jm}(L)|^2, \tag{4.10}$$

$$\langle[\Delta n_j(L)]^2\rangle \approx n_0|\boldsymbol{T}_{jm}|^2[\sum_{k=1}^{4}|\boldsymbol{T}_{jk}|^2 + \langle \hat{\boldsymbol{N}}_j\hat{\boldsymbol{N}}_j^\dagger + \hat{\boldsymbol{N}}_j^\dagger\hat{\boldsymbol{N}}_j\rangle]. \tag{4.11}$$

Signal-to-noise ratio (SNR) of the wave at $\omega_j$ is defined as $SNR(\omega_j) = \langle n_j\rangle^2/\langle(\Delta n_j)^2\rangle$. Assuming that the input signal stays in a coherent state, its SNR is given by $SNR_{in}(\omega_m) = n_0$. In practice, amplifier noise is quantified by the noise figure (NF) defined as $NF(\omega_j) = SNR_{in}(\omega_m)/SNR_{out}(\omega_j)$, where $SNR_{out}(\omega_j)$ stands for the SNR of $\omega_j$ $(j = 1-4)$ at the output end. When $n_0 \gg 1$, $NF(\omega_j)$ is found to be

$$NF(\omega_j) \approx |\boldsymbol{T}_{jm}|^{-2}\Big[\sum_{k=1}^{4}|\boldsymbol{T}_{jk}|^2 + \langle \hat{\boldsymbol{N}}_j\hat{\boldsymbol{N}}_j^\dagger + \hat{\boldsymbol{N}}_j^\dagger\hat{\boldsymbol{N}}_j\rangle\Big]. \tag{4.12}$$

The FOPA NF at $\omega_j$ originates from three dominant sources. Both the quantum noise at the input signal and the vacuum fluctuations at other sidebands are converted to the fluctuations at $\omega_j$ through FWM [8]. Moreover, two pumps introduce extra noise through ASRS.

Because of the symmetry of four sidebands with respect to the two pumps, only three phonon modes participate with frequencies of $\Omega_\mu$ ($\mu = 1$ to 3) in Raman scattering (see Fig. 4.1). A detailed analysis shows that

$$\begin{aligned}\langle \hat{\boldsymbol{N}}_j \hat{\boldsymbol{N}}_j^\dagger + \hat{\boldsymbol{N}}_j^\dagger \hat{\boldsymbol{N}}_j \rangle = {} & \Gamma_1 \int_0^L dz \big| \boldsymbol{T}_{j1} A_l + \boldsymbol{T}_{j4} A_h - \boldsymbol{T}_{j2} A_h^* - \boldsymbol{T}_{j3} A_l^* \big|^2 \\ & + \Gamma_2 \int_0^L dz \big| \boldsymbol{T}_{j1} A_h - \boldsymbol{T}_{j2} A_l^* \big|^2 + \Gamma_3 \int_0^L dz \big| \boldsymbol{T}_{j4} A_l - \boldsymbol{T}_{j3} A_h^* \big|^2, \end{aligned} \tag{4.13}$$

where $\Gamma_\mu = |g_R(\Omega_\mu)|(2n_\mu^{th} + 1)$. In Eq. (4.13), $T_{jk}$ denotes $T_{jk}(L-z)$ and $A_j$ denotes $A_j(z)$. Equation (4.13) shows clearly that ASRS at each phonon mode is seeded by multiple spontaneous Raman scattering: 4 channels at $\Omega_1$, 2 channels at $\Omega_2$, and 2 channels at $\Omega_3$, respectively (see Fig. 4.1). They are amplified by FWM and interfere with each other within each phonon mode.

We now apply our analysis to a FOPA made of a 500-m-long HNLF with a zero-dispersion wavelength (ZDWL) at 1550 nm and an effective area of $a_{\text{eff}} = 10\ \mu\text{m}^2$, corresponding to $\gamma \approx 10.5\ \text{W}^{-1}/\text{km}$. The Raman gain spectrum is obtained from Ref. [21]. The peak value of $g \equiv 2n_2\omega_0 f_R \text{Im}[\widetilde{H}_R(\Omega_R)]/c = 0.62 \times 10^{-13}\text{m/W}$ is used in the 1550-nm regime [19, 22], where $\Omega_R/(2\pi) = 13.2$ THz is the Raman frequency shift. The classical equation governing the transfer matrix $\boldsymbol{T}(z)$ can be easily solved numerically. Using this solution in Eqs. (4.12) and (4.13), we obtain the noise figure. Figure 4.2 shows the gain and NF spectra for a 50-nm pump spacing, similar to a typical experimental configuration [6].

In the absence of Raman scattering, the FOPA exhibits a uniform 34-dB gain and a 3-dB noise figure within a broad central region where the parametric generation is dominated by the single non-degenerate FWM process $\omega_h + \omega_l \to \omega_1 + \omega_2$. However, NF exhibits oscillations with increased peak values as the signal is tuned towards the pumps. Such oscillations result from the participation of multiple FWM processes that are close to satisfying the phase-matching conditions. Especially, the FWM processes, $\omega_l + \omega_2 \to \omega_h + \omega_3$ and $\omega_h + \omega_1 \to \omega_l + \omega_4$ (sometimes called Bragg scattering [6]), introduce considerable internal losses for the waves at $\omega_1$ and $\omega_2$. They are also responsible for the decrease of FOPA gain around these regions. As seen in Fig. 4.2, a reduced gain always accompanies NF oscillations.

Raman scattering introduces power transfer between the two pumps and thus affects the FWM efficiency, leading to a gain reduction by 2 dB in Fig. 4.2. Moreover, the induced ASRS is proportional to both the Raman gain coefficient and the phonon populations. In the central part of the gain spectrum, the signal acts as the Stokes of high-frequency pump and simultaneously as the anti-Stokes of the low-frequency one. The balance between these two produces a nearly frequency-independent noise plateau

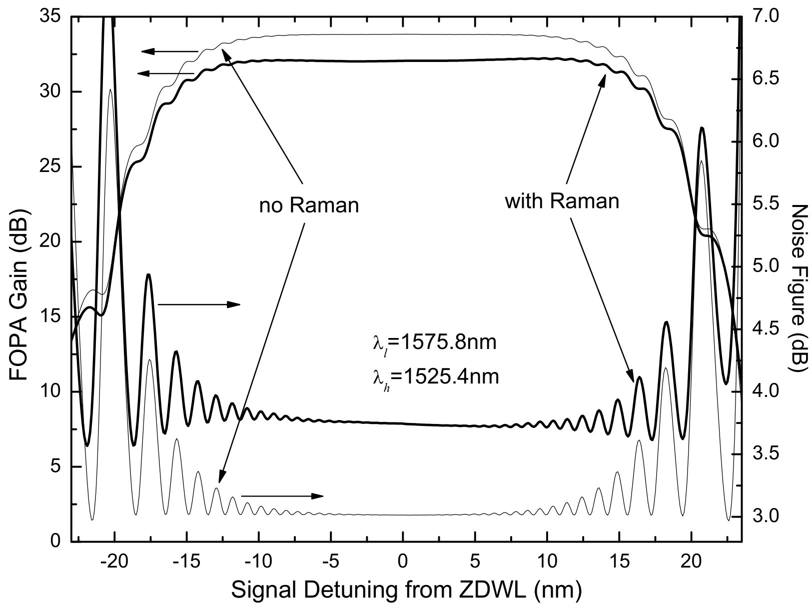


Figure 4.2: Spectra of FOPA gain and noise figure as a function of signal detuning from the ZDWL. The HNLF is assumed to have third- and fourth-order dispersions of $0.0378\ \mathrm{ps}^3/\mathrm{km}$ and $1.0\times10^{-4}\ \mathrm{ps}^4/\mathrm{km}$, respectively, and kept at room temperature of $\mathscr{T} = 300$ K. Two pumps are launched with equal input powers of 0.5 W in the absence of Raman scattering (thin curves), but their powers are optimized to $P_l =$ 0.37 W and $P_h = 0.63$ W for optimal gain in the presence of Raman scattering (thick curves). Pump wavelengths are shown in the figure.

with a magnitude of 3.7 dB over a broad spectral range where the FOPA gain is uniform. At the same time, the oscillatory nature of NF persists.

Although the gain reduction induced by pump power transfer can be mitigated by reducing pump spacing, it has little impact on the noise floor. The reason is that phonon population increases significantly when the two pumps are tuned closer to the signal. A detailed analysis shows that the noise floor remains nearly unchanged for all typical pump spacings from 20 to 50 nm. This can be seen in Fig. 4.3 where the pump spacing is reduced to around 30 nm. Clearly, same noise floor also remains for the two outer bands, with a small amount ($\sim 0.1-0.2$ dB) increased for that $> \omega_h$ but decreased for that $< \omega_l$. On the other hand, decreasing pump spacing also enhances FWM couplings and thus increases NF oscillations over the whole gain spectrum, although it helps to realize a multi-band operation [6].

The situation changes when the two pumps are far from each other. Figure 4.3 shows the case of 90-nm pump spacing. The FOPA gain is almost completely dominated by the single non-degenerate FWM process, $\omega_h + \omega_l \to \omega_1 + \omega_2$, leading to disappearance of NF oscillations over a 70-nm bandwidth. However, pump-power transfer is enhanced and the signal and idlers start to experiences Raman gain/loss

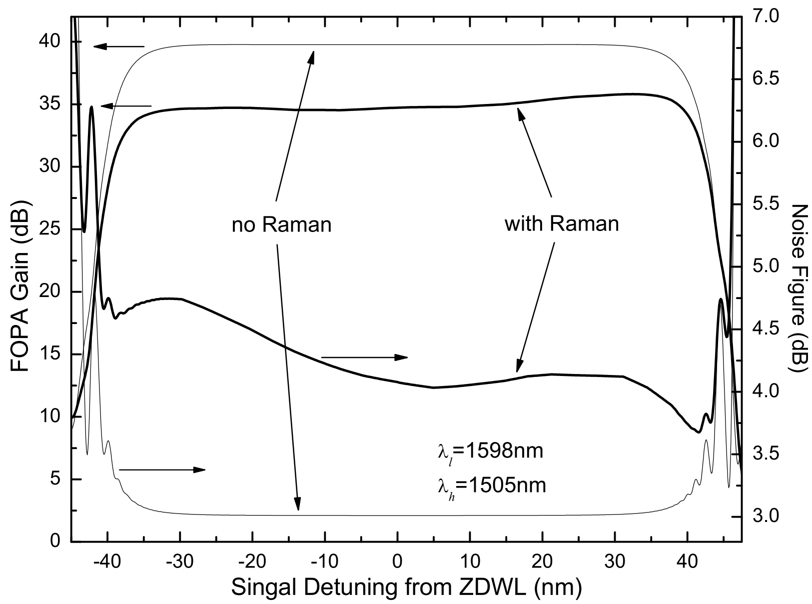


Figure 4.3: Same as Fig. 2 but with pump spacing increased to 90 nm. Input pump powers are optimized and are $P_l = 0.20$ W and $P_h = 0.80$ W. In the absence of Raman scattering, two pumps have equal powers of 0.5 W.

from the two pumps, resulting in a 5-dB gain reduction and a spectral tilt in the FOPA gain spectrum. Enhanced Raman scattering also leads to more noise. Consequently, the NF floor increases to above 4 dB, and becomes 4.75 dB when signal is tuned close to the high-frequency pump.

To conclude this section, We have found that the noise figure is limited to a minimum of 3.7 dB and may exceed 4.5 dB depending on the pump spacing. It exhibits oscillations stemming from the Bragg-scattering induced internal losses. Quite different from the single pump case [10] where the noise figure is strongly spectrally dependent, noise figure in copolarized dual-pump configuration has a nearly spectrally independent noise floor.

## 4.4 Orthogonal Pumping Configuration

### 4.4.1 Physical origin of polarization properties of FWM: Spin Conservation

In this section, we investigate the intrinsic polarization-dependent nature of FWM inside optical fibers. To do this, we focus only on the nondegenerate FWM process $\omega_l + \omega_h \rightarrow \omega_s + \omega_i$ ($\omega_s$ and $\omega_i$ can be the pair of $\omega_1$ and $\omega_2$, or that of $\omega_3$ and $\omega_4$) but neglect all other processes. Physically, the polarization-dependent nature of FWM stems from the requirement of spin conservation among the four interacting photons in an isotropic medium. This requirement can be described most simply in a basis in which $\uparrow$ and $\downarrow$ denote left and right circular polarization states and carry the intrinsic angular momentum (spin) of $+\hbar$ and $-\hbar$, respectively [23]. To describe FWM among arbitrarily polarized optical fields, we decompose each field in this circular-polarization basis as $|A_j\rangle = \mathscr{U}_j|\uparrow\rangle + \mathscr{D}_j|\downarrow\rangle$, where $\mathscr{U}_j$ and $\mathscr{D}_j$ represent the field amplitudes in the $\uparrow$ and $\downarrow$ states, respectively, for the $j$th wave ($j = l,h,s,i$). Using this expansion, we can find from Eq. (4.2) that the creation of idler photons in the two orthogonal spin states is governed by the following two equations (in the absence of XPM) [2]:

$$\frac{d\mathscr{U}_i}{dz} = i\beta_i\mathscr{U}_i + \frac{4i\gamma}{3}\left[\mathscr{U}_l\mathscr{U}_h\mathscr{U}_s^* + (\mathscr{U}_l\mathscr{D}_h + \mathscr{D}_l\mathscr{U}_h)\,\mathscr{D}_s^*\right], \tag{4.14}$$

$$\frac{d\mathscr{D}_i}{dz} = i\beta_i\mathscr{D}_i + \frac{4i\gamma}{3}\left[\mathscr{D}_l\mathscr{D}_h\mathscr{D}_s^* + (\mathscr{U}_l\mathscr{D}_h + \mathscr{D}_l\mathscr{U}_h)\,\mathscr{U}_s^*\right]. \tag{4.15}$$

The same equations hold for the signal if we exchange the subscript $s$ and $i$.

The three terms on the right side of Eqs. (4.14) and (4.15) show clearly the different spin combinations of the interacting photons and lead to the following selection rules for the FWM process. The first term $\mathscr{U}_1\mathscr{U}_2\mathscr{U}_s^*$ in Eq. (4.14) correspond to the path $\uparrow_1 + \uparrow_2 \rightarrow \uparrow_s + \uparrow_i$ while the first term $\mathscr{D}_1\mathscr{D}_2\mathscr{D}_s^*$ in Eq. (4.15) corresponds to the path $\downarrow_1 + \downarrow_2 \rightarrow \downarrow_s + \downarrow_i$, where a subscript denote photons at that specific frequency. Physically, if both pump photons are in the $\uparrow$ or $\downarrow$ state with a total angular momentum of $\pm 2\hbar$, the signal and idler photons must also be in the same state to conserve the total angular momentum.

The last two terms in Eq. (4.14) correspond to the paths $\uparrow_1 + \downarrow_2 \rightarrow \downarrow_s + \uparrow_i$ and $\downarrow_1 + \uparrow_2 \rightarrow \downarrow_s + \uparrow_i$. The only difference for the last two terms in Eq. (4.15) is that the same two combinations of pump photons produce signal-idler pair as $\uparrow_s + \downarrow_i$. The main point to note is that these four terms use orthogonally polarized pump photons with zero net angular momentum and thus must produce orthogonally polarized signal and idler photons in the basis used. A signal photon with state $\uparrow_s$ can only couple to an idler photon with state $\downarrow_i$, and vice versa. This leads to two possible combinations, $\uparrow_s + \downarrow_i$ and $\downarrow_s + \uparrow_i$, both of which are equally probable.

A pump with an arbitrary polarization is composed of photons in both the $\uparrow$ and $\downarrow$ states with different amplitudes and phases. FWM in this case includes both scenarios discussed above. Its polarization dependence is a consequence of the fact that different paths occur with different probabilities and couple with each other, and one must add probability amplitudes to sum over various paths (as is done in quantum mechanics). The coupling of different paths and the addition of amplitudes can lead to constructive or destructive interference. For example, if the two pumps are right-circularly polarized, no FWM can occur for a signal that is left-circularly polarized (and vice versa). The spin selection rules are summarized in the following table 4.4.1.

The same selection rules hold for degenerate FWM. It follows immediately that degenerate FWM is always polarization dependent because the two pump photons have the same SOP. More importantly, it

<table>
<tr><th>Waves</th><th colspan="6">Spin Combinations</th></tr>
<tr><td>$\omega_l$</td><td>$\uparrow$</td><td>$\downarrow$</td><td colspan="2">$\uparrow$</td><td colspan="2">$\downarrow$</td></tr>
<tr><td>$\omega_h$</td><td>$\uparrow$</td><td>$\downarrow$</td><td colspan="2">$\downarrow$</td><td colspan="2">$\uparrow$</td></tr>
<tr><td>$\omega_s$</td><td>$\uparrow$</td><td>$\downarrow$</td><td>$\uparrow$</td><td>$\downarrow$</td><td>$\uparrow$</td><td>$\downarrow$</td></tr>
<tr><td>$\omega_i$</td><td>$\uparrow$</td><td>$\downarrow$</td><td>$\downarrow$</td><td>$\uparrow$</td><td>$\downarrow$</td><td>$\uparrow$</td></tr>
</table>

Table 4.1: Spin Selection rules for Non-Degenerate FWM

is impossible to balance the FWM efficiency experienced by the $\uparrow$ and $\downarrow$ components of the signal unless a polarization diversity loop is used.

From an application point of view, one is interested in the FOPA configuration that would yield the same signal gain irrespective of the SOP of the input signal (polarization-independent gain). A detailed analysis of Eqs. (4.14) and (4.15) shows that this can be realized by two pumps with orthogonal polarizations, no matter what their individual SOPs are. Although an elliptically polarized pump consists of a mixture of $\uparrow$ and $\downarrow$ states, it turns out that, for two pumps with orthogonal elliptical polarizations, the two paths, $\uparrow_1 + \uparrow_2 \rightarrow \uparrow_s + \uparrow_i$ and $\downarrow_1 + \downarrow_2 \rightarrow \downarrow_s + \downarrow_i$, not only have a same efficiency but also have appropriate relative phases with the polarization-independent paths $(\uparrow_1 + \downarrow_2 \text{ or } \downarrow_1 + \uparrow_2) \rightarrow (\downarrow_s + \uparrow_i \text{ or } \uparrow_s + \downarrow_i)$. As a result, elliptically but orthogonally polarized pumps can provide a polarization-independent FWM. More specifically, if the two pumps are orthogonally and circularly polarized the terms containing $\mathscr{U}_1\mathscr{U}_2$ and $\mathscr{D}_1\mathscr{D}_2$, vanish, and the FWM process becomes polarization independent. If the two pumps are orthogonally but linearly polarized, it turns out that $\mathscr{U}_1\mathscr{D}_2 + \mathscr{D}_1\mathscr{U}_2 = 0$. The possible paths in this case, $(\uparrow_1 + \downarrow_2) \rightarrow (\downarrow_s + \uparrow_i \text{ or } \uparrow_s + \downarrow_i)$ and $(\downarrow_1 + \uparrow_2) \rightarrow (\downarrow_s + \uparrow_i \text{ or } \uparrow_s + \downarrow_i)$, are out of phase with each other and thus cancel. The remaining two paths, $\uparrow_1 + \uparrow_2 \rightarrow \uparrow_s + \uparrow_i$ and $\downarrow_1 + \downarrow_2 \rightarrow \downarrow_s + \downarrow_i$, have a same efficiency.

Based on discussion above, the relative FWM efficiencies for typical pumping schemes, such as those in the linear or circular polarizations, can be found by simply counting the possible paths in Table 4.4.1 together with the power fraction of pumps in the spin up and down states. The following table 4.4.1 illustrates the relative FWM efficiencies, normalized to the one of linear copolarized pumping configuration.

Table 4.4.1 shows that linear copolarized pumping exhibits the maximum FWM efficiency. However, it is strongly polarization dependent. FWM efficiency reduces to one third when the signal is orthogonally polarized to the pumps. However, both linear and circular orthogonal pumping are polarization independent, but the latter has twice FWM efficiency. All other elliptical orthogonal pumping will has a FWM efficiency between these two. In practice, pump powers remain high to obtain enough signal

| Pump 1 SOP | Pump 2 SOP | Fraction of pump ↑ & ↓ | Signal SOP | # of paths for individual signal ↑ or ↓ | Relative FWM Efficiency |
|---|---|---|---|---|---|
| \| | \| | 1/2 | \| | 3 | 1 |
| | | | −− | 1 | 1/3 |
| \| | −− | 1/2 | \| | 1 | 1/3 |
| | | | −− | 1 | 1/3 |
| ↑ | ↓ | 1 | ↑ | 1 | 2/3 |
| | | | ↓ | 1 | 2/3 |
| ↑ | ↑ | 1 | ↑ | 1 | 2/3 |
| | | | ↓ | 0 | 0 |

Table 4.2: Relative FWM efficiencies for typical pumping configuration. FWM efficiency provides the probability of creation photons at specific signal SOP. It is directly proportional to the product of the number of possible paths and the fraction of pump power. $--$ and $|$ denote linear polarization along $x$ and $y$ axis, respectively.

gain. In this case, two pumps introduce significant SPM and XPM, leading to considerable nonlinear polarization rotation (NPR). In this case, only the linear and circular polarizations are eigen-states of NPR and can maintain along the isotropic fiber. On the other hand, if fibers exhibit considerable birefringence, circular polarization becomes unstable. This is the reason why linear orthogonal pumping is most widely used for polarization independent operation of FOPAs, although it has relatively low efficiency. However, by use of specific technique (*i.e.*, by using twisted fibers) [24], circular polarization can be maintained along the fiber, which would significantly increase FWM efficiency. As the linear orthogonal pumping is most popular in practice, we focus on this configuration in the following sections and show that other effects also affect its polarization dependence.

### 4.4.2 Effect of Raman scattering

In this section, we consider the orthogonal pumping configuration. To simplify the analysis, we assume the fiber to be isotropic and neglect birefringence. When the two pumps are orthogonally and linearly polarized, it turns out that they maintain their SOPs along the fiber. We assume that the two pumps are polarized along the $x$ and $y$ axes, respectively, and that they remain nearly undepleted. Using $\mathbf{A}_l = A_l \hat{e}_x$ and $\mathbf{A}_h = A_h \hat{e}_y$, pumps are found to satisfy

$$\frac{dA_j}{dz} = ik_j A_j + i\gamma[P_j + (2+f_R)P_s/3]A_j. \tag{4.16}$$

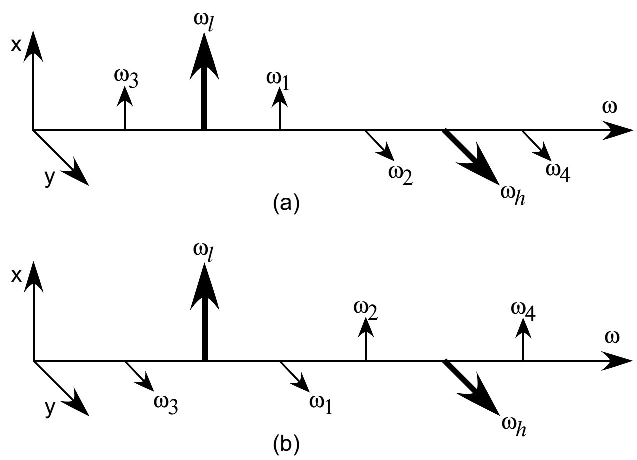


Figure 4.4: Illustration of two independent FWM processes for the pumping configuration in which two pumps at $\omega_l$ and $\omega_h$ are linearly polarized along the orthogonal $x$ and $y$ axes. A signal at $\omega_1$ produces three distinct idlers at $\omega_2$, $\omega_3$, and $\omega_4$.

Equation (4.16) can be easily solved analytically. We find that $P_j$ does not change with $z$ because the Kerr nonlinearity only leads to a nonlinear phase shift through self- and cross-phase modulation. Note that, for the orthogonal pumping configuration, power transfer between the two pumps is negligible as it can be realized only through anisotropic Raman response. We have neglect such effect in Eq. (4.16).

We next consider evolution of the signal along the fiber. A detailed analysis shows that various FWM processes can be decoupled into two sets of independent eigen-processes shown in Fig. 4.4, resulting in the following equation:

$$\begin{aligned} \frac{d\hat{A}_{1x}}{dz} &= ik_1\hat{A}_{1x} + i\gamma\Big\{\eta_{1l}(4)P_l\hat{A}_{1x} + \eta_{h2}(2)A_lA_h\hat{A}^{\dagger}_{2y} \\ &\quad + \eta_{l3}(3)A_l^2\hat{A}^{\dagger}_{3x} + \eta_{4h}(2)A_lA_h^*\hat{A}_{4y}\Big\} + i\hat{m}_{1l}A_l, \end{aligned} \tag{4.17}$$

$$\begin{aligned} \frac{d\hat{A}_{1y}}{dz} &= ik_1\hat{A}_{1y} + i\gamma\Big\{\eta_{1h}(4)P_h\hat{A}_{1y} + \eta_{l2}(2)A_lA_h\hat{A}^{\dagger}_{2x} \\ &\quad + \tfrac{f_E}{3}A_l^2\hat{A}^{\dagger}_{3y} + \tfrac{2f_E}{3}A_lA_h^*\hat{A}_{4x}\Big\} + i\hat{m}_{1h}A_h. \end{aligned} \tag{4.18}$$

To obtain Eqs. (4.17) and (4.18), a common phase factor has been removed from all waves with the transformation $\mathbf{A} \to \mathbf{A}\exp[-i(2+f_R)\gamma P_0 z/3]$. Similar equations for the three idlers can be obtained from Eqs. (4.17) and (4.18) by considering the symmetry among the four sidebands. For example, Equations for the idler at $\omega_3$ are obtained by exchanging subscripts 1 and 2 with 3 and 4, respectively; those for the idler at $\omega_2$ are obtained by exchanging subscripts $l$, 1, 3, $x$ with $h$, 2, 4, $y$, respectively; and those for the idler at $\omega_4$ are obtained by exchanging subscripts $l$, 1, 2, $x$ with $h$, 4, 3, $y$, respectively.

In this section, we consider first the polarization-dependent gain (PDG) in the orthogonal pumping

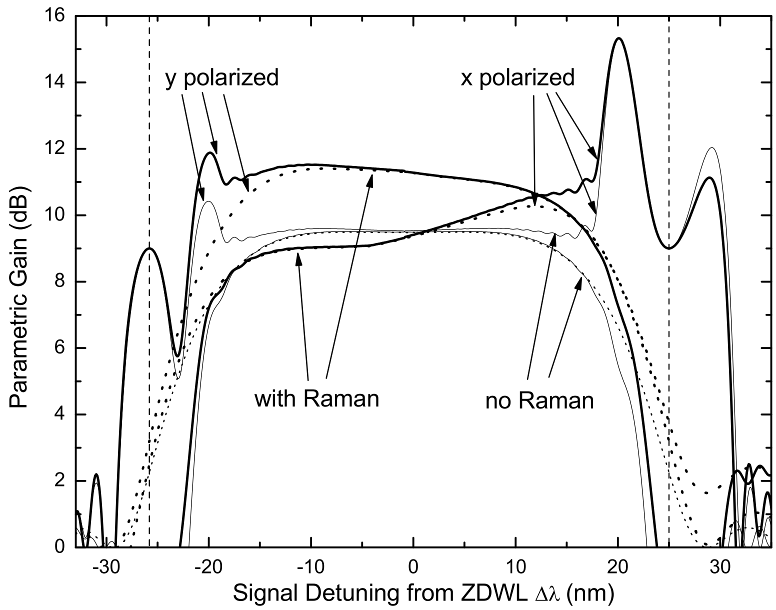


Figure 4.5: Parametric gain spectrum for $x$- and $y$-polarized signals as a function of signal detuning from the ZDWL of the fiber. The FOPA is pumped at $\lambda_l$ =1575.0 nm and $\lambda_h = 1524.2$ nm (vertical dashed lines) with equal powers of 0.5 W. Thick and thin curves show the cases with and without Raman scattering, respectively. Dotted curves show the analytic solution when only the single non-degenerate FWM process is considered.

configuration and ignore quantum noise (discussed in the next section). Therefore, the noise operators in Eq. (4.17) and (4.18) are neglected temporarily, and all the fields are treated classically. As the two pump powers are constant along the fiber, the resulting set of linear equations can be easily solved to obtain the parametric gain. Figure 4.5 shows examples of the gain spectra for $x$- and $y$-polarized signals using the same fiber as Fig. 4.2. The gain spectra without Raman response ($f_R = 0$) are also presented for comparison with thin solid lines.

When the Raman scattering is absent, the central portion of gain spectra is polarization-independent, as expected, since it arises mainly from the polarization-independent FWM process $\omega_l + \omega_h \rightarrow \omega_1 + \omega_2$. The residual polarization dependence near the spectral edges is due to the modulational instability (MI) induced by the two pumps ($2\omega_l \rightarrow \omega_1 + \omega_3$ and $2\omega_h \rightarrow \omega_2 + \omega_4$). For the same reason, MI peaks appear in the vicinity of the pumps. However, parametric gain spectra change in the presence of Raman scattering both qualitatively and quantitatively. The central part of the gain spectrum is no longer uniform even for a fixed signal SOP. When signal is $x$-polarized, FOPA gain increases with increasing signal wavelength, and the opposite occurs when signal is $y$-polarized. Moreover, the FOPA gain in the central part becomes significantly polarization dependent. Indeed, PDG can exceed 2 dB depending on the signal wavelength. Such a large PDG has its origin in the polarization dependence of Raman scattering and has consequences for practical applications of FOPAs.

The MI-induced polarization dependence can be mitigated by unbalancing the pump power such that it is smaller for the pump located in the anomalous-dispersion region of the fiber. This is so because MI gain is very sensitive to the pump power. For example, in the absence of Raman scattering, MI-induced PDG can be mitigated almost completely over 25-nm-wide central part of gain spectrum by changing equal 0.5-W pump powers to $P_l = 0.4$ W and $P_h = 0.6$ W. However, this power imbalance has little impact on the Raman-induced polarization dependence because of its intrinsic fundamental nature.

Although a complete description of FOPA based on Eqs. (4.17) and (4.18) is relatively complicated, the central portion of FOPA gain spectrum results mainly from the non-degenerate FWM process $\omega_l + \omega_h \to \omega_1 + \omega_2$. If only this process is considered, Eqs. (4.17) and (4.18) can be simplified by neglecting the terms containing $\mathbf{A}_3$ and $\mathbf{A}_4$. The resulting simplified equations, together with those for $\omega_2$, can be solved to provide the following analytical solution when only signal at $\omega_1$ is launched at the input:

$$P_{1x}(L) = P_{1x}(0)\rho_l(L)\left|\cosh(g_l L) + i\kappa_l \sinh(g_l L)/(2g_l)\right|^2, \tag{4.19}$$

$$P_{2x}(L) = \gamma^2|\eta_{1h}(2)|^2 P_l P_h P_{1y}(0)\rho_h(L)\left|\sinh(g_h L)\right|^2/|g_h|^2, \tag{4.20}$$

where $\kappa_j = k_1 + k_2 - k_l - k_h + \gamma\eta_{1j}(3)P_0$ $(j = l, h)$ is the total phase mismatch, $g_j^2 = [\gamma\eta_{1j}(2)]^2 P_l P_h - (\kappa_j/2)^2$, and $\rho_j(L) = \exp\{\gamma f_R L \Delta_j \mathrm{Im}[\widetilde{R}_a(\omega_1 - \omega_j)]\}$, where $\Delta_j = P_h - P_l$ when $j = l$ but $\Delta_j = P_l - P_h$ when $j = h$. The expressions for $P_{1y}$ and $P_{2y}$ can be obtained from Eqs. (4.19) and (4.20) by exchanging the subscript $l$ and $x$ with $h$ and $y$, respectively. The dotted curves in Fig. 4.5 shows the analytical results. As expected, they agree well with those obtained with the complete four-sideband model over the central portion of gain spectrum.

The physical origin of PDG observed in Fig. 4.5 can now be easily understood from Eq. (4.19) [where $P_{1x}$ and $P_{1y}$ depend only on $\widetilde{R}_a(\omega_1 - \omega_l)$ and $\widetilde{R}_a(\omega_1 - \omega_h)$, respectively]. Raman scattering affects parametric generation in two ways. First, although the Raman response has no impact on orthogonally polarized waves, it produces gain for the *copolarized* Stokes and loss for the *copolarized* anti-Stokes [determined by $\mathrm{Im}(\widetilde{R}_a)$]. In the case of Fig. 4.4(a), $\omega_1$ experiences Raman loss from the $\omega_l$ pump but $\omega_2$ experiences Raman gain from the $\omega_h$ one. The situation is reversed in the case of Fig. 4.4(b), where $\omega_1$ experiences Raman gain from the $\omega_h$ pump but $\omega_2$ suffers from Raman loss from the $\omega_l$ one. The gain/loss amount depends on the frequency separation between the pumps and signal. Although typical frequency separations in a FOPA are not close to the Raman gain peak, the broadband nature of the

Raman gain spectrum contributes considerable gain/loss to the signal and idlers in the central portion of parametric gain spectrum.

Second, a retarded Raman response changes fiber's refractive index [through $\mathrm{Re}(\widetilde{R}_a)$] by an amount that depends on frequency separation between the pumps, signal, and idler. For example, change is about 5% when signal is detuned from the pump by 30 nm. As the Raman response affects only the *copolarized* waves, variations in the refractive index are determined by the frequency separation $|\omega_1 - \omega_l|$ in the case of Fig. 4.4(a), but by $|\omega_h - \omega_1|$ in the case of Fig. 4.4(b). Asymmetry between these two processes produces different FWM efficiencies: It not only induces polarization dependence of parametric generation for a fixed signal frequency but also affects the spectral dependence of parametric gain for a fixed signal SOP. Note that this is quite different from the copolarized pumping configuration in which the signal and idler act simultaneously as the Stokes of one pump and anti-Stokes of the other, resulting in negligible impact on the refractive index.

Figure 4.6 shows PDG as a function of parametric gain obtained from Eq. (4.19), assuming perfect phase matching [$\mathrm{Re}(\kappa_j) = 0$, $j = l,h$], and using $\mathrm{PDG} \equiv G_y - G_x$, where $G_j = 10\log_{10}[P_{1j}(L)/P_{1j}(0)]$ ($j = x,y$) is the parametric gain for two signal SOPs. The PDG caused by pure Raman gain/loss, defined as $\mathrm{PDG_R} \equiv (10/\ln 10)L[g_R(\omega_h - \omega_1)P_h - g_R(\omega_l - \omega_1)P_l]$, is also shown by thin curves for comparison. When parametric gain is small, PDG increases with parametric gain and is close to $\mathrm{PDG_R}$. This is because Raman scattering dominates when FWM is negligible, and Eq. (4.19) reduces to $P_{3x}(L) \sim P_{3x}(0)\exp[LP_l g_R(\omega_l - \omega_1)]$. When parametric gain becomes significant, PDG changes almost linearly with it, but at a smaller rate compared with $\mathrm{PDG_R}$. When $\Delta\lambda = -10$ nm, PDG increases to only 3.7 dB even for a 30-dB gain, much smaller than 8-dB $\mathrm{PDG_R}$. Around the center of parametric gain spectrum ($\Delta\lambda = -1$ nm), PDG is almost constant at 2 dB. However, PDG remains small when $\Delta\lambda = 10$ nm and even vanishes or becomes negative for specific gain. The reason for this behavior is that, when FWM dominates, Eq. (4.19) is approximated by $P_{3x}(L) \sim P_{3x}(0)\exp\{\gamma L\sqrt{P_h P_l}\{4/3 + 2\mathrm{Re}[\widetilde{R}_a(\omega_l - \omega_1)]\}\}$. Raman scattering is suppressed by FWM [26] and PDG is dominated by refractive index changes induced by $\mathrm{Re}(\widetilde{R}_a)$, which are smaller than those induced directly by Raman gain/loss. In this case, FWM helps to mitigate the amount of PDG.

To conclude this section, we have shown that, in contrast to a prevailing belief, the orthogonal-pumping configuration is intrinsically polarization dependent, and thus does not provide polarization-independent parametric gain even for isotropic fibers. Retarded Raman response of optical fibers set a fundamental limit on its polarization dependence. For practical applications of FOPAs, additional techniques may be necessary to reduce such PDG.

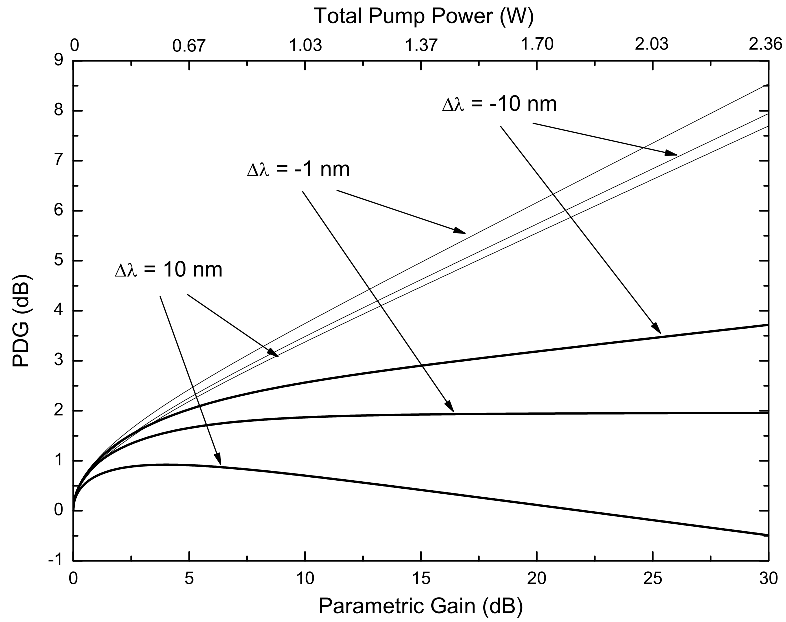


Figure 4.6: PDG as a function of parametric gain and total pump power at three signal wavelengths under a perfect phase-matching condition. Two pumps are assumed to have equal powers, $P_l = P_h$. Other conditions are identical to Fig. 2. The parametric gain on the horizontal axis is defined as the polarization-independent FOPA gain in the absence of Raman scattering. Thin curves shows for comparison the PDG induced by pure Raman gain/loss at the same signal wavelengths.

## 4.5 Quantum Noise in Orthogonal Pumping Configuration

In this section, we investigate the quantum noise properties of parametric amplifiers with orthogonal pumps. The technique used in Section 3 can be transferred directly to the orthogonal pumping case. As the FWM processes are decoupled into two independent processes, we define two column vectors as $\hat{\boldsymbol{F}}_x = [\hat{A}_{1x};\hat{A}^\dagger_{2y};\hat{A}^\dagger_{3x};\hat{A}_{4y}]$ and $\hat{\boldsymbol{F}}_y = [\hat{A}_{1y};\hat{A}^\dagger_{2x};\hat{A}^\dagger_{3y};\hat{A}_{4x}]$. Eq. (4.17) together with those for three other waves in a vector form as:

$$d\hat{\boldsymbol{F}}_j/dz = \boldsymbol{M}_j\hat{\boldsymbol{F}}_j + \hat{\boldsymbol{u}}_j, \quad (j = x, y) \tag{4.21}$$

where $\boldsymbol{M}_x$ and $\boldsymbol{M}_y$ are related to Eq. (4.17) and (4.18), respectively. the SRS noise operators are given by

$$\hat{\boldsymbol{u}}_x = i[A_l\hat{\eta}_{1l}; -A_h^*\hat{\eta}^\dagger_{2h}; -A_l^*\hat{\eta}^\dagger_{3l}; A_h\hat{\eta}_{4h}], \tag{4.22}$$

$$\hat{\boldsymbol{u}}_y = i[A_h\hat{\eta}_{1h}; -A_l^*\hat{\eta}^\dagger_{2l}; -A_h^*\hat{\eta}^\dagger_{3h}; A_l\hat{\eta}_{4l}]. \tag{4.23}$$

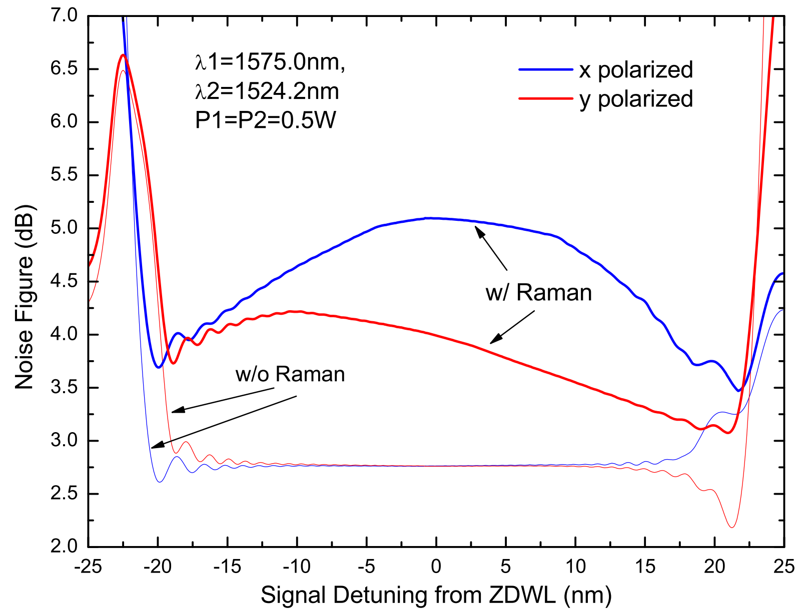


Figure 4.7: Parametric gain spectrum for $x$- and $y$-polarized signals as a function of signal detuning from the ZDWL of the fiber, under the same conditions as Fig. 4.5. Thick and thin curves show the cases with and without Raman scattering, respectively.

Clearly, Raman scattering only introduces noise to copolarized sidebands. Define the evolution matrixes for the two eigen-processes as:

$$\hat{\boldsymbol{F}}_x(L) = \boldsymbol{T}_x(L)\hat{\boldsymbol{F}}_x(0) + \hat{\boldsymbol{N}}_x, \tag{4.24}$$

$$\hat{\boldsymbol{F}}_y(L) = \boldsymbol{T}_y(L)\hat{\boldsymbol{F}}_y(0) + \hat{\boldsymbol{N}}_y, \tag{4.25}$$

where $\hat{\boldsymbol{N}}_x$ and $\hat{\boldsymbol{N}}_y$ are given by $\hat{\boldsymbol{N}}_x = \int_0^L \boldsymbol{T}_x(L-z)\hat{\boldsymbol{u}}_x(z)dz$ and $\hat{\boldsymbol{N}}_y = \int_0^L \boldsymbol{T}_y(L-z)\hat{\boldsymbol{u}}_y(z)dz$, respectively. As a result, Eqs. (4.7)-(4.12) can be used for the two eigen-processes provided that we replace the evolution matrix and the noise operator with these appropriate ones. For these two processes, Eq. (4.13) then becomes

$$\langle \hat{\boldsymbol{N}}_{xj}\hat{\boldsymbol{N}}_{xj}^\dagger + \hat{\boldsymbol{N}}_{xj}^\dagger\hat{\boldsymbol{N}}_{xj}\rangle = \Gamma_1 \int_0^L dz \big|\boldsymbol{T}_{xj1}A_l + \boldsymbol{T}_{xj4}A_h - \boldsymbol{T}_{xj2}A_h^* - \boldsymbol{T}_{xj3}A_l^*\big|^2, \tag{4.26}$$

$$\langle \hat{\boldsymbol{N}}_{yj}\hat{\boldsymbol{N}}_{yj}^\dagger + \hat{\boldsymbol{N}}_{yj}^\dagger\hat{\boldsymbol{N}}_{yj}\rangle = \Gamma_2 \int_0^L dz \big|\boldsymbol{T}_{yj1}A_h - \boldsymbol{T}_{yj2}A_l^*\big|^2 + \Gamma_3 \int_0^L dz \big|\boldsymbol{T}_{yj4}A_l - \boldsymbol{T}_{yj3}A_h^*\big|^2. \tag{4.27}$$

The three phonon modes creates noises in different FWM processes, as shown clearly in Fig. 4.4. The eigen-process (a) is only affected by the mode at $\Omega_1$, and (b) is affected by both $\Omega_2$ and $\Omega_3$. As $\Omega_2$ and $\Omega_3$ are in general different from $\Omega_1$, the ASRS would have different magnitudes in the two FWM processes, resulting in different noise figures.

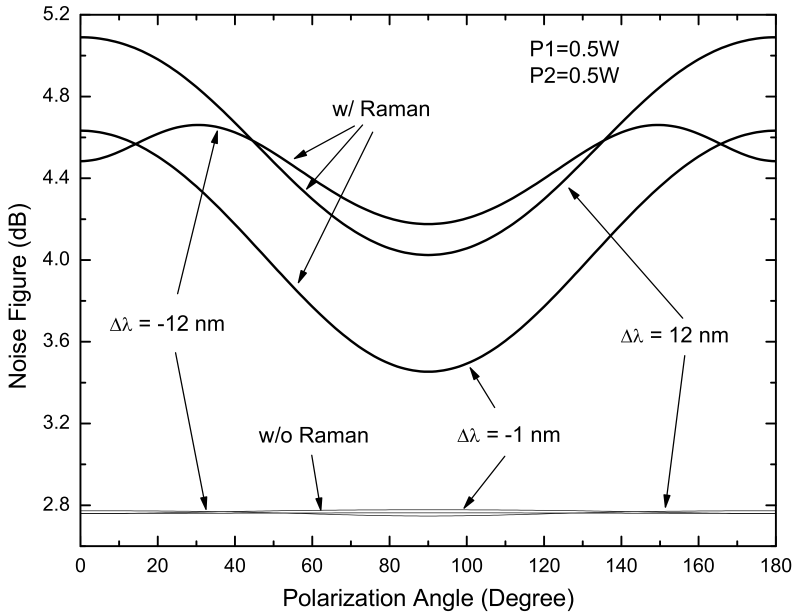


Figure 4.8: Parametric gain spectrum for *x*- and *y*-polarized signals as a function of signal detuning from the ZDWL of the fiber, under the same conditions as Fig. 4.5. Thick and thin curves show the cases with and without Raman scattering, respectively.

Figure 4.7 shows the noise figures for the two eigen-processes as shown in Fig. 4.4. In the absence of Raman scattering, noise figure is independent of signal polarization (thin curves) over a broad spectrum with a magnitude of about 2.8 dB, corresponding to the polarization-independent gain shown in Fig. 4.5. The magnitude of NF is smaller than 3 dB because of the relatively small parametric gain. The slight polarization dependence of noise figure at the edge of gain spectrum is due to the participation of polarization-dependent modulation instabilities. Raman scattering significantly enhances noise figure, by more than 1 dB in the central portion of the gain spectrum. Moreover, noise figure becomes considerably dependent on signal wavelength in both processes because of both frequency-dependent Raman gain coefficient and phonon population, as discussed above. For example, when the signal is *x*-polarized, noise figure peaks at the spectrum center where it can be as high as 5 dB. When the signal is *y*-polarized, noise figure decreases with increased signal wavelength.

Because of the asymmetry of Raman scattering between the two eigen-processes in Fig. 4.4, noise figure becomes strongly polarization dependent. This can be seen clearly in Fig. 4.8, which shows the noise figures as a function of signal polarization at three different signal wavelengths. In the absence of Raman scattering, NF is independent of signal polarization. However, Raman scattering introduces strong polarization dependence in NF, by about 1 dB. In general, NF is minimum when the signal is copolarized with the high-frequency pump, but is maximized when it is close to copolarization with the low-frequency pump. Figure 4.8 shows that, although Raman scattering only introduces a small amount of PDG to the parametric gain, as discussed in the previous section, it cause the amplified spontaneous emission to be very strongly polarization dependent.

To conclude this section, we have developed a theory to quantify the noise properties of orthogonally-pumped FOPAs. We show that, in contrast to a common belief, the amplified spontaneous emission becomes strongly dependent on both the signal wavelength and polarization.

## 4.6 Summary

In a summary, we have developed general theory to quantify the noise properties and polarization dependence of FOPAs in different pumping configurations. We show that the participation of Raman scattering in four-wave mixing process significantly changes the fundamental noise properties of FOPAs. In the copolarized pumping configuration, NF not only exhibits an oscillation feature because of the interference of multiple FWM processes, but also becomes considerably higher than the 3-dB fundamental limit because of the involvement of thermal phonons through Raman scattering. We show that, in contrast to a common belief, orthogonal pumping configuration is intrinsically polarization dependent because of the inevitable accompany of SRS to the FWM process. At the same time, the amplified spontaneous scattering in this configuration becomes dependent on both signal wavelength and polarization.

## References

[1] Q. Lin, F. Yaman, S. Radic, and G. P. Agrawal, Proc. CLEO, vol. 2, 980 (2005).

[2] Q. Lin and G. P. Agrawal, J. Opt. Soc. Am. B **21**, 1216 (2004).

[3] Q. Lin, F. Yaman, and G. P. Agrawal, IEEE Photon. Technol. Lett. **18**, 397 (2006).

[4] J. Hansryd, P. A. Andrekson, M. Westlund, J. Li, and P. O. Hedekvist, IEEE J. Sel. Top. Quan. Electron. **8**, 506 (2002).

[5] C. J. McKinstrie, S. Radic, and A. R. Chraplyvy, IEEE J. Sel. Top. Quantum Electron. **8**, 538 (2002).

[6] S. Radic and C. J. McKinstrie, Opt. Fiber Technol. **9**, 7 (2003).

[7] P. Kylemark, P. O. Hedekvist, H. Sunnerud, M. Karlsson, and P. A. Andrekson, J. Lightwave Technol. **22**, 409 (2004).

[8] C. J. McKinstrie, S. Radic, and M. G. Raymer, Opt. Exp. **12**, 5037 (2004).

[9] L. Boivin, F. X. Kartner, and H. A. Haus, Phys. Rev. Lett. **73**, 240 (1994).

[10] P. L. Voss and P. Kumar, Opt. Lett. **29**, 445 (2004).

[11] R. Jopson and R. E. Tench, IEE Electron. Lett. **29**, 2216 (1993).

[12] K. Inoue, J. Lightwave Technol. **12**, 1916 (1994).

[13] K. K. Y. Wong, M. E. Marhic, K. Uesaka, and L. G. Kazovsky, IEEE Photon. Technol. Lett. **14**, 911 (2002).

[14] T. Tanemura and K. Kikuchi, IEEE Photon. Technol. Lett. **15**, 1573 (2003).

[15] S. Radic, C. Mckinstrie, R. Jopson, C. Jorgensen, K. Brar, C. Headley, Proc. OFC, v. 2, 508 (2003).

[16] C. J. McKinstrie, S. Radic, and C. Xie, J. Opt. Soc. Am. B **20**, 1437 (2003).

[17] F. Yaman, Q. Lin, and G. P. Agrawal, IEEE Photon. Technol. Lett. **16**, 431 (2004).

[18] E. A. Golovchenko and A. N. Pilipetskii, J. Opt. Soc. Am. B **11**, 92 (1994).

[19] D. J. Dougherty, F. X. Karnter, H. A. Haus, and E. P. Ippen, Opt. Lett. **20**, 31 (1995).

[20] P. D. Drummond, in *Coherence and Quantum Optics VII*, J. H. Eberly, L. Mandel, and E. Wolf (Eds.) (Plenum Press, New York), 323 (1996).

[21] S. Namiki and Y. Emori, IEEE J. Sel. Top. Quan. Electron. **7**, 3 (2001).

[22] D. Mahgerefteh, D. L. Butler, J. Goldhar, B. Rosenberg, and G. L. Burdge, Opt. Lett. **21**, 2026 (1996).

[23] L. Mandel and E. Wolf, *Optical Coherence and Quantum Optics*, Chap. 10. (Cambridge University Press, New York, 1995).

[24] T. Tanemura, K. Katoh, and K. Kikuchi, Opt. Exp. **13**, 7497 (2005).

[25] R. H. Stolen, in *Raman Amplifiers for Telecommunications 1*, M. N. Islam Ed. (Springer, New York, 2003), Chap. 2.

[26] F. Vanholsbeeck, P. Emplit, and S. Coen, Opt. Lett. **28**, 1960 (2003).

# 5 Applications of Four-Wave Mixing

In this chapter, we turn to the experimental applications of four-wave mixing. We used dual-pump parametric amplification, discussed in Chap. 4, to realize all-optical signal processing at a bit rate of 40 Gb/s with high quality [1]. We demonstrated all-optical packet and bit-level switching at OC-768 data rates with multi-band operation. This work is done in collaboration with Prof. S. Radic's group at University of California, San Diego.

We also used degenerate FWM inside a short photonic-crystal fiber to realize a subpicosecond fiber-optic parametric oscillator with a wavelength tunability of about 200 nm around 1.0 $\mu$m, the first clear demonstration, to the best of our knowledge, of such a broadly tunable short-pulse fiber-optic parametric oscillator (FOPO) in this spectral region. This work is done in collaboration with Prof. W. H. Knox's group [2].

## 5.1 Optical Switching and Wavelength Multicasting

### 5.1.1 Introduction

Fast all-optical signal processing is essential for future optical networks. A variety of semiconductor and fiber platforms have been used to realize related optical functionalities [3, 4]. Compared with semiconductors, four-wave mixing (FWM) occurring inside optical fibers exhibits the advantage of an ultrafast response [3] and an intrinsic low-noise nature [5]. Indeed, degenerate FWM (single pump) has been used for applications such as wavelength conversion, pulse generation, and optical sampling [6].

Dual-pump FOPAs introduce additional degrees of freedom for practical applications because the wavelengths, powers, and state of polarizations (SOPs) of two pumps can be independently controlled. Such a two-pump parametric (TPP) architecture can provide uniform broadband amplification [7, 8], wavelength conversion [9], optical signal regeneration [12], and polarization-independent operation [10, 11]. Moreover, as discussed in the previous chapter, the coupling between non-degenerate and degenerate FWM processes simultaneously creates photons in four spectral bands [13], leading to significantly enhanced available spectral range and operational functionality since all four bands can be used in practice [14] and parametric generation can be emphasized in any of them [9].

Most previous work on signal processing has focused at bit rates of 10 Gb/s [14]. Future optical networks are likely to operate at 40 Gb/s or more. Attempts have been made to realize signal generation and phase conjugation at such high bit rates [15]-[17]. However, FWM-based all-optical routing and switching at such high bit rates was not demonstrated before our work reported here. We employed a TPP configuration to demonstrate high-quality, all-optical, multiple-band, packet and bit-level switching at a bit rate of 40 Gb/s, with a conversion efficiency of at least 21.2 dB and an extinction ratio exceeding 25 dB. Moreover, the feasibility of subrate pump control was realized for OC-768 signal processing.

### 5.1.2 Operating Principle

Multi-band response is the most important function provided by the TPP architecture. As shown in Fig. 5.1(a), within the parametric gain bandwidth, a signal band is replicated to three idler bands, irrespective of its relative spectral location. The multi-band operation requires the presence of both pumps, and is uniquely controlled by the pump spectral and power configuration. When the two pumps are nearly symmetrically located at opposite sides of the zero-dispersion wavelength (ZDWL) of a fiber, because of the instantaneous response of FWM process, switching of Pump 2 located in the anomalous-dispersion regime instantly excites three idler creation as well as signal amplification. As a result, by simply using

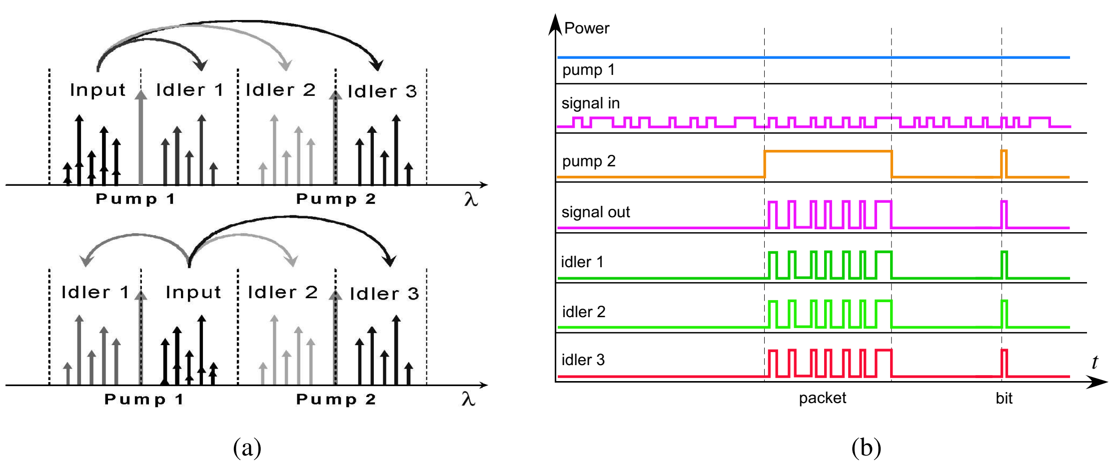


Figure 5.1: Illustration of wavelength multicasting in two-pump parametric devices.

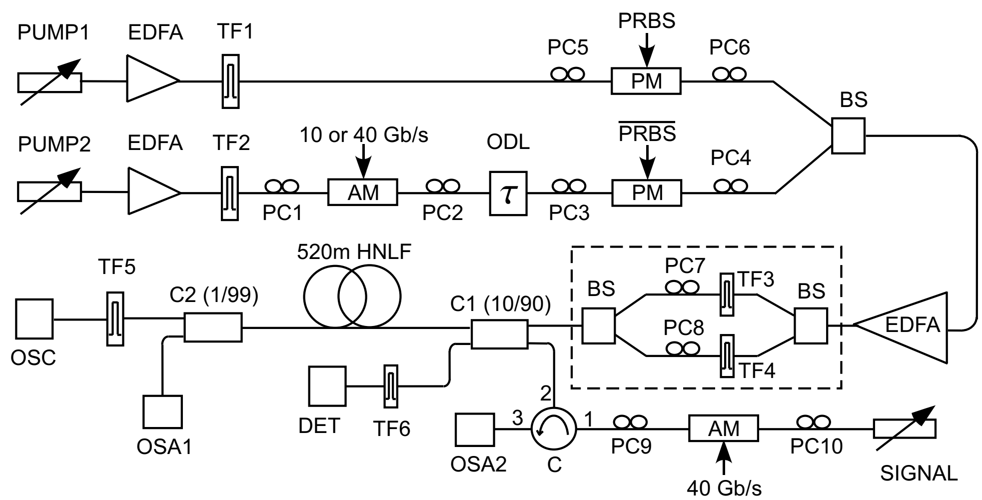


Figure 5.2: Experimental setup. TF: tunable filter. PM: phase modulator. AM: amplitude modulator. PC: polarization controller. ODL: optical delay line. EDFA: erbium-doped fiber amplifier. OSA: optical spectrum analyzer. OSC: oscilloscope. BS: band splitter. C1: 10/90 coupler. C2: 1/99 coupler. C: circulator. DET: detector; it can be either an OSA, an OSC, or a power meter used for characterizing the input signal, C- or L-band pump. OSA2 is used for monitoring Brillouin scattering of the pumps.

a specific temporal waveform for Pump 2, while maintaining Pump 1 at a constant level, it is possible to realize various fast switching functions, as shown clearly in Fig. 5.1(b). When the signal is located in the normal-dispersion regime, the same function can be realized by controlling the Pump 1.

Because of the instantaneous response of FWM, the switching speed is ultimately limited by the speed of pump control. In general, it needs to be comparable to input data rates. However, the exponential dependence of parametric gain on the pump powers significantly reduces the requirement of pump switching speed, enabling the use of subrate pump control. This is discussed in detail in what follows.

### 5.1.3 Experimental Setup

Our two-pump experimental setup is shown in Fig. 5.2. Two continuous-wave (CW) tunable lasers ($\lambda_1$ = 1568.5 nm and $\lambda_2$ = 1598.0 nm) served as the pump seeds, and were amplified and filtered by two 0.25-nm filters (TF1 and TF2) to reduce the amplified spontaneous emission (ASE) prior to the booster amplifier. The anomalous pump was controlled using a programmed nonreturn-to-zero (NRZ) bit sequence in both packet and bit-level switching experiments. A tunable optical delay line (ODL) was used to adjust the relative delay between the pump and the signal. The two pumps were counterphased using a 5-Gb/s pseudo-random bit sequence (PRBS) to suppress stimulated Brillioun scattering generated inside both the booster amplifier (EDFA) and the highly nonlinear fiber (HNLF). The EDFA booster provided an average output power of 2.3 W, measured prior to the ASE-filtering section (dashed box in Fig. 5.2). The booster ASE was filtered out using two 1-nm tunable filters (TF3 and TF4) in order to guarantee pump spectral purity [6] greater than 75 dB (measured within 0.2-nm bandwidth). A third tunable CW laser served as the signal. It was modulated using a 40-Gb/s NRZ pattern and was inserted into the HNLF through a 10/90 coupler. PC7, PC8, and PC9 were all adjusted to achieve a copolarized SOP for the pumps and the signal inside HNLF. The 520-m HNLF used in the experiments had an effective area of 11 $\mu$m$^2$, a dispersion slope of 0.025 ps/(nm$^2$km) and a ZDWL of 1582 nm. The four sidebands generated through modulational instability coupling were selected using a 2-nm-wide optical filter (TF5) and observed using a fast oscilloscope (37-GHz response).

### 5.1.4 Packet Switching

As a first goal of this study, we investigated the performance of arbitrary-bit-sequence (packet) extraction from the input OC-768 stream. Unlike the previously reported result [14], the switching of the OC-768 sequence required a precise control beyond that of the OC-192 rate. Indeed, while the length of the switched sequence ($\sim$ 1000 ps, see experiments below) allows for slow pump control, extraction with zero guardband does require speed comparable to the input data rate (OC-768) or even faster. However, parametric generation inside a HNLF helps to reduce significantly such requirement on the pumps because the output signal/idler powers are related to the pumps by an exponential gain function. For simplicity, if the parametric process is assumed to be dominated by a single phase-matched FWM process, the true switching rise/fall time is determined by the parametric response as $\exp\left[2\gamma L P_{\mathrm{eff}}(\tau)\right]/4$, where $P_{\mathrm{eff}}(\tau)$ represents the effective pump power, defined as $2\sqrt{P_1 P_2(\tau)}$ for the non-degenerate (two-pump) interaction and $P(\tau)$ for the degenerate (one-pump) interaction; $L$ is the HNLF length and $\gamma$ is the nonlinear parameter [3]. For a parametric gain of $20-30$ dB, this formula yields a parametric response $2-4$ times faster than the corresponding pump rise/fall time. In general, the single-pump configuration exhibits faster response [17]. However, dual-pumping provides more functional sidebands and thus enables wavelength multicasting. The parametric rise/fall time associated with 10-Gb/s pump control ($\sim$ 25 ps rise/fall time) was indistinguishable from that of the 40-Gb/s sequence in practice. This indicates that 10-Gb/s pump control could be effectively used to achieve the practical packet switching at OC-768 rates. Consequently, it allowed a control of the anomalous pump by a 10-Gb/s, rather than a 40-Gb/s programmed sequence.

To demonstrate OC-768 packet switching, the long-wavelength pump was modulated using a 1-ns-long rectangular pulse (composed of 10 successive logical ones at 10 Gb/s, corresponding to 40 bits at

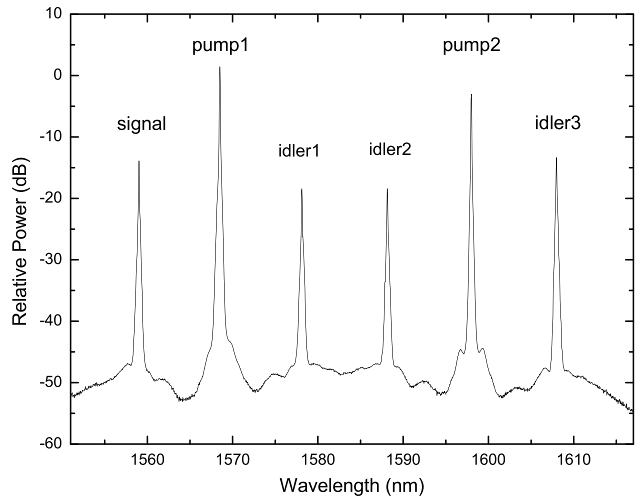


Figure 5.3: Optical spectrum measured at the output of HNLF, recorded with 0.2-nm resolution when a 1559-nm signal is launched. Other details are given in the text.

40 Gb/s) in order to extract a selected sequence from the data stream of the small input signal ($P_{in} = -14$ dBm). The average pump powers launched into the HNLF were 545 mW and 155 mW for the normal (C-band) and anomalous (L-band) pumps, respectively. The TPP spectrum is shown in Fig. 5.3, illustrating three new switched wavelengths at 1578.1, 1588.1 and 1608.0 nm. The input signal at 1559.0 nm is simultaneously amplified by 25.2 dB ("on/off" value, measured at the HNLF output) and multicasted with conversion efficiencies of 21.2 dB, 21.4 dB, and 25.9 dB, respectively, covering a spectral range of 49 nm. The corresponding 0.2-nm optical signal-to-noise ratios (OSNRs) were measured to be 33.6 dB (1559.0 nm), 28.5 dB (1578.1 nm), 28.9 dB (1588.1 nm), 34.8 dB (1608.0 nm). The absence of higher-order wave [12] in the vicinity of the switched sidebands confirms the linear TPP operation required for crosstalk-free waveband switching.

The temporal waveforms of the four sidebands and the L-band pump are shown in Fig. 5.4. The input signal had a mark density of 1/2 [Fig. 5.4 (a)], with the extinction ratio limited by the electronic driver used for the 40-GHz AM modulator. Figure 5.4 (b) shows the square waveform imposed on anomalous pump used for OC-768 sequence extraction. Switched packets were obtained from all four parametric bands. That at the signal wavelength (1559.0 nm) is shown in Fig. 5.4 (c), and the corresponding idler packets at 1578.1, 1588.1 and 1608.0 nm are shown in Figs. 5.4 (d)-(f), respectively. Switched packet traces were recorded by a simple tuning of the output (TF5) filter, since high power ($>$ 5 dBm) in any of the four streams eliminated the need for postamplification. The switching is realized with low noise and high extinction ratio: no artifacts were observed in the immediate vicinity outside the switched window [indicated by an arrow in Fig. 5.4 (c)], in spite of the dense bit content carried by the input signal in this

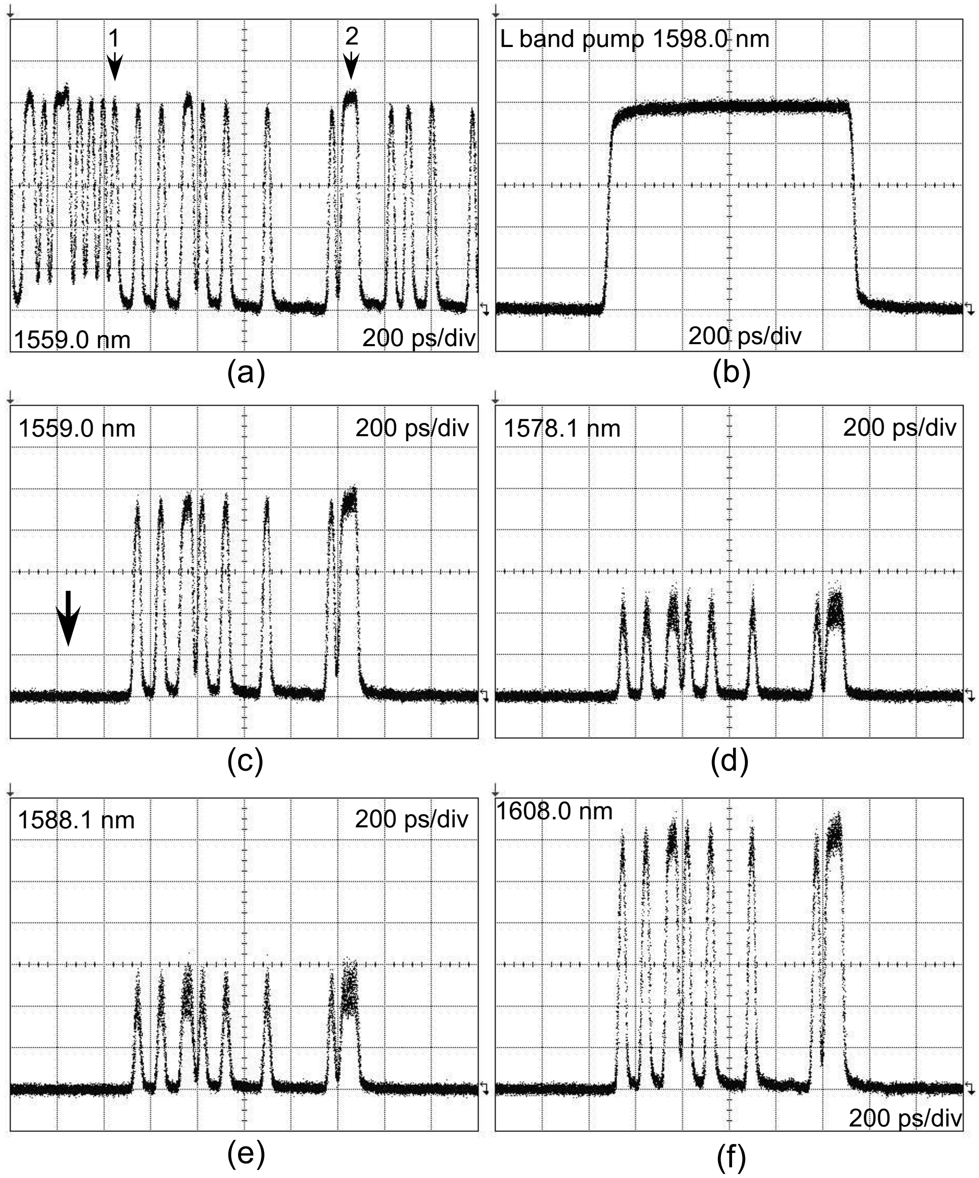


Figure 5.4: Temporal waveforms showing packet switching. A fixed input level was used in the oscilloscope for all signal/idlers waves. (a) Input 1559.0-nm signal; (b) L-band pump; (c) amplified signal; (d) switched 1578.1-nm idler; (e) switched 1588.1-nm idler; (f) switched 1608.0-nm idler.

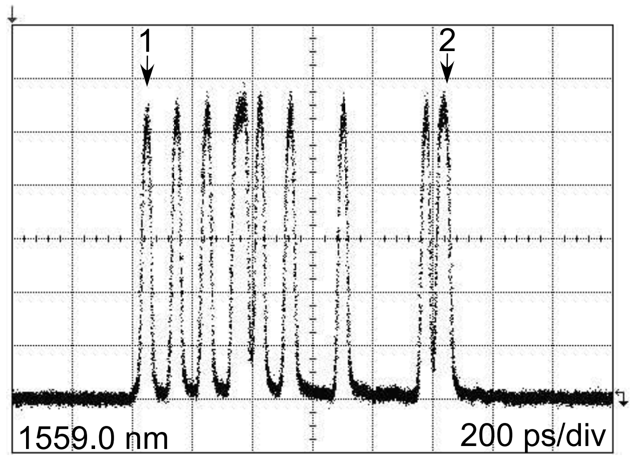


Figure 5.5: Amplified 1-ns packet of the 1559.0-nm signal when the L-band pump is temporally shifted in such a way that its leading edge coincides with the signal bit marked by arrow 1 in Fig. 5.4 (a).

region. The higher noise levels seen with inner-band packets (1578.1 and 1588.1 nm) are attributed to lower conversion efficiencies and the fixed input level used with the oscilloscope; no attempt was made to adjust the power levels to reduce the receiver noise.

Physically, a high extinction ratio stems from the exponential dependence of the parametric gain on the pump powers [13]. For example, in the phase-matched region of a HNLF with a length $L$ and a nonlinear parameter $\gamma$, the parametric gain (in dB) produced via non-degenerate FWM scales with pump powers as $\sqrt{P_1 P_2}$, where $P_1$ and $P_2$ are the normal and anomalous pump powers [3]. In contrast, neither is the signal amplified nor are the idlers created in the absence of L-band pump, since the C-band CW pump located in the normal-dispersion region produces negligible FWM. Clearly, high parametric gain guarantees switching with high extinction ratios in all four sidebands.

The TPP process allows for arbitrarily long packets to be switched simply by varying the time interval in which both pumps are simultaneously present. More importantly, the effective compression of rise/fall time allows the use of slow pump control to achieve precise bit control. Indeed, the pump rise/fall time of 25 ps in this experiment was sufficient to achieve zero-guardband packet switching. To demonstrate this capability, the anomalous pump switching window was shifted to cover the selected ”1” bit, as indicated by the arrow 1 in Fig. 5.4 (a). The switched packet is shown in Fig. 5.5: it can be seen clearly that the selected ”1” was switched in, with the preceding bits eliminated completely. At the same time, the last bit in the sequence, ”1” indicated by arrow 2, was steeply carved out from the successive logical ones. Clearly, the instantaneous parametric response of FWM dramatically reduces the requirement of the guard time for packet switching [18] and thus would help to increase the efficiency of optical processing schemes required in transparent networks.

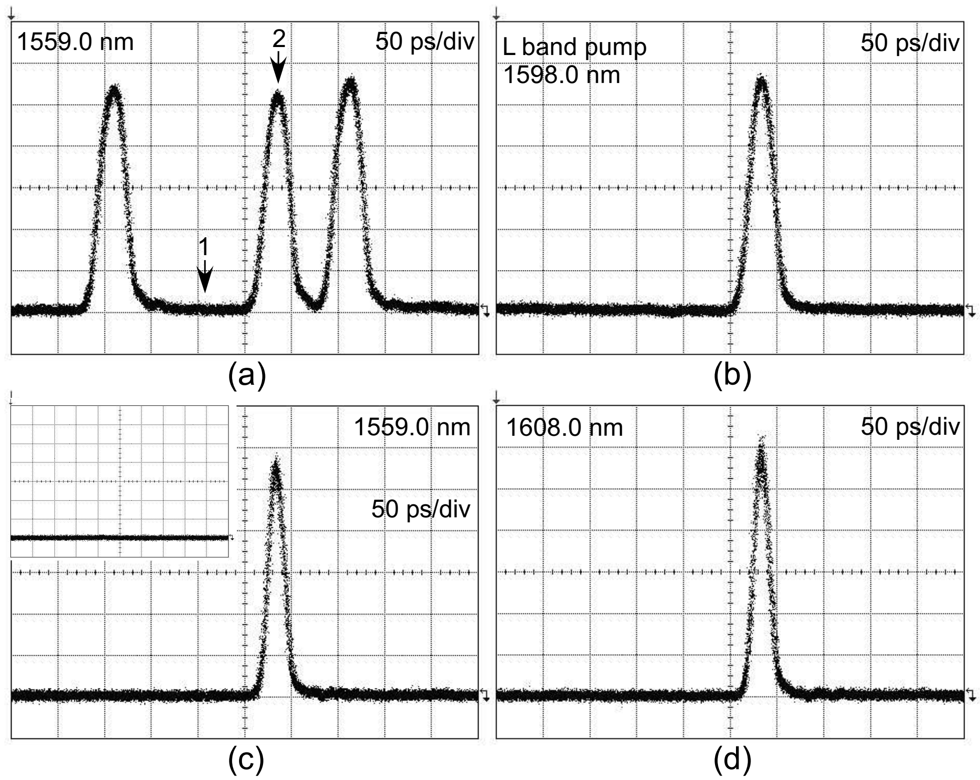


Figure 5.6: Temporal waveforms showing bit-level switching. (a) Input 1559.0-nm signal; (b) L-band pump; (c) amplified signal bit when the pump bit is located at position 2. The inset shows the signal waveform when the pump bit is located at position 1. (d) Switched bit for the outer-band idler at 1608.0 nm.

### 5.1.5 Bit-Level Switching

As a second goal of this study, we demonstrated optical switching at the bit level. The input signal was modulated with a 40-Gb/s NRZ bit pattern, as shown in Fig. 5.6 (a) (other bit patterns can also be used). The anomalous pump was controlled by an isolated bit, as illustrated in Fig. 5.6 (b). The pump was used to select the bits of a logical ”0” and a logical ”1” from the input sequence, as indicated by arrows in Fig. 5.6 (a). High extinction ratio is demonstrated by comparing the contrast between switched ”0” (inset in Fig. 5.6 (c)) and switched ”1” (Fig. 5.6 (c)). When the selected bit represents a high logical level, the signal is simultaneously amplified and replicated to three idler waves. Bit-level wavelength casting at 40 Gb/s is illustrated in Fig. 5.6 (d), corresponding to translation of the selected bit ”1” in the sequence to the outer parametric band (1559 nm → 1608 nm). Similar switched bits (with smaller amplitudes) were obtained for the two inner bands.

The switched bits had full widths at half maximum (FWHM) of 20 ps (1559.0 nm), 17 ps (1578.1

nm), 16 ps (1588.1 nm), and 20 ps (1608.0 nm), clearly indicating compression with respect to the original bits in the input sequence. The two inner bands had higher compression ratios, as expected by the different contributions of degenerate and non-degenerate FWM. Such pulse compression can be used to reshape the switched pulse and provide an efficient way for signal regeneration within the routing node itself.

### 5.1.6 Conclusion

In concluding this section, we demonstrated optical switching with wavelength conversion at 40 Gb/s by using a two-pump parametric architecture. Our scheme can realize packet switching for arbitrary packet lengths with negligible guard-time requirements and subrate pump controls. The experiment validated TPP performance that was sufficient to switch individual bits at 40 Gb/s, while maintaining high extinction ratios and conversion efficiencies above 20 dB. We note that the architecture also possesses an inherent ability to selectively conjugate a switched packets or bit sequences, thereby enabling the possibility for applications involving simultaneous high-speed switching and transmission-impairment mitigation.

## 5.2 Highly Tunable Fiber-Optic Parametric Oscillators

### 5.2.1 Introduction

Short-pulse optical parametric oscillators exhibit great potential for many applications ranging from physics, chemistry, to biology [19]. Conventionally, the $\chi^{(2)}$ nonlinearity inside a crystal is used for parametric oscillation [20]. However, this approach requires a complicated cavity alignment for regenerative oscillation and phase matching. Recently, fiber-optic parametric oscillators (FOPOs), based on FWM occurring inside optical fibers, have attracted considerable attention [21]-[24]. It was shown that picosecond and subpicosecond pulses can be obtained from FOPOs made of a conventional single-mode or dispersion-shifted fiber [21, 22]. However, a low fiber nonlinearity requires long fiber lengths, leading inevitably to a significant pulse pedestal [21]. Moreover, because of the phase matching required for efficient FWM, operating wavelengths of these FOPOs are confined to the vicinity of ZDWL of conventional fibers ($\geq 1.3\ \mu$m) [21, 22].

Newly developed photonic crystal fibers (PCF), however, exhibit significant flexibility in engineering fiber dispersion [25]. ZDWLs ranging for visible to far infrared can be simply obtained by manipulating the fiber structure. On the other hand, strong mode confinement inside such fibers provides an enhanced nonlinearity, leading to a significantly improved FWM efficiency [26]. By using PCFs, FOPOs were shown to be able to operate near 800 nm [23]. However, all previous FOPOs are based on the conventional modulation instability (MI) pumped in the anomalous dispersion regime. Although a tunability of tens of nanometers can be obtained [22, 23], it is well known that this kind of MI is generally confined to a narrow spectral region, resulting in a limited tunable bandwidth [3]. In this section, we show that, by the use of a new kind of MI pumped in the normal dispersion regime, clean subpicosecond pulses can be obtained over a 200-nm-wide spectral region around 1.1 $\mu$m from a FOPO made of a PCF with proper dispersion and with an optimal cavity design.

### 5.2.2 Operating Principle

As discussed in previous chapters, the parametric gain coefficient of degenerate FWM is given by $g^2 = (\gamma P_0)^2 - (\kappa/2)^2$, where $\kappa$ is phase mismatch given by $\kappa = 2\gamma P_0 + 2\sum_{m=1} \frac{1}{(2m)!}\beta_{2m}\Omega_{sp}^{2m}$, $P_0$ is the pump power, $\Omega_{sp} = |\omega_s - \omega_p|$ is the frequency detuning between the pump and the signal (Stokes), and $\beta_{2m}$ is the $(2m)^{th}$-order dispersion at the pump frequency. If we balance the phase mismatch contribution from different-order dispersions, it is possible to create phase-matched MI sidebands very far from the pump wavelength. It turns out that this can be done by pumping the PCF in the normal dispersion regime [28]. Figure 5.7 (a) shows numerical examples of parametric gain spectra pumped in both the

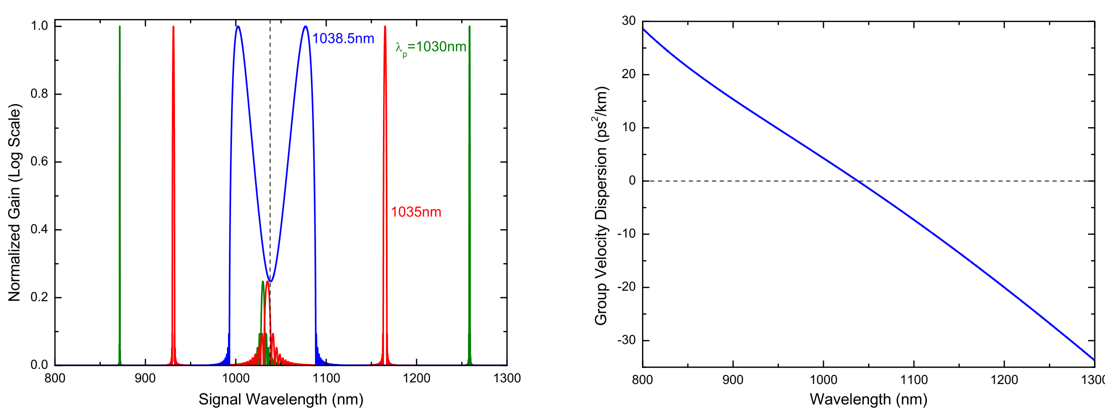


(a) (b)

Figure 5.7: (a) Numerical examples of parametric gain spectra pumped in both normal and anomalous dispersion regimes of a PCF with a dispersion profile shown in (b). The dispersion coefficients at the ZDWL (1038 nm) are : $\beta_3 = 0.06541$ ps$^3$/km, $\beta_4 = -1.0382 \times 10^{-4}$ ps$^4$/km, $\beta_5 = 3.3756 \times 10^{-7}$ ps$^5$/km, $\beta_6 = -1.1407 \times 10^{-10}$ ps$^6$/km. The PCF has a mode field diameter of 3.2 $\mu$m, corresponding to a nonlinear coefficient $\gamma$ estimated to be 22.7 W$^{-1}$/km.

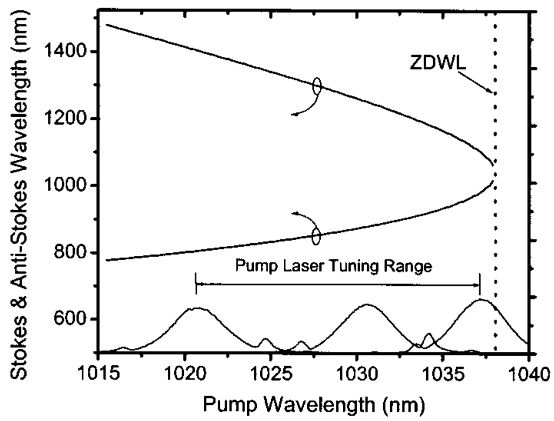


Figure 5.8: Phase matching curve for the PCF shown in Fig. 5.7(b).

normal and anomalous dispersion regimes of a PCF whose dispersion is shown in Fig. 5.7 (b). It can be seen clearly that, by pumping in the normal-dispersion regime just a few nanometers away from the ZDWL, it is possible to generate sideband more than 100 nm away from the pump. Moreover, a slight tuning of the pump wavelength results in a dramatic change in the wavelength of created sideband. The complete curve of phase-matched wavelengths is shown in Fig. 5.8. Clearly, when pumping in the normal dispersion regime, outputs between 800 nm to 1400 nm can, in principle, be covered with only 20-nm pump tuning, indicating the significant advantage of this new kind of MI for wavelength tunability. Since MI can be dramatically extended to visible and far infrared regimes, it is possible to provide parametric generation in the spectral region that can not be reached by other techniques.

Note that the large wavelength separation between the pump and Stokes/anti-Stokes waves would lead to considerable walk-off. Therefore, a short piece of PCF (65cm in the following experiment) is required to be used as the gain medium in order to minimize the round-trip walk-off delay between the pump pulse and the signal pulse, thus enabling generation of short pulses. Such walk-off limits the ultimate tuning range of the constructed FOPO, as discussed in detail in the following.

### 5.2.3 Experimental Setup

The experiments were performed in collaboration with Prof. Knox's group [2]. The experimental setup is shown in Fig. 5.9. The ring oscillator cavity consists of 65-cm of PCF [SC-5.0-1040, Blaze Photonics Inc., GVD is shown in Fig. 5.7(b)]. The loss of 65-cm fiber in the wavelength range of 970 to 1230 nm is estimated to be less than 0.0016 dB, which is negligible compared with 2 dB coupling loss at the input end of the fiber. The FOPO is pumped through a long-pass dichroic filter, which has a cutoff wavelength

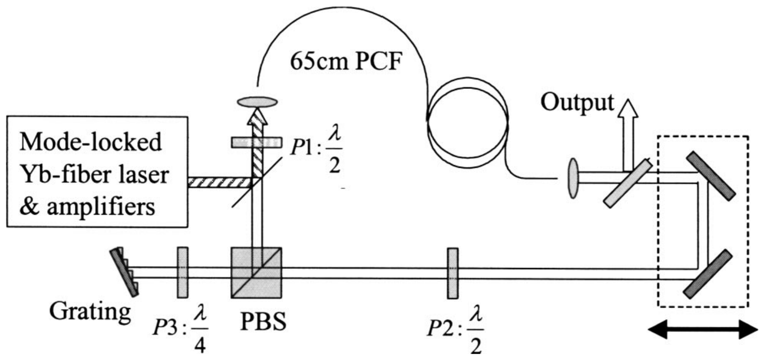


Figure 5.9: Experimental setup for FOPO. PBS: polarization beam splitter; P1, P2, P3: achromatic wave plates.

at 1040 nm. The pump light is launched in a linear polarization. The first achromatic half-waveplate P1 is adjusted so that the pump SOP coincides with a principle axis of the birefringent PCF. The extinction ratio of $> 1 : 1000$ between orthogonal linear polarizations is maintained for the pump wave after it passes the PCF, indicating a good preservation of polarization. The polarization beam splitter (PBS) cube combined with a diffraction grating (300-line/mm) in the Littrow configuration is used as a tunable band-pass filter with 2 nm bandwidth [23]. It also ensures the signal wave to copolarize with the pump for maximum parametric generation. The output coupler is a broadband-coated parallel window (BK7) with 15% output coupling. All mirrors in the cavity are ER.2-protected silver-coated mirrors (Newport Inc.). A newly developed passively mode-locked Yb-doped fiber laser [29] with two stages of fiber amplifiers is used as a pumping source. It is operated in soliton mode-locked region, producing sub-picosecond pulses at 36.6 MHz with 5 nm bandwidth (FWHM). The center wavelength of pulses can be tuned from 1020 to 1038 nm. The bandwidth of pump pulses is filtered down to 1.5nm (FWHM) with a tunable filter before being sent to two fiber amplifiers. After the amplifiers, the pulse-width is measured to be 1.3 ps with up to 260 mW of average power. The total cavity length of the FOPO is precisely adjusted to match the length of the pumping laser cavity for synchronously pumping.

### 5.2.4 Results and Discussion

Figure 5.10 shows the tuning range of signal and idler. By turning the intracavity grating and re-matching the cavity length, the signal wavelength can be tuned over 140 nm on the longer wavelength side (1060 nm to 1200 nm), while the idler covers 60 nm in shorter wavelength side (930 nm to 990 nm). The total tuning range is over 200 nm. This is a significantly broader tuning range than a tunable mode-locked Yb-doped fiber laser. Further tuning is limited by walk-off between the pump and signal. When the signal wavelength passes 1200 nm, the walk-off delay becomes $> 1.4$ ps, which is comparable with the

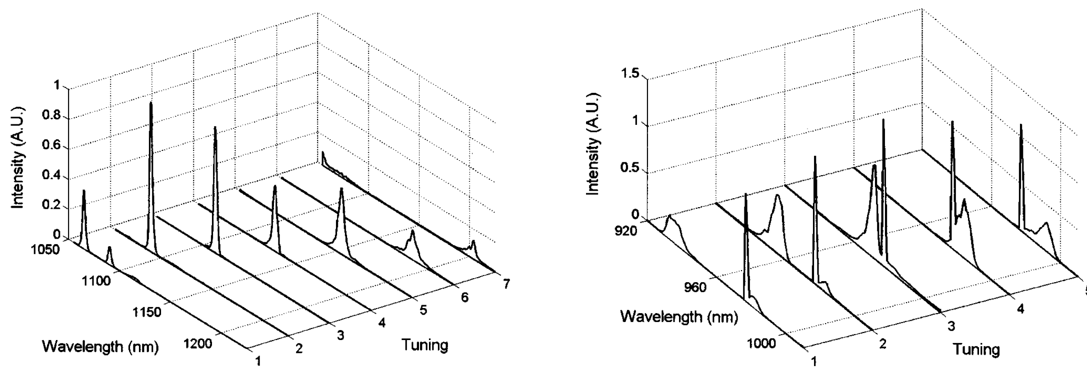


(a) (b)

Figure 5.10: Tuning range of signal (a) and idler (b). The small peak at $\sim$ 1090 nm in the first trace of (a) is a cascade FWM component. The spectral component near 977 nm is the residual diode pump light (used for the Yb-doped fiber amplifier) leaking into the FOPO.

pump pulse width. This deceases the interaction length between the pump and signal, thus limits the gain beyond 1200 nm. It is worth noting that, when pumping close to ZDWL, the walk-off delay is largely contributed from the slope of the GVD curve; while the phase-matching condition depends only on the even-order dispersions, as shown in the expression of $\kappa$. This decoupling between the walk-off and the phase matching condition may allow one to design a specific PCF that offers ultra-broad tunability for short pulse parametric amplification.

Typical characteristics of the Stokes component are shown in Fig. 5.11. The saturation of the output power is likely due to the spectral broadening of the pump pulse when its power increases, as the pump depletion is much stronger in some part of its spectrum. The autocorrelation trace [Fig. 5.11(b)] shows that the signal pulse has a FWHM width of 460 fs, assuming a sech$^2$ pulse shape. It is narrower than the 1.3-ps pump pulse [wider trace in Fig. 5.11(b)] because of the gain narrowing effect. The spectrum of the signal pulse has a FWHM bandwidth of $\sim$ 4 nm. The time-bandwidth product of the pulse is about 0.44. The chirp of the pulse is likely induced by the cross-phase modulation (XPM) from the pump pulse, as indicated by the asymmetry in the pulse spectrum.

### 5.2.5 Conclusion

In concluding this section, we have demonstrated the first (to the best of our knowledge), subpicosecond FOPO using the MI gain in the normal-dispersion regime of a PCF. With this novel scheme, a tuning range as wide as 200 nm around 1 $\mu$m is achieved and pulses as short as 460 fs are generated through synchronously pumping by a tunable passively mode-locked Yb-fiber laser. This scheme has the potential

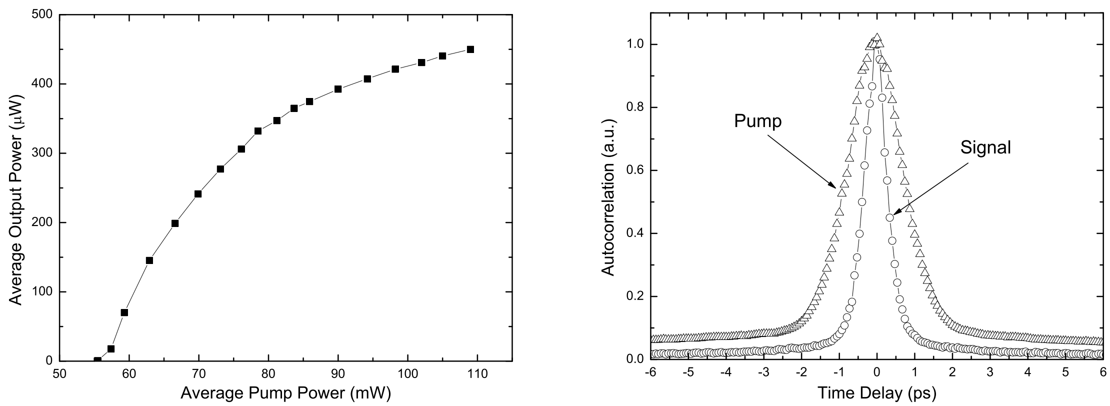


(a) (b)

Figure 5.11: (a) Output power of the Stokes component near 1110 nm as the function of average pump power. (b) Typical autocorrelation traces of the pump pulse and the output signal pulse. The wider trace shows the autocorrelation trace for the 1.3-ps-wide pump pulse.

of becoming a practical, fiber-based, broadly tunable, subpicosecond pulse source around 1 $\mu$m.

# References


[1] Q. Lin, R. Jiang, C. F. Marki, C. J. McKinstrie, R. Jopson, J. Ford, G. P. Agrawal, and S. Radic, IEEE Photon. Technol. Lett. **17**, 2376 (2005).

[2] Y. Deng, Q. Lin, F. Lu, G. P. Agrawal, and W. H. Knox, Opt. Lett. **30**, 1234 (2005).

[3] G. P. Agrawal, Nonlinear Fiber Optics, 3rd ed. (Academic Press, San Diego, 2001).

[4] J. Leuthold, B. Mikkelsen, R. E. Behringer, G. Raybon, C. H. Joyner, and P. A. Besse, IEEE Photon. Technol. Lett. **13**, 860 (2001).

[5] Y. Yamamoto and T. Mukai, Opt. Quan. Electron. **21**, S1 (1989).

[6] J. Hansryd, P. A. Andrekson, M. Westlund, J. Li, and P. O. Hedekvist, IEEE J. Sel. Top. Quant. Electron. **8**, 506 (2002).

[7] S. Radic, C. J. McKinstrie, R. M. Jopson, J. C. Centanni, Q. Lin, and G. P. Agrawal, Electron. Lett. **39**, 838 (2003).

[8] S. Radic and C. J. McKinstrie, Opt. Fiber Technol. **9**, 7 (2003).

[9] T. Tanemura, C. S. Goh, K. Kikuchi, and S. Y. Set, IEEE Photon. Technol. Lett. **16**, 551 (2004).

[10] K. K. Y. wong, M. E. Marhic, K. Uesaka, and L. G. Kazovsky, IEEE Photon. Technol. Lett. **14**, 911 (2002).

[11] K. Uesaka, K. K. Y. Wong, M. E. Marhic, and L. G. Kazovsky, IEEE J. Sel. Top. Quantum Electron. **8**, 560 (2002).

[12] S. Radic, C. J. McKinstrie, R. M. Jopson, J. C. Centanni, and A. R. Chraplyvy, IEEE Photon. Technol. Lett. **15**, 957 (2003).

[13] C. J. McKinstrie, S. Radic, and A. R. Chraplyvy, IEEE J. Sel. Top. Quantum Electron. **8**, 538 (2002).

[14] S. Radic, C. J. McKinstrie, R. M. Jopson, A. H. Gnauck, J. C. Centanni, and A. R. Chraplyvy, IEEE Photon. Technol. Lett. **16**, 852 (2004).

[15] S. Watanabe, S. Takeda, G. Ishikawa, H. Ooi, J. G. Nielsen, and C. Sonne, Proc. European Conf. Opt. Commun. (ECOC), Vol. 5, p.1 (1997).

[16] T. Torounidis, H. Sunnerud, P. O. Hedekvist, and P. A. Andrekson, IEEE Photon. Technol. Lett. **15**, 1159 (2003).

[17] T. Torounidis, M. Westlund, H. Sunnerud, B. E. Olsson, and P. A. Andrekson, IEEE Photon. Technol. Lett. **17**, 312 (2005).

[18] K. Onohara, Y. Awaji, N. Wada, F. Kubota, and K. Kitayama, IEEE Photon. Technol. Lett. **17**, 627 (2005).

[19] M. H. Dunn and M. Ebrahimzadeh, Science, **286**, 1513 (1999).

[20] G. Cerullo and S. De Silvestri, Rev. Scient. Instr. **74**, 1 (2003).

[21] K. Suzuki, M. Nakazawa and H. A. Haus, Opt. Lett. **14**, 320 (1989).

[22] D. K. Serkland and P. Kumar, Opt. Lett. **24**, 92 (1999).

[23] J. E. Sharping, M. Fiorentino, P. Kumar and R. S. Windeler, Opt. Lett. **27**, 1675 (2002).

[24] C. J. S. de Matos, J. R. Taylor and K. P. Hansen, Opt. Lett. **29**, 983 (2004).

[25] W. H. Reeves, D. V. Skryabin, F. Biancalana, J. C. Knight, P. St. J. Russell, F. Omenetto, A. Efimov, and A. J. Taylor, Nature **424**, 511, (2003).

[26] J. E. Sharping, M. Fiorentino, A. Coker, P. Kumar and R. S. Windeler, Opt. Lett. **26**, 1048 (2001).

[27] W. J. Wadsworth, N. Joly, J. C. Knight, T. A. Birks, F. Biancalana, and P. St. J. Russell, Opt. Express **12**, 299 (2004).

[28] J. D. Harvey, R. Leonhardt, S. Coen, G. K. L. Wong, J. C. Knight, W. J. Wadsworth, and P. St. J. Russell, Opt. Lett. **28**, 2225 (2003).

[29] Y. Deng and W. H. Knox, Opt. Lett. **29**, 2121 (2004).

# 6 Vector Soliton Fission and Supercontinuum Generation

In this chapter, we look into the propagation regime in which a femtosecond pulse propagates inside a photonic-crystal or tapered fiber. In this case, all the nonlinear processes, like SPM, XPM, SRS, FWM, would participate in the pulse evolution and the pulse dynamics exhibits peculiar features. We investigate the vectorial nature of soliton fission in an isotropic nonlinear medium both theoretically and experimentally. As a specific example, we show that supercontinuum generation in a tapered fiber is extremely sensitive to the input state of polarization. Multiple vector solitons generated through soliton fission exhibit different states of elliptical polarization, while emitting nonsolitonic radiation with complicated polarization features. Experiments performed with a tapered fiber agree with our theoretical description. This work is done in collaboration with Prof. W. H. Knox's group [1].

## 6.1 Introduction

Solitons represent a fascinating manifestation of the nonlinear phenomena in nature and occur in many branches of physics [2]-[4]. In the context of optics, solitons forming inside optical fibers have attracted the most attention [5]. It was discovered during the 1980s that higher-order optical solitons undergo *fission* when input pulses exciting them were relatively short [6]. This fission process has become relevant in recent years with the advent of new types of fibers, such as photonic-crystal fibers (PCF) and tapered fibers, because of their unique nonlinear and dispersive properties [7]. Femtosecond optical pulses propagating inside such fibers can generate *supercontinuum* (SC), spanning a broad spectral region from violet to infrared, even when the spectrum of input pulses is only a few nanometer wide [8, 9]. The underlying physical mechanism behind SC generation in the anomalous-dispersion regime is believed to be associated with the fission of higher-order solitons [10].

Although SC generated inside birefringent PCF exhibits polarization-dependent features [11]-[13], soliton-fission process in nearly isotropic fibers has so far been modelled using a scalar nonlinear Schrödinger (NLS) equation [10]. Nonlinear effects in optical fibers are known to be highly polarization-dependent [6]. For this reason, we expect the soliton-fission process to be sensitive to pulse polarization even in an *isotropic* fiber. Indeed, the polarization issues were first studied in 1974 in the context of collisions of two vector solitons [14]. In this chapter, we study, both theoretically and experimentally, SC generation inside isotropic tapered fibers and show that the vectorial nature of soliton fission is important and affects the SC even in the absence of fiber birefringence. Our results show that the fission of a higher-order soliton generates multiple vector solitons that are polarized elliptically along well-defined directions on the Poincaré sphere.

## 6.2 Numerical Simulations

Our numerically simulations are performed using parameter values appropriate for the tapered fiber used in the experiment. $n_2 \approx 3\times10^{-20}$ m$^2$/W is used for silica fibers and the effective core area $a_{\text{eff}}$ is $\sim$3 $\mu$m$^2$ at 920 nm. We estimate $\beta_2 = -24.18$ ps$^2$/km and $\gamma = 44.8$ W$^{-1}$/km; other dispersion parameters were calculated using a known technique [9]. The group-velocity dispersion (GVD) curve for the tapered fiber is shown in Fig. 6.1. GVD is anomalous in the spectral region above the zero-dispersion wavelength of 802.6 nm. An intense pulse launched in this spectral region will split into multiple solitons which simultaneously emit dispersive waves because of high-order fiber dispersion, leading to dramatic temporal and spectral variations of the whole pulse [10].

The propagation of ultrashort pulses inside an isotropic optical fiber is governed by Eq. (2.26) without the birefringence and PMD term. The third-order nonlinear polarization takes the form of Eq. (2.27),

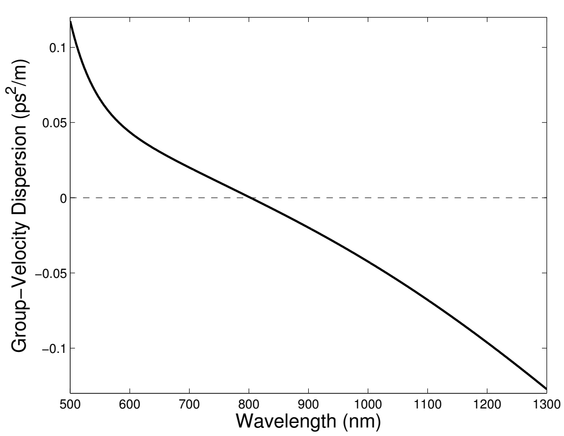


Figure 6.1: Group-velocity curve for the tapered fiber used for simulation.

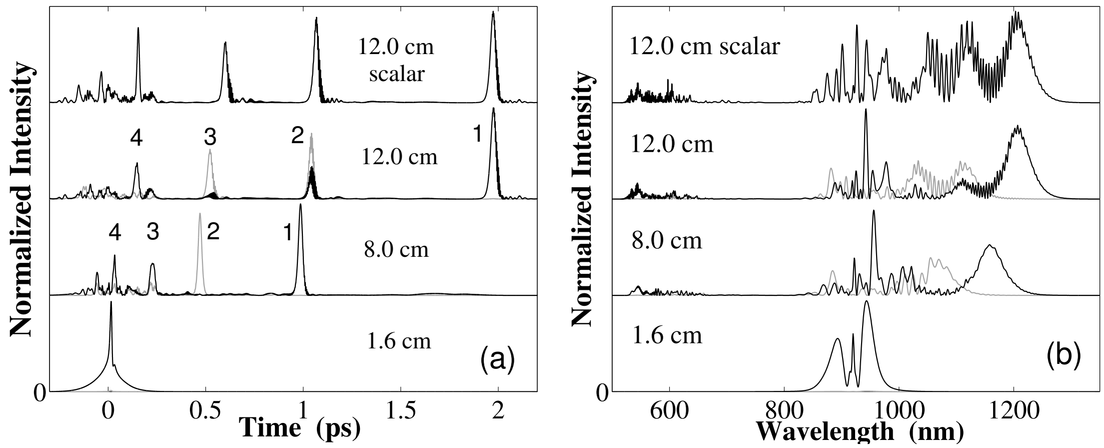


Figure 6.2: Numerically simulated temporal (a) and spectral (b) patterns at a distance of 1.6, 8, and 12 cm when a 150-fs pulse is launched into a tapered fiber. The black and gray curves show the two linearly polarized components, respectively. The scalar case at $z = 12$ cm is also shown for comparison.

where the nonlinear response is given by Eq. (2.6). We neglect the anisotropic part of Raman response because of its negligible magnitude compared with the isotropic one [15]. The isotropic Raman response is taken to be the most-often used Lorentzian form of [6]

$$R_a(\tau) = \frac{\tau_1^2 + \tau_2^2}{\tau_1 \tau_2^2} \exp(-\tau/\tau_2) \sin(\tau/\tau_1), \tag{6.1}$$

where $\tau_1 = 12.2$ fs and $\tau_2 = 32$ fs [6].

We solve Eq. (2.26) numerically with the split-step Fourier method [6] for an almost linearly polarized input "sech" pulse. More specifically, we use $\mathbf{A}(0,\tau) = \sqrt{P_0}\,\mathrm{sech}(\tau/\tau_0)(\cos\theta, i\sin\theta)$, where the ellipticity angle $\theta = 1.43^\circ$ corresponds to $<0.1\%$ of the input power into the $y$-polarized component of the pulse. For a peak power $P_0 = 10$ kW and a pulse width $\tau_0 = 85$ fs (FWHM = 150 fs), the input pulse excites a soliton whose order is $N = (\gamma P_0 \tau_0^2/|\beta_2|)^{1/2} \approx 12$.

Figure 6.2 shows the temporal and spectral evolution of the pulse at three propagation distances. During the initial stage of pulse compression, the pulse remains almost linearly polarized, and no splitting occurs until $z = 1.6$ cm. Beyond that distance, the higher-order soliton undergoes fission and breaks into multiple fundamental vector solitons with different states of polarization (SOPs). The SOP of the rightmost soliton in Fig. 6.2(a) is close to linear, but others are elliptically polarized. For example, the second soliton has an ellipticity angle of 5.4°, but the third one has an ellipticity angle of 15.4°. The fourth soliton has an ellipticity angle of 16°, and its SOP rotates in a direction opposite to the second and third solitons. The temporal structure near $\tau = 0$ contains the remaining pulse energy and exhibits even more complex polarization features. Successive solitons emerge from this structure. In general, the later the vector soliton is created, the more complicated is its polarization behavior. A comparison of the scalar and vector traces at a distance of 12 cm shows that the vectorial nature of the fission affects the delay experienced by individual solitons.

The spectra shown in Fig. 6.2(b) reveal the details of SC generation in a tapered fiber. After the fission of the higher-order soliton, all individual solitons experience a large frequency downshift and time dalay because of intrapulse Raman scattering [6, 16]. The soliton created the earliest is delayed the most because it undergoes the most red shift. As the spectra of these solitons overlap, they interfere with each other and produce the fine oscillatory structure seen in Fig. 6.2(b). However, since the orthogonally polarized components do not interfere with each other, the magnitude of such oscillations varies dramatically with distance. The spectrum at 12 cm is quite different from that predicted by the scalar NLS equation, indicating that the vectorial effects must be included even when the fiber has almost no birefringence.

The important question is why the SOP of the input pulse changes so drastically in an isotropic nonlinear medium. The answer is provided by the fact that as long as the $y$ component of the field is not zero, the two polarization components are coupled nonlinearly. More precisely, self-phase modulation (SPM), XPM, and other higher-order nonlinear effects such as self-steepening and stimulated Raman scattering induce energy transfer between them. Under conditions appropriate for SC generation, the combined effects of SPM and higher-order dispersion dramatically amplify the energy transfer and split the input pulse into multiple parts interacting with each other through XPM. Such interactions induce drastic polarization variations as the input pulse evolves into individual solitons and dispersive waves.

To gain more physical insight, we introduce a time-dependent Stokes vector $\hat{S}(z,\tau)$, whose tip moves on the Poincaré sphere with north pole as the left circular polarization [17]. Figure 6.3 depicts the motion of $\hat{S}$ on this sphere under four different conditions. Figure 6.3(a) shows $\hat{S}$ across the pulse at $z = 1.6$ cm. Since the input pulse is almost linearly polarized, SPM rotates the Stokes vector around the vertical axis [6]. Different parts of the pulse acquire slightly different SOPs but all parts remain nearly linearly polarized. As the compressed pulse is highly chirped, such temporal SOP variations are associated with different frequency components and are responsible for the vectorial nature of the fission process.

After 1.6 cm, higher-order dispersive effects keep moving the upshifted and downshifted frequency components of the pulse toward its tailing edge and initiate the fission process. The compressed pulse splits into multiple components that develop different SOPs through the intense interactions between nonlinearity and dispersion. Various temporal components of the pulse with different SOPs collide with one another as they evolve into individual solitons and generate dispersive waves, as seen in Fig. 6.2(a). The soliton that is created first (at a distance of about 2 cm in our case) has nearly the same polarization as the input pulse because such collisions do not last long enough to induce large polarization variations.

Solitons created further down the fiber acquire elliptical SOPs since their interactions with other temporal components last longer and hence can induce considerable polarization rotation on individual solitons. Generally speaking, the ellipticity of a vector soliton created through fission depends on the time it is perturbed by the induced nonlinear polarization rotation; the earlier the soliton is formed, the less its SOP changes.

Figure 6.3(b) and 6.3(c) show the front and the back of the Poincaré sphere on which we depict the SOPs of the entire temporal pattern created at a distance of 12 cm (see Fig. 6.2). Once a vector soliton is formed, its SOP is no longer affected by XPM since its two orthogonally polarized components are bound together and form a pair (the so-called soliton trapping). However, its SOP still evolves in a periodic fashion along the fiber because of SPM. This periodic evolution is shown in Fig. 6.3(d) for the 4 solitons up to a distance of 20 cm. The Stokes vector, averaged over the soliton profile, rotates around the vertical axis for each soliton. Note that Fig. 6.3(d) shows SOP changes as function of distance in

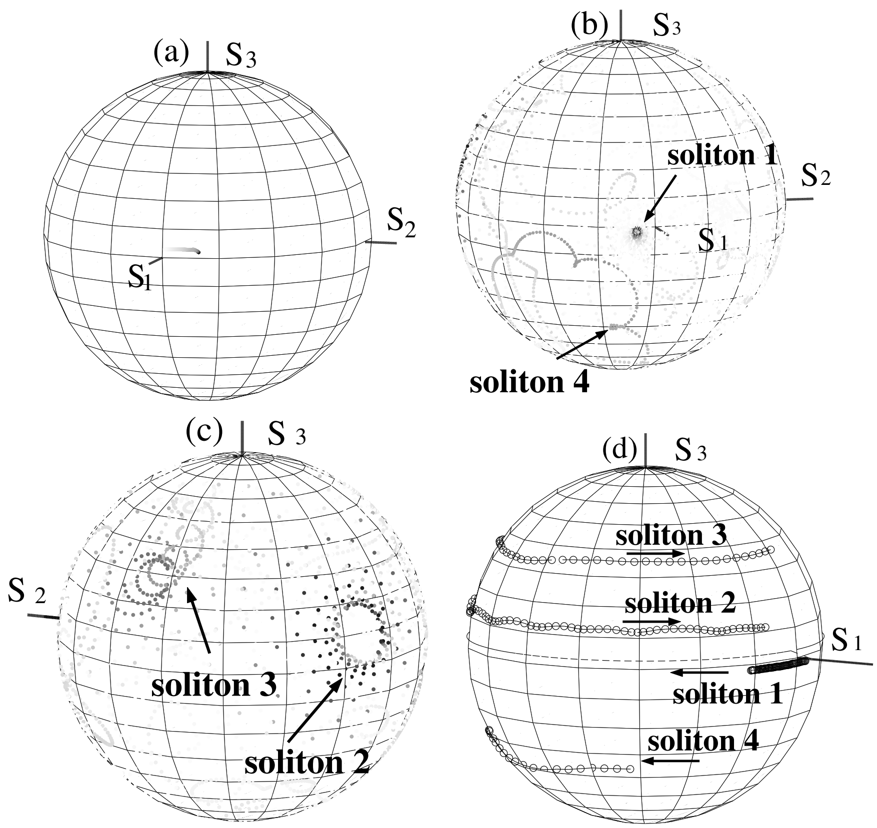


Figure 6.3: Polarization patterns in 4 different cases; grayness of dots indicates intensity. (a) temporal pattern at $z = 1.6$ cm; (b) temporal pattern at $z = 12$ cm; (c) back of the Poincaré sphere at $z = 12$ cm; (d) $z$-dependent polarization evolution of four vector solitons.

contrast with the other 3 parts of Fig. 6.3 where SOP varies with time at a fixed distance. Several other features of Fig. 6.3(d) are noteworthy. As explained earlier, the SOP of the first soliton changes little and it remains almost linearly polarized. The second and third solitons rotate their SOPs counterclockwise, whereas those of the first and fourth solitons rotate clockwise. The rotation rates are also different for all solitons. For example, the second soliton changes polarization in a periodic fashion with a 19.8-cm period but the third one with a period of about 10.4 cm.

An interesting feature seen in Figs. 6.3(b) and 6.3(c) is that the SOPs of nonsoliton radiation, or dispersive waves (light gray dots), is spread over the entire Poincaré sphere. Physically, as solitons are perturbed by higher-order dispersive and nonlinear effects, they shed part of their energy in the form of dispersive waves. Frequencies of these waves are often shifted toward the blue side, as seen in Fig. 6.2(b), because of a phase-matching condition related to four-wave mixing. The SOP of a dispersive wave is set by the SOP of the soliton at the time the radiation is emitted. Since SOPs of the solitons are not fixed but evolve with distance, the SOPs of dispersive waves eventually spread over the entire Poincaré sphere. In the spectral domain, dispersive waves show quite complicated polarization characteristics since each spectral component may get its power from several different solitons. However, because of the phase-matching condition, a soliton with the most red shift generates dispersive waves with the most blue shift and correlates in their polarizations.

Our numerical simulations show that the vectorial fission process is very sensitive to the parameters associated with the input pulse and the fiber. For example even a slight increase in the relative intensity of the $y$ component at the input end (-30 dB in place of -32 dB) changes the situation enough that even the first soliton in Fig. 6.2 becomes elliptically polarized. On the other hand, vectorial nature of the soliton fission persists numerically even when the relative intensity level of the $y$ component is down to -50 dB. A commercial mode-locked laser typically contains more power in the orthogonally polarized component than that, indicating that such polarization effects should be observable experimentally. As realistic fibers inevitably exhibit some birefringence, we have included its effects in our numerical simulations using an index difference of $\delta n = 10^{-8}$ for the two polarization components. We find that the results and our conclusions do not change as long as the beat length is much longer than the fiber length used for SC generation.

## 6.3 Experimental Verification

Our experiments were performed in collaboration with Prof. Knox's group using a tapered fiber which has a 17-cm-long waist with 2.7 $\mu$m diameter, two 2-cm-long transition regions, and the head and tail sections of 10 cm [18]. As the fiber is carefully tapered, its birefringence is expected to be small ($\delta n \sim$

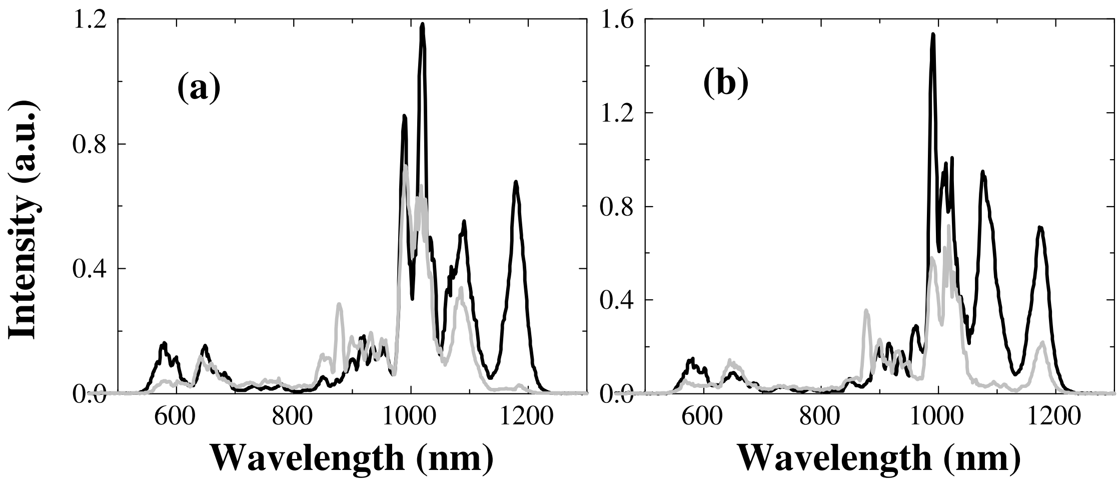


Figure 6.4: Experimental SC spectra obtained by rotating a polarizer placed at the output end of the tapered fiber. The black and gray curves show orthogonally polarized components. Polarization contrast is maximized (a) for the rightmost spectral peak and (b) for the peak before that.

$10^{-8}$). We verified that this indeed was the case by sending a linearly polarized low-power beam into the fiber and varying the input polarization angle. Mode-locked pulses of 100-fs width, generated from a Ti:sapphire laser (Mai Tai) operating at 920 nm at a repetition rate of 80 MHz with an average power of 300 mW, are coupled into the fiber and the generated SC spectrum is recorded with a resolution of 10 nm using an optical spectrum analyzer. In contrast with the case of birefringent PCF [11]-[13], we did not observe any significant change in the recorded spectrum while rotating the input polarization angle; this feature verifies that our fiber has negligible birefringence.

To analyze the polarization properties of the SC, we inserted a frequency-independent polarizer at the output end. Figure 6.4(a) shows the spectra for orthogonal polarizations when the polarizer was oriented to maximize the contrast between the two components for the rightmost spectral peak located at 1180 nm. We recorded a series of such spectra to average the experimental data reported below. We found that the first soliton is elliptically polarized, and the polarization ellipse is oriented at about 3° with respect to the input. The 17.9-dB contrast (average value) for this peak corresponds to an ellipticity angle of $\theta = 7.3° \pm 1.5°$. Notice that the polarization properties of this soliton correlate well with the most blue-shifted dispersive-wave component near 580 nm, as expected from our theory. Figure 6.4(b) shows the cases in which polarizer is oriented to provide maximum contrast of 15.5 dB for the second spectral peak at 1080 nm. The ellipticity angle is $9.5° \pm 2°$ for this soliton, and its principal axes are oriented at 30° with respect to the input. Other spectral peaks at 990 nm and 1020 nm are even more elliptically polarized. However, since their spectra overlap considerably, it is difficult to distinguish between them. In general, the closer the peak to the input wavelength, the more complicated and unstable is its polarization behavior. We have performed numerical simulations using parameter values most appropriate to our experiment. We find that the ellipticity angles for the first two solitons are 7.2° and 8.6°, respectively. These numbers agree reasonably well with our data within experimental errors. Some discrepancy may also be due to our neglect of the slight anisotropic nature of Raman process. The oscillatory structure seen in Fig. 6.2(b) does not appear in the experimental spectra because of a relatively low resolution of the optical spectrum analyzer and the averaging induced by its long response time [19]-[21].

## 6.4 Conclustions

In conclusion, we have shown that the vectorial nature of soliton fission plays an important role in SC generation in weakly birefringent and isotropic fibers. The fission-generated vector solitons are elliptically polarized even when the input pulse is almost linearly polarized. Experiments performed with a tapered fiber agree well with the theory and numerical simulations. Our research suggests that SC generation in weakly birefringent fibers is rarely a scalar process, as often assumed in previous work. The polarization effects discussed here might affect not only the coherence properties of SC [19] but also its characterization through polarization gating [20] or frequency-resolved optical gating [21], both of which are sensitive to the polarization properties of the SC. As a final remark, although we have focused on tapered fibers, our conclusions should hold for soliton fission in any fast-responding medium with Kerr-type nonlinearity.

## References


[1] F. Lu, Q. Lin, W. H. Knox, and G. P. Agrawal, Phys. Rev. Lett. **93**, 183901 (2004).

[2] Y. Yang, *Solitons in Field Theory and Nonlinear Analysis* (Springer, New York, 2001).

[3] L. A. Dickey, *Soliton Equations and Hamiltonian Systems* (World Scientific, New York, 2003).

[4] Y. S. Kivshar and G. P. Agrawal, *Optical Solitons: From Fibers to Photonic Crystals*, (Academic, San Diego, 2003).

[5] G. P. Agrawal, *Fiber-Optic Communication Systems*, 3rd ed. (Wiley, New York, 2002).

[6] G. P. Agrawal, *Nonlinear Fiber Optics*, 3rd ed. (Academic, San Diego, 2001).

[7] P. S. J. Russell, *Science* **299**, 358 (2003).

[8] J. K. Ranka, R. S. Windeler, and A. J. Stentz, Opt. Lett. **25**, 25 (2000).

[9] T. A. Birks, W. J. Wadsworth, and P. St. J. Russell, Opt. Lett. **25**, 1415 (2000).

[10] A. V. Husakou and J. Herrmann, Phys. Rev. Lett. **87**, 203901 (2001).

[11] A. Apolonski, B. Povazay, A. Unterhuber, W. Drexler, W. J. Wadsworth, J. C. Knight, and P. St. J. Russell, J. Opt. Soc. Am. B **19**, 2165 (2002).

[12] M. Lentonen, G. Genty, and H. Ludvigsen, App. Phys. Lett. **82**, 2197 (2003).

[13] Z. Zhu and T. G. Brown, J. Opt. Soc. Am. B **21**, 249 (2004).

[14] S. V. Manakov, Sov. Phys. JETP **38**, 248 (1974).

[15] R. H. Stolen, in *Raman Amplifiers for Telecommunications 1*, M. N. Islam Ed. (Springer, New York 2003).

[16] J. P. Gordon, Opt. Lett. **11**, 662 (1986).

[17] M Born and E. Wolf, *Principles of Optics*, 7th ed. (Cambridge University Press, New York, 1999).

[18] F. Lu and W. H. Knox. Opt. Exp. **12**, 347 (2004).

[19] J. M. Dudley and S. Coen, Opt. Lett. **27**, 1180 (2002).

[20] H. Kano and H. Hamaguchi, Opt. Lett. **28**, 2360 (2003).

[21] X. Gu, L. Xu, M. Kimmel, E. Zeek, P. O'Shea, A. P. Shreenath, and R. Trebino, Opt. Lett. **27**, 1174 (2002).

# 7 Raman Response Function for Silica Fibers

In this chapter, we show [1] that the commonly used Lorentzian form of the Raman response function for studying propagation of ultrashort pulses in silica fibers does not properly account for the shoulder in the Raman gain spectrum originating from the Boson peak. We propose [1] a more accurate form of this response function and show that its predictions for the Raman-induced frequency shift are in better agreement with experiments.

## 7.1 Introduction

The nonlinear effects in optical fibers affect considerably the propagation of ultrashort pulses and lead to a variety of interesting optical phenomena such as Raman-induced frequency shifts (RIFS), soliton fission, and supercontinuum generation [2]. The Raman effect is known to impact ultrashort pulses, and its inclusion is essential in any theoretical modeling. Indeed, numerous efforts have been made to characterize the nonlinear properties of silica glass and fibers [3]–[9], and to model the associated nonlinear response [10]-[13]. In general, it has the form $R(\tau) = (1 - f_R)\delta(\tau) + f_R h_R(\tau)$, where the two terms account for the instantaneous electronic and retarded molecular responses, respectively [2]. The Raman response function $h_R(\tau)$ exhibits complicated dynamics [11] because of the amorphous nature of silica glass [3, 4].

Although Raman response can be modeled fairly accurately by a superposition of 13 Lorentzian–Gaussian functions [13], such a model is often impractical owing to its complexity. At the other extreme, Raman response is approximated by damping oscillations associated with a single vibrational mode [12], resulting in a Lorentzian-shape gain spectrum (thin dashed curve in Fig. 7.1). It uses three parameters to provide the correct location and peak value of the dominant peak in the Raman gain spectrum (thin solid curve with dots in Fig. 7.1). Because of its simplicity, this simple model is widely used to investigate

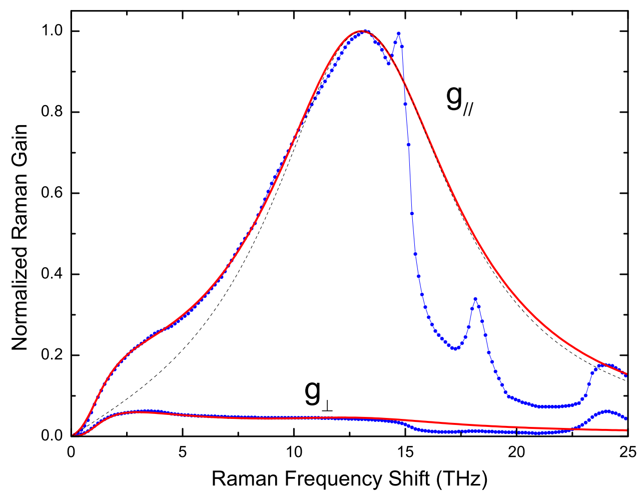


Figure 7.1: Raman gain spectra for two polarization configurations (thin solid curves with dots) based on experimental data [7]. The dashed curve shows the conventional Lorentzian model; thick solid curves show our model.

ultrafast nonlinear phenomena in optical fibers. Although it explains the qualitative behavior reasonably well, this model underestimates the magnitude of Raman gain considerably in the frequency range below 10 THz, while overestimating it beyond 15 THz. Consequently, it does not provide a correct quantitative description of Raman-induced phenomena and leads to difficulty in comparing theory and experiments. We show in this chapter that the problem can be fixed by considering the anisotropic nature of Raman scattering and introducing an appropriate but simple form for the anisotropic part of the Raman response.

## 7.2 Tensor Nature of Raman Response Function

In general, the third-order nonlinear response of silica fibers should be described by a tensor in the form of Eq. (2.6) in Chap. 2 [3]. The often-used scalar form of the nonlinear response is given by $R^{(3)}_{xxxx}(\tau) = (1-f_R)\delta(\tau) + f_R[R_a(\tau)+R_b(\tau)]$. Equation (2.6) indicates that the Raman gain in silica fibers consists of contributions from isotropic and anisotropic molecular responses given by $g_a(\Omega) \equiv 2\gamma f_R \mathrm{Im}[\widetilde{R}_a(\Omega)]$ and $g_b(\Omega) \equiv 2\gamma f_R \mathrm{Im}[\widetilde{R}_b(\Omega)]$, respectively, where $\gamma = n_2\omega_0/c$ is the nonlinear parameter [2]. Here, $\widetilde{R}_\varepsilon(\Omega)$ ($\varepsilon = a, b$) is the Fourier transform of $R_\varepsilon(\tau)$ defined as $\widetilde{R}_\varepsilon(\Omega) = \int_{-\infty}^{\infty} R_\varepsilon(\tau)\exp(i\Omega\tau)d\tau$. From Eq. (2.6), the Raman gain for copolarized and orthogonally polarized pumps is found to be [3] $g_\parallel(\Omega) = g_a(\Omega) + g_b(\Omega)$ and $g_\perp(\Omega) = g_b(\Omega)/2$. Figure 7.2 shows the spectra of $g_\parallel$ [7] and the associated decomposed $g_a$ and $g_b$ ($g_\perp$ is shown in Fig. 7.1). Although the anisotropic part provides a relatively small Raman gain for an orthogonally polarized signal, its contribution to the copolarized Raman gain

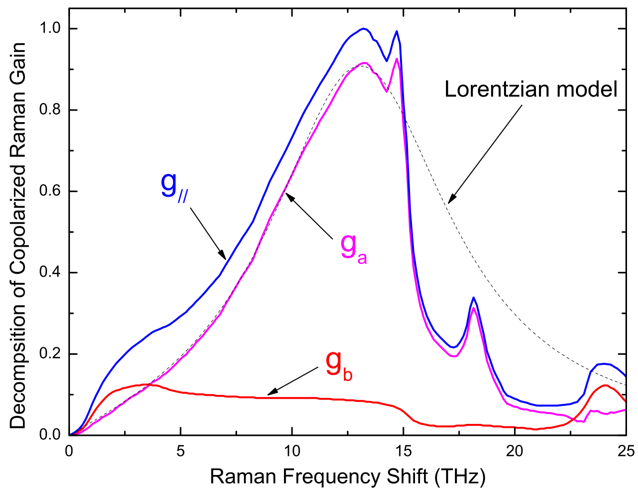


Figure 7.2: Decomposition of the copolarized Raman gain into its two parts $g_a$ and $g_b$. The dashed curve shows the fit based on the simple Lorentzian model.

dominates in the low-frequency region. Figure 7.2 shows clearly that it is the anisotropic response that is responsible for the shoulder around 3 THz in the copolarized Raman gain.

Physically, the isotropic Raman response stems dominantly from the symmetric stretching motion of the bridging oxygen atom in the Si-O-Si bond [4]. It turns out that this motion, and the resulting Raman gain $g_a$, can be described well by the widely used single-Lorentzian model. For this reason, we adopt it for the isotropic response and use $R_a(\tau) = f_a h_a(\tau)$, where $h_a(\tau)$ is given by [12]

$$h_a(\tau) = \frac{\tau_1^2 + \tau_2^2}{\tau_1 \tau_2^2} \exp(-\tau/\tau_2) \sin(\tau/\tau_1), \tag{7.1}$$

and $f_a$ represents the fractional contribution of $R_a$ to total copolarized Raman response. By using the values $\tau_1 = 12.2$ fs and $\tau_2 = 32$ fs [12], and choosing $f_a = 0.75$, we find that $g_a$ in Fig. 2 can be fitted quite well with Eq. (7.1), especially in the spectral region below 14 THz. If we can find an appropriate function for the anisotropic Raman response $R_b(\tau)$, we should be able to provide an accurate description of the total nonlinear response.

Figure 7.2 shows that $g_b$, and the corresponding $g_\perp$ in Fig. 1, exhibit a broad peak in the frequency region around 3 THz. Such a low-frequency peak is known as the Boson peak and is a universal feature of amorphous glassy substances [14, 15]. Although its physical nature is still under debate [14]-[20], the Boson peak reflects an excessive density of vibrational states, resulting from multiple effects (such as localization of vibrational motions in a vitreous state). The Boson peak in $g_\perp$ can be described by a Lorentzian function with a cubic dependence on frequency on its low-frequency side [14, 16]. We have found that the corresponding temporal response can be modeled by a simple function of the form

$$h_b(\tau) = \frac{1}{\tau_b}\left(2 - \frac{\tau}{\tau_b}\right)\exp(-\tau/\tau_b), \tag{7.2}$$

where a single time constant $\tau_b$ governs the response because of the low-frequency nature of the Boson peak.

Moreover, $g_b$ exhibits a flat spectral plateau between $8-15$ THz which cannot be completely accounted for by Eq. (7.2). It not only coincides with the broadband peak of $g_a$, but it also exhibits a drop-off around 15 THz similar to $g_a$. These features suggest that this spectral portion of $g_b$ shares a common physical origin with the dominant peak of $g_a$, probably because of the participation of other bond-bending motions or the existence of strong intermediate-range correlations between nearby bonds [4]. Based on the preceding discussion, we propose the following form for the anisotropic part of the Raman response in fused silica:

$$R_b(\tau) = f_b h_b(\tau) + f_c h_a(\tau), \tag{7.3}$$

where $f_b$ and $f_c$ represent the fractional contributions of $h_b(\tau)$ and $h_a(\tau)$, respectively. In our model, the copolarized nonlinear response is given by

$$R^{(3)}_{xxxx}(\tau) = (1 - f_R)\delta(\tau) + f_R[(f_a + f_c)h_a(\tau) + f_b h_b(\tau)] \tag{7.4}$$

with $f_a + f_c + f_b = 1$. By choosing $\tau_b = 96$ fs to account for the spectral width of the Boson peak together with $f_b = 0.21$ and $f_c = 0.04$, we find in Fig. 7.1 that both $g_\parallel$ and $g_\perp$ are fitted very well by our model over the frequency range 0–15 THz.

Figures 7.1 and 7.2 show only the normalized Raman gain spectra. To obtain a realistic value of the peak Raman gain, we need to assign an appropriate value to the factor $f_R$ in Eq. (2.6). If we use $n_2 = 2.6 \times 10^{-20}$ m$^2$/W for silica fibers [2], the choice $f_R = 0.245$ in our model yields a peak Raman gain equal to the experimental value of $g_R = 1.2 \times 10^{-11}$ cm/W at 795.5 nm [5] (corresponding to $g_R = 1.81 \times 10^{-11}$ cm/W at 526 nm [7]). With this choice, not only our model provides Raman gain accurately over the spectral range 0–15 THz, but it also describes well the Raman-induced changes in the nonlinear refractive index over the same frequency range, since the two are related through the Kramers–Kronig relation [3]. This can be seen clearly in Fig. 7.3, where we plot the nonlinear refractive index given by the real part of $\widetilde{R}^{(3)}_{xxxx}(\Omega)$.

Our value of $f_R$ is slightly higher than the experimental value of about 0.2 [11, 12] because our model overestimates the Raman gain in the spectral region beyond 15 THz. This causes an underestimation of the electronic contribution to nonlinear refractive index by 5% or so, as seen in Fig. 7.3, when the frequency shift exceeds 20 THz and where Raman contribution is negligible. However, this underestimation

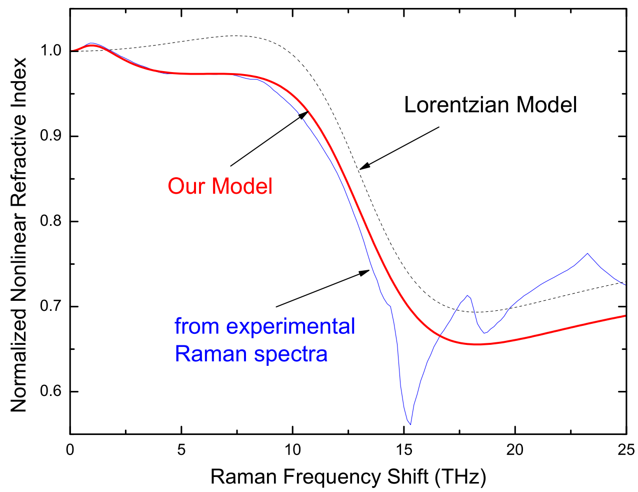


Figure 7.3: Normalized nonlinear refractive index. Thin solid curve: experimental data [7]; thin dashed curve: conventional Lorentzian model; thick solid curve: our model.

does not affect the description of nonlinear effects until the pulse becomes so short that it contains only a few optical cycles. We expect our model to provide a relatively accurate description of nonlinear effects for pulses as short as 30 fs.

## 7.3 Application to Short-Pulse Propagation

As a simple application of our model, we focus on the RIFS of solitons. For a linearly polarized soliton, the RIFS increases along the fiber at a rate governed by [21]

$$\frac{d\bar{\omega}}{dz} = -\frac{E_s\Omega_0}{2\pi A_{\text{eff}}}\int_0^{\infty}\frac{g_{\parallel}(\Omega)(\Omega/\Omega_0)^3}{\sinh^2(\Omega/\Omega_0)}d\Omega, \tag{7.5}$$

where $\bar{\omega}$ is the carrier frequency of soliton, $E_s$ is the soliton energy, $\Omega_0 = 4\ln(1+\sqrt{2})/(\pi T_s)$ is related to the soliton width $T_s$ (FWHM), and $A_{\text{eff}}$ is the effective mode area. Figure 7.4 shows the normalized rate of RIFS, defined as $|d\bar{\omega}/dz|A_{\text{eff}}/(g_R E_s)$. Clearly, our model provides a relatively accurate description of RIFS and its predictions nearly coincide with that based on the experimental Raman spectrum. However, the conventional single-Lorentzian model [12] underestimates RIFS rate by about 40% for pulse widths in the range of 100 to 500 fs. When pulse width decreases below 100 fs, the contribution of the broad Raman-gain peak begins to dominate, and the discrepancy between the two models decreases.

To further explore the implications of our model, we have studied propagation of a 300-fs sech pulse at 1200 nm with 960-W peak power along a 5-m-long microstructured fiber numerically by solving the generalized NLSE (2.26). The fiber with a 2.5-$\mu$m core diameter is assumed to have a large air-filling

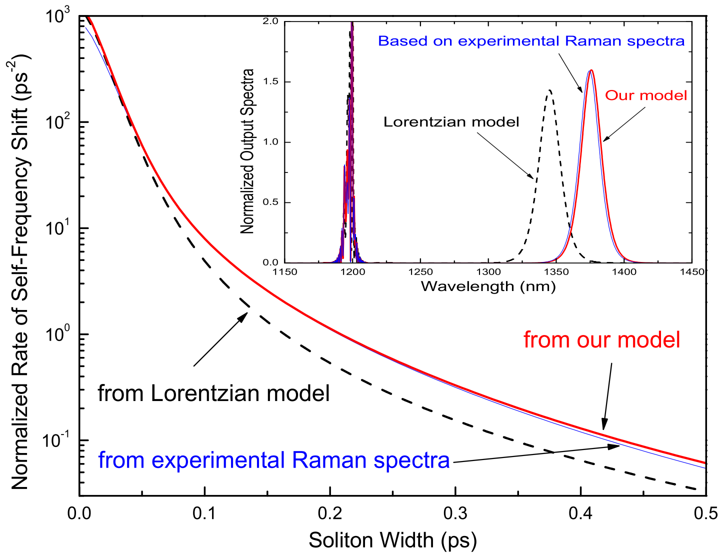


Figure 7.4: RIFS rate as a function of soliton width $T_s$ for our model (thick solid line) and for the conventional model (dashed line). Thin solid curves is based on the experimental Raman spectrum. The inset shows output spectra obtained numerically for a 300-fs pulse, assumed to maintain its linear polarization.

fraction so that its dispersion can be modeled as a glass rod surrounded by air. The inset of Fig. 7.4 shows the output spectra. Because of fiber dispersion, the input pulse splits into two parts, one of which forms a soliton whose width changes from about 60 to 100 fs along the fiber, resulting in a net RIFS of 175 nm. Our proposed model shows excellent agreement with the one obtained using the experimental Raman spectrum. However, the conventional model based on Eq. (7.1) underestimates the RIFS by about 20%.

## 7.4 Conclusions

In conclusion, we show that the conventional single-Lorentzian model does not provide an accurate quantitative description of the Raman response. The reason is found to be related to the anisotropic part of the Raman response that is ignored by this often-used model. Based on the notion of the Boson peak, we introduce a simple function to account for this anisotropic part and show that the new model fits quite well both the Raman gain and the Raman-induced changes in the nonlinear refractive index over a frequency range 0–15 THz. We show that the predictions of our model for the RIFS are expected to be much closer to the experimental predictions. Our model can also be used to describe quantitatively various Raman-related vectorial nonlinear phenomena.

## References

[1] Q. Lin and G. P. Agrawal, "Raman response function for silica fibers", Opt. Lett. **31**, November (2006).

[2] G. P. Agrawal, *Nonlinear Fiber Optics*, 3*rd* ed. (Academic, Boston, 2001), Chap. 2.

[3] R. W. Hellwarth, Progress in Quantum Electronics **5**, 1 (1977).

[4] F. L. Galeener, A. J. Leadbetter, and M. W. Stringfello, Phys. Rev. B **27**, 1052 (1983); see also references therein.

[5] D. J. Dougherty, F. X. Kärnter, H. A. Haus, and E. P. Ippen, Opt. Lett. **20**, 31 (1995).

[6] A. K. Atieh, P. Myslinski, J. Chrostowski, and P. Galko, J. Lightwave Technol. **17**, 216 (1999).

[7] R. H. Stolen, in *Raman Amplifiers for Telecommunications 1*, M. N. Islam Ed. (Springer, New York 2003). Experiemental Raman spectra are provided by Dr. R. H. Stolen.

[8] F. A. Oguama, H. Garcia, and A. M. Johnson, J. Opt. Soc. Am. B **22**, 426 (2005); see also references therein.

[9] I. Mandelbaum, M. Bolshtyansky, T. F. Heinz, and A. R. H. Walker, J. Opt. Soc. Am. B **23**, 621 (2006).

[10] G. E. Walrafen and P. N. Krishnan, Appl. Opt. **21**, 359 (1982).

[11] R. H. Stolen, J. P. Gordon, W. J. Tomlinson, and H. A. Haus, J. Opt. Soc. Am. B **6**, 1159 (1989).

[12] K. J. Blow and D. Wood, IEEE J. Quant. Electron. **25**, 2665 (1989).

[13] D. Hollenbeck and C. D. Cantrell, J. Opt. Soc. Am. B **19**, 2886 (2002).

[14] V. K. Malinovsky and A. P. Sokolov, Solid State Commun. **57**, 757 (1986); Glass Phys. Chem. **22**, 152 (1996).

[15] C. A. Angell, K. L. Ngai, G. B. McKenna, P. F. McMillan, and S. W. Martin, J. Appl. Phys. **88**, 3113 (2000).

[16] C. McIntosh, J. Toulouse, and P. Tick, J. Non-Cryst. Solids **222**, 335 (1997).

[17] E. Courtens, M. Foret, B. Hehlen, and R. Vacher, Solid State Commun. **117**, 187 (2001); see also references therein.

[18] V. L. Gurevich, D. A. Parshin, and H. R. Schober, Phys. Rev. B **67**, 094203 (2003); see also references therein.

[19] N. Shimodaira, K. Saito, N. Hiramitsu, S. Matsushita, and A. J. Ikushima, Phys. Rev. B **71**, 024209 (2005).

[20] G. N. Greaves, F. Meneau, O. Majérus, D. G. Jones, and J. Taylor, Science **308**, 1299 (2005).

[21] J. P. Gordon, Opt. Lett. **11**, 662 (1986).

# 8 Nonlinear Effects in Long Fibers

In this chapter, we provide the derivation of the general formalism that will be used in the following chapters to describe various nonlinear effects in optical fibers that are long enough that the effects of random birefringence cannot be ignored.

## 8.1 Introduction

In the following few chapters, we will turn our attention to nonlinear effects occurring in optical fibers whose lengths are in a scale of kilometer or even longer. In this case, fiber properties cannot be treated constant along the fiber because, in practice, both internal manufacturing imperfections and external environmental factors introduce perturbations to fiber properties and result in residual birefringence inside fibers. Such birefringence not only changes randomly in both its magnitude and orientation along the fiber length, but also varies in time because of time-dependent environmental variations (such as temperature and stress variations).

Randomly varying birefringence may lead to several significant effects on optical waves propagating inside a fiber. First, it would change the state of polarization (SOP) randomly on a length scale of birefringence correlation length, which is of the order of 10–100 meters depending on fiber handling conditions [1]-[3]. Second, fiber birefringence is frequency dependent, which would depolarize randomly the relative polarizations among optical waves of different frequencies. This phenomenon is known as random polarization-mode dispersion (PMD) and the relative depolarization occurs on a length scale of PMD diffusion length, which depends on frequency separation between the two optical waves. If the optical wave is in the form of pulses, relative depolarization would occur across its spectrum, which manifests in the time domain as random differential group delay (DGD) between its two polarization modes and eventually broadens and distorts the pulse. The PMD phenomenon has been extensively studied in recent years in the context of optical communications [1]-[12] as it is found to be a serious limiting factor to high-speed fiber-optic communications.

On the other hand, as discussed in previous chapters, third-order nonlinear effects in optical fibers, such as SPM, XPM, SRS, FWM, are all strongly polarization dependent because of the spin conservation among the interacting photons. Therefore, if nonlinear interactions occur inside a long fiber, they would be significantly impacted by random birefringence and associated PMD. As various nonlinear effects are widely used in many applications such as soliton transmission, optical amplification, wavelength conversion, optical switching, signal shaping and regeneration, etc., fiber nonlinearities have become essential to realize future all-optical networks. Random birefringence and PMD would have serious impacts on the performance of all fiber devices based on long-length-scale nonlinearities. Therefore, it is important to find a way to quantify such impacts and to find possible ways to mitigate the impacts. In this short chapter, I develop a general formalism of nonlinear wave propagation in the presence of random birefringence and PMD. It will be used in the following chapters to discuss various nonlinear effects.

## 8.2 Jones and Stokes Formalisms for Wave Propagation

It is convenient to use the Jones-matrix notation to discuss the polarization effects [6]. In the Jones space, the GNLSE, Eq. (2.26), for the field vector $|A(z,t)\rangle$ becomes

$$\frac{\partial|A\rangle}{\partial z} = \sum_{m=0}^{+\infty} \frac{i^{m+1}\beta_m}{m!}\frac{\partial^m|A\rangle}{\partial t^m} - \frac{i}{2}\boldsymbol{B}\cdot\boldsymbol{\sigma}\left(\omega_0 + i\frac{\partial}{\partial t}\right)|A\rangle + i\gamma\left[1 + i\eta\frac{\partial}{\partial t}\right]|P^{NL}\rangle, \tag{8.1}$$

where the nonlinear polarization vector of Eq. (2.27) now appears as

$$\begin{aligned}|P^{NL}(z,t)\rangle = &\ \frac{f_E}{3}\left[2\langle A(z,t)|A(z,t)\rangle + |A^*(z,t)\rangle\langle A^*(z,t)|\right]|A(z,t)\rangle \\ &+ f_R\left\{\int_{-\infty}^{t} R_a(t-\tau)\langle A(z,\tau)|A(z,\tau)\rangle d\tau\right\}|A(z,t)\rangle \\ &+ \frac{f_R}{2}\left\{\int_{-\infty}^{t} R_b(t-\tau)\left[|A(z,\tau)\rangle\langle A(z,\tau)| + |A^*(z,\tau)\rangle\langle A^*(z,\tau)|\right]d\tau\right\}|A(z,t)\rangle,\end{aligned} \tag{8.2}$$

where $\langle A^*(z,t)|$ and $|A^*(z,t)\rangle$ denotes the Hermitian and complex conjugate of $|A(z,t)\rangle$, respectively. In Eq. (8.1), we have rewritten the birefringence tensor in the form of Pauli spin vector [6] as $\overleftrightarrow{\boldsymbol{B}} \equiv \boldsymbol{B}\cdot\boldsymbol{\sigma}$, where $\boldsymbol{B}$ is a three-dimensional Stokes vector and the spin vector is formed by use of Pauli matrices as $\boldsymbol{\sigma} = \sigma_1\hat{e}_1 + \sigma_2\hat{e}_2 + \sigma_3\hat{e}_3$, where $\hat{e}_1$, $\hat{e}_2$, and $\hat{e}_3$ are the three unit vectors in the Stokes space and [6]

$$\sigma_1 = \begin{pmatrix} 1 & 0 \\ 0 & -1 \end{pmatrix}, \qquad \sigma_2 = \begin{pmatrix} 0 & 1 \\ 1 & 0 \end{pmatrix}, \qquad \sigma_3 = \begin{pmatrix} 0 & -i \\ i & 0 \end{pmatrix}. \tag{8.3}$$

## 8.3 Birefringence Fluctuations

In practice, a moderate power is generally used to excite the nonlinear effects in practical devices. The interaction length scale is about $\sim$1 km, much longer than both the beat length and the correlation length of random residual birefringence ($\sim$ 10 m [2]). Clearly, residual birefringence would introduce rapid random polarization variations even before nonlinearities start to have an effect. Equation (8.1) shows that such rapid SOP variations can be described by a Jones matrix $\overleftrightarrow{\boldsymbol{T}}$ which satisfies

$$\frac{d\overleftrightarrow{\boldsymbol{T}}}{dz} = -\frac{i\omega_0}{2}\boldsymbol{B}\cdot\boldsymbol{\sigma}\overleftrightarrow{\boldsymbol{T}}. \tag{8.4}$$

The unitary matrix $\overleftrightarrow{\boldsymbol{T}}$ in Eq. (8.4) corresponds to random rotations of the Stokes vector on the Poincaré sphere that do not change the vector length. In the Jones (SU2) space, it can be written in the form [13]

$$\overleftrightarrow{\boldsymbol{T}} = \begin{pmatrix} a_1 & -a_2^* \\ a_2 & a_1^* \end{pmatrix}, \tag{8.5}$$

where $|a_1|^2+|a_2|^2=1$. If we introduce a Jones vector $|a\rangle$ with its two elements as $a_1$ and $a_2$, this vector satisfies

$$\frac{d|a\rangle}{dz} = -\frac{i\omega_0}{2}\boldsymbol{B}\cdot\boldsymbol{\sigma}|a\rangle. \tag{8.6}$$

Since random birefringence makes all SOPs equally likely, $|a\rangle$ can be expressed in its most general form as

$$|a(z)\rangle = e^{-i\varphi_0/2}\begin{pmatrix} \cos(\theta/2)e^{-i\varphi/2} \\ \sin(\theta/2)e^{+i\varphi/2} \end{pmatrix}, \tag{8.7}$$

where $\varphi_0(z)$ and $\varphi(z)$ are uniformly distributed in the range $[0,2\pi]$ and $\cos\theta(z)$ is uniformly distributed in the range $[-1,1]$. Thus, the most general form of the transformation matrix $\overleftrightarrow{\boldsymbol{T}}$ is given by

$$\overleftrightarrow{\boldsymbol{T}}(z) = \begin{pmatrix} \cos(\theta/2)e^{-i(\varphi_0+\varphi)/2} & -\sin(\theta/2)e^{i(\varphi_0-\varphi)/2} \\ \sin(\theta/2)e^{-i(\varphi_0-\varphi)/2} & \cos(\theta/2)e^{i(\varphi_0+\varphi)/2} \end{pmatrix}. \tag{8.8}$$

As $\overleftrightarrow{\boldsymbol{T}}(z)$ evolves only on a length scale of the birefringence correlation length, SOPs of optical waves vary so rapidly and randomly during nonlinear interaction along the fiber that only the average SOPs have an effect on nonlinear interactions. As we are only concerned about the nonlinear interactions, we can remove such rapid SOP variations by adopting a rotating frame through a unitary transformation $|A(z,t)\rangle = \overleftrightarrow{\boldsymbol{T}}(z)|A'(z,t)\rangle$. Eq. (8.1) in such a rotating frame then becomes

$$\frac{\partial|A'\rangle}{\partial z} = \sum_{m=0}^{+\infty}\frac{i^{m+1}\beta_m}{m!}\frac{\partial^m|A'\rangle}{\partial t^m} + \frac{1}{2}\boldsymbol{b}\cdot\boldsymbol{\sigma}\frac{\partial|A'\rangle}{\partial t} + i\gamma\left[1+i\eta\frac{\partial}{\partial t}\right]|(P^{NL})'\rangle, \tag{8.9}$$

where the transformed nonlinear polarization $|(P^{NL})'\rangle$ becomes

$$\begin{aligned}|(P^{NL})'(z,t)\rangle = &\ \frac{f_E}{3}\left[3\langle A'(z,t)|A'(z,t)\rangle - \langle A'(z,t)|\overleftrightarrow{\boldsymbol{T}}^{\dagger}\sigma_3\overleftrightarrow{\boldsymbol{T}}|A'(z,t)\rangle\overleftrightarrow{\boldsymbol{T}}^{\dagger}\sigma_3\overleftrightarrow{\boldsymbol{T}}\right]|A'(z,t)\rangle \\ &+ \ f_R\left\{\int_{-\infty}^{t} R_a(t-\tau)\langle A'(z,\tau)|A'(z,\tau)\rangle d\tau\right\}|A'(z,t)\rangle + \frac{f_R}{2}\left\{\int_{-\infty}^{t} R_b(t-\tau)\right. \\ &\left.\left[2|A'(z,\tau)\rangle\langle A'(z,\tau)| - \langle A'(z,\tau)|\overleftrightarrow{\boldsymbol{T}}^{\dagger}\sigma_3\overleftrightarrow{\boldsymbol{T}}|A'(z,\tau)\rangle\overleftrightarrow{\boldsymbol{T}}^{\dagger}\sigma_3\overleftrightarrow{\boldsymbol{T}}\right]d\tau\right\}|A'(z,t)\rangle, \end{aligned} \tag{8.10}$$

and we have used the relations

$$|A^*\rangle\langle A^*| = |A\rangle\langle A| - \langle A|\sigma_3|A\rangle\sigma_3, \tag{8.11}$$

$$|A\rangle\langle A| = [\langle A|A\rangle + \langle A|\boldsymbol{\sigma}|A\rangle\cdot\boldsymbol{\sigma}]/2. \tag{8.12}$$

## 8.4 Slowly Varying Polarization Approximation

Similar to the SVEA discussed in Chapter 2, we can employ a slowly varying polarization approximation (SVPA), by averaging over random $\overleftrightarrow{\boldsymbol{T}}$ in Eq. (8.10), to study the nonlinear dynamics on a length scale of the nonlinear length. It is easy to show that [13]

$$\overline{\langle A'|\overleftrightarrow{\boldsymbol{T}}^{\dagger}\sigma_3\overleftrightarrow{\boldsymbol{T}}|A'\rangle\overleftrightarrow{\boldsymbol{T}}^{\dagger}\sigma_3\overleftrightarrow{\boldsymbol{T}}} = \frac{1}{3}\langle A'|\boldsymbol{\sigma}|A'\rangle\cdot\boldsymbol{\sigma}, \tag{8.13}$$

where an overbar denotes an average over the random polarization variation induced by $\overleftrightarrow{\boldsymbol{T}}$. Substituting Eq. (8.13) into Eq. (8.10) and dropping the prime and average notation in both Eqs. (8.9) and (8.10), we obtain

$$\frac{\partial|A\rangle}{\partial z} = \sum_{m=0}^{+\infty}\frac{i^{m+1}\beta_m}{m!}\frac{\partial^m|A\rangle}{\partial t^m} + \frac{1}{2}\boldsymbol{b}\cdot\boldsymbol{\sigma}\frac{\partial|A\rangle}{\partial t} + i\gamma\left[1 + i\eta\frac{\partial}{\partial t}\right]|P^{NL}\rangle, \tag{8.14}$$

where the nonlinear polarization $|P^{NL}\rangle$ is now given by

$$\begin{aligned}|P^{NL}(z,t)\rangle = &\ \frac{8f_E}{9}\langle A(z,t)|A(z,t)\rangle|A(z,t)\rangle \\ &+ \ f_R\left\{\int_{-\infty}^{t}\left[R_a(t-\tau) + \frac{1}{6}R_b(t-\tau)\right]\langle A(z,\tau)|A(z,\tau)\rangle d\tau\right\}|A(z,t)\rangle \\ &+ \ \frac{2f_R}{3}\left\{\int_{-\infty}^{t} R_b(t-\tau)|A(z,\tau)\rangle\langle A(z,\tau)|d\tau\right\}|A(z,t)\rangle. \end{aligned} \tag{8.15}$$

In Eq. (8.14), $\boldsymbol{b}$ is related to $\boldsymbol{B}$ by a rotation as $\boldsymbol{b} = \overleftrightarrow{\boldsymbol{R}}^{-1}\boldsymbol{B}$, where $\overleftrightarrow{\boldsymbol{R}}$ is the three-dimensional rotation matrix in the Stokes space that is isomorphic to $\overleftrightarrow{\boldsymbol{T}}$ in the Jones space, i.e., $\overleftrightarrow{\boldsymbol{R}}\boldsymbol{\sigma} = \overleftrightarrow{\boldsymbol{T}}^{\dagger}\boldsymbol{\sigma}\overleftrightarrow{\boldsymbol{T}}$. As the rotation induced by $\overleftrightarrow{\boldsymbol{R}}$ is completely random in the three dimensions of Stokes space (as long as the fiber length is much longer than the birefringence correlation length), the vector $\boldsymbol{b}(z)$ can be modeled as a three-dimensional stochastic process whose first-order and second-order moments are given by [14]

$$\overline{\boldsymbol{b}(z)} = 0, \qquad \overline{\boldsymbol{b}(z_1)\boldsymbol{b}(z_2)} = \frac{1}{3}D_p^2\overleftrightarrow{\boldsymbol{I}}\delta(z_2 - z_1), \tag{8.16}$$

where $\overleftrightarrow{\boldsymbol{I}}$ is the second-order unit tensor and $D_p$ is the PMD parameter of the fiber [1, 5].

## References


[1] C. D. Poole, in *Optical Fiber Telecommunications III A*, I. P. Kaminow and T. L. Koch, eds. (Academic, San Diego, 1997), Chap. 6.

[2] A. Galtarossa, L. Palmieri, M. Schiano, and T. Tambosso, Opt. Lett. **25**, 384 (2000); **26**, 962 (2001).

[3] A. Galtarossa and L. Palmieri, J. Lightwave Technol. **22**, 1103 (2004).

[4] B. Huttner, C. Geiser, and N. Gisin, IEEE J. Sel. Top. Quan. Electron. **6**, 317 (2000).

[5] H. Kogelnik, R. Jopson, and L. Nelson, in *Optical Fiber Telecommunications IV B*, I. P. Kaminow and T. L. Koch, eds. (Academic, San Diego, 2002), Chap. 15.

[6] J. P. Gordon and H. Kogelnik, Proc. Natl. Acad. Sci. USA **97**, 4541 (2000).

[7] C. Xie, M. Karlsson, P. A. Andrekson, H. Sunnerud, and J. Li, IEEE J. Sel. Top. Quan. Electron. **8**, 575 (2002).

[8] H. Sunnerud, M. Karlsson, C. Xie, P. A. Andrekson, J. Lightwave Technol. **20**, 2204 (2002).

[9] H. Kogelnik, L. E. Nelson, J. P. Gordon, J. Lightwave Technol. **21**, 482 (2003).

[10] A. E. Willner, S. M. R. Motaghian, L. S. Yan, Z. Q. Pan, M. C. Hauer, J. Lightwave Technol. **22**, 106 (2004).

[11] D. A. Nolan, X. Chen, and M. Li, J. Lightwave Technol. **22**, 1066 (2004).

[12] R. Noé, D. Sandel, and V. Mirvoda, IEEE J. Sel. Top. Quan. Electron. **10**, 341 (2004).

[13] P. K. A. Wai and C. R. Menyuk, J. Lightwave Technol. **14**, 148 (1996).

[14] C. W. Gardiner, *Handbook of Stochastic Methods*, $2^{nd}$ ed. (Springer, New York, 1985).

# 9 PMD and Stimulated Raman Scattering

In this chapter, we develop a vector theory of the stimulated Raman scattering process for describing the polarization effects in fiber-based Raman amplifiers [1]-[3]. We use this theory to show that polarization-mode dispersion (PMD) induces large fluctuations in the amplified signal. It is found that PMD-induced fluctuations follow a log-normal distribution. We also discuss the random nature of the polarization-dependent gain (PDG) in Raman amplifiers. Using the concept of a PDG vector, we find the probability distribution of PDG in an analytic form and use it to show that both the mean and standard deviation of PDG depend on the PMD parameter inversely when the effective fiber length is much larger than the PMD diffusion length. We apply our theory to study how PDG can be reduced by scrambling pump polarization randomly and show that the mean value of PDG is directly proportional to the degree of pump polarization.

## 9.1 Introduction

The Raman effect, first observed in 1928 [4], has attracted considerable attention since 1962 when the phenomenon of stimulated Raman scattering (SRS) was discovered [5]. SRS was first observed in silica fibers in 1972 [6] and by 1981 it was used to make fiber-based Raman amplifiers capable of providing more than 30-dB gain [7]. Such Raman amplifiers have attracted considerable attention recently [8]–[10] because of their potential for providing a relatively flat gain over a wide bandwidth. The theoretical treatment of Raman amplifiers is often based on a scalar approach [9] even though the Raman gain is known to be polarization dependent [11]-[16]. A scalar approach can be justified if the polarization states of the pump and the signal fields do not change along the fiber. This is, however, not the case in most fibers in which birefringence fluctuations lead to randomization of the state of polarization (SOP) of any optical field. This effect is known as polarization-mode dispersion (PMD) and has been studied extensively in recent years [17]–[20]. Although the effects of PMD on Raman amplification have been observed experimentally [13]–[16], a vector theory of the SRS process has not yet been fully developed.

In this Chapter, we develop a vector theory of Raman amplification capable of including the PMD-induced random evolution of the pump and signal polarization states [1, 2]. We use this theory to show that the amplified signal fluctuates over a wide range because of PMD, and the average gain is significantly lower than that expected in the absence of PMD. Based on this theory, we find the statistics of polarization-dependent gain (PDG) and its relationship with the operating parameters of Raman amplifiers. The chapter is organized as follows. In Section 9.2 we develop the basic theory using the Stokes-vector formalism and discuss the simplifying approximations made for obtaining the analytical results. The average value of the amplified signal and the variance of its PMD-induced fluctuations are discussed in Section 9.3. The probability density of signal fluctuations is shown to be a log-normal distribution in Section 9.4. In Section 9.5, we consider the statistics of PDG and show that both the average and RMS values of PDG can be found in an analytic form. We apply in Section 9.6 the vector theory to the case in which pump polarization is scrambled randomly to reduce the impact of PMD effects. The main results are summarized in Section 9.7.

## 9.2 Vector Theory for SRS

In a Raman amplifier, the pump and signal waves propagate simultaneously, and the total field is given by

$$|A(z,t)\rangle = |A_p(z)\rangle \exp(-i\omega_p t) + |A_s(z)\rangle \exp(-i\omega_s t), \tag{9.1}$$

where we have assumed the pump and signal fields are both in the form of continuous waves (CW) oscillating at frequencies $\omega_p$ and $\omega_s$, respectively. Substituting Eq. (9.1) into Eq. (8.14) and decomposing into individual frequency components, we obtain the dynamic equations governing the pump and signal fields along the fiber. For convenience, we set the carrier frequency $\omega_0 = \omega_p$ [see Eq. (8.14)], and the governing equation becomes

$$\begin{aligned}
\xi \frac{d|A_j\rangle}{dz} &= \left(i\beta_j - \frac{\alpha_j}{2}\right)|A_j\rangle - \frac{i}{2}\Omega_{jp}\boldsymbol{b}\cdot\boldsymbol{\sigma}|A_j\rangle + i\gamma_j\left[\frac{8f_E}{9} + f_R\widetilde{R}_a(0) + \frac{5f_R}{6}\widetilde{R}_b(0)\right]\langle A_j|A_j\rangle|A_j\rangle \\
&+ i\gamma_j\left[\frac{8f_E}{9} + f_R\widetilde{R}_a(0) + \frac{f_R}{6}\widetilde{R}_b(0) + \frac{2f_R}{3}\widetilde{R}_b(\Omega_{jm})\right]\langle A_m|A_m\rangle|A_j\rangle \\
&+ i\gamma_j\left[\frac{8f_E}{9} + \frac{2f_R}{3}\widetilde{R}_b(0) + f_R\widetilde{R}_a(\Omega_{jm}) + \frac{f_R}{6}\widetilde{R}_b(\Omega_{jm})\right]\langle A_m|A_j\rangle|A_m\rangle,
\end{aligned} \tag{9.2}$$

where $j,\ m = p$ or $s$ $(m \neq j)$, $\Omega_{jm} = \omega_j - \omega_m$, and $\beta_j$ and $\alpha_j$ account for propagation constants and fiber losses at $\omega_j$. The PMD effects in Eq. (9.2) are governed by the birefringence vector $\boldsymbol{b}$ [23]. We have included the propagation direction through $\xi$: $\xi = \pm 1$ depending on the pumping configuration. In the following analysis, we assume the signal propagates forward but the pump can propagate forward ($\xi = 1$) or backward ($\xi = -1$), depending on the pumping configuration. The nonlinear parameters are given by $\gamma_j = \omega_j n_2/(ca_{\text{eff}})$.

Equation (9.2) looks complicated in the Jones-matrix formalism. It can be simplified considerably by writing it in the Stokes space [17]. After introducing the Stokes vectors for the pump and signal as

$$\boldsymbol{P} = \langle A_p|\boldsymbol{\sigma}|A_p\rangle \equiv P_1\hat{\boldsymbol{e}}_1 + P_2\hat{\boldsymbol{e}}_2 + P_3\hat{\boldsymbol{e}}_3, \tag{9.3}$$

$$\boldsymbol{S} = \langle A_s|\boldsymbol{\sigma}|A_s\rangle \equiv S_1\hat{\boldsymbol{e}}_1 + S_2\hat{\boldsymbol{e}}_2 + S_3\hat{\boldsymbol{e}}_3, \tag{9.4}$$

and using the relations in Eqs. (8.11) and (8.12), we obtain the following two vector equations governing the dynamics of $\boldsymbol{P}$ and $\boldsymbol{S}$ in the Stokes space:

$$\xi\frac{d\boldsymbol{P}}{dz} = -\alpha_p\boldsymbol{P} - \frac{\omega_p}{2\omega_s}g_a\left[(1+3\mu)S_0\boldsymbol{P} + (1+\mu/3)P_0\boldsymbol{S}\right] - \varepsilon_{ps}\boldsymbol{S}\times\boldsymbol{P}, \tag{9.5}$$

$$\frac{d\boldsymbol{S}}{dz} = -\alpha_s\boldsymbol{S} + \frac{g_a}{2}\left[(1+3\mu)P_0\boldsymbol{S} + (1+\mu/3)S_0\boldsymbol{P}\right] - (\Omega_R\boldsymbol{b} + \varepsilon_{sp}\boldsymbol{P})\times\boldsymbol{S}, \tag{9.6}$$

where $\Omega_R = \xi\omega_p - \omega_s$, $\mu = g_b/(2g_a)$, $g_a$ and $g_b$ are Raman gain associated with the isotropic and anisotropic Raman response, respectively, and $\varepsilon_{jm}$ provides the magnitude of XPM-induced nonlinear polarization rotation (NPR). They are given by

$$g_a = 2\gamma_s\text{Im}[\widetilde{R}_a(\Omega_{ps})], \qquad g_b = 2\gamma_s\text{Im}[\widetilde{R}_b(\Omega_{ps})], \tag{9.7}$$

$$\varepsilon_{jm} = \gamma_j\{8f_E/9 + 2f_R\widetilde{R}_b(0)/3 + f_R\text{Re}[\widetilde{R}_a(\Omega_{jm}) + \widetilde{R}_b(\Omega_{jm})/6]\}. \tag{9.8}$$

Equations (9.5) and (9.6) describe SRS under quite general conditions. We make two further simplifications in the following analysis. We neglect both the pump depletion and the signal-induced XPM on the pump because the pump power is much larger than the signal power in practice. The pump equation (9.5) then contains only the loss term and can be easily integrated. The effect of fiber losses is to reduce the magnitude of $\boldsymbol{P}$ but the direction of $\boldsymbol{P}$ remains fixed in the rotating frame.

Equation (9.6) shows clearly that the Raman gain is polarization dependent. The gain coefficient varies from $g_a(1+5\mu/3)$ to $4\mu g_a/3$, depending on the angle between the Stokes vectors of the pump and the signal. Random variations in the fiber birefringence change the relative orientation between $\boldsymbol{S}$ and $\boldsymbol{P}$ and produce random changes in the Raman gain. However, the last term $\varepsilon_{sp}\boldsymbol{P}\times\boldsymbol{S}$ in Eq. (9.6) accounts for the XPM-induced NPR and does not affect the Raman gain because of its deterministic nature. We can eliminate this term by making a further transformation

$$\boldsymbol{V} = \exp\left\{-\varepsilon_{sp}\left[\int_0^z P_0(z)dz\right]\hat{\boldsymbol{p}}\times\right\}\boldsymbol{V}', \tag{9.9}$$

where $\hat{\boldsymbol{p}}$ represents the unit vector on the Poincaré sphere in the direction of $\boldsymbol{P}$ and $\boldsymbol{V}$ is an arbitrary vector in the Stokes space. After doing so, Eq. (9.6) reduces to

$$\frac{d\boldsymbol{S}}{dz} = -\alpha_s \boldsymbol{S} + \frac{g_a}{2}[(1+3\mu)P_0\boldsymbol{S} + (1+\mu/3)S_0\boldsymbol{P}] - \Omega_R \boldsymbol{b}' \times \boldsymbol{S}, \tag{9.10}$$

where $\boldsymbol{b}'$ is related to $\boldsymbol{b}$ in Eq. (9.6) by a deterministic rotation. From now on, we will drop the prime notation. As optical fibers used for Raman amplification are much longer than the birefringence correlation length, $\boldsymbol{b}(z)$ can be modelled as a three-dimensional stochastic process whose first-order and second-order moments are given by Eq. (8.16). As discussed in Appendix B, we should treat all stochastic differential equations in the Stratonovich sense [25].

Equation (9.10) can be further simplified by noting that the first two terms on its right side do not change the direction of $\boldsymbol{S}$ and can be removed by a suitable transformation. Making the final transformation as

$$\boldsymbol{S} = \boldsymbol{s} \exp\left\{ \int_0^z \left[ \frac{g_a}{2}(1+3\mu)P_0(z) - \alpha_s \right] dz \right\}, \tag{9.11}$$

the dynamic equations governing the power and the SOP of the signal are given by

$$\frac{ds_0}{dz} = \frac{g_R}{2} P_0(z) \hat{\boldsymbol{p}} \cdot \boldsymbol{s}, \tag{9.12}$$

$$\frac{d\boldsymbol{s}}{dz} = \frac{g_R}{2} P_0(z) s_0 \hat{\boldsymbol{p}} - \Omega_R \boldsymbol{b} \times \boldsymbol{s}, \tag{9.13}$$

where $g_R \equiv g_a(1+\mu/3)$, $s_0 = |\boldsymbol{s}|$, and $\hat{\boldsymbol{p}}$ is the input SOP of the pump.

Equations (9.12) and (9.13) apply for both the forward and backward pumping schemes, but the $z$ dependence of $P_0(z)$ and the magnitude of $\Omega_R$ depend on the pumping configuration. More specifically, $P_0(z) = P_{\text{in}} \exp(-\alpha_p z)$ and $\Omega_R = \omega_p - \omega_s$ in the case of forward pumping but $P_0(z) = P_{\text{in}} \exp[-\alpha_p(L-z)]$ and $\Omega_R = -(\omega_p + \omega_s)$ in the case of backward pumping, where $P_{\text{in}}$ is the input pump power. In the absence of birefringence ($\boldsymbol{b} = 0$), $\boldsymbol{s}$ remains oriented along $\hat{\boldsymbol{p}}$, and we recover the scalar case.

## 9.3 Average Raman Gain and Output Signal Fluctuations

Equations (9.12) and (9.13) can be used to calculate the power $S_0$ of the amplified signal as well its SOP at any distance within the amplifier. When the birefringence vector $\boldsymbol{b}$ is $z$ dependent, the solution depends on how $\boldsymbol{b}(z)$ changes. In the case of PMD, $\boldsymbol{b}(z)$ fluctuates with time. As a result, the amplified signal $S_0(L)$ at the output of an amplifier of length $L$ also fluctuates. Such fluctuations would affect the performance of any lightwave system making use of Raman amplification. In this section we calculate the average and the variance of such PMD-induced fluctuations. We focus on the forward-pumping case for definiteness. All results can be converted to the case of backward pumping by replacing $\alpha_p$ with $-\alpha_p$, $P_{\text{in}}$ with $P_{\text{in}}\exp(-\alpha_p L)$, and $\Omega_R = \omega_p - \omega_s$ with $\Omega_R = -(\omega_p + \omega_s)$.

It is useful to introduce the instantaneous amplifier gain $G$ defined as $G = S_0(L)/S_0(0)$. We use the vector theory to find the average Raman gain $G_{av}$ and the signal variance $\sigma_s^2$ by using the definitions

$$G_{av} = \frac{\langle S_0(L)\rangle}{S_0(0)}, \qquad \sigma_s^2 = \frac{\langle S_0^2(L)\rangle}{\langle S_0(L)\rangle^2} - 1. \tag{9.14}$$

To calculate the average signal power $\langle S_0(L)\rangle$ at the end of a Raman amplifier of length $L$, we need to average Eqs. (9.12) and (9.13) using a well-known technique discussed in Ref. [25]. Appendix B provides the details of the averaging procedure. The final result leads to the following two coupled but deterministic equations:

$$\frac{d\langle s_0\rangle}{dz} = \frac{g_R}{2}P_0(z)\langle s_0\cos\theta\rangle, \tag{9.15}$$

$$\frac{d\langle s_0\cos\theta\rangle}{dz} = \frac{g_R}{2}P_0(z)\langle s_0\rangle - \eta\langle s_0\cos\theta\rangle, \tag{9.16}$$

where $\eta = 1/L_d = D_p^2\Omega_R^2/3$, $L_d$ is the PMD diffusion length, and $\theta$ is the angle between $\boldsymbol{P}$ and $\boldsymbol{S}$.

Equations (9.15) and (9.16) are two linear first-order differential equations that can be easily integrated. When PMD effects are quite large, the diffusion length $L_d$ becomes so small that $\langle S_0\cos\theta\rangle$ reduces to zero over a short fiber length $\sim L_d$. The average gain is then given by (in dB)

$$G_{av} = a[g_a(1+3\mu)P_{\text{in}}L_{\text{eff}}/2 - \alpha_s L], \tag{9.17}$$

where $a = 10/\ln 10 \approx 4.343$ and the effective amplifier length $L_{\text{eff}} = [1-\exp(-\alpha_p L)]/\alpha_p$ is $< L$ because of pump losses. In this case, the PMD reduces the Raman gain coefficient to $g_a(1+3\mu)/2$, exactly the average of the copolarized $[g_a(1+5\mu/3)]$ and orthogonally-polarized $(4\mu g_a/3)$ Raman gain coefficients [11]. If pump losses can be neglected ($\alpha_p = 0$), Eqs. (9.15) and (9.16) can be integrated analytically because $P_0$ becomes $z$ independent. The average gain in this special case is given by

$$G_{av} = [\cosh(\kappa L/2) + \sinh(\kappa L/2)\,(g_R P_{\text{in}}\cos\theta_0 + \eta)\,/\kappa]\exp\{[g_a(1+3\mu)P_{\text{in}} - \eta - 2\alpha_s]L/2\}, \tag{9.18}$$

where $\theta_0$ is the initial angle between $\boldsymbol{S}$ and $\boldsymbol{P}$ and $\kappa = \left[(g_R P_{\text{in}})^2 + \eta^2\right]^{1/2}$.

The variance of signal fluctuations requires the second-order moment $\langle S_0^2(L)\rangle$ of the amplified signal. Following the averaging procedure discussed in Appendix B, Eqs. (9.12) and (9.13) lead to the following set of three linear equations [25]:

$$\frac{d\langle s_0^2\rangle}{dz} = g_R P_0(z)\langle s_0^2\cos\theta\rangle, \tag{9.19}$$

$$\frac{d\langle s_0^2\cos\theta\rangle}{dz} = -\eta\langle s_0^2\cos\theta\rangle + \frac{g_R}{2}P_0(z)[\langle s_0^2\rangle + \langle s_0^2\cos^2\theta\rangle], \tag{9.20}$$

$$\frac{d\langle s_0^2\cos^2\theta\rangle}{dz} = -3\eta\langle s_0^2\cos^2\theta\rangle + \eta\langle s_0^2\rangle + g_R P_0(z)\langle s_0^2\cos\theta\rangle. \tag{9.21}$$

These equations show that signal fluctuations have their origin in fluctuations of the angle $\theta$ between the pump and signal's Stokes vectors. The SRS process amplifies the copolarized signal component with the pump but keeps the orthogonally-polarized one almost unchanged. Because of this imbalance, SRS rotates $\boldsymbol{S}$ toward $\boldsymbol{P}$ as dictated by Eq. (9.13). However, PMD scatters the signal SOP away from the pump. If PMD is relatively large, $\theta$ changes so fast that the signal only experiences an average local gain everywhere, and the accumulative fluctuations of the output signal are small. Also, if PMD is negligible, $\theta$ changes almost deterministically, and the signal fluctuations are again small. However, when the effective fiber length is comparable to the PMD diffusion length, the signal experiences random gain from section to section, resulting in large signal fluctuations.

To illustrate the impact of PMD on the performance of Raman amplifiers, we focus on a 10-km-long amplifier pumped with 1 W of power using a 1.45-$\mu$m laser. The 1.55-$\mu$m signal is assumed to be located at the Raman gain peak ($\Omega_R/2\pi = 13.2$ THz). The Raman gain coefficients have values $g_a = 0.60$ W$^{-1}$/km and $g_b/2 = 0.0071$W$^{-1}$/km [8, 12]. Fiber losses are taken to be 0.273 dB/km and 0.2 dB/km at the pump and signal wavelengths, respectively. Figure 9.1 shows how the average gain and $\sigma_s$ change with the PMD parameter $D_p$ when the input signal is copolarized (solid curves) or orthogonally-polarized (dashed curves) to the pump. The curves are shown for both the forward and backward pumping schemes. When $D_p$ is zero, the two beams maintain their SOPs, and the copolarized signal experiences a maximum gain of 17.6 dB but the orthogonally-polarized one has a 1.7-dB loss, irrespective of the pumping configuration. The loss is not exactly 2 dB because a small gain exists for the orthogonally-polarized input signal ($2ag_bP_{\text{in}}L_{\text{eff}}/3$). As PMD increases, the gain difference between the copolarized and orthogonally-polarized cases decreases and disappears eventually.

The level of signal fluctuations in Fig. 9.1 increases quickly with the PMD parameter, reaches a peak, and then decreases slowly to zero with further increase in $D_p$. The location of the peak depends on the pumping scheme as well as on the initial polarization of pump. The noise level can exceed 20% for $D_p = 0.05$ ps/$\sqrt{\text{km}}$ in the case of forward pumping. If a fiber with low PMD is used, the noise level can exceed 70% under some conditions. These results suggest that forward-pumped Raman amplifiers will perform better if a fiber with $D_p > 0.1$ ps/$\sqrt{\text{km}}$ is used. The curves for backward pumping are similar to those for forward pumping but shift to smaller $D_p$ values and have a higher peak. In spite of an enhanced peak, the backward pumping produces least fluctuations for all fibers for which $D_p > 0.01$ ps/$\sqrt{\text{km}}$.

Note in Fig. 9.1 that the curves in the case of backward pumping are nearly identical to those for forward pumping except that they are shifted to left. As a result, the solid and dashed curves merge at a value of $D_p$ that is smaller by about a factor of 30. This difference is related to the definition of $\Omega_R = \xi\omega_p - \omega_s$ in Eq. (9.13). In the case of backward pumping, $|\Omega_R| = \omega_p + \omega_s$ is about 30 times larger than the value of $\Omega_R = \omega_p - \omega_s$ in the forward-pumping case.

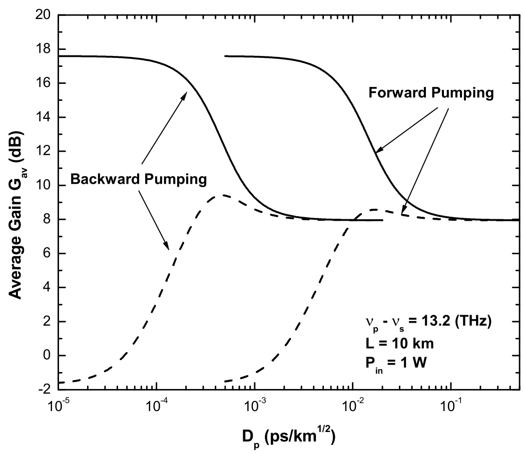


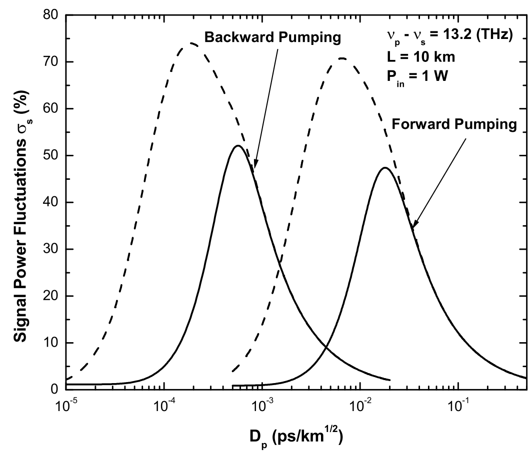


Figure 9.1: (a) Average gain and (b) standard deviation of signal fluctuations at the output of a Raman amplifier as a function of PMD parameter in the cases of forward and backward pumping. The solid and dashed curves correspond to the cases of copolarized and orthogonally-polarized signal, respectively.

In practice, fibers used to make a Raman amplifier have a constant value of $D_p$. Figure 9.2 shows the average Raman gain and $\sigma_s$ as a function of amplifier length for a fiber with $D_p = 0.05$ ps$/\sqrt{\text{km}}$. All other parameters are the same as in Fig. 9.1. The solid and dashed lines correspond to copolarized and orthogonally polarized cases, respectively (the two lines are indistinguishable in the case of backward pumping). Physically, it takes some distance for the orthogonally polarized signal to adjust its SOP through PMD before it can experience the full Raman gain. Within the PMD diffusion length (around 175 m in this case of forward pumping), fiber loss dominates and the signal power decreases; beyond the diffusion length, Raman gain dominates and the signal power increases. The gain difference seen in Fig. 9.1 between the copolarized and orthogonally-polarized cases comes from this initial difference. In the case of backward pumping, The PMD diffusion length becomes so small (about 0.2 m) that this difference completely disappears. The level of signal fluctuations depends strongly on the relative directions of pump and signal propagation. In the case of forward pumping, $\sigma_s$ grows monotonically with the distance, reaching 24% at the end of the 10-km fiber. In contrast, $\sigma_s$ is only 0.8 % even for a 10-km long amplifier in the case of backward pumping, a value 30 times smaller than that occurring in the forward-pumping case. The curves are almost identical for all input signal SOPs when $D_p = 0.05\text{ps}/\sqrt{\text{km}}$.

So far, we assumed that the signal wavelength coincided with the Raman-gain peak. Figure 9.3 shows the effect of pump-signal detuning for a 10-km long amplifier under the same conditions. The frequency dependence of Raman gain coefficients was taken from Ref. [8, 12]. In the case of forward pumping, the average Raman gain is different for copolarized (solid curve) and orthogonally polarized (dashed curve) signals, and the difference is larger when the signal frequency is close to the pump. However,

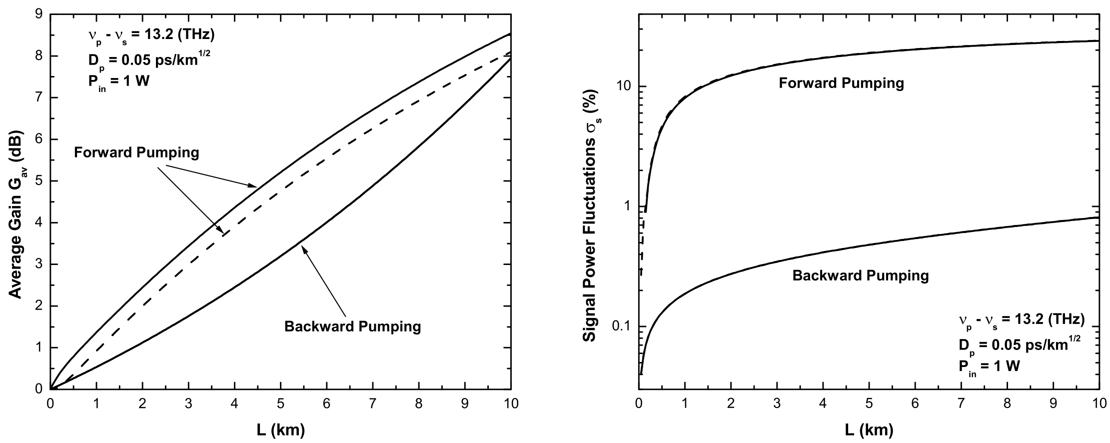


Figure 9.2: (a) Average gain and (b) level of signal fluctuations as a function of amplifier length for a fiber with $D_p = 0.05$ ps$/\sqrt{\text{km}}$. The solid and dashed curves correspond to the cases of copolarized and orthogonally-polarized signal, respectively. The two curves nearly coincide in the case of backward pumping.

the difference disappears when the signal frequency deviates more than 15 THz from the pump because of increased PMD effects. In the case of backward pumping, PMD effects are so huge over the whole spectrum that the differences disappear completely, and the same spectrum (thin line) is obtained for all input SOPs of the signal. Signal fluctuations depend on the PMD parameter as well as on the Raman gain. The lager the gain, the larger the fluctuations. For this reason, $\sigma_s$ is maximum at the Raman gain peak. Again, fluctuations in the case of backward pumping are 30 times smaller than those in the case of forward pumping because of the ratio $(\omega_p + \omega_s)/(\omega_p - \omega_s) \approx 30$.

## 9.4 Probability Distribution of the Amplified Signal

The moment method used in Section 9.3 to obtain the average and variance of the amplified signal becomes increasingly complex for higher-order moments. It will be much better if we can determine the probability distribution of the amplified signal because it contains, by definition, all the statistical information. To this end, we begin by finding the instantaneous gain of the Raman amplifier.

The fluctuating amplifier gain $G(L)$ for a Raman amplifier of length $L$ can be found from Eq. (9.11)–(9.13) as (in dB)

$$G_{\text{dB}} = a \ln\left[\frac{S_0(L)}{S_0(0)}\right] = a\left[\frac{g_a}{2}(1+3\mu)P_{\text{in}}L_{\text{eff}} - \alpha_s L\right] + \frac{a}{2} g_R \int_0^L P_0(z)\,[\hat{\boldsymbol{p}}(z)\cdot\hat{\boldsymbol{s}}(z)]\,dz, \qquad (9.22)$$

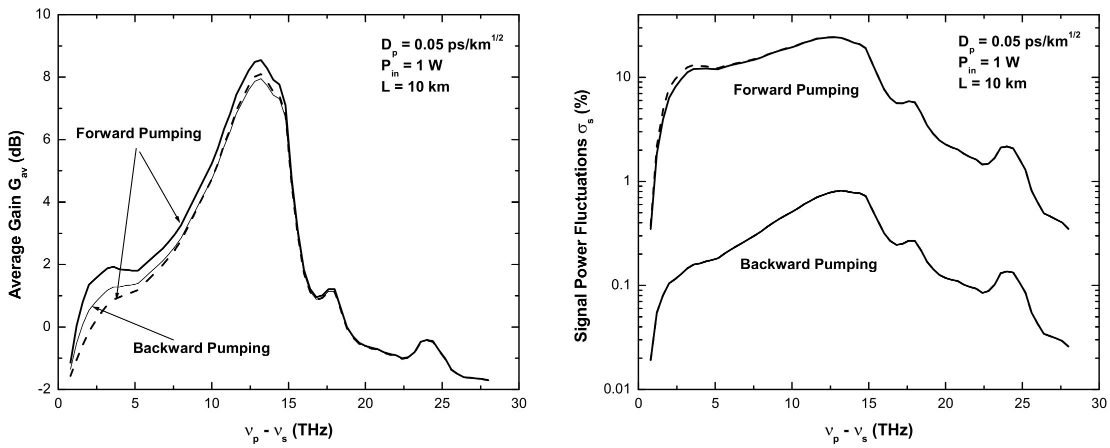


Figure 9.3: (a) Average gain and (b) level of signal fluctuations plotted as a function of pump-signal detuning. The solid and dashed curves correspond to copolarized and orthogonally polarized cases, respectively. The thin solid curve is for a backward-pumped Raman amplifier and does not change much with signal polarization.

where $a = 10/\ln(10) = 4.343$ and $\hat{\boldsymbol{s}}$ is the unit vector in the direction of $\boldsymbol{s}$. Using $\boldsymbol{s} = s_0\hat{\boldsymbol{s}}$ in Eq. (9.13), $\hat{\boldsymbol{s}}$ is found to satisfy

$$\frac{d\hat{\boldsymbol{s}}}{dz} = \frac{g_R}{2} P_0(z)\,[\hat{\boldsymbol{p}} - (\hat{\boldsymbol{p}}\cdot\hat{\boldsymbol{s}})\,\hat{\boldsymbol{s}}] - \Omega_R \boldsymbol{b}\times\hat{\boldsymbol{s}}. \tag{9.23}$$

In this equation $\hat{\boldsymbol{p}}$ represents the pump polarization at the input end. Thus, $\hat{\boldsymbol{s}}$ becomes random only because of birefringence fluctuations. If polarization scrambling is used to randomize $\hat{\boldsymbol{p}}$, $\hat{\boldsymbol{p}}$ and $\hat{\boldsymbol{s}}$ both become random (see Section 9.6). However, it is only the scalar product $\hat{\boldsymbol{p}}\cdot\hat{\boldsymbol{s}} \equiv \cos\theta$ that determines $G_{\text{dB}}$.

To find the probability distribution of $G_{\text{dB}}$, we note that the second term in Eq. (9.22) can be written as $\sum_{i=1}^{N} P_0(z_i)\cos[\theta(z_i)]\Delta z$ if we divide the fiber length $L$ into $N$ segments of length $\Delta z$. Thus the random variable $G_{\text{dB}}$ is formed from a sum of many random variables with identical statistics. According to the central limit theorem [25], the probability density of $G(L)$ should be Gaussian as long as the correlation between $\cos[\theta(z)]$ and $\cos[\theta(z')]$ goes to zero sufficiently rapidly as $|z-z'|$ increases, no matter what the statistics of $\hat{\boldsymbol{p}}(z)$ and $\hat{\boldsymbol{s}}(z)$ are. In practice, we expect this correlation to decay exponentially over a length of PMD diffusion length $L_d$. For fiber lengths $L \gg L_d$, we thus expect $G_{\text{dB}}$ to have a Gaussian distribution. Such a Gaussian distribution of $G_{\text{dB}}$ has been observed experimentally in Ref. [26]. Our vector theory explains this experimental result in a simple way.

It is clear from Eq. (9.22) that $\ln[S_0(L)]$ will also follow a Gaussian distribution. As a result, the probability distribution of the amplified signal power, $S_0(L)$, at the amplifier output corresponds to a

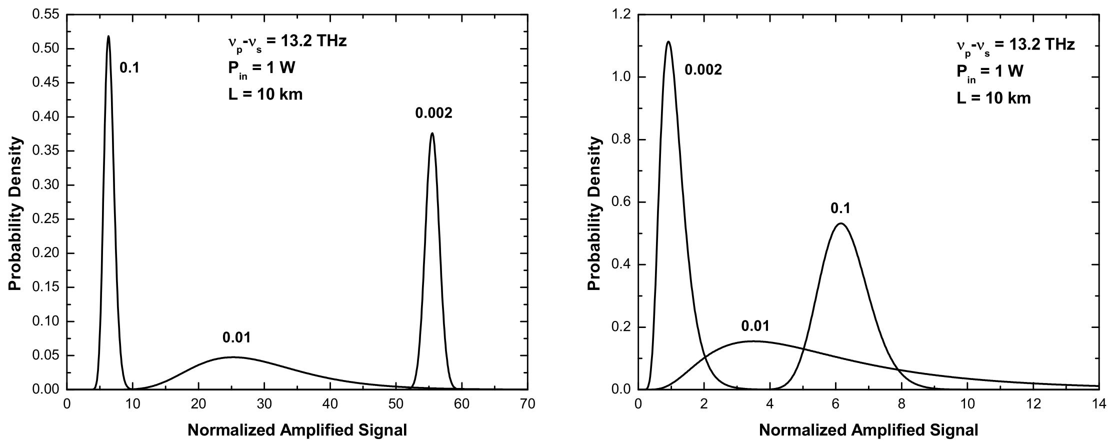


Figure 9.4: Probability density of amplified signal for three values of $D_p$ (in units of $D_p$ is ps/$\sqrt{\text{km}}$) in the cases of (a) copolarized and (b) orthogonally polarized signals. The amplified signal is normalized to the input signal power.

*lognormal distribution* [27] and can be written as

$$p[S_0(L)] = \frac{[\ln(\sigma_s^2+1)]^{-1/2}}{S_0(L)\sqrt{2\pi}} \exp\left[-\frac{1}{2\ln(\sigma_s^2+1)} \ln^2\left(\frac{S_0(L)\sqrt{\sigma_s^2+1}}{\langle S_0(L)\rangle}\right)\right], \tag{9.24}$$

where $\sigma_s^2$ is defined in Eq. (9.14) and can be calculated explicitly as discussed in the last section.

Figures 9.4 shows how the probability density changes with the PMD parameter in the cases of copolarized and orthogonally polarized input signals, respectively, under the conditions of Fig. 9.1. When the PMD effects are relatively small, the two distributions are relatively narrow and are centered at quite different locations in the copolarized and orthogonally-polarized cases. When $D_p = 0.01$ ps/$\sqrt{\text{km}}$, the two distributions broaden considerably and begin to approach each other. For larger values of the PMD parameter $D_p = 0.1$ ps/$\sqrt{\text{km}}$, they become narrow again and their peaks almost overlap because the amplified signal becomes independent of the input SOP.

## 9.5 Polarization-Dependent Gain

Similar to the importance of the concept of differential group delay in describing the PMD effects on pulse propagation, the PMD effects in Raman amplifiers can be quantified using the concept of polarization-dependent gain (PDG), a quantity defined as the difference between the maximum and minimum values of $G$ while varying the SOP of the input signal. The gain difference $\Delta = G_{\max} - G_{\min}$ is itself random because both $G_{\max}$ and $G_{\min}$ are random. It is important to know the statistics of $\Delta$ and its relationship to the operating parameters of a Raman amplifier, because they can identify the conditions under which the PDG can be reduced to acceptable low levels. In this section, we introduce a PDG vector and use it to describe the statistics of PDG.

The polarization-dependent loss (PDL) is often described by introducing a PDL vector [28, 29]. The same technique can be used for the PDG in Raman amplifiers. The PDG vector $\boldsymbol{\Delta}$ is introduced in such a way that its magnitude gives the PDG value $\Delta$ (in dB) but its direction coincides with the direction of $\boldsymbol{S}(L)$ for which the gain is maximum. From Eq. (9.12) and (9.13), the dynamic equation for $\boldsymbol{\Delta}$ is found to be

$$\frac{d\boldsymbol{\Delta}}{dz} = \frac{g_R}{2}\Delta\coth\left(\frac{\Delta}{2a}\right)\left[\boldsymbol{P} - \left(\boldsymbol{P}\cdot\hat{\boldsymbol{\Delta}}\right)\hat{\boldsymbol{\Delta}}\right] + ag_R\left(\boldsymbol{P}\cdot\hat{\boldsymbol{\Delta}}\right)\hat{\boldsymbol{\Delta}} - \Omega_R\boldsymbol{b}\times\boldsymbol{\Delta}. \tag{9.25}$$

where $\hat{\boldsymbol{\Delta}}$ is the unit vector in the direction of $\boldsymbol{\Delta}$. Appendix C provides details of the derivation of this equation. If the PDG is not too large, $\Delta\coth(\Delta/2a)$ can be expanded in a Taylor series as

$$\Delta\coth\left(\frac{\Delta}{2a}\right) \approx 2a + \frac{\Delta^2}{6a}. \tag{9.26}$$

Keeping only the terms linear in $\Delta$, Eq. (9.25) reduces to the following linear Langevin equation

$$\frac{d\boldsymbol{\Delta}}{dz} = ag_R\boldsymbol{P} - \Omega_R\boldsymbol{b}\times\boldsymbol{\Delta}. \tag{9.27}$$

The validity of this linearized equation depends on the conditions under which the $\Delta^2$ term in Eq. (9.26) can be neglected. The validity condition can be written as $\Delta_{\max} \ll \sqrt{12}a \approx 15$ dB. This requirement is satisfied in practice for most Raman amplifiers.

Equation (9.27) can be readily solved because of its linear nature. The solution is given by

$$\boldsymbol{\Delta}(L) = ag_R\overleftrightarrow{\boldsymbol{R}}(L)\int_0^L \overleftrightarrow{\boldsymbol{R}}^{-1}(z)\boldsymbol{P}(z)dz, \tag{9.28}$$

where the PMD-induced rotation matrix $\overleftrightarrow{\boldsymbol{R}}(z)$ is obtained from $d\overleftrightarrow{\boldsymbol{R}}/dz = -\Omega_R\boldsymbol{b}\times\overleftrightarrow{\boldsymbol{R}}$. For fibers much longer than the birefringence correlation length, the dynamics of $\boldsymbol{\Delta}$ corresponds to that of the Brownian motion in three dimensions (see Ref. [30], where Eq. (9.28) is used for the PMD vector). As a result, $\boldsymbol{\Delta}$ follows a three-dimensional Gaussian distribution.

The moments of $\boldsymbol{\Delta}$ can be obtained from Eq. (9.27) using the same procedure used in the last section for calculating the average gain and signal fluctuations [25]. In Appendix D, we provide the details. As shown there, the first two moments and the covariance matrix $\overleftrightarrow{\boldsymbol{C}}$ defined as $\overleftrightarrow{\boldsymbol{C}} = \langle\boldsymbol{\Delta}\boldsymbol{\Delta}\rangle - \langle\boldsymbol{\Delta}\rangle\langle\boldsymbol{\Delta}\rangle$ satisfy

$$\frac{d\langle\Delta^2\rangle}{dz} = 2ag_RP_0(z)\hat{\boldsymbol{p}}\cdot\langle\boldsymbol{\Delta}\rangle, \tag{9.29}$$

$$\frac{d\langle\boldsymbol{\Delta}\rangle}{dz} = -\eta\langle\boldsymbol{\Delta}\rangle + ag_RP_0(z)\hat{\boldsymbol{p}}, \tag{9.30}$$

$$\frac{d\overleftrightarrow{\boldsymbol{C}}}{dz} = -3\eta\overleftrightarrow{\boldsymbol{C}} + \eta[\langle\Delta^2\rangle\overleftrightarrow{\boldsymbol{I}} - \langle\boldsymbol{\Delta}\rangle\langle\boldsymbol{\Delta}\rangle]. \tag{9.31}$$

Equations (9.29) and (9.30) can be easily integrated over the fiber length $L$. They provide the following analytical results in the case of forward pumping:

$$\langle \boldsymbol{\Delta} \rangle = \frac{a g_R P_{\rm in} \hat{\boldsymbol{p}}}{\eta - \alpha_p}[1 - \alpha_p L_{\rm eff} - \exp(-\eta L)], \tag{9.32}$$

$$\langle \Delta^2 \rangle = \frac{2(a g_R P_{\rm in})^2}{\eta^2 - \alpha_p^2}[(1 - \alpha_p L_{\rm eff})\exp(-\eta L) - 1 + (\alpha_p + \eta) L_{\rm eff}(1 - \alpha_p L_{\rm eff}/2)]. \tag{9.33}$$

In the case of backward pumping, $\langle \boldsymbol{\Delta} \rangle$ and $\langle \Delta^2 \rangle$ are also given by these equations provided $\alpha_p$ is replaced with $-\alpha_p$, $P_{\rm in}$ is replaced with $P_{\rm in}\exp(-\alpha_p L)$, $L_{\rm eff}$ is redefined as $[\exp(\alpha_p L) - 1]/\alpha_p$, and $\Omega_R = \omega_p - \omega_s$ in the expression of $\eta$ is replaced by $\Omega_R = -(\omega_p + \omega_s)$. An analytical expression for $\overleftrightarrow{C}$ can also be obtained by integrating Eq. (9.31).

We now consider the probability distribution of the PDG vector. It is convenient to choose $\hat{\boldsymbol{p}}$ along an axis of the Stoke space, say $\hat{\boldsymbol{p}} = \hat{e}_1$, because the matrix $\overleftrightarrow{C}$ is then diagonal. The probability density function of $\boldsymbol{\Delta} \equiv \Delta_1 \hat{e}_1 + \Delta_2 \hat{e}_2 + \Delta_3 \hat{e}_3$ in this case can be written as

$$p(\boldsymbol{\Delta}) = \frac{(2\pi)^{-3/2}}{\sigma_\parallel \sigma_\perp^2} \exp\left[-\frac{(\Delta_1 - \Delta_0)^2}{2\sigma_\parallel^2} - \frac{\Delta_2^2 + \Delta_3^2}{2\sigma_\perp^2}\right], \tag{9.34}$$

where $\Delta_0 = |\langle \boldsymbol{\Delta} \rangle|$ while $\sigma_\parallel^2$ and $\sigma_\perp^2$ are the variances of the PDG vector in the parallel and perpendicular direction of $\hat{\boldsymbol{p}}$, respectively. Both of them can be found from Eq. (9.31) in an analytical form as

$$\sigma_\parallel^2 = \eta \int_0^L [\langle \Delta^2 \rangle - \langle \boldsymbol{\Delta} \rangle^2] \exp[-3\eta(L - z)] dz, \tag{9.35}$$

$$\sigma_\perp^2 = \eta \int_0^L \langle \Delta^2 \rangle \exp[-3\eta(L - z)] dz. \tag{9.36}$$

These equations show that $\sigma_\parallel < \sigma_\perp$ when PMD is small because the pump mostly amplifies the copolarized signal. When the effective fiber length $L_{\rm eff}$ is much larger than the PMD diffusion length $L_d$, $\langle \Delta^2 \rangle \gg \langle \boldsymbol{\Delta} \rangle^2 \approx 0$, and $\sigma_\parallel \approx \sigma_\perp$. In this case, $p(\boldsymbol{\Delta})$ becomes a uniform three-dimensional Gaussian distribution centered at zero.

In practice, one is often interested in the statistics of the PDG magnitude $\Delta$. Its probability density can be found from Eq. (9.34) after writing $\boldsymbol{\Delta}$ in spherical coordinates and integrating over the two angles. The result is found to be

$$p(\Delta) = \frac{\Delta}{2\sigma_\parallel \sigma} \exp\left[-\frac{\Delta^2(r-1) - r\Delta_0^2}{2\sigma^2}\right] \left\{ \mathrm{erf}\left[\frac{\Delta(\mathrm{r}-1) + \mathrm{r}\Delta_0}{\sqrt{2}\sigma}\right] + \mathrm{erf}\left[\frac{\Delta(\mathrm{r}-1) - \mathrm{r}\Delta_0}{\sqrt{2}\sigma}\right] \right\}, \tag{9.37}$$

where $\sigma^2 = \sigma_\perp^2(r-1)$, $r = \sigma_\perp^2/\sigma_\parallel^2$, and the error function is defined as $\mathrm{erf}(x) = \frac{2}{\sqrt{\pi}}\int_0^x e^{-y^2} dy$. Figure 9.5 shows how $p(\Delta)$ changes with $D_p$ in the case of forward pumping. All parameters are the same as in Fig. 9.1. The PDG values are normalized to the average gain $G_{av} = a g_a (1 + 3\mu) P_{\rm in} L_{\rm eff}/2$ (in dB) so that the curves are pump-power independent. In the limit $D_p \to 0$, $p(\Delta)$ becomes a delta function located

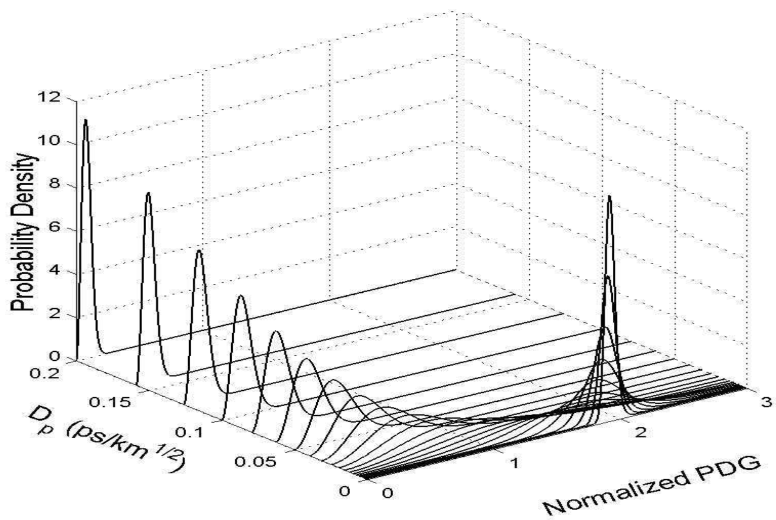


Figure 9.5: The probability distribution of PDG as a function of $D_p$ under conditions of Fig. 1. The PDG value is normalized to the average gain $G_{av}$.

at the maximum gain difference (almost $2G_{av}$) as little gain exists for the orthogonally-polarized signal. As $D_p$ increases, $p(\Delta)$ broadens quickly because PMD changes the signal SOP randomly. If $D_p$ is relatively small, the diffusion length $L_d$ is larger than or comparable to the effective fiber length $L_{\text{eff}}$, and $p(\Delta)$ remains centered at almost the same location but broadens because of large fluctuations. Its shape mimics a Gaussian distribution. When $D_p$ is large enough that $L_{\text{eff}} \gg L_d$, $p(\Delta)$ becomes Maxwellian and its peaks shifts to smaller values. This is the behavior observed experimentally in Ref. [15].

The mean value of PDG, $\langle\Delta\rangle$, and the variance of PDG fluctuations, $\sigma_\Delta^2 = \langle\Delta^2\rangle - \langle\Delta\rangle^2$, can be found using the PDG distribution in Eq. (9.37). Figure 9.6 shows how these two quantities vary with the PMD parameter for the same Raman amplifier used for Fig. 9.1. Both $\langle\Delta\rangle$ and $\sigma_\Delta$ are normalized to the average gain $G_{av}$. As expected, the mean PDG decreases monotonically as $D_p$ increases. The mean PDG $\langle\Delta\rangle$ is not exactly $2G_{av}$ when $D_p = 0$ because the gain is not zero when pump and signal are orthogonally-polarized. Note however that $\langle\Delta\rangle$ can be as large as 30% of the average gain for $D_p = 0.05$ ps/$\sqrt{\text{km}}$ in the case of forward pumping and it decreases slowly with $D_p$ after that, reaching a value of 8% for $D_p = 0.2$ ps/$\sqrt{\text{km}}$. This is precisely what was observed in Ref. [15] through experiments and numerical simulations. In the case of backward pumping, the behavior is nearly identical to that in the case of forward pumping except that the curve shifts to a value of $D_p$ smaller by about a factor of 30.

As seen in Fig. 9.6(b), the RMS value of PDG fluctuations increases rapidly as $D_p$ becomes nonzero, peaks to a value close to 56% of $G_{av}$ for $D_p$ near 0.01 ps/$\sqrt{\text{km}}$ in the case of forward pumping and then begins to decrease. Again, fluctuations can exceed 7% of the average gain level even for $D_p =$

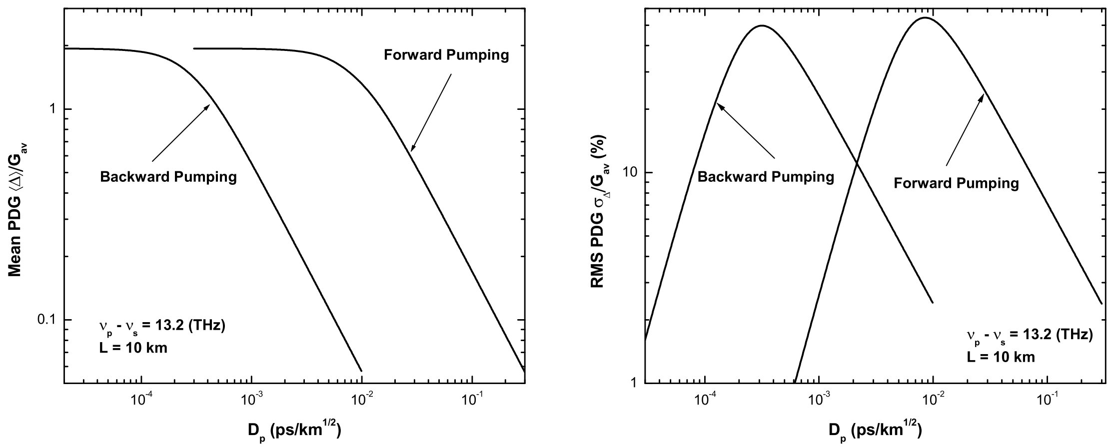


Figure 9.6: (a) Mean PDG and (b) variance $\sigma_\Delta$ (both normalized to the average gain $G_{av}$) as a function of PMD parameter under forward and backward pumping conditions.

0.1 ps/$\sqrt{\text{km}}$. A similar behavior holds for backward pumping, as seen in Fig. 9.6. Both the mean and the RMS values of PDG fluctuations decrease with $D_p$ inversely for $D_p > 0.03$ ps/$\sqrt{\text{km}}$ ($L_d < 0.5$ km for $\Omega_R/2\pi = 13.2$ THz). This $D_p^{-1}$ dependence agrees very well with the experimental results in Ref. [15].

The $D_p^{-1}$ dependence of $\langle\Delta\rangle$ and $\sigma_\Delta$ can be deduced analytically from Eq. (9.37) in the limit $L_{\text{eff}} \gg L_d$. In this limit, the PDG distribution $p(\Delta)$ becomes approximately Maxwellian and the average and RMS values of PDG in the case of forward pumping are given by

$$\langle\Delta\rangle \approx \frac{4ag_R P_{\text{in}}}{\sqrt{\pi} D_p |\Omega_R|} \sqrt{L_{\text{eff}}(1-\alpha_p L_{\text{eff}}/2)}. \tag{9.38}$$

$$\sigma_\Delta \approx \sqrt{(3\pi/8-1)}\langle\Delta\rangle. \tag{9.39}$$

The same equations hold in the case of backward pumping except that $|\Omega_R| = \omega_p - \omega_s$ should be replaced with $\omega_p + \omega_s$. Figure 9.7 shows the mean PDG and the RMS value of PDG as a function of propagation distance for a Raman amplifier with $D_p = 0.05$ ps/$\sqrt{\text{km}}$. All parameters are the same as in Fig. 9.2. Both $\langle\Delta\rangle$ and $\sigma_\Delta$ are negligibly small in the case of backward pumping, indicating the advantages of such a pumping scheme.

## 9.6 Polarization Scrambling of the Pump

The technique of polarization scrambling is sometimes used to reduce the PDG in Raman amplifiers [31, 32]. In this technique, the pump SOP is changed randomly as the signal is amplified so that the signal experiences different local gain in different parts of the fiber, resulting effectively in an average

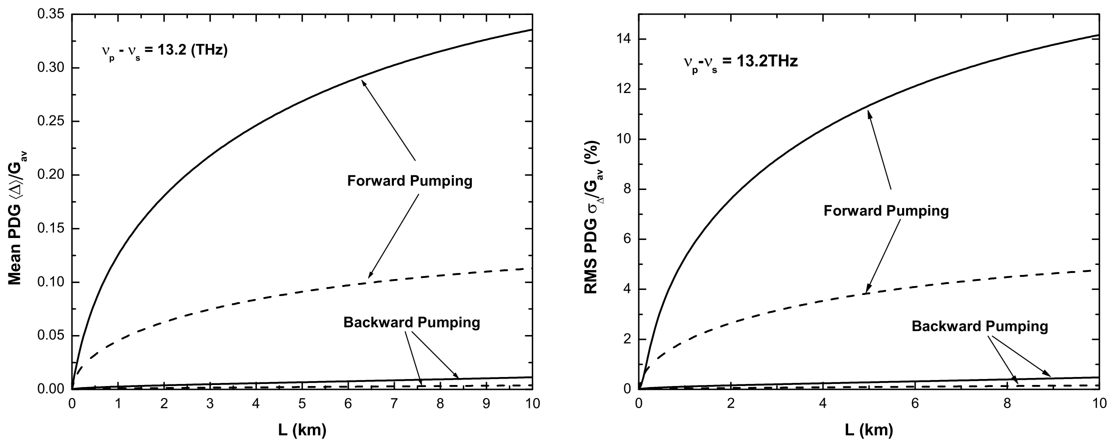


Figure 9.7: (a) Mean PDG and (b) variance $\sigma_\Delta$ (both normalized to the average gain $G_{av}$) as a function of amplifier length under forward and backward pumping. The solid and dashed curve correspond to $D_p = 0.05$ and 0.15 ps$/\sqrt{\text{km}}$, respectively.

gain that is independent of the signal SOP. The theory developed in the last section can be used to find the dependence of the PDG on the degree of polarization (DOP) of the pump wave.

Polarization scrambling does not change the total power of pump as only its SOP is changed randomly. If we assume that $\hat{\boldsymbol{p}}(z)$ is a stationary stochastic process, its correlation at two points within the fiber can be written as

$$\langle[\hat{\boldsymbol{p}}(z_1) - \langle\hat{\boldsymbol{p}}\rangle]\,[\hat{\boldsymbol{p}}(z_2) - \langle\hat{\boldsymbol{p}}\rangle]\rangle \equiv \overleftrightarrow{\boldsymbol{\Gamma}}(z_2 - z_1) = \overleftrightarrow{\boldsymbol{\Gamma}}_0\Gamma(z_2 - z_1), \tag{9.40}$$

where the correlation matrix $\overleftrightarrow{\boldsymbol{\Gamma}}(z_2 - z_1)$ is assumed to be separable as shown in Eq. (9.40). The DOP of the pump is related to the average of $\hat{\boldsymbol{p}}$ as $d_p = |\langle\hat{\boldsymbol{p}}\rangle|$ [33].

The pump DOP $d_p$, the covariance matrix $\overleftrightarrow{\boldsymbol{\Gamma}}_0$, and the correlation function $\Gamma(z_2 - z_1)$ depend on how scrambling rotates $\hat{\boldsymbol{p}}$ randomly on the Poincaré sphere. When the pump is completely polarized (no scrambling), $d_p = 1$ and $\overleftrightarrow{\boldsymbol{\Gamma}}_0 = 0$; in the opposite limit in which the pump is completely unpolarized, $d_p = 0$ and $\overleftrightarrow{\boldsymbol{\Gamma}}_0 = \overleftrightarrow{\boldsymbol{I}}/3$. The form of $\Gamma(z_2 - z_1)$ depends on the specific scrambling technique used in practice. In the following discussion, we assume it to vary as $\Gamma(z_2 - z_1) = \exp(-\gamma_c|z_2 - z_1|)$, where $\gamma_c = 1/l_c$ and $l_c$ is the correlation length . In practice, $l_c$ depends on the coherence length of the pump source and is typically $\sim$1 m.

Due to the randomness of the pump polarization, the XPM-induced NPR term in Eq. (9.6) becomes random as well. However, The correlation length $l_c$ is so small compared with the NPR beat length ($\sim$ 10 km) that the NPR term only contributes from the rotation around the average pump polarization $\langle\hat{\boldsymbol{p}}\rangle$. The NPR induced by the pump polarization fluctuations is negligible if we replace the deterministic transformation in Eq. (9.9) with

$$\boldsymbol{V} = \exp\left\{-\varepsilon_{sp}\left[\int_0^z P_0(z)dz\right]\langle\hat{\boldsymbol{p}}\rangle\times\right\}\boldsymbol{V}', \tag{9.41}$$

where $\boldsymbol{V}$ is an arbitrary vector in the Stoke space (Appendix E provides more details). Therefore, Eqs. (9.12) and (9.13) remain valid even in the presence of pump polarization scrambling.

As before, the PDG vector satisfies Eq. (9.25). This equation can again be simplified to obtain Eq. (9.27) with the only difference that now both $\hat{\boldsymbol{p}}$ and $\boldsymbol{b}$ are random. The solution is still given by Eq. (9.28). More importantly, the probability distribution of $\boldsymbol{\Delta}$ remains Gaussian (in all three dimensions) as long as the fiber length $L$ is much longer than the correlation length associated with pump polarization scrambling. However, as the pump polarization varies with $z$, the solution of Eqs. (9.29) and (9.30) is given by

$$\langle\boldsymbol{\Delta}(L)\rangle_b = ag_R\int_0^L P_0(z)\hat{\boldsymbol{p}}(z)\exp[-\eta(L-z)]dz, \tag{9.42}$$

$$\begin{aligned}\langle\Delta^2(L)\rangle_b &= 2ag_R\int_0^L P_0(z)\hat{\boldsymbol{p}}(z)\cdot\langle\boldsymbol{\Delta}(z)\rangle_b\,dz,\\ &= 2(ag_R)^2\int_0^L dz_1\int_0^{z_1} dz_2 P_0(z_1)P_0(z_2)\hat{\boldsymbol{p}}(z_1)\cdot\hat{\boldsymbol{p}}(z_2)\exp[-\eta(z_1-z_2)],\end{aligned} \tag{9.43}$$

where the subscript $b$ denotes the average over the birefringence fluctuations. Since $\hat{\boldsymbol{p}}(z)$ is random as well, we need to average Eqs. (9.42) and (9.43) over the pump SOP. In the case of forward pumping, the final analytic expressions are found to be

$$\langle\langle\boldsymbol{\Delta}(L)\rangle_b\rangle_p = \frac{ag_R P_{\text{in}}\langle\hat{\boldsymbol{p}}\rangle}{\eta-\alpha_p}\left[1-\alpha_p L_{\text{eff}}-\exp(-\eta L)\right], \tag{9.44}$$

$$\begin{aligned}\langle\langle\Delta^2(L)\rangle_b\rangle_p &= \frac{2(ag_R P_{\text{in}})^2\text{Tr}(\overleftrightarrow{\boldsymbol{\Gamma}}_0)}{(\gamma_c+\eta)^2-\alpha_p^2}\{(1-\alpha_p L_{\text{eff}})\exp[-(\gamma_c+\eta)L]-1+L_{\text{eff}}(\gamma_c+\eta+\alpha_p)(1-\alpha_p L_{\text{eff}}/2)\}\\ &+\frac{2(ag_R P_{\text{in}})^2 d_p^2}{\eta^2-\alpha_p^2}\{(1-\alpha_p L_{\text{eff}})\exp(-\eta L)-1+L_{\text{eff}}(\eta+\alpha_p)(1-\alpha_p L_{\text{eff}}/2)\},\end{aligned} \tag{9.45}$$

where the subscript $p$ denotes average over the ensemble of pump polarization and Tr stands for the trace. From Eq. (9.40), $\text{Tr}(\overleftrightarrow{\boldsymbol{\Gamma}}_0)$ is related to the DOP of pump as $\text{Tr}(\overleftrightarrow{\boldsymbol{\Gamma}}_0) = 1-d_p^2$.

The covariance matrix $\overleftrightarrow{\boldsymbol{C}}$ as defined as in Section 9.5 can also be found using the same technique and requires averaging over both ensembles of birefringence and pump polarization. It satisfies the following equation (see Appendix D for details):

$$\frac{d\overleftrightarrow{\boldsymbol{C}}}{dz} = -3\eta\overleftrightarrow{\boldsymbol{C}}+\eta\left[\langle\langle\Delta^2\rangle\rangle\overleftrightarrow{\boldsymbol{I}}-\langle\langle\boldsymbol{\Delta}\rangle\rangle\langle\langle\boldsymbol{\Delta}\rangle\rangle\right]+H_p, \tag{9.46}$$

where the last term depends on polarization scrambling and is found to be

$$\begin{aligned}H_p &= ag_R P_0(z)\left[\langle\hat{\boldsymbol{p}}(z)\langle\boldsymbol{\Delta}(z)\rangle_b\rangle_p+\langle\hat{\boldsymbol{p}}(z)\langle\boldsymbol{\Delta}(z)\rangle_b\rangle_p-\langle\hat{\boldsymbol{p}}\rangle\langle\langle\boldsymbol{\Delta}\rangle\rangle-\langle\langle\boldsymbol{\Delta}\rangle\rangle\langle\hat{\boldsymbol{p}}\rangle\right].\\ &= \frac{2(ag_R P_{\text{in}})^2\overleftrightarrow{\boldsymbol{\Gamma}}_0}{\gamma_c+\eta-\alpha_p}\{\exp(-2\alpha_p z)-\exp[-(\gamma_c+\eta+\alpha_p)z]\}.\end{aligned} \tag{9.47}$$

If the pump polarization is not scrambled, $d_p = 1$ and $\overleftrightarrow{\mathbf{\Gamma}}_0 = 0$. In that case Eqs. (9.44)–(9.46) reduce to Eqs. (9.31)–(9.33), as expected. The same results hold in the case of backward pumping except that $\alpha_p$ is replaced with $-\alpha_p$, $P_{\text{in}}$ is replaced with $P_{\text{in}} \exp(-\alpha_p L)$, $L_{\text{eff}}$ is redefined as $[\exp(\alpha_p L) - 1]/\alpha_p$, and $\Omega_R = \omega_p - \omega_s$ in the expression of $\eta$ is replaced by $\Omega_R = -(\omega_p + \omega_s)$.

It is evident from Eqs. (9.44)–(9.46) that scrambling affects the PDG considerably. Although the results are quite complicated when the correlation length $l_c$ and the effective fiber length $L_{\text{eff}}$ are comparable, they can be simplified considerably in a practical situation in which $L_{\text{eff}} \gg l_c$. This is almost always the case since $l_c$ is typically $\sim$1 m while $L_{\text{eff}}$ is likely to exceed 1 km. In this limit, $H_p$ in Eq. (9.47) reduces to

$$H_p \approx 2(a g_R P_{\text{in}})^2 \overleftrightarrow{\mathbf{\Gamma}}_0 l_c (1 - \alpha_p L_{\text{eff}})^2, \tag{9.48}$$

and it becomes negligible in Eq. (9.46) for $l_c \ll L_{\text{eff}}$ . In the same limit, the first term in Eq. (9.45) becomes much smaller than the second term and $\langle\langle \Delta^2(L) \rangle\rangle$ is given by

$$\langle\langle \Delta^2(L) \rangle_b \rangle_p \approx \frac{2(a g_R P_{\text{in}} d_p)^2}{\eta^2 - \alpha_p^2} [(1 - \alpha_p L_{\text{eff}}) \exp(-\eta L) - 1 + L_{\text{eff}}(\eta + \alpha_p)(1 - \alpha_p L_{\text{eff}}/2)]. \tag{9.49}$$

Comparing Eqs. (9.44), (9.46), and (9.49) with Eqs. (9.31)-(9.33) of Section 9.5, we conclude that the statistics of the PDG vector remains the same in the presence of polarization scrambling provided $P_{\text{in}}$ is replaced by $P_{\text{in}} d_p$ in all expressions for the moments of PDG. As a result, the mean and RMS value of PDG are reduced by a factor of $d_p$. This is exactly what has been observed experimentally [31, 32].

The general conclusion that the main effect of polarization scrambling is to reduce the input pump power by a factor of $d_p$ as far as PDG is concerned allows us to translate all results of Section 9.5 with this simple change. In particular, the probability distributions of the PDG vector $\mathbf{\Delta}$ and the PDG value $\Delta$ follow Eq. (9.34) and (9.37), respectively. When the effective fiber length $L_{\text{eff}}$ is much larger than the PMD diffusion length $L_d$, $\langle \Delta \rangle$ and $\sigma_\Delta$ are still given by Eqs. (9.38) and (9.39) except that $P_{\text{in}}$ is replaced by $P_{\text{in}} d_p$. Although we assumed $\overleftrightarrow{\mathbf{\Gamma}}_0$ and $\Gamma(z_2 - z_1)$ to be separable and $\Gamma(z_2 - z_1)$ to be exponential in the preceding discussion, the qualitative behavior is expected to be the same for any form of the correlation matrix $\overleftrightarrow{\mathbf{\Gamma}}(z_2 - z_1)$ as long as $l_c \ll L_{\text{eff}}$.

## 9.7 Summary

In this chapter, we have developed a general vector theory for analyzing fiber-based Raman amplifiers. We have shown that PMD can induce large fluctuations in the amplified signal depending on the value of the PMD parameter, although it also reduces the polarization dependence of the average gain. The amplification factor is found to follow the Gaussian statistics if it is measured in decibel units but the amplified signal itself follows a lognormal distribution.

We introduced a PDG vector to describe the nature of PDG in Raman amplifiers. We found that the probability distribution of the PDG mimics a Gaussian distribution when PMD is relatively small but becomes Maxwellian when the effective fiber length is much larger than the PMD diffusion length. Based on this probability distribution, we were able to find an analytic form of the dependence of the mean and variance of PDG on the operating parameters of Raman amplifiers. Both of these quantities depend inversely on the PMD parameter as well as on the frequency difference between the signal and the pump. We applied our vector theory to the case in which pump polarization is scrambled randomly and found that the mean PDG depends on the DOP of the pump polarization linearly.

We used the vector theory to compare the forward and backward pumping schemes used for making Raman amplifiers from the standpoint of PMD effects. In general, the use of backward pumping provides superior performance because it reduces the PDG as well as signal fluctuations to negligible levels as long as the PMD parameter $D_p$ exceeds a relatively small value of $0.01\ \mathrm{ps}/\sqrt{\mathrm{km}}$. If forward pumping must be employed for practical reasons, one should use fibers with $D_p$ values larger than $0.1\ \mathrm{ps}/\sqrt{\mathrm{km}}$. Physically speaking, backward pumping works better since the Stokes vectors $\boldsymbol{P}$ and $\boldsymbol{S}$ rotate in opposite directions and produce such rapid variations in their relative orientation angle $\theta$ that the PMD effects are averaged over a distance of 0.2 m or so.

In long-haul fiber links, PMD is intensionally reduced to minimize its effects on pulse broadening. However, our theory shows that PMD induces large signal fluctuations when the effective fiber length is comparable to the PMD diffusion length. Discrete Raman amplifiers typically use a few kilometer long fiber for providing sufficient gain. In the case of forward pumping, large signal fluctuations (>50%) are predicted to occur for $D_p$ values $\sim$0.02 ps/$\sqrt{\mathrm{km}}$. In the case of backward pumping, such $D_P$ values can be tolerated but large signal fluctuations will reappear for $D_p \sim 0.001\ \mathrm{ps}/\sqrt{\mathrm{km}}$. If SRS is used for distributed amplification, one should balance the effect of PMD-induced pulse broadening and PMD-induced signal fluctuations carefully. Some of the predictions in this chapter have been verified recently through experiments and numerical simulations in Ref. [35]-[37].

# Appendix A

In this appendix, we provides details on the derivation of the averaged equations (9.15)–(9.20) used to find the average and the variance of the output signal. Our method follows the technique discussed in Ref. [25]. The basic idea is to introduce a new vector $d\boldsymbol{W} = \boldsymbol{b}dz$ over a fiber segment of length $dz$ that is much shorter than the total fiber length $L$ but still much longer than the birefringence correlation length. Owing to the delta-function correlation of the birefringence vector $\boldsymbol{b}$ in Eq. (8.16), the vector $d\boldsymbol{W}$ is a Wiener process with the following properties [25]:

$$\langle d\boldsymbol{W}\rangle = 0, \quad \langle d\boldsymbol{W}d\boldsymbol{W}\rangle = \frac{1}{3}D_p^2\overleftrightarrow{\boldsymbol{I}}dz, \qquad \langle d\boldsymbol{W}\cdot d\boldsymbol{W}\rangle = D_p^2 dz. \tag{A9.1}$$

All other higher-order moments of $d\boldsymbol{W}$ vanish.

As discussed in Ref. [25], all differential equations involving $d\boldsymbol{W}$ should be interpreted in the Stratonovich sense in the limit in which $\boldsymbol{b}$ reduces to a delta-correlated process from a general Markov process. In this interpretation, any nonanticipating function $f(z)$ appearing in the integral $\int f(z)d\boldsymbol{W}$ over a short length segment $z$ to $z+dz$ is evaluated in the middle of the segment at the point $z+dz/2$. In contrast, the Ito calculus evaluates it at the left boundary point of the integral. As the Ito integral $\int f(z)d\boldsymbol{W}$ does not depend on the future, the average value of this integral vanishes. However, this does not happen for the Stratonovich integral because $f(z+dz/2)$ depends not only on its history, but also on $d\boldsymbol{W}$ within the interval $z$ to $z+dz$.

Consider now the stochastic differential equations (9.12) and (9.13). Before we can calculate any moments, we need to convert them from the Stratonovich to the Ito form. The conversion process is described in Chap. 4 of Ref. [25] and we follow it here. To illustrate the main steps, we consider Eq. (9.13) without the drift term and write it as

$$d\boldsymbol{s} = \boldsymbol{s}(z+dz) - \boldsymbol{s}(z) = -\Omega_R d\boldsymbol{W}\times\boldsymbol{s}(z+dz/2). \qquad \text{(Stratonovich)}, \tag{A9.2}$$

Note that $\boldsymbol{s}$ on the right side is evaluated in the middle of the segment. We expand it in a Taylor series as

$$\boldsymbol{s}(z+dz/2) = \boldsymbol{s}(z) + \frac{dz}{2}\frac{d\boldsymbol{s}(z)}{dz} + \cdots = \boldsymbol{s}(z) - \frac{\Omega_R}{2}d\boldsymbol{W}\times\boldsymbol{s}(z) + \cdots. \tag{A9.3}$$

Substituting this expansion in Eq. (A9.2), we obtain the Ito version of this equation as

$$d\boldsymbol{s} = -\Omega_R d\boldsymbol{W}\times\boldsymbol{s}(z) + \frac{\Omega_R^2}{2}d\boldsymbol{W}\times[d\boldsymbol{W}\times\boldsymbol{s}(z)] + \cdots. \tag{A9.4}$$

We now average over the second- and higher-order terms using the vector identity

$$d\boldsymbol{W}\times(d\boldsymbol{W}\times\boldsymbol{s}) = d\boldsymbol{W}(d\boldsymbol{W}\cdot\boldsymbol{s}) - \boldsymbol{s}(d\boldsymbol{W}\cdot d\boldsymbol{W}), \tag{A9.5}$$

and obtain the following Ito equation in the sense of mean-square limit [25]:

$$d\boldsymbol{s} = -\Omega_R d\boldsymbol{W}\times\boldsymbol{s}(z) - \frac{1}{3}D_p^2\Omega_R^2\boldsymbol{s}(z)dz. \qquad \text{(Ito)} \tag{A9.6}$$

The net effect of conversion is the appearance of a new term in the original equation (A9.2) when it is converted to the Ito sense.

Following this procedure, Eqs. (9.12) and (9.13) can be converted to the following Ito version of these equations

$$ds_0 = \frac{g_R}{2}\boldsymbol{P}\cdot\boldsymbol{s}dz, \tag{A9.7}$$

$$d\boldsymbol{s} = \frac{g_R}{2}\boldsymbol{P}s_0 dz - \eta\boldsymbol{s}dz + \Omega_R\boldsymbol{s}\times d\boldsymbol{W}, \tag{A9.8}$$

where $\eta = D_p^2\Omega_R^2/3$ as defined in the text. If we average Eqs. (A9.7) and (A9.8) over $d\boldsymbol{W}$, the last term in Eq. (A9.8) disappears, resulting in two deterministic equations. As $\hat{\boldsymbol{p}}$ is fixed, we can introduce the angle $\theta$ using $\boldsymbol{s}\cdot\hat{\boldsymbol{p}} = s_0\cos\theta$, and obtain Eqs. (9.15) and (9.16).

To calculate the second-order moments of $\boldsymbol{s}$, one can use Eqs. (9.12) and (9.13) to find the Stratonovich differential equations governing $s_0^2$, $s_0\boldsymbol{s}$, and $\boldsymbol{ss}$ and then convert them to the Ito form using the procedure described above. An alternative method uses Eqs. (A9.7) and (A9.8) together with the Ito formula given in Ref. [25]. The final equations become

$$ds_0^2 = g_R\boldsymbol{P}\cdot(s_0\boldsymbol{s})dz, \tag{A9.9}$$

$$d(s_0\boldsymbol{s}) = \frac{g_R}{2}\left[\boldsymbol{P}\cdot(\boldsymbol{ss}) + \boldsymbol{P}s_0^2\right]dz - \eta(s_0\boldsymbol{s})dz + \Omega_R(s_0\boldsymbol{s})\times d\boldsymbol{W}, \tag{A9.10}$$

$$\begin{aligned} d(\boldsymbol{ss}) &= \frac{g_R}{2}(\boldsymbol{P}s_0\boldsymbol{s} + s_0\boldsymbol{s}\boldsymbol{P}) - 3\eta(\boldsymbol{ss})dz + \eta s_0^2\overleftrightarrow{\boldsymbol{I}}dz \\ &\quad + \Omega_R(\boldsymbol{ss})\times d\boldsymbol{W} - \Omega_R d\boldsymbol{W}\times(\boldsymbol{ss}). \end{aligned} \tag{A9.11}$$

When we average over $d\boldsymbol{W}$, all terms containing $d\boldsymbol{W}$ disappear and the three equations become deterministic. Making inner products $s_0\boldsymbol{s}\cdot\hat{\boldsymbol{p}}$ and $(\boldsymbol{s}\cdot\hat{\boldsymbol{p}})^2$ and rewriting them as $s_0^2\cos\theta$ and $s_0^2\cos^2\theta$, we finally obtain Eqs. (9.19)–(9.21).

# Appendix B

In this appendix we give the derivation of Eq. (9.25), following the technique discussed in Ref. [28]. Consider the evolution of an arbitrary Jones vector through the linear equation

$$\frac{d|A\rangle}{dz} = M(z)|A\rangle \equiv [m_0(z) + \boldsymbol{m}(z)\cdot\boldsymbol{\sigma}]\,|A\rangle. \tag{B9.12}$$

In general, $M(z)$ is not unitary, and $m_0(z)$ and $\boldsymbol{m}(z)$ can be complex. Since Eq. (B9.12) is linear, we can introduce a transfer matrix $T(z)$ as $|A_{\rm out}\rangle = T(z)|A_{\rm in}\rangle$, where $|A_{\rm in}\rangle$ and $|A_{\rm out}\rangle$ are input and output optical fields. This matrix satisfies

$$\frac{dT(z)}{dz} = [m_0(z) + \boldsymbol{m}(z)\cdot\boldsymbol{\sigma}]T(z). \tag{B9.13}$$

In terms of the transfer matrix $T$, the input and output powers are related as

$$\langle A|A\rangle_{\rm in} = \langle A|[T(z)T^\dagger(z)]^{-1}|A\rangle_{\rm out}. \tag{B9.14}$$

The Hermitian matrix $T(z)T^\dagger(z)$ can be expanded in terms of the Pauli matrices as $T(z)T^\dagger(z) \equiv t_0(z) + \boldsymbol{t}(z)\cdot\boldsymbol{\sigma}$. It thus evolves as

$$\frac{d[T(z)T^\dagger(z)]}{dz} = \frac{dt_0(z)}{dz} + \frac{d\boldsymbol{t}(z)}{dz}\cdot\boldsymbol{\sigma}. \tag{B9.15}$$

In place of $\boldsymbol{t}$, we introduce $\boldsymbol{u}$ through the transformation

$$\boldsymbol{t}(z) = \boldsymbol{u}(z)\exp\left\{\int_0^z [m_0(z') + m_0^*(z')]dz'\right\}. \tag{B9.16}$$

The same relation holds between $t_0$ and $u_0$. The new quantities $u_0(z)$ and $\boldsymbol{u}(z)$ are found to evolve with $z$ as

$$\frac{du_0}{dz} = 2\boldsymbol{m}_r\cdot\boldsymbol{u}, \tag{B9.17}$$

$$\frac{d\boldsymbol{u}}{dz} = 2\boldsymbol{m}_r u_0 - 2\boldsymbol{m}_i\times\boldsymbol{u}, \tag{B9.18}$$

where $\boldsymbol{m}_r$ and $\boldsymbol{m}_i$ are the real and imaginary parts of $\boldsymbol{m}$, respectively. Equations (B9.17) and (B9.18) show that $u_0^2 - u^2 = 1$ for all $z$, and thus the operator $(TT^\dagger)^{-1}$ can be written as

$$[T(z)T^\dagger(z)]^{-1} = [u_0(z) - \boldsymbol{u}(z)\cdot\boldsymbol{\sigma}]\exp\left\{-\int_0^z dz'\left[m_0(z') + m_0^*(z')\right]\right\}. \tag{B9.19}$$

We now apply Eq. (B9.14) to the signal being amplified by a Raman amplifier of length $L$ and replace $A$ with $A_s$. Using the definition $S_0 = \langle A_s|A_s\rangle$, where $S_0(z)$ is the signal power at a distance $z$, we obtain

$$S_0(0) = S_0(L)[u_0(L) - \boldsymbol{u}(L)\cdot\hat{\boldsymbol{s}}_{\text{out}}]\exp\left(-\int_0^L [m_0(z) + m_0^*(z)]dz\right), \tag{B9.20}$$

where $\hat{\boldsymbol{s}}_{\text{out}}$ is the unit vector in the direction of $\boldsymbol{S}(L) = \langle A_s|\boldsymbol{\sigma}|A_s\rangle$. The amplifier gain (in decibels) can now be written as

$$G = a\ln\left(\frac{S_0(L)}{S_0(0)}\right) = a\int_0^L [m_0(z) + m_0^*(z)]dz - a\ln[u_0(L) - \boldsymbol{u}(L)\cdot\hat{\boldsymbol{s}}_{\text{out}}]. \tag{B9.21}$$

Notice that $G$ takes its maximum value when $\hat{\boldsymbol{s}}_{\text{out}}$ is along $\boldsymbol{u}$. In contrast, $G$ is minimum when the two vectors are anti-parallel.

The PDG can now be found using $\Delta = G_{\max} - G_{\min}$ and introducing the PDG vector as

$$\boldsymbol{\Delta} \equiv \hat{\boldsymbol{u}}\Delta = a\hat{\boldsymbol{u}}\ln\left(\frac{u_0 + u}{u_0 - u}\right), \tag{B9.22}$$

where $\hat{\boldsymbol{u}}$ is the unit vector in the direction of $\boldsymbol{u}$ and $u = |\boldsymbol{u}|$. From Eqs. (B9.17) and (B9.18), $\boldsymbol{\Delta}$ is found to satisfy

$$\begin{aligned}\frac{d\boldsymbol{\Delta}}{dz} &= \frac{du_0}{dz}\frac{\partial\boldsymbol{\Delta}}{\partial u_0} + \frac{d\boldsymbol{u}}{dz}\cdot\nabla_{\boldsymbol{u}}(\boldsymbol{\Delta}) \\ &= 2\Delta\coth\left(\frac{\Delta}{2a}\right)\left[\boldsymbol{m}_r - (\boldsymbol{m}_r\cdot\hat{\boldsymbol{\Delta}})\hat{\boldsymbol{\Delta}}\right] + 4a(\boldsymbol{m}_r\cdot\hat{\boldsymbol{\Delta}})\hat{\boldsymbol{\Delta}} - 2\boldsymbol{m}_i\times\boldsymbol{\Delta}.\end{aligned} \tag{B9.23}$$

where $\nabla_{\boldsymbol{u}}$ operates on $\boldsymbol{u}$ and $\hat{\boldsymbol{\Delta}} \equiv \hat{\boldsymbol{u}}$ is the unit vector in the direction of $\boldsymbol{\Delta}$.

We now only need to find $\boldsymbol{m}_r$ and $\boldsymbol{m}_i$. If we replace $A$ with $A_s$ in Eq. (B9.12) and follow the steps outlined in this Appendix, we find that Eqs. (9.12) and (9.13) take the form of Eqs. (B9.17) and (B9.18). Comparing these equations, we obtain $\boldsymbol{m}_r = g_R \boldsymbol{P}/4$ and $\boldsymbol{m}_i = \Omega_R \boldsymbol{b}/2$. Using them in Eq. (B9.23), we obtain the final result given as Eq. (9.25).

# Appendix C

In this appendix, we provide details on the derivation of Eqs. (9.29)-(9.31) and (9.46). As discussed in Appendix B, Eq. (9.27) can be converted into an Ito equation as

$$d\boldsymbol{\Delta} = a g_R \boldsymbol{P} dz - \eta \boldsymbol{\Delta} dz + \Omega_R \boldsymbol{\Delta} \times d\boldsymbol{W}. \tag{C9.24}$$

From this equations, we can calculate $d\Delta^2$ and $d(\boldsymbol{\Delta\Delta})$ in the Ito sense and find

$$d\Delta^2 = 2 a g_R \boldsymbol{P} \cdot \boldsymbol{\Delta} dz, \tag{C9.25}$$

$$\begin{aligned} d(\boldsymbol{\Delta\Delta}) = {} & a g_R (\boldsymbol{P\Delta} + \boldsymbol{\Delta P}) dz - 3\eta (\boldsymbol{\Delta\Delta}) dz + \eta \Delta^2 \overleftrightarrow{\boldsymbol{I}} dz \\ & + \Omega_R (\boldsymbol{\Delta\Delta}) \times d\boldsymbol{W} - \Omega_R d\boldsymbol{W} \times (\boldsymbol{\Delta\Delta}). \end{aligned} \tag{C9.26}$$

When we average Eqs. (C9.24)-(C9.26) over $d\boldsymbol{W}$, all terms containing $d\boldsymbol{W}$ disappear, and we obtain three deterministic equations as

$$d\langle \boldsymbol{\Delta} \rangle = a g_R \boldsymbol{P} dz - \eta \langle \boldsymbol{\Delta} \rangle dz, \tag{C9.27}$$

$$d\langle \Delta^2 \rangle = 2 a g_R \boldsymbol{P} \cdot \langle \boldsymbol{\Delta} \rangle dz, \tag{C9.28}$$

$$d\langle \boldsymbol{\Delta\Delta} \rangle = a g_R (\boldsymbol{P} \langle \boldsymbol{\Delta} \rangle + \langle \boldsymbol{\Delta} \rangle \boldsymbol{P}) dz - 3\eta \langle \boldsymbol{\Delta\Delta} \rangle dz + \eta \langle \Delta^2 \rangle \overleftrightarrow{\boldsymbol{I}} dz. \tag{C9.29}$$

Using the definition of the $\overleftrightarrow{\boldsymbol{C}}$ and noting that

$$d\overleftrightarrow{\boldsymbol{C}} = d\langle \boldsymbol{\Delta\Delta} \rangle - (d\langle \boldsymbol{\Delta} \rangle) \langle \boldsymbol{\Delta} \rangle - \langle \boldsymbol{\Delta} \rangle (d\langle \boldsymbol{\Delta} \rangle), \tag{C9.30}$$

we finally obtain Eqs. (9.29)-(9.31).

In the case of pump-polarization scrambling, $\boldsymbol{P}(z) = P_0(z)\hat{\boldsymbol{p}}(z)$, where $\hat{\boldsymbol{p}}(z)$ is random along the fiber. The covariance matrix $\overleftrightarrow{\boldsymbol{C}}$ is then redefined as the double average over both random variables. The differential of $\overleftrightarrow{\boldsymbol{C}}$ is then given by

$$d\overleftrightarrow{\boldsymbol{C}} = d\langle\langle \boldsymbol{\Delta\Delta} \rangle\rangle - (d\langle\langle \boldsymbol{\Delta} \rangle\rangle) \langle\langle \boldsymbol{\Delta} \rangle\rangle - \langle\langle \boldsymbol{\Delta} \rangle\rangle (d\langle\langle \boldsymbol{\Delta} \rangle\rangle). \tag{C9.31}$$

Average Eqs. (C9.27)-(C9.29) over the ensemble of pump polarization, we obtain

$$d\langle\langle \boldsymbol{\Delta} \rangle\rangle = ag_R \langle \boldsymbol{P} \rangle dz - \eta \langle\langle \boldsymbol{\Delta} \rangle\rangle dz, \tag{C9.32}$$

$$d\langle\langle \Delta^2 \rangle\rangle = 2ag_R \langle \boldsymbol{P} \cdot \langle \boldsymbol{\Delta} \rangle_b \rangle_p dz, \tag{C9.33}$$

$$d\langle\langle \boldsymbol{\Delta\Delta} \rangle\rangle = ag_R \left( \langle \boldsymbol{P} \langle \boldsymbol{\Delta} \rangle_b \rangle_p + \langle \langle \boldsymbol{\Delta} \rangle_b \boldsymbol{P} \rangle_p \right) dz - 3\eta \langle\langle \boldsymbol{\Delta\Delta} \rangle\rangle dz + \eta \langle\langle \Delta^2 \rangle\rangle \overleftrightarrow{\boldsymbol{I}} dz. \tag{C9.34}$$

Substituting Eqs. (C9.32) and (C9.34) into Eq. (C9.31), we obtain Eq. (9.46).

# Appendix D

In this appendix we provide details on the effects of NPR induced by the pump when pump polarization is scrambled. We neglect other effects temporarily and consider Eq. (9.6) with only the XPM-induced NPR term. After making the transformation in Eq. (9.41), Eq. (9.6) becomes

$$d\boldsymbol{S} = -\varepsilon_{sp} P_0(z) \delta\hat{\boldsymbol{p}}(z + dz/2) \times \boldsymbol{S}(z + dz/2) dz \qquad \text{(Stratonovich)}, \tag{D9.35}$$

where $\delta\hat{\boldsymbol{p}}(z+dz/2) = \hat{\boldsymbol{p}}(z+dz/2) - \langle \hat{\boldsymbol{p}} \rangle$ and we have dropped the prime notation for simplicity. Since the correlation length $l_c$ is much smaller than the beat length of NPR ($\sim$ 10 km), we cut the fiber into many sections of $l_c$ long, i.e., $dz = l_c$. According to the correlation matrix in Eq. (9.40), $\hat{\boldsymbol{p}}(z)$ is approximately correlated within each section of length $dz$ but is approximately uncorrelated from one section to another. Expanding $\boldsymbol{S}(z + dz/2)$ in Eq. (D9.35) into a Taylor series, this equation becomes

$$d\boldsymbol{S} = -\varepsilon_{sp} P_0(z) \delta\hat{\boldsymbol{p}}(z + dz/2) \times \left[ \boldsymbol{S}(z) + \frac{dz}{2} \frac{d\boldsymbol{S}}{dz} + \cdots \right] dz. \tag{D9.36}$$

Substituting Eq. (D9.35) into Eq. (D9.36), we obtain the Ito version of this equation as

$$\begin{aligned} d\boldsymbol{S} = &-\varepsilon_{sp} P_0(z) \delta\hat{\boldsymbol{p}}(z + dz/2) \times \boldsymbol{S}(z) dz \\ &+ \frac{1}{2} [\varepsilon_{sp} P_0(z) dz]^2 \left\{ \delta\hat{\boldsymbol{p}}(z) \delta\hat{\boldsymbol{p}}(z + dz/2) \cdot \boldsymbol{S}(z) - [\delta\hat{\boldsymbol{p}}(z) \cdot \delta\hat{\boldsymbol{p}}(z + dz/2)] \boldsymbol{S}(z) \right\} \\ &+ \cdots \qquad\qquad\qquad \text{(Ito)}. \end{aligned} \tag{D9.37}$$

When we average this equation over $\hat{\boldsymbol{p}}$, the first term disappears. As $\hat{\boldsymbol{p}}$ is correlated within $dz$ and does not change much, we can replace $\hat{\boldsymbol{p}}(z + dz/2)$ with $\hat{\boldsymbol{p}}(z)$ and perform the average. The final result is

$$d\langle \boldsymbol{S} \rangle \approx \frac{1}{2} [\varepsilon_{sp} P_0(z) dz]^2 \left[ \overleftrightarrow{\boldsymbol{\Gamma}}_0 - \mathrm{Tr}(\overleftrightarrow{\boldsymbol{\Gamma}}_0) \overleftrightarrow{\boldsymbol{I}} \right] \cdot \langle \boldsymbol{S}(z) \rangle + \cdots = O\left[ (dz)^2 \right], \tag{D9.38}$$

in the sense of mean-square limit [25]. When the correlation length $l_c$ is relatively small, $d\langle \boldsymbol{S} \rangle / dz \to 0$. As a result, NPR induced through pump-polarization fluctuations does not diffuse the signal SOP. The net XPM-induced NPR contribution comes from only the average value $\langle \hat{\boldsymbol{p}} \rangle$, as shown in Eq. (9.41). This result is easy to understand physically. It takes some distance for the signal to experience NPR. However, the pump polarization fluctuates so fast that the signal can only follow the rotation around the average pump polarization $\langle \hat{\boldsymbol{p}} \rangle$.

# References


[1] Q. Lin and G. P. Agrawal, Opt. Lett. **27**, 2194 (2002).

[2] Q. Lin and G. P. Agrawal, Opt. Lett. **28**, 227 (2003).

[3] Q. Lin and G. P. Agrawal, J. Opt. Soc. Am. B **20**, 1616 (2003).

[4] C. V. Raman, Indian J. Phys. **2**, 387 (1928).

[5] E. J. Woodbury and W. K. Ng, Proc. IRE **50**, 2347 (1962).

[6] R. H. Stolen, E. P. Ippen, and A. R. Tynes, Appl. Phys. Lett. **20**, 62 (1972).

[7] M. Ikeda, Opt. Commun. **39**, 148 (1981).

[8] S. Namiki and Y. Emori, IEEE Sel. Top. Quan. Electron. **7**, 3 (2001).

[9] G. P. Agrawal, *Nonlinear Fiber Optics*, $3^{rd}$ ed. (Academic, San Diego, CA, 2001).

[10] K. Rottwitt and A. J. Stentz, in *Optical Fiber Telecommunications IV A*, I. Kaminow and T. Li, Eds. (Academic, San Diego, 2002), Chap. 5.

[11] R. H. Stolen, IEEE J. Quan. Electron. **QE-15**, 1157 (1979).

[12] D. J. Dougherty, F. X. Kartner, H. A. Haus, and E. P. Ippen, Opt. Lett. **20**, 31 (1995).

[13] D. Mahgerefteh, H. Yu, D. L. Butler, J. Goldhar, D. Wang, E. Golovchenko, A. N. Phlipetskii, C. R. Menyuk, L. Joneckis, Proc. Conf. on Lasers and Electro-optics (Optical Society of America, Washington D.C., 1997), p.447.

[14] A. Berntson, S. Popov, E. Vanin, G. Jacobsen, and J. Karlsson, Proc. Opt. Commun. Conf. (Optical Society of America, Washington D.C., 2001), MI2-1.

[15] P. Ebrahimi, M. C. Hauer, Q. Yu, R. Khosravani, D. Gurkan, D. W. kim, D. W. Lee, and A. E. Willner, Proc. Conf. on Lasers and Electro-optics (Optical Society of America, Washington D.C., 2001), p. 143.

[16] S. Popov, E. Vanin, and G. Jacobsen, Opt. Lett. **27**, 848 (2002).

[17] J. P. Gordon and H. Kogelnik, Proc. Natl. Acad. Sci. USA **97**, 4541 (2000).

[18] S. J. Savory and F. P. Payne, J. Lightwave Technol. **19** 350 (2001).

[19] D. Wang and C. R. Menyuk, J. Lightwave Technol. **19** 487 (2001).

[20] H. Kogelnik, R. M. Jopson, and L. E. Nelson, in *Optical Fiber Telecommunications IV B*, I. P. Kaminow and T. Li, Eds. (Academic, San Diego, 2002), Chap. 15.

[21] R. Hellwarth, J. Cherlow, and T. Yang, Phys. Rev. B **11**, 964 (1975).

[22] R. W. Hellwarth, Prog. Quantum Electron. **5**, 1 (1977).

[23] P. Ciprut, B. Gisin, N. Gisin, R. Passy, J. P. Von der Weid, F. Prieto, and C. W. Zimmer, J. lightwave Technol. **16** 757 (1998).

[24] R. W. Boyd, *Nonlinear Optics*, 2$^{\mathrm{nd}}$ Ed. (Academic, San Diego, CA, 2003).

[25] C. W. Gardiner, *Handbook of Stochastic Methods*, 2$^{nd}$ ed. (Springer, New York, 1985).

[26] H. H. Kee, C. R. S. Fludger and V. Handerek, Technical Digest, Opt. Fiber Commun. (Optical Society of America, Washington D.C., 2002), p. 180.

[27] A. Papoulis, *Probability, Random Variables, and Stochastic Processes*, 3$^{rd}$ ed. (WCB/McGraw-Hill, New York, 1991).

[28] B. Huttner, C. Geiser, and N. Gisin, IEEE J. Sel. Top. Quan. Electron. **6**, 317-329 (2000).

[29] A. Mecozzi and M. Shtaif, IEEE Photon. Technol. Lett. **14**, 313 (2002).

[30] G. J. Foschini and C. D. Poole, J. Lightwave Technol. **9**, 1439 (1991).

[31] Y. Emori, S. Matsushita, and S. Namiki, Technical Digest, Opt. Fiber Commun. (Optical Society of America, Washington D.C., 2000), p.106.

[32] J. Zhang, V. Dominic, M. Missey, S. Sanders, and D. Mehuys, Technical Digest, Optical Amplifiers and Their Applications (Optical Society of America, Washington D.C., 2000), p. 30.

[33] L. Mandel and E. Wolf, *Optical Coherence and Quantum Optics*, (Cambridge University Press, New York, 1995), Chap. 6.

[34] P. K. A. Wai and C. R. Menyuk, J. Lightwave Technol. **14**, 148 (1996).

[35] A. dos Santos and J. von der Weid, Opt. Lett. **29**, 1324 (2004).

[36] E. Son, J. Lee, and Y. Chung, J. Lightwave Technol. **23**, 1219 (2005).

[37] A. Galtarossa, L. Palmieri, M. Santagiustina, and L. Ursini, Proc. Opt. Commun. Conf. (Optical Society of America, Washington D.C., 2006), PWD6.

# 10 PMD and Cross-Phase Modulation

In this chapter, we focus on the interaction between PMD and XPM while ignoring other nonlinear effects. We show [1] that the combination of XPM and PMD inside optical fibers leads to a novel phenomenon of intrapulse depolarization manifested as different random states of polarizations across the pulse profile. Such polarization evolution of optical pulses is directly analogous to the phenomenon of spin decoherence in semiconductors or pseudospin relaxation in atoms. The intrapulse depolarization has a significant impact on optical switching based on a nonlinear optical loop mirror (NOLM). We develop a theory [2] to quantify this impact. It is found that the interaction between PMD and XPM transfers spatial randomness of residual birefringence to temporal power fluctuations within the switching window.

## 10.1 Intrapulse Depolarization

Some physical systems, although quite different in their origins, can exhibit the same dynamic behavior. A well-known example is the similarity between the spin precession of an electron in a magnetic field [3]-[6] and the interaction of a two-level atom with an optical field [7, 8]. An electron in a superposition state of Zeeman sublevels precesses its spin at a Larmor frequency until environmental factors induce decoherence [3]-[6]. In the case of a two-level atom (modelled as a pseudospin), an optical field induces Rabi oscillations of the atomic dipole, while vacuum or laser fluctuations, or atomic collisions relax the pseudospin motion [7, 8]. Spin/pseudospin decoherence is considered to be a universal phenomenon associated with two-level quantum systems. Here we show that it has a classical analog in the polarization evolution of an optical pulse propagating inside a fiber in the presence of both PMD and XPM. The combined effect of these two mechanisms leads to a novel phenomenon of *intrapulse depolarization* in a fashion analogous to spin decoherence in quantum systems.

### 10.1.1 Pump-Probe Equations

To illustrate the underlying physics as simply as possible, we consider a pump-probe configuration with two copropagating waves at frequencies $\omega_p$ and $\omega_s$. The pump wave has a peak power much higher than the probe (called signal from now on), such that it modulates the phases of both waves through SPM and XPM, but those induced by the signal are assumed to be negligible. The total field is thus given by

$$|A(z,t)\rangle = |A_p(z,t)\rangle \exp(-i\omega_p t) + |A_s(z,t)\rangle \exp(-i\omega_s t). \tag{10.1}$$

Substituting Eq. (10.1) into Eq. (8.14), neglecting the Raman effect by setting $f_R = 0$, decomposing into individual frequency component, we can obtain the dynamic equations governing the pump and signal waves. For convenience, we set the carrier frequency at the pump: $\omega_0 = \omega_p$. We also make a time transformation to the signal frame to remove the temporal propagation at the signal velocity. We then obtain the following vector equations governing propagation of two waves inside an optical fiber [9]:

$$\frac{\partial |A_p\rangle}{\partial z} + \delta \frac{\partial |A_p\rangle}{\partial \tau} = i\gamma_e P |A_p\rangle, \tag{10.2}$$

$$\frac{\partial |A_s\rangle}{\partial z} = \frac{i\gamma_e}{2} P (3 + \hat{p}\cdot\boldsymbol{\sigma}) |A_s\rangle - \frac{i}{2}\Omega \boldsymbol{b}\cdot\boldsymbol{\sigma} |A_s\rangle, \tag{10.3}$$

where $\gamma_e = 8\gamma/9$, $\Omega = \omega_s - \omega_p$, $P = \langle A_p|A_p\rangle$ is the pump power, and the unit vector $\hat{p} = \langle A_p|\boldsymbol{\sigma}|A_p\rangle/P$ represents the pump SOP on the Poincaré sphere [10]. Random birefringence enters through the vector $\boldsymbol{b}(z)$, whose statistics is given by Eq. (8.16). As fiber length and nonlinear length are both typically much longer than the birefringence correlation length $l_c$, the situation we encounter here corresponds to the *motional narrowing regime* of spin relaxation [3, 5].

Equations (10.2) and (10.3) show that $P(z,\tau) = P(0, \tau - \delta z)$, but the signal power profile $S(z,\tau) \equiv \langle A_s|A_s\rangle = S(0,\tau)$. However, the signal SOP changes in a random fashion. To consider polarization effects for the signal, we convert Eq. (10.3) into the Stokes space by introducing a unit Stokes vector as $\hat{s} = \langle A_s|\boldsymbol{\sigma}|A_s\rangle/S$. From Eq. (10.3), $\hat{s}(z,\tau)$ is found to satisfy

$$\partial \hat{s}/\partial z = (\Omega \boldsymbol{b} - \gamma_e P \hat{p}) \times \hat{s}. \tag{10.4}$$

The pump pulse changes the signal SOP through XPM-indued nonlinear polarization rotation (NPR), while PMD perturbs it randomly at a rate dictated by the magnitude of $\Omega \boldsymbol{b}$.

Equation (10.4) is isomorphic to the Bloch equation governing the motion of spin density in a solid [3]-[6]. The pump acts like a static magnetic field, and perturbations induced by PMD correspond to a fluctuating magnetic field induced by nuclei or phonons. Clearly, the polarization of signal pulse would evolve along the fiber statistically in a fashion similar to the phenomenon of spin decoherence in time. This can be seen clearly by averaging Eq. (10.4) over the random $\boldsymbol{b}$ to obtain [12]: $\partial\langle\hat{s}\rangle/\partial z =$

$-\eta\langle\hat{s}\rangle - \gamma_e P\hat{p}\times\langle\hat{s}\rangle$, where $\eta$ is the polarization relaxation rate related to the PMD diffusion length $L_d$ as $\eta = 1/L_d = (D_p\Omega)^2/3$. Statistically, PMD causes signal polarization to relax along the fiber. However, XPM forces signal polarization to precess around the pump Stokes vector $\hat{p}$ with a Larmor frequency of $\gamma_e P$. The global SOP of the signal, $\hat{S}(z) \propto \int_{-\infty}^{+\infty}\langle A_s|\boldsymbol{\sigma}|A_s\rangle d\tau / \int_{-\infty}^{+\infty}\langle A_s|A_s\rangle d\tau$, would evolve analogous to the macroscopic magnetization in semiconductors.

There is one crucial difference between the quantum spin dynamics and the classical pulse propagation. In the quantum system, spin flipping requires energy dissipation, resulting in different longitudinal and transversal relaxation times, and electrons relax eventually to a thermal equilibrium among the Zeeman sublevels [3]-[5]. However, no such levels exist in the classical system, and PMD-induced polarization relaxation is uniform in three dimensions of the Stokes space. The signal SOP is completely randomized on the Poincaré sphere after a sufficiently long distance. In the absence of pump, PMD changes the signal SOP randomly but uniformly across the entire signal pulse, resulting in no intrapulse decoherence. Similarly, in the absence of PMD, pump pulse induces inhomogeneous but coherent polarization precession across the signal pulse, creating again no intrapulse decoherence. However, the combination of XPM and PMD produces a new effect we refer to as *intrapulse depolarization* (IPD).

### 10.1.2 IPD Coefficient

IPD can be quantified by considering the relative orientation of the signal SOPs at two different times. Defining $\hat{s}_1 = \hat{s}(z,\tau_1)$ and $\hat{s}_2 = \hat{s}(z,\tau_2)$, we introduce a scalar averaged quantity $d = \overline{\hat{s}_1\cdot\hat{s}_2}$ as the IPD coefficient. Note that $\hat{s}_1$ and $\hat{s}_2$ evolve according to Eq. (10.4) with different pump powers. Even though they are defined in a relative rotating frame, $d$ is invariant to such a global polarization rotation. Averaging over the random birefringence [12], we obtain the following equations governing the evolution of IPD coefficient:

$$\partial d/\partial z = \gamma_e P_- U, \tag{10.5}$$

$$\partial U/\partial z = -\eta U + \gamma_e P_-(V-d), \tag{10.6}$$

$$\partial V/\partial z = -3\eta V + \eta d, \tag{10.7}$$

where $P_- = P(z,\tau_2) - P(z,\tau_1)$, and $U$ and $V$ were introduced as $U = \overline{\hat{p}\cdot(\hat{s}_1\times\hat{s}_2)}$ and $V = \overline{\hat{p}\cdot(\hat{s}_1\hat{s}_2)\cdot\hat{p}}$.

To show how $d(z,\tau_1,\tau_2)$ changes along the fiber, we consider first the case of a signal pulse much wider than the pump pulse and neglect GVM for simplicity ($\delta = 0$, corresponding to choosing wavelengths of two waves symmetrically around the zero-dispersion wavelength $\lambda_0$). Time $\tau_1$ is set outside the pump pulse (no XPM) but $\tau_2$ is set at the peak of the pump pulse where XPM is maximum. Figure 10.1 shows $d$ as a function of $\xi = z/L_n$ for three values of the ratio $\mu = L_n/L_d$, where the nonlinear length

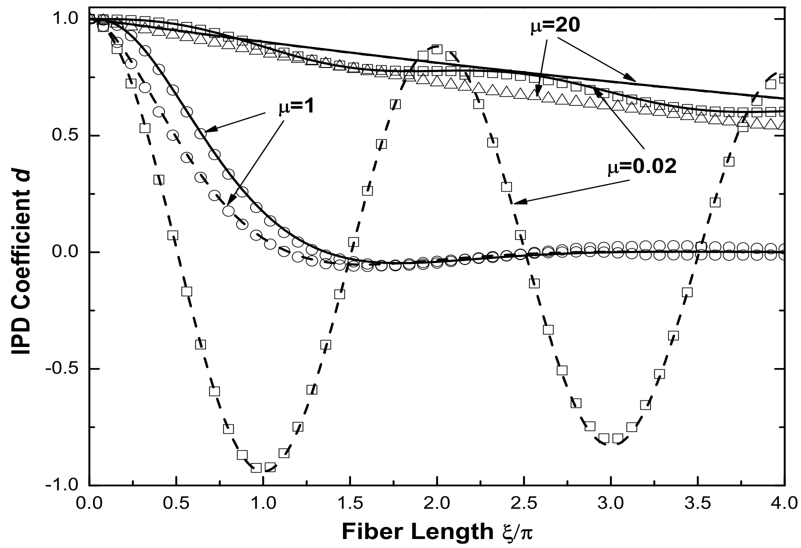


Figure 10.1: IPD coefficient $d$ for three values of $\mu = L_n/L_d$. Solid and dashed curves show the Faraday and Voigt geometries, respectively. Symbols show the simulation results performed with $P_0 = 1.41$ W. $\mu = 0.02$, 1, 20 correspond to $\Omega/2\pi = 0.31$, 2.19, 9.77 THz, respectively.

is defined as $L_n = (\gamma_e P_0)^{-1}$ and $P_0$ is the peak power of the pump pulse. The ratio $\mu$ plays an important role as it governs the relative length scales of the PMD and XPM processes. Numerical simulations based on Eqs. (10.9) and (10.11) are also presented in Fig. 10.1. Simulations were carried out for a 5-km long fiber with $\gamma = 2$ W$^{-1}$/km, $D_p = 0.2$ ps/$\sqrt{\text{km}}$, $l_c = 10$ m, $\lambda_0 = 1550$ nm and $\beta_3 = 0.1$ ps$^3$/km. For completeness, GVD, which as well as GVM can be obtained from $\beta_3$, was indeed included in the simulations. The fiber is divided into 10-m-long sections with birefringence varying randomly from section to section. The FWHM of the Gaussian pump pulse is 166.5 ps. Statistical averages are computed using 1000 realizations. The good agreement justifies the use of a simple model based on Eqs. (10.5)–(10.7).

If the pump and signal are copolarized at the input end (solid curves), a situation that corresponds to the Faraday geometry in the spin analogy [5], little nonlinear precession of SOP occurs. When $L_d \gg L_n$ ($\mu \ll 1$), $d$ decays slowly along the fiber as PMD effects occur over a length scale much longer than $L_n$. When the two lengths become comparable ($\mu = 1$), XPM and PMD affect each other strongly, resulting in considerable IPD. As seen in Fig. 10.1, $d$ decreases rapidly and becomes almost zero for $\xi > 2$. However, when $L_d \ll L_n$ ($\mu \gg 1$), $\hat{s}$ changes randomly within a diffusion length even before XPM has any chance to act. Because of its averaging, the XPM effects become polarization independent, and the intrapulse polarization coherence is significantly recovered.

When $\hat{p}$ and $\hat{s}$ are initially orthogonal (corresponding to the Voigt geometry in spin precession [5]), the dashed curve for $\mu = 0.02$ in Fig. 10.1 shows that $d$ exhibits relaxation oscillations that are analo-

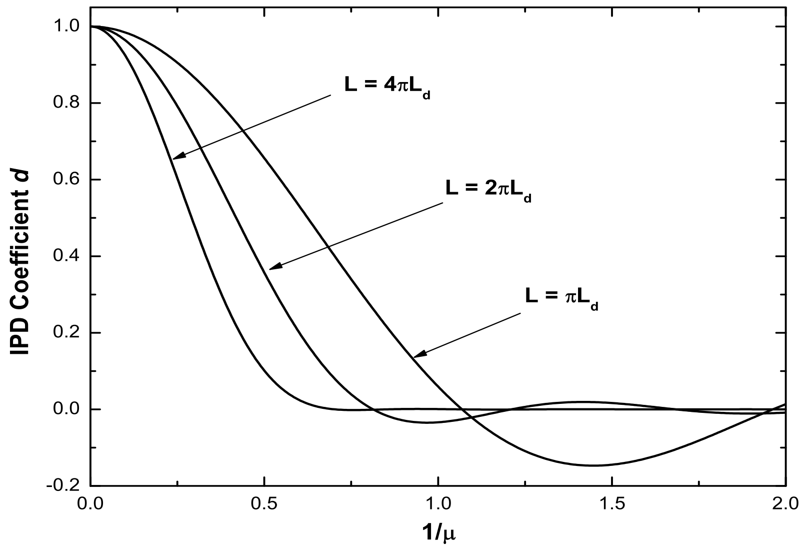


Figure 10.2: IPD coefficient $d$ as a function of $1/\mu = \gamma_e P_0 L_d$ for three fiber lengths in the Faraday geometry.

gous to the free-induction decay in spin/pseudospin relaxation dynamics [3, 7]. These oscillations are suppressed by PMD, and maximum IPD occurs when $\mu = 1$. In contrast, when $\mu \gg 1$, not only are precessions suppressed, but IPD is also considerably reduced because PMD-induced rapid SOP variations average out the XPM-induced NPR.

IPD strongly depends on the pump power. Figure 10.2 shows $d$ as a function of $1/\mu \equiv \gamma_e P_0 L_d$ for a fixed $L_d$ in the Faraday geometry (a similar behavior occurs for the Voigt geometry). If pump power is small, little IPD occurs even for $L \gg L_d$, although the global SOP of the signal varies randomly. IPD increases dramatically with pump power, and $d \to 0$ when $\mu^{-1} \approx 0.7$ for $L = 4\pi L_d$. Spin decoherence induced by a magnetic field and its effects on photoluminescence (the Hanle effect) are widely used for measuring the spin relaxation time [4, 5]. Analogously, the sensitivity of IPD to pump power might provide a simple way for PMD characterization.

Evolution of the signal polarization depends on the local interaction between PMD and XPM along the fiber. Interplay between PMD and XPM transfers spatial randomness of fiber birefringence into temporal randomness of signal polarization. Figure 10.3 shows IPD induced by a Gaussian pump pulse. In the temporal region outside the pump pulse, signal only experiences PMD, and thus no IPD occurs. But within the overlap region, the signal SOP is affected by both PMD and XPM. If walk-off is zero, IPD is relatively large in the vicinity of the pump peak. Pulse walk-off broadens the depolarization region but reduces the IPD magnitude because of a decrease in the XPM strength.

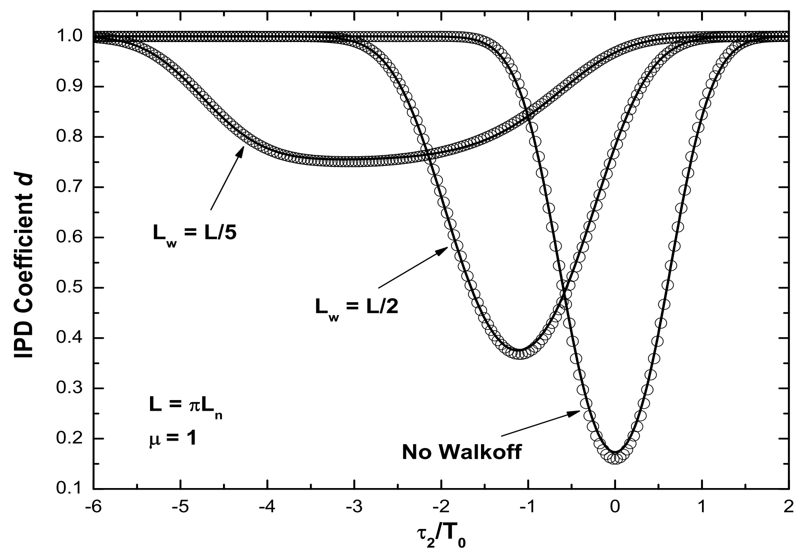


Figure 10.3: IPD across the signal pulse for three walk-off lengths $L_w$. $L = \pi L_n$ and $\mu = 1$. Simulation results (circles) use $\Omega/2\pi = 1.09$ THz and $P_0 = 0.353$ W. The width of Gaussian pump pulse $T_0 = \text{FWHM}/1.665$.

### 10.1.3 Conclusions

In concluding this section, we have shown that the combination of XPM and PMD leads to the novel phenomenon of intrapulse depolarization. We have also discussed how this behavior is analogous to spin/pseudospin decoherence in two-level quantum systems. From a practical perspective, such intrapulse depolarization affect the chirp imposed on the signal pulse and lead to spectral distortion even though the temporal profile of signal pulse may not change at all. On the other hand, it would affect the performance of XPM-based nonlinear fiber devices such as optical switches and wavelength converters. It would also affect PMD monitoring and PMD compensation in communication systems based on the measurement of degree of polarization.

## 10.2 Effects of PMD on Nonlinear Switching

XPM inside a nonlinear optical loop mirror (NOLM) is used often for ultrafast optical switching [13]–[18]. It has been noted in several experiments that the performance of an NOLM is significantly affected by the residual birefringence of optical fiber used to make the Sagnac loop [19]–[22] if a polarization-maintaining fiber is not used. Residual birefringence was indeed used as a method to reduce the polarization dependence of optical switching [23]. Physically, residual birefringence of optical fibers randomizes

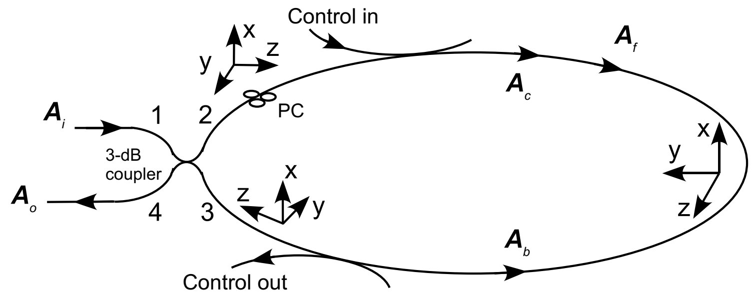


Figure 10.4: Notation used for describing optical switching in a nonlinear optical loop mirror; PC stands for polarization controller.

the state of polarization (SOP) of both the signal and control pulses and induces differential polarization variations between them through PMD when the two have different carrier frequencies. Since the XPM process responsible for optical switching is polarization dependent [24], PMD induces considerable random variations in the NOLM output. This impact of PMD on optical switching becomes a serious issue for practical implementation of such optical switches.

The scalar theory commonly used for describing NOLM operation [24] cannot include the polarization effects. We have recently developed a vector theory of XPM and have used it to study the combined effects of PMD and XPM on the performance of lightwave systems [9]. In this Chapter we use the same approach for studying the effects of PMD on optical switching in NOLMs and show that PMD not only affects the switching window of such devices but also induces considerable fluctuations in the shape, width, and energy of switched pulses. We quantify these fluctuations by solving the underlying equations analytically after appropriate simplifications and compare them with full numerical simulations.

### 10.2.1 Theoretical Model

Figure 10.4 shows an NOLM schematically and the notation used. The input field $A_i$ splits after the polarization-independent 3-dB coupler into forward (clockwise) and backward (counterclockwise) components denoted as $A_f(z,t)$ and $A_b(z,t)$ at a distance $z$ inside the loop. An intense control pulse at a different wavelength is injected after the coupler. It introduces different XPM-induced phase shifts on $A_f$ and $A_b$ as it propagates only in the forward direction. The two signal components interfere at the 3-dB coupler after one round trip. The loop transmissivity depends on the relative phase shift induced by XPM and becomes 100% for a $\pi$ phase shift provided both pulses maintain their SOP along the same direction.

To include the polarization effects, we express all optical fields by a Jones vector, denoted by $|A_j\rangle$

[10], where the subscript $j = f, b$, or $c$. The total field is given by

$$|A(z,t)\rangle = |A_c(z,t)\rangle \exp(-i\omega_c t) + [|A_f(z,t)\rangle + |A_b(z,t)\rangle] \exp(-i\omega_s t). \tag{10.8}$$

As there is a signal wave propagating backward inside the loop, to investigate the polarization, we need to stay first in the laboratory reference frame by using Eq. (2.26) rather than directly go to the rotating frame of Eq. (8.14). Substituting Eq. (10.8) into Eq. (2.26) and decomposing into individual fields, we obtain the following set of three vector equations governing the propagation of three optical fields inside the NOLM:

$$\frac{\partial |A_c\rangle}{\partial z} + \frac{1}{v_c}\frac{\partial |A_c\rangle}{\partial t} = -\frac{i}{2}\omega_c \boldsymbol{B}\cdot\boldsymbol{\sigma}|A_c\rangle + \frac{i\gamma}{3}[2\langle A_c|A_c\rangle + |A_c^*\rangle\langle A_c^*|]\,|A_c\rangle, \tag{10.9}$$

$$\frac{\partial |A_f\rangle}{\partial z} + \frac{1}{v_s}\frac{\partial |A_f\rangle}{\partial t} = -\frac{i}{2}\omega_s \boldsymbol{B}\cdot\boldsymbol{\sigma}|A_f\rangle + \frac{2i\gamma}{3}[\langle A_c|A_c\rangle + |A_c\rangle\langle A_c| + |A_c^*\rangle\langle A_c^*|]\,|A_f\rangle, \tag{10.10}$$

$$-\frac{\partial |A_b\rangle}{\partial z} + \frac{1}{v_s}\frac{\partial |A_b\rangle}{\partial t} = -\frac{i}{2}\omega_s \boldsymbol{B}\cdot\boldsymbol{\sigma}|A_b\rangle + \frac{2i\gamma}{3}[\langle A_c|A_c\rangle + |A_c\rangle\langle A_c| + |A_c^*\rangle\langle A_c^*|]\,|A_b\rangle, \tag{10.11}$$

where $\omega_j$ and $v_j$ ($j = c, s$) are the carrier frequency and the group velocity for the control and signal pulses, respectively. The nonlinear parameter $\gamma$ is taken to be nearly the same for the two waves assuming that their frequency difference $|\omega_s - \omega_c|$ is relatively small compared with the carrier frequencies themselves.

The main approximation made in deriving Eqs. (10.9)–(10.11) is that the control pulse is assumed to be much more intense than signal pulses. Thus, self-phase modulation (SPM) and XPM induced by the control pulse are included but those induced by the signal pulse are neglected because of its weak nature. Fiber losses are neglected because length of the loop is typically only a few kilometers. The effects of group-velocity dispersion (GVD) are also ignored assuming that pulses are wide enough that dispersion length exceeds the loop length considerably. To solve Eqs. (10.9)–(10.11), we make one more simplification. In practice, the XPM effects on the backward field $|A_b\rangle$ induced by the control pulse are so small because of the counterpropagating nature of two pulses (walk-off length $\sim 1$ cm even for a 100-ps pulse) that we can ignore them. The backward propagating field $|A_b\rangle$ is then only affected by fiber birefringence, and Eq. (10.11) can be solved analytically after setting $\gamma = 0$.

Because of the counterpropagating nature of the two signal pulses [26, 27], the Jones matrices associated with birefringence-induced SOP evolution for $|A_f\rangle$ and $|A_b\rangle$ are $\overleftrightarrow{\boldsymbol{T}}$ and $\overleftrightarrow{\boldsymbol{T}}^t$, respectively, where $\overleftrightarrow{\boldsymbol{T}}^t$ is the transpose of $\overleftrightarrow{\boldsymbol{T}}$, and $\overleftrightarrow{\boldsymbol{T}}$ is the solution of $d\overleftrightarrow{\boldsymbol{T}}/dz = -(i/2)\omega_s \boldsymbol{B}\cdot\boldsymbol{\sigma}\overleftrightarrow{\boldsymbol{T}}$. The solution of Eq. (10.11) can now be used to write $|A_b\rangle$ at port 2 after one round trip as

$$|A_b(0,t)\rangle = \overleftrightarrow{\boldsymbol{T}}^t(L)|A_b(L, t - L/v_s)\rangle = i\overleftrightarrow{\boldsymbol{T}}^t(L)\sigma_1|A_i(t - L/v_s)\rangle/\sqrt{2}, \tag{10.12}$$

where $|A_i\rangle$ is the input field at port 1 and $\sigma_1$ is one of the Pauli matrices [10]. The factor of $i/\sqrt{2}$ results from the transfer matrix of a 3-dB coupler, which not only splits the power into half but also introduces a $\pi/2$ phase shift [16]. The origin of $\sigma_1$ matrix lies in the fact that we are working in a reference frame associated with the forward-propagating pulse that flips its $y$-axis after a round trip (See Fig. 10.4). It is also useful to introduce a retarded time in this frame as $\tau = t - z/v_s$.

The NOLM output at port 4 corresponds to the switched pulse. The power profile of this pulse is obtained by interfering the two counterpropagating field components at the 3-dB coupler and is given by

$$P_o(\tau) = \{P_i(\tau) - \mathrm{Re}[\rho_0(L,\tau)]\}/2, \tag{10.13}$$

where Re denotes the real part, $P_i(\tau) = \langle A_i(\tau)|A_i(\tau)\rangle$ is the input pulse profile at port 1 of the coupler, and the scalar quantity $\rho_0$ describes the interference effects and is defined as

$$\rho_0(z,\tau) = \langle A_i(\tau)|\sigma_1 \overleftrightarrow{\boldsymbol{T}}^*(L)\sigma_1 \overleftrightarrow{\boldsymbol{T}}(L)|A'_f(z,\tau)\rangle, \tag{10.14}$$

where $\overleftrightarrow{\boldsymbol{T}}^*$ is the complex conjugate of $\overleftrightarrow{\boldsymbol{T}}$ and we used the relation $|A_f(z,\tau)\rangle = \overleftrightarrow{\boldsymbol{T}}(z)|A'_f(z,\tau)\rangle$ since $|A'_f(z,\tau)\rangle$ is only affected by the XPM from the control pulse; it would remain constant in the absence of the XPM effects. All birefringence-induced polarization effects are included through the random quantity $\rho_0$.

Residual birefringence affects the NOLM output in two ways. First, it randomizes the SOPs of the control and signal pulses along the fiber and thus affects the XPM process locally. Second, because of the interferometric nature of the NOLM, SOP variations affect the output even in the absence of any control pulse [26], [27]. To optimize the performance, a polarization controller is adjusted inside the loop such that $P_o$ is minimum in the absence of control pulses. Mathematically, this is equivalent to setting $\sigma_1 \overleftrightarrow{\boldsymbol{T}}^* \sigma_1 \overleftrightarrow{\boldsymbol{T}} = \sigma_0$ [28], where $\sigma_0$ is a unit matrix and $\overleftrightarrow{\boldsymbol{T}}$ includes the SOP rotation induced by the polarization controller. If residual birefringence varies with time because of environmental perturbations, $\overleftrightarrow{\boldsymbol{T}}$ also changes randomly on a time scale associated with birefringence fluctuations. We assume that optimization is maintained by adjusting the polarization controller adaptively and focus only on the PMD effects on XPM inside the NOLM. The quantity $\rho_0$ is then given by $\rho_0(z,\tau) = \langle A_i(\tau)|A'_f(z,\tau)\rangle$ and does not require knowledge of the matrix $\overleftrightarrow{\boldsymbol{T}}(L)$.

### 10.2.2 XPM-Induced Switching

To calculate $\rho_0$, we need the field $|A'_f(L,\tau)\rangle$ after its phase has been affected by the control pulse through XPM. By noting that $|A'_f(L,\tau)\rangle$ is the field vector in the rotating frame as what discussed in Chapter 7, and that rapid SOP variations induced by $\overleftrightarrow{\boldsymbol{T}}(z)$ average over the nonlinear effects, rather than performing SVPA on Eqs. (10.9) and (10.10), we can directly use Eq. (8.14) to find the dynamic equation for the forward propagating signal and control waves. After decomposing Eq. (8.14) into two frequency components as what we did in the last section, we find that $|A'_f(z,\tau)\rangle$ and $|A'_c(z,\tau)\rangle = \overleftrightarrow{\boldsymbol{T}}^{-1}(z)|A_c(z,\tau)\rangle$ evolve inside the loop as [9]

$$\frac{\partial|A'_f\rangle}{\partial z} = \frac{i\gamma_e}{2}P_c(z,\tau)\,(3+\hat{p}\cdot\boldsymbol{\sigma})\,|A'_f\rangle, \tag{10.15}$$

$$\frac{\partial|A'_c\rangle}{\partial z} + \delta\beta_1\frac{\partial|A'_c\rangle}{\partial\tau} = -\frac{i}{2}\Omega\boldsymbol{b}\cdot\boldsymbol{\sigma}|A'_c\rangle + i\gamma_e P_c(z,\tau)|A'_c\rangle, \tag{10.16}$$

where $\Omega = \omega_c - \omega_s$ is the carrier frequency difference between the two pulses and $\delta\beta_1 = 1/v_c - 1/v_s$ describes their group-velocity mismatch. Different from the last section, we use the signal frequency as the carrier when we used Eq. (8.14), just for convenience.

Equations (10.15) and (10.16) show that both the power $P_c$ and the SOP $\hat{p}$ of the control pulse affect the XPM-induced phase shift. The power of the control pulse is given by $P_c(z,\tau) = \langle A'_c|A'_c\rangle = \langle A_c|A_c\rangle$. Its SOP is governed by the unit vector $\hat{p}(z,\tau) = \langle A'_c|\boldsymbol{\sigma}|A'_c\rangle/P_c$, representing the direction of its Stokes vector on the Poincaré sphere. Both the control and signal pulses maintain their shape inside the NOLM (assuming negligible dispersion-induced pulse broadening) although two pulses walk away from each other because of group-velocity mismatch. Thus $P_c(z,\tau) = P_c(0,\tau-\delta\beta_1 z)$ in Eqs. (10.15) and (10.16). This feature simplifies the following analysis considerably.

The output power $P_o$ of the switched pulse is determined by the interference term $\rho_0$. We use its expression together with Eqs. (10.15) and (10.16) to arrive at the following set of three closed equations:

$$\frac{\partial\rho_0}{\partial z} = \frac{i\gamma_e P_c}{2}\,(3\rho_0 + \hat{p}\cdot\boldsymbol{\rho})\,, \tag{10.17}$$

$$\frac{\partial\boldsymbol{\rho}}{\partial z} = \frac{i\gamma_e P_c}{2}\,(3\boldsymbol{\rho} + \rho_0\hat{p}) - \frac{\gamma_e}{2}P_c\hat{p}\times\boldsymbol{\rho}, \tag{10.18}$$

$$\frac{\partial\hat{p}}{\partial z} = \Omega\boldsymbol{b}\times\hat{p}, \tag{10.19}$$

where the vector $\boldsymbol{\rho}$ is introduced as $\boldsymbol{\rho}(z,\tau) = \langle A_i(\tau)|\boldsymbol{\sigma}|A'_f(z,\tau)\rangle$. Notice that both $\rho_0$ and $\boldsymbol{\rho}$ are complex quantities and related through the identities $\rho_0^2 = \boldsymbol{\rho}^2$ and $|\rho_0|^2 + |\boldsymbol{\rho}|^2 = 2P_i^2$. The statistics of $\boldsymbol{b}$ is given by Eq. (8.16). Equations (10.17)-(10.19) are three linear stochastic equations and can be easily solved numerically to find $\rho_0$ and then calculate transmitted power $P_o(\tau)$ for given temporal profiles, $P_i(\tau)$ and $P_c(0,\tau)$, for the input and control pulses, respectively.

To show the effects of PMD on the switching window of an NOLM, we consider a 3-km long NOLM with $\gamma = 2\mathrm{W}^{-1}/\mathrm{km}$, $D_p = 0.1\mathrm{ps}/\sqrt{\mathrm{km}}$, $\beta_3 = 0.1\mathrm{ps}^3/\mathrm{km}$, and a zero-dispersion wavelength (ZDWL) of $\lambda_0 = 1550$ nm. The power of the Gaussian-shape control pulse at 1545 nm varies as $P_c(0,\tau) = P_0\exp(-\tau^2/T_0^2)$, where $T_0 = 10$ ps and peak power $P_0 = 820$ mW. The signal is assumed to have a continuum-wave (CW) form at a wavelength of 1575 nm. The switching window is defined as the loop transmissivity as $P_o(\tau)/P_i(\tau)$. The 30-nm wavelength difference between the signal and control waves

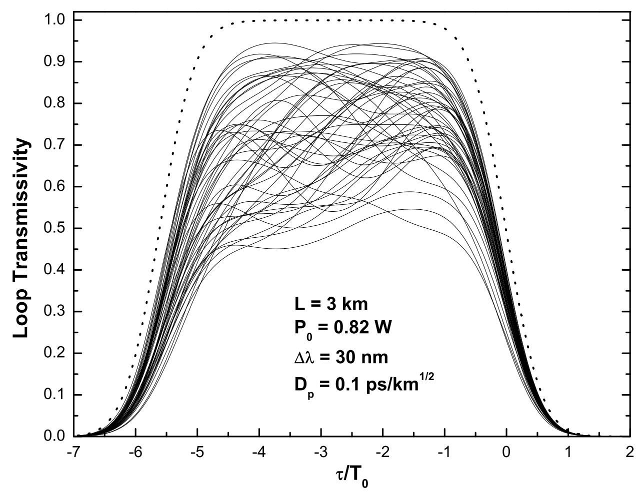


Figure 10.5: Switching windows of a NOLM under the impact of residual birefringence (solid curves) created by a Gaussian-shape control pulse. The dotted curve shows for comparison the switching window in the absence of residual birefringence. For all the curves, the control and signal waves are linearly copolarized at the location where the control pulse is injected into the loop. Parameters are given in the text.

introduces considerable walk off between the two and produces a nearly rectangular 40-ps switching window shown by the dotted line in Fig. 10.5 when fiber has no birefringence (the ideal case). When residual birefringence is included by choosing $D_p = 0.1\text{ps}/\sqrt{\text{km}}$ and a correlation length of 10 m, the switching window depends on the birefringence distribution along the fiber length and varies for each realization of the stochastic process. Figure 10.5 shows some examples of the switching window obtained by solving Eqs. (10.9)-(10.11) numerically, assuming that the signal and control are linearly copolarized at the location where the control is injected to the loop. A comparison of these curves with the dotted curve shows that PMD effects not only reduce the NOLM transmission during switching but also make the transmissivity to vary with time along the switching window. As a result, switching window become distorted, and the extent of distortion depends on the specific distribution of residual birefringence inside the NOLM. Since this distribution will change from fiber to fiber, different NOLMs made from the same spool of fiber would exhibit quite different switching performances.

One may wonder what makes NOLM transmission to vary randomly within the switching window for a given NOLM if nothing is changing with time. More specifically, if both $P_i$ and $P_c$ are deterministic quantities at any time $\tau$, why $P_o$ fluctuates in a random fashion with $\tau$. From a physical standpoint, this is a consequence of PMD-induced changes in the SOP of various fields and resulting variations in the XPM efficiency. The combination of the two effects produces *intrapulse* depolarization for the signal manifested as a random SOP of the signal along the pulse profile [1], as discussed in Section 1. In effect, spatial randomness of residual birefringence is translated into temporal randomness at the NOLM output by the Sagnac interferometer.

### 10.2.3 Average Output Power and Fluctuation Level

As seen in Fig. 10.5, the NOLM output is random in two ways because of PMD. First, if birefringence distribution along the fiber length is frozen and does not change with time, switching window is distorted but is static. The output power then varies along the switching window in a random fashion but does not fluctuate at any given moment. Second, if birefringence distribution along the fiber length changes with time in a dynamic fashion because of environmental perturbations, the output power at any instant of time itself begins to fluctuate on a time scale associated with such perturbations. Although this time scale is relatively long (ranging from a few seconds to several hours), such random fluctuations in the output of an NOLM are not acceptable in practice. It is thus important to estimate the average and variance of such environment-induced power fluctuations. It turns out that these two moments of the output power can be calculated in a semi-analytical fashion.

The average value $\langle P_o \rangle$ and variance $\sigma_o^2 = \langle P_o^2 \rangle - \langle P_o \rangle^2$ of the output power are obtained from Eq. (10.13) and are related to the moments of $\rho_0$ as

$$\langle P_o \rangle(\tau) = \{P_i(\tau) - \mathrm{Re}[\langle \rho_0 \rangle(L,\tau)]\}/2, \tag{10.20}$$

$$\sigma_o^2(\tau) = [\mathrm{Re}(\langle \rho_0^2 \rangle - \langle \rho_0 \rangle^2) + \langle |\rho_0|^2 \rangle - |\langle \rho_0 \rangle|^2]/8. \tag{10.21}$$

The evolution equations for $\langle \rho_0 \rangle$, $\langle \rho_0^2 \rangle$, and $\langle |\rho_0|^2 \rangle$ can be obtained from Eqs. (10.17)-(10.19) after averaging over random residual birefringence using a procedure described in Ref. [25]. For the mean value of $\rho_0$, we obtain the following two coupled equations:

$$\frac{\partial \langle \rho_0 \rangle}{\partial z} = \frac{i\gamma_e P_c}{2} \left(3\langle \rho_0 \rangle + \langle \hat{p} \cdot \rho \rangle\right), \tag{10.22}$$

$$\frac{\partial \left(\langle \hat{p} \cdot \rho \rangle\right)}{\partial z} = -\eta \left(\langle \hat{p} \cdot \rho \rangle\right) + \frac{i\gamma_e P_c}{2} \left(\langle \rho_0 \rangle + 3\langle \hat{p} \cdot \rho \rangle\right), \tag{10.23}$$

where $\eta = 1/L_d = (D_p \Omega)^2/3$ and $L_d$ is the PMD diffusion length of the relative SOP orientation between the two pulses. Note that $L_d$ is not only a function of the PMD parameter of fiber, but also depends on the the carrier frequency separation between the control and signal pulses, which plays an important role on the switching performance.

Following the same procedure, the second-order moment $\langle \rho_0^2 \rangle$ is obtained by solving the following three coupled equations:

$$\frac{\partial\langle\rho_0^2\rangle}{\partial z} = i\gamma_e P_c \left(3\langle\rho_0^2\rangle + U_1\right), \tag{10.24}$$

$$\frac{\partial U_1}{\partial z} = (3i\gamma_e P_c - \eta)U_1 + \frac{i\gamma_e P_c}{2}\left(V_1 + \langle\rho_0^2\rangle\right), \tag{10.25}$$

$$\frac{\partial V_1}{\partial z} = (3i\gamma_e P_c - 3\eta)V_1 + \eta\langle\rho_0^2\rangle + i\gamma_e P_c U_1, \tag{10.26}$$

where $U_1 = \langle\hat{p}\cdot\rho_0\boldsymbol{\rho}\rangle$ and $V_1 = \langle(\hat{p}\cdot\boldsymbol{\rho})^2\rangle$. Similarly, $\langle|\rho_0|^2\rangle$ can be obtained by solving

$$\frac{\partial\langle|\rho_0|^2\rangle}{\partial z} = \gamma_e P_c U_2, \tag{10.27}$$

$$\frac{\partial U_2}{\partial z} = -\eta U_2 + \gamma_e P_c\left(V_2 - \langle|\rho_0|^2\rangle\right), \tag{10.28}$$

$$\frac{\partial V_2}{\partial z} = -3\eta V_2 - \gamma_e P_c U_2 + \eta\left(2P_i^2 - \langle|\rho_0|^2\rangle\right). \tag{10.29}$$

where $U_2 = \mathrm{Im}(\langle\hat{p}\cdot\rho_0\boldsymbol{\rho}^*\rangle)$, $V_2 = \langle|\hat{p}\cdot\boldsymbol{\rho}|^2\rangle$, and Im denotes the imaginary part. All of these deterministic equations can be solved easily on a computer. Analytical solutions can also be obtained in some specific cases.

We first consider the loop transmissivity for a square-shape control pulse when the control and signal wavelengths are tuned symmetrically around the ZDWL so that their group velocities always match. The switching window under such conditions has the same shape and duration as the control pulse. We focus on the same 3-km long fiber loop used for Fig. 10.5 but set the control peak power to $P_\pi = 262$ mW, a value that represents the control power for which the entire copolarized signal is transmitted in the absence of residual birefringence when there is no walk-off between the two pulses. Figure 10.6(a) shows the average loop transmissivity (or switching contrast) defined as $T_L = \langle P_o\rangle/P_i$ at the control pulse peak by plotting $T_L$ as a function of signal-control wavelength detuning $\Delta\lambda = |\lambda_s - \lambda_c|$ for three values of the PMD parameter $D_p$. Figure 10.6(b) shows the fluctuation level, defined as $\sigma_o/P_i$, under the same conditions. In both cases, solid and dashed curves are respectively for the copolarized and orthogonally polarized control pulse with respect to the signal SOP at the input end. Dotted curves show for comparison the no-birefringence case for these two polarization configurations. The control only imposes a phase shift of $\pi/3$ on the signal when the two are orthogonally polarized, resulting in only 25% transmission in the ideal case (lower dotted line).

To justify the semi-analytical theory presented here, we carried out full numerical simulations based on Eqs. (10.9)–(10.11) by dividing the 3-km-long fiber into 10-m long sections. Birefringence was kept constant inside each section but both its magnitude and axes are changed randomly from section to section. More precisely, the magnitude of birefringence follows a Gaussian distribution with zero mean while the principal axes are rotated uniformly after each section. The results averaged over 300 runs are

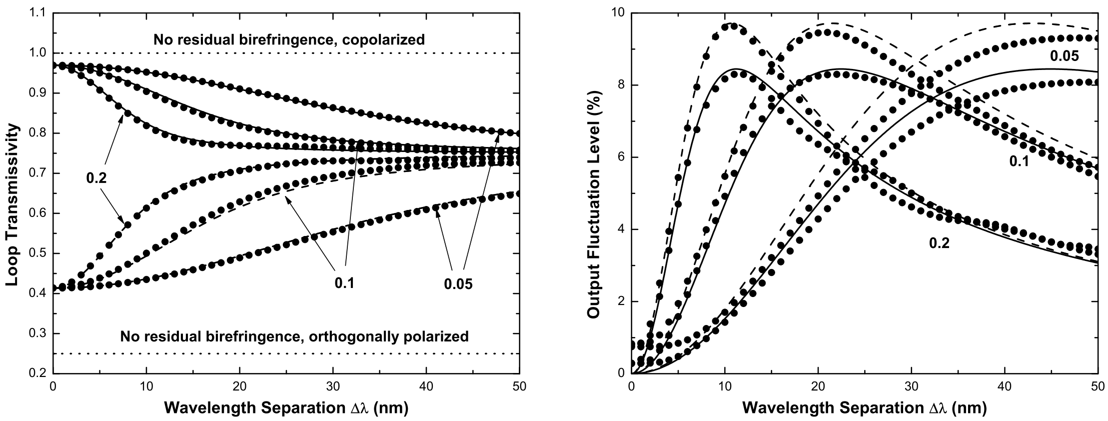


Figure 10.6: Switching contrast (a) and fluctuation level of output (b) plotted as a function of wavelength separation between the signal and control for three values of PMD parameter $D_p$ (in units of ps/$\sqrt{\text{km}}$) for the copolarized (solid curves) and orthogonally polarized (dashed curves) cases. Dotted lines show the no-birefringence case for the same two polarization configurations. Filled circles shows the Monte–Carlo simulation results.

shown as filled circles in Fig. 10.6. The semi-analytical results agree quite well with the Monte–Carlo numerical simulations. In particular, the predicted average transmissivity almost coincides in the two cases. A small discrepancy seen in the prediction of the fluctuation level comes from the sample size of 300 used for numerical simulations. It decreases as the sample size is increased but only at the expense of a longer computational time.

As seen in Fig. 10.6(a), residual birefringence of the fiber loop reduces the NOLM transmission considerably on average for copolarized signal and control pulses, thereby degrading the switch performance. When $\Delta\lambda$ is small enough to make PMD diffusion length $L_d$ larger than the NOLM length $L$, the signal and control nearly maintain their relative SOPs inside the NOLM even though the SOP of each field can change considerably. The switching contrast is then only affected by reduction in $\gamma$ by a factor of 8/9 and is reduced by a mere 3% for $\Delta\lambda = 1$ or 2 nm. The similar effect in the orthogonally polarized case increases the XPM-induced nonlinear phase from $\pi/3$ to $4\pi/9$, resulting in a loop transmissivity of 41.3%. However, the average switching contrast changes quickly with increase in $\Delta\lambda$ or $D_p$, as seen in Fig. 10.6(a). In fact, the NOLM approaches a polarization-independent switching contrast of 75% (corresponding to a nonlinear phase shift of $2\pi/3$) for large wavelength separations such that $L_d \ll L$. These results are qualitatively consistent with the experimental results of [23]. The level of PMD-induced fluctuations depends on the length ratio $\mu = L_n/L_d$, where $L_n = (2\gamma_e P_0)^{-1}$ is the nonlinear length for XPM-induced phase shift. It becomes maximum when $\mu \approx 1$, resulting in a peak value of about 9% in Fig. 10.6(b). Around the spectral region where $\mu \approx 1$, the NOLM is most susceptible to environmental

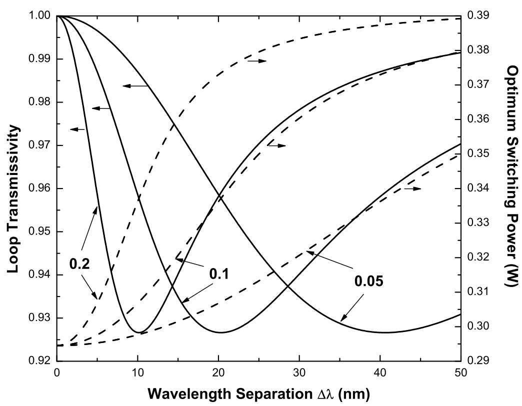


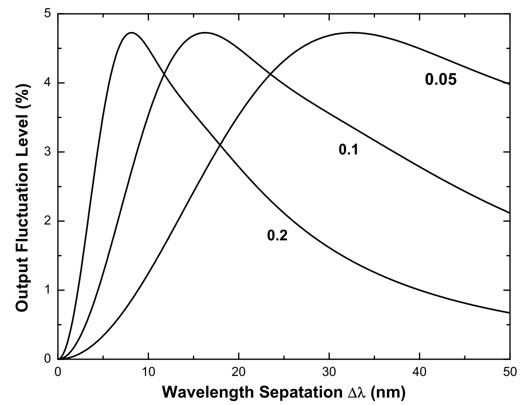


Figure 10.7: (a) Maximum switching contrast (solid curves) and optimum control power (dashed curves) as a function of wavelength separation between the signal and control (both linearly copolarized initially) for three values of PMD parameter $D_p$ (in units of ps/$\sqrt{\text{km}}$). (b) Output fluctuation level under the optimum conditions.

perturbations. The qualitative behavior is similar for all values of $D_p$. The only difference is that the peak in Fig. 10.6(b) shifts to smaller values of $\Delta\lambda$ for larger values of $D_p$.

The PMD-induced reduction in the switching contrast can be compensated to some extent by increasing the control power $P_c$. This increase in control power was observed in the experiment of [21]. Of course, the optimum value of power depends on both the wavelength separation $\Delta\lambda$ and the value of the PMD parameter $D_p$. Moreover, it is not possible to realize 100% switching contrast even with this optimization. The solid and dashed curves in Fig. 10.7(a) show, respectively, the optimized switching contrast and the control power required for it as a function of $\Delta\lambda$ for copolarized control and signal at the input end. When $\Delta\lambda \approx 0$, the reduction in $\gamma$ can be overcome by increasing $P_\pi$ from 262 to 295 mW for complete switching. However, this power level increases to 380 mW for $\Delta\lambda = 50$ nm inside a fiber with $D_p = 0.1$ ps$/\sqrt{\text{km}}$, even if there is no walk off between the two waves. Complete switching with 100% contrast becomes difficult to realize when $\mu \approx 1$. As seen in Fig. 10.7(a), the optimized switching contrast is close to 92% when $\mu$ is close to 1. Figure 10.7(b) shows the the fluctuation level under optimum conditions. It is reduced considerably compared with the values seen in Fig. 10.6(b). Maximum fluctuation level is about 4.5% and occurs again when $\mu$ is close to 1.

### 10.2.4 Switching Window

We now consider the temporal switching window and assume that the NOLM output is being switched for a short duration using control pulses of Gaussian shape with $T_0 = 10$ ps and a peak power of 262 mW.

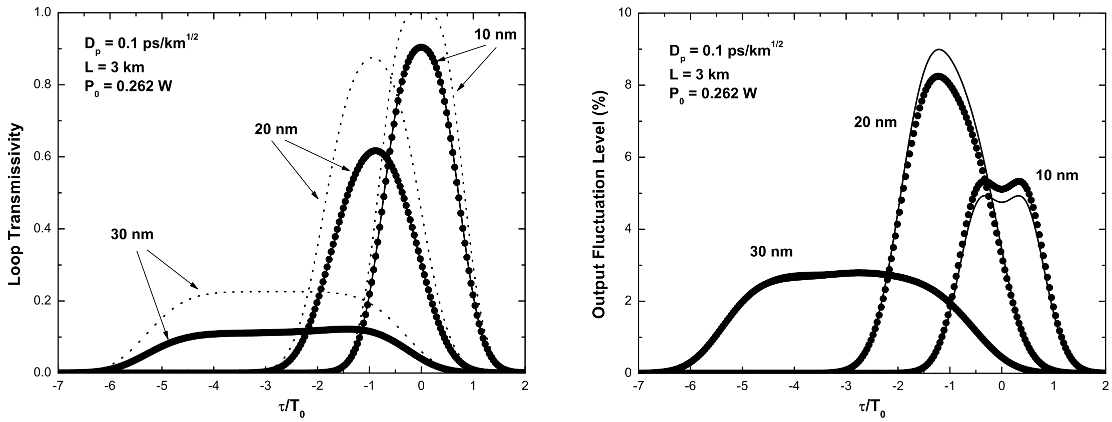


Figure 10.8: Switching windows (a) and fluctuation level of output (b) for three values of wavelength separation between the signal and control waves. The control is fixed at 1545 nm but the signal wavelengths are 1555, 1565, 1575 nm for the three cases, respectively. In each case, NOLM transmissivity is plotted as a function of time for Gaussian-shape control pulses. Solid lines show the analytical results and dotted lines show for comparison the no-birefringence case. Filled circles show the Monte-Carlo simulation results, which overlap with the solid curves in most of the cases.

The control wavelength of 1545 nm is 5-nm shorter than the 1550-nm ZDWL of the fiber loop. The signal is again in the CW form but our results also apply for a pulsed signal as long as the signal pulse is much wider than the control pulse. The two waves are linearly copolarized at the location where the control is injected to the loop. The signal wavelength is varied from 1555 to 1575 nm to study the impact of the group-velocity mismatch, whose magnitude can be calculated from the third-order dispersion of the fiber using $\delta\beta_1 = 1/v_c - 1/v_s = \beta_3(\omega_c - \omega_s)(\omega_c + \omega_s - 2\omega_0)/2$, where $\omega_0 = 2\pi c/\lambda_0$ is the zero-dispersion frequency. The fiber is assumed to have a third-order dispersion of $\beta_3 = 0.1$ ps$^3$/km at ZDWL. The GVD-induced pulse broadening can be neglected because the dispersion lengths exceed 50 km in all cases.

Solid curves in Figure 10.8(a) show the "averaged" switching window by plotting average value of the NOLM transmissivity $\langle P \rangle_o(\tau)/P_i(\tau)$ as a function of time for three signal wavelengths separated from the control wavelength by 10, 20, and 30 nm. All NOLM parameters are the same as those used for Fig. 10.6 except for $D_p = 0.1$ ps/$\sqrt{\text{km}}$. Dotted curves show the switching window in the absence of residual birefringence. The switching window is relatively narrow and has 100% contrast at its peak for $\Delta\lambda = 10$ nm because the walk-off effects disappear when the control and signal wavelengths are located symmetrically around the ZDWL. The walk-off effects broaden the switching window and reduce the transmissivity as $\Delta\lambda$ increases to 20 and 30 nm. The PMD effects make the situation worse because they reduce the transmissivity even further and also make the switching window asymmetric. The asymmetry is related to the fact that control pulse overlaps with different slices of the signal pulse at different locations inside the fiber.

When $\Delta\lambda = 20$ nm, a value for which $\mu \approx 1$, only 60% of signal power can be switched to output port on average and this value drops to below 15% for $\Delta\lambda = 30$ nm. Figure 10.8(b) shows the fluctuation level within the switching window under the conditions of Fig. 10.8(a). The peak fluctuation level is under 5% for $\Delta\lambda = 10$ nm, increases to around 9% for $\Delta\lambda = 20$ nm and then drops to below 3% for $\Delta\lambda = 30$ nm. This behavior is similar to that seen in Fig. 10.6 but is modified significantly because of the reduction in the XPM effects induced by pulse walk-off. For $D_p = 0.1$ ps/$\sqrt{\text{km}}$, large fluctuations occur for $\Delta\lambda = 20$ nm but are reduced considerably for smaller or larger wavelength separations. Again, the analytical results agree well with the numerical ones based on full Monte–Carlo simulations (filled circles). Note that the fluctuation level depends on the control peak power as well as the loop length. If the control peak power is increased to achieve a maximum peak switching contrast as shown in Fig. 10.5 for $\Delta\lambda = 30$ nm, the fluctuation level will increase considerably.

### 10.2.5 Conclusions

In this section we have presented a vector theory of XPM that is capable of including the PMD effects while describing the switching performance of an NOLM. The interaction between the PMD and XPM phenomena transfers the spatial randomness of residual birefringence to temporal fluctuations on the switched-pulse profile. Physically speaking, the combination of PMD and XPM induces intrapulse depolarization on the signal in the sense that different parts of the signal pulse have different randomly varying SOPs. Because of this depolarization, PMD reduces the switching contrast and the polarization dependence when signal and control wavelengths are chosen to be further apart than a few nanometers. The contrast can be improved to some extent by increasing the control power but it cannot be made 100% in the spectral region where the PMD diffusion length becomes comparable to the nonlinear length. Under environmental perturbations, PMD induced fluctuations on the switched pulse can be up to 9% of the input power, depending on the fiber length and the value of the PMD parameter for that fiber. Our results qualitatively agree with the existing experimental observations [21, 23]. Further experiments would help to verify our predictions.

The use of a polarization-diversity loop has been proposed to reduce the polarization dependence of an NOLM-vased optical switch [22], [32]. Our analysis shows that such a loop cannot mitigate the PMD effects on XPM because of the PMD and XPM effects interact locally all along the loop length. For the same reason, a Faraday mirror inside a folded ultrafast nonlinear interferometer can reduce the effect of global SOP evolution induced by linear birefringence [21], [33] but it cannot eliminate the degradation induced by local interaction between the PMD and XPM. For these reasons, PMD is likely to remain a limiting factor for XPM-based optical switching whenever fiber-loop lengths exceeds a few kilometers. The ultimate solution of this problem relies on the availability of fibers with ultra-low PMD and high nonlinearity. Even though the intrinsic nonlinearity of silica, governed by the $n_2$ parameter, cannot be changed, the nonlinear parameter $\gamma$ can be enhanced by reducing the effective core area $a_{\mathrm{eff}}$ of the fiber since the two are related as $\gamma = 2\pi n_2/(\lambda a_{\mathrm{eff}})$ [24]. A fiber with large values of $\gamma$ is referred to as a highly nonlinear fiber. An increase in $\gamma$ by a factor of 8–10 will reduce the loop length of NOLMs to below 400 m and will help to increase the device performance considerably [34], [35].

We should stress that our analytic theory is based on the assumption of a delta-function correlation among residual birefringence fluctuations. We have performed numerical simulations to judge the validity of this approximation by changing the birefringence correlation length $l_c$. The results shown in Figs. 10.6-10.8 change only by a small amount even when $l_c$ is increased up to 100 m. Numerical simulations show that our analytic theory works reasonably well when the NOLM length is 10 to 15 larger than the birefringence correlation length. In the case of highly nonlinear fibers, loop lengths of less than 100 m may be sufficient for optical switching. Similarly, for pulses shorter than a few picoseconds, loop length is generally kept short as $\sim$ 100 m to prevent pulse broadening. In these cases, residual birefringence fluctuations cannot be treated as delta-correlated (white noise), and a numerical approach should be used. On the other hand, even though it is easy to include numerically pulse broadening induced by GVD and higher-order dispersion, we have not done so since the loop length is generally kept shorter than the dispersion length in almost all practical situations.

## References

[1] Q. Lin and G. P. Agrawal, Opt. Lett. **30**, 821 (2005).

[2] Q. Lin and G. P. Agrawal, IEEE J. Sel. Top. Quant. Electron. **10**, 1107 (2004).

[3] C. P. Slichter, *Principles of Magnetic Resonance*, 3rd ed. (Springer, New York, 1990).

[4] F. Meier and B. Zakharchenya, Eds., *Optical Orientation* (North-Holland, New York, 1984).

[5] D. Awschalom, D. Loss, and N. Samarth, Eds., *Semiconductor Spintronics and Quantum Computation* (Springer, New York, 2002).

[6] Y. Semenov and K. Kim, Phys. Rev. Lett. **92**, 026601 (2004), and references therein.

[7] L. Allen and J. H. Eberly, *Optical Resonance and Two-level atoms* (Wiley, New York, 1975).

[8] J. H. Eberly, K. Wódkiewicz, and B. W. Shore, Phys. Rev. A **30**, 2381 (1984), and references therein.

[9] Q. Lin and Govind P. Agrawal, J. Lightwave Technol. **22**, 977 (2004).

[10] J. P. Gordon and H. Kogelnik, Proc. Natl. Acad. Sci. USA **97**, 4541 (2000).

[11] A. Galtarossa, L. Palmieri, M. Schiano, and T. Tambosso, Opt. Lett. **25**, 384 (2000); Opt. Lett. **26**, 962 (2001).

[12] C. W. Gardiner, *Handbook of Stochastic Methods*, 2nd ed. (Springer, New York, 1985).

[13] K. J. Blow, N. J. Doran, B. K. Nayar, and B. P. Nelson, Opt. Lett. **15**, 248 (1990).

[14] P. Boffi, L. Marazzi, and M. Martinelli, IEEE Photon. Technol. Lett. **11**, 1393 (1999).

[15] J. Yu, X. Zheng, C. Peucheret, A. T. Clausen, H. N. Poulsen, and P. Jeppesen, J. Lightwave Technol. **18**, 1007 (2000).

[16] G. P. Agrawal, *Applications of Nonlinear Fiber Optics*, 3*rd* ed. (Academic Press, San Diego, 2001), Chap. 3.

[17] J. H. Lee, P. C. Teh, P. Petropoulos, M. Ibsen, and D. Richardson, IEEE Photon. Technol. Lett. 203 (2002).

[18] N. Chi, L. Xu, K. S. Berg, T. Torger, and P. Jeppesen, IEEE Photon. Technol. Lett. **14**, 1581 (2002).

[19] N. Finlayson, B. K. Nayar, and N. J. Doran, Opt. Lett. **17**, 112 (1992).

[20] M. F. Arend, M. L. Dennis, I. N. Duling III, E. A. Golovchenko, A. N. Pilipetskii, and C. R. Menyuk, Opt. Lett. **. 22**, 886 (1997).

[21] C. Vinegoni, M. Wegmuller, B. Huttner, and N. Gisin, Opt. Commun. **182**, 335 (2000).

[22] T. Sakamoto, H. C. Lim, and K. Kikuchi, IEEE Photon. Technol. Lett. **14**, 1737 (2002).

[23] B. Olsson and P. A. Andrekson, Proc. Optical Fiber Commun. Conf., paper FA7 (Optical Society of America, Washington, DC, 1998).

[24] G. P. Agrawal, *Nonlinear Fiber Optics*, 3rd ed. (Academic Press, San Diego, 2001).

[25] Q. Lin and G. P. Agrawal, J. Opt. Soc. Am. B **20**, 1616 (2003).

[26] D. B. Mortimore, J. Lightwave Technol. **6**, 1217 (1988).

[27] T. A. Birks and P. Morkel, Appl. Opt. **27**, 3107 (1988).

[28] C. Kolleck and U. Hempelmann, J. Lightwave Technol. **15**, 1906 (1997).

[29] P. K. A. Wai and C. R. Menyuk, J. Lightwave Technol, vol. 14, 148 (1996).

[30] G. J. Foschini and C. D. Poole, J. Lightwave Technol. **9**, 1439 (1991).

[31] M. Shtaif, A. Mecozzi, and J. A. Nagel, IEEE Photon. Technol. Lett. **12**, 53 (2000).

[32] B. Olsson and P. A. Andrekson, IEEE Photon. Technol. Lett. **9**, 764 (1997).

[33] S. J. Savage, B. S. Robinson, S. A. Hanilton, and E. P. Ippen, Opt. Lett. **28**, 13 (2003).

[34] J. E. Sharping, M. Fiorentino, P. Kumar, and R. S. Windeler, IEEE Photon. Technol. Lett. **14**, 77 (2002).

[35] H. Sotobayashi, C. Sawaguchi, Y. Koyamada, W. Chujo, Opt. Lett. **27**, 1555 (2002).

# 11 PMD and Four-Wave Mixing

In this chapter, we investigate a more complicated situation in which the nonlinear interaction is based on the mixing of three or four waves: FWM. We investigate the mechanism underlying the interaction between PMD and FWM, and discuss its impact on fiber optic parametric amplifiers (FOPAs) and wavelength converters [1, 2]. We show that PMD is likely to be one of the limiting factor to current FOPAs. It distorts the gain spectrum and makes it less uniform than that expected in the absence of residual birefringence. It also induces large fluctuations in the amplified or wavelength-converted signal. Such PMD-FWM interactions affect all techniques based on FWM. For another example, we show how it affects the mapping of zero-dispersion wavelength (ZDWL) in optical fibers [3]. Some of the work were done in collaboration with Fatih Yaman in Prof. Agarawal's group and with Dr. Stojan Radic's group at UCSD (previously at Bell Lab, Lucent Technologies).

## 11.1 Introduction

Fiber-optic parametric amplifiers (FOPAs), based on FWM occurring inside optical fibers, can provide high gain over a relatively wide bandwidth [4]-[6]. However, the underlying FWM process is highly polarization dependent [7]. Residual birefringence inside optical fibers not only randomizes the state of polarization (SOP) of any optical wave, but also induces differential polarization variations among waves of different frequencies through PMD [8]. In the presence of PMD, the pump, signal, and idler waves cannot maintain their relative SOPs along the fiber, resulting in degradation of the FOPA performance unless a polarization-maintaining fiber is used. Moreover, since PMD can change with time because of environmental variations, it would induce fluctuations in the amplified signal in practice. Although PMD effects have been observed in experiments [6],[9]-[11], theory describing such effects is not yet fully developed. In this chapter, we present a vector theory for the FWM process and use it to quantify the impact of PMD on the performance of FOPAs and wavelength converters.

On the other hand, accurate knowledge of fiber dispersion is very important for the applications of optical fibers. As FWM is a coherent parametric process very sensitive to phase matching condition, it becomes an ideal nondestructive technique for dispersion characterization. Clearly, PMD would affect the characterization accuracy. In this chapter, we will also use the theory to quantify the measurement accuracy of zero-dispersion-wavelength mapping based on FWM inside fibers.

## 11.2 Single-Pump Configuration

In this section, we focus the simplest FWM which induced by a single pump and the total field is given by

$$|A(z,t)\rangle = |A_p(z)\rangle \exp(-i\omega_p t) + |A_s(z)\rangle \exp(-i\omega_s t) + |A_i(z)\rangle \exp(-i\omega_i t), \tag{11.1}$$

where energy conservation requires $2\omega_p = \omega_s + \omega_i$, which indicates that the signal and idler frequencies are symmetrically located around the pump. For convenience, we set the carrier frequency at the pump ($\omega_0 = \omega_p$) in Eq. (8.14). Substituting Eq. (11.1) into Eq. (8.14), neglecting the Raman contribution by setting $f_R = 0$, and decomposing into different frequency components, we find the pump wave is governed by a simple equation as

$$\frac{d|A_p\rangle}{dz} = i\beta_p |A_p\rangle + i\gamma_e \langle A_P|A_P\rangle |A_p\rangle, \tag{11.2}$$

where $\gamma_e = 8\gamma/9$ and $\beta_p$ is the propagation constant for the pump. Equation (11.2) provides a simple solution for the pump as $|A_p(z)\rangle = |A_p(0)\rangle \exp[i\int_0^z(\beta_p + \gamma_e P_0)dz]$, where $P_0 = \langle A_p|A_p\rangle$ is the pump power. Making a transformation for the signal and idler fields as $|A(z)\rangle = |A'(z)\rangle \exp[i\int_0^z(\beta_p + \gamma_e P_0)dz]$, We obtain the signal and idler equations as

$$\frac{d|A_s\rangle}{dz} = i\left(\Delta\beta_s - \frac{1}{2}\Delta\omega \boldsymbol{b}\cdot\boldsymbol{\sigma}\right)|A_s\rangle + i\gamma_e\left[\langle A_p|A_s\rangle + \langle A_i|A_p\rangle\right]|A_p\rangle, \tag{11.3}$$

$$\frac{d|A_i\rangle}{dz} = i\left(\Delta\beta_i + \frac{1}{2}\Delta\omega \boldsymbol{b}\cdot\boldsymbol{\sigma}\right)|A_i\rangle + i\gamma_e\left[\langle A_p|A_i\rangle + \langle A_s|A_p\rangle\right]|A_p\rangle, \tag{11.4}$$

where $\Delta\beta_j = \beta_j - \beta_p,\ (j = s, i)$, $\Delta\omega = \omega_s - \omega_p$, and we have dropped the prime for simplicity. The statistics for the birefringence vector $\boldsymbol{b}$ is given by Eq. (8.16).

Several approximations were made in deriving Eqs. (11.2)-(11.4). Fiber losses were neglected because of short fiber lengths used commonly for making FOPAs. We also neglected pump depletion because pump power is much larger than the signal and idler powers in practice. For the same reason, SPM is included for the pump but neglected for the signal and idler. Equations (11.3) and (11.4) includes XPM induced by the pump because XPM affects phase matching of the FWM process and leads to nonlinear polarization rotation (NPR) of the signal and idler waves.

In the absence of birefringence, Eqs. (11.3) and (11.4) reduce to the scalar case when the three waves are linearly copolarized since they maintain their input SOP. In the presence of residual birefringence, the XPM and FWM processes depend only on $\langle A_s|A_p\rangle$ and $\langle A_i|A_p\rangle$. Since PMD changes the SOPs of the signal and idler with respect to the pump randomly along the fiber , the XPM and FWM efficiencies vary randomly in different sections of fiber. Consequently, the amplified signal and idler powers will fluctuate from fiber to fiber even if fibers were otherwise identical. For the same reason, these powers can fluctuate with time for a given FOPA at time scales associated with environmental variations [5]. The inset in Fig. 11.1 shows examples of such variations in the FOPA gain spectrum for $D_p = 0.05$ ps/$\sqrt{\text{km}}$.

The general solution of Eqs. (11.3) and (11.4) requires a numerical approach. However, it turns out that the evolution of the signal and idler powers, $S_0 = \langle A_s|A_s\rangle$ and $I_0 = \langle A_i|A_i\rangle$, is determined by the relationship among the Stokes vectors of the three waves, $\boldsymbol{P} \equiv \langle A_p|\boldsymbol{\sigma}|A_p\rangle$, $\boldsymbol{S} \equiv \langle A_s|\boldsymbol{\sigma}|A_s\rangle$, $\boldsymbol{I} \equiv \langle A_i|\boldsymbol{\sigma}|A_i\rangle$, and the complex variables $\rho_j \equiv \langle A_j|A_p\rangle$ and $\boldsymbol{\Gamma}_j \equiv \langle A_j|\boldsymbol{\sigma}|A_p\rangle$ ($j = s, i$) which are associated with the relative orientations between the pump and signal/idler SOPs. The average gain and signal-power fluctuations are obtained using $G_{av} = \overline{S_0(L)}/S_0(0)$ and $\sigma_s^2 = \overline{S_0^2(L)}/\overline{S_0(L)}^2 - 1$.

Finding the evolution equations for $S_0$ and $I_0$ from Eqs. (11.3) and (11.4) and averaging them over the birefringence fluctuations by following the technique used in Ref. [14], we obtain the following equations governing the average signal and idler powers:

$$\frac{d\overline{S_0}}{dz} = \frac{d\overline{I_0}}{dz} = \gamma_e P_0 \Re(U), \tag{11.5}$$
$$\frac{dU}{dz} = -(\eta/2 + i\kappa)U + \gamma_e P_0 \left[\overline{S_0} + \overline{I_0} + V\right], \tag{11.6}$$
$$\frac{dV}{dz} = -\eta V + 2\gamma_e P_0 \Re(U), \tag{11.7}$$

where $\Re$ denotes the real part, $\eta = 1/L_d = D_p^2 (\Delta\omega)^2/3$, and $L_d$ is the PMD diffusion length. The auxiliary variable $U$ and $V$ are defined as $U = 2i\overline{\rho_s\rho_i}/P_0$ and $V = (\overline{\boldsymbol{S}} + \overline{\boldsymbol{I}}) \cdot \hat{p}$, where $\hat{p} = \boldsymbol{P}/P_0$ is the unit vector along the pump SOP. Also, $\kappa = \beta_s + \beta_i - 2\beta_p + 2\gamma_e P_0$ describes the net phase mismatch among the three waves.

Equations (11.5)–(11.7) are easy to solve to obtain the *average* FOPA gain spectrum. Although such an *average* gain spectrum does not correspond to a single experimental measurement, it provides a good indication of the impact of PMD on FOPA performance. Figure 11.1 shows such gain spectra for two $D_p$ values when the input signal is linearly copolarized with the pump. The solid lines show the analytical results using $\gamma = 2$ W$^{-1}$/km, $L = 2$ km, $\lambda_0 = 1550$ nm, $\beta_3 = 0.1$ ps$^3$/km, $\beta_4 = 1 \times 10^{-4}$ ps$^4$/km, and $P_0 = 1$ W. The dotted line shows for comparison the case of an isotropic fiber without birefringence. The pump wavelength ($\lambda_p = 1550.15$ nm) was chosen such that the signal has a fairly flat gain over 40-nm bandwidth in the absence of birefringence. Since the FOPA gain is very susceptible to any perturbations

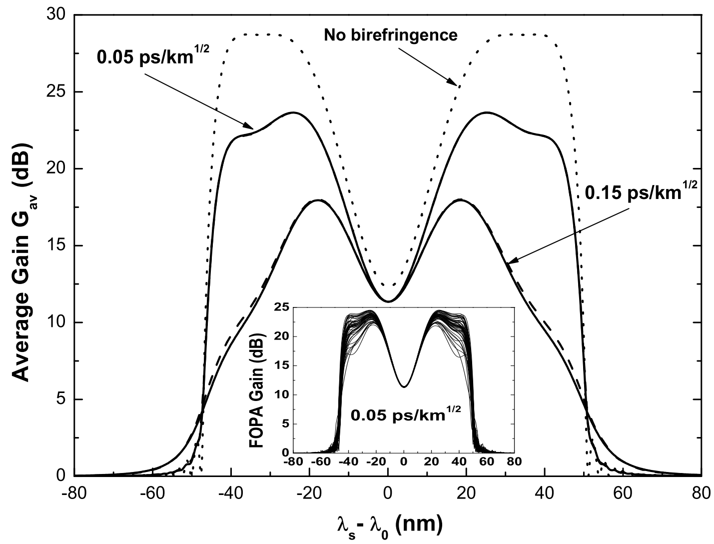


Figure 11.1: Average FOPA gain as a function of signal detuning from the zero-dispersion wavelength for two values of $D_p$. Solid and dashed curves show the analytical and numerical results, respectively; two curves cannot be distinguished for $D_p = 0.05$ ps/$\sqrt{\text{km}}$ on the scale used. The dotted curves shows for comparison the case without birefringence. The inset shows examples of FOPA gain spectra numerically obtained from Eqs. (10.9) and (3.11) for different realizations of residual birefringence.

to the phase matching condition, PMD-induced random variations of the signal and idler SOPs affect the average gain spectra considerably. Their impact increases with increased wavelength separation between the pump and signal. As a result, PMD not only reduces the peak gain value but also severely degrades the flatness of the gain spectrum.

When signal wavelength $\lambda_s$ is close to the pump, the PMD diffusion length becomes longer than the FOPA length, and the signal and idler can remain nearly copolarized with the pump along the fiber. The impact of PMD is small in this region, and the FOPA gain is only reduced by 1 dB or so because of the reduction in $\gamma$ by a factor of 8/9. When $\lambda_s$ is relatively far from $\lambda_p$, the situation becomes different because the PMD diffusion length is now comparable or even shorter than the FOPA length. As a result, PMD induces considerable random variations in the signal and idler SOPs, leading to further reduction in the FOPA gain and degrading severely the gain uniformity. Even for a small $D_p$ value of 0.05 ps/$\sqrt{\text{km}}$, a significant tilt appears in the gain spectrum. For larger values of $D_p$, the gain spectrum is degraded even more. For example, $L_d = 2.16$ km for $|\lambda_s - \lambda_p| = 30$ nm when $D_p = 0.05$ ps/$\sqrt{\text{km}}$ but this value reduces to 0.24 km when $D_p = 0.15$ ps/$\sqrt{\text{km}}$. As a result, the average gain spectrum is distorted drastically for such large values of $D_p$.

To justify the approximations made in deriving the averaged equations, we performed numerical

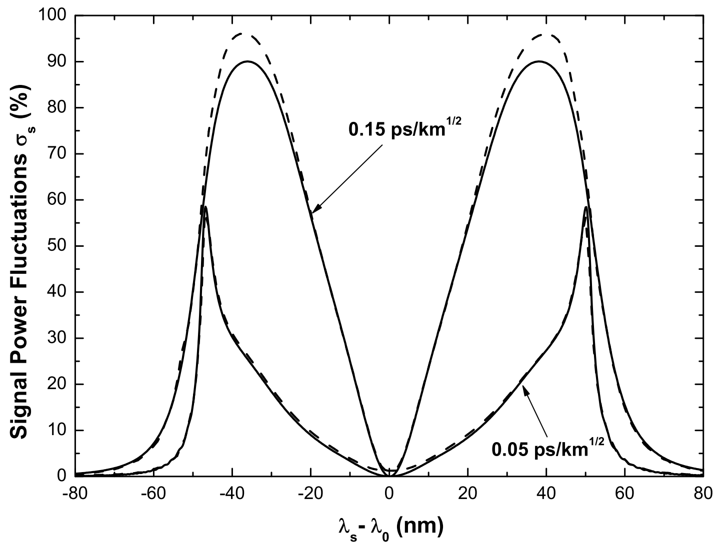


Figure 11.2: Signal fluctuation level $\sigma_s$ plotted as a function of signal detuning, under conditions of Fig. 11.1.

simulations using the full vector model based on Eqs. (10.9) and (3.11) and dividing the fiber into many 10-m long-sections. Birefringence was kept constant inside each section but changed randomly from section to section. The signal and idler powers were averaged over 500 runs. The analytical results based on Eqs. (11.5)-(11.7) agree quite well with the simulation ones (dashed lines).

PMD-induced signal fluctuations are quantified by the variance of the amplified signal. This quantity is related to the second-order moments and correlations of $S_0$, $\boldsymbol{S}$, $I_0$, $\boldsymbol{I}$, $\rho_s$, $\rho_i$, $\boldsymbol{\Gamma}_s$, and $\boldsymbol{\Gamma}_i$ and can be calculated by solving a set of coupled averaged equations. Figure 11.2 shows the level of signal fluctuations as a function of signal detuning for the same parameters used for Fig. 11.1. When $\lambda_s$ is close to $\lambda_p$, fluctuations are small because the PMD diffusion length is much longer than the FOPA length. However, level of fluctuations increases quickly in the useful region where gain is large. Over the main peak of the gain spectrum, output signal fluctuations can exceed 30 % even for a relatively small value of $D_p = 0.05$ ps/$\sqrt{\text{km}}$. Signal fluctuations increase drastically for $D_p = 0.15$ ps/$\sqrt{\text{km}}$, approaching a 90% level. Numerical simulations (dashed curves) agree well with this analytical prediction.

Although Figures 11.1 and 11.2 focus on signal amplification, the theory and the results also apply for wavelength converters because the idler power is related to the signal power as $I_0(L) = S_0(L) - S_0(0)$. Since the conversion efficiency $\zeta$ is related to the signal gain $G$ as $\zeta \equiv I_0(L)/S_0(0) = G - 1$, the average conversion efficiency $\overline{\zeta} = G_{av} - 1$. The level of idler-power fluctuations is related to that of the signal simply as $\sigma_i^2 \equiv \overline{I_0^2(L)}/\overline{I_0(L)}^2 - 1 = \sigma_s^2 G_{av}^2/(G_{av} - 1)^2$. The curves in Figs. 11.1 and 11.2 can be used to find $\overline{\zeta}$ and $\sigma_i$ using the above relations. In particular, all the qualitative features of these figures apply to wavelength converters as well.

The preceding analysis is based on the assumption that the correlation length $l_c$ of birefringence fluctuations is much shorter than the fiber length. One might ask if this assumption is justified for fiber lengths $< 1$ km. Extensive numerical simulations show that our analytic theory works well as long as the FOPA length exceeds 10–15 $l_c$. The results shown in Fig. 11.1 and 11.2 change only by a small amount even when $l_c$ is up to 100 m for a 2-km-long FOPA. High-nonlinearity fibers are increasingly being used for making FOPAs, and lengths $\sim$100 m are sufficient for them. Our analytic results apply in this case for $l_c = 10$ m but becomes questionable when $l_c$ exceeds 50 m. Residual birefringence can no longer be treated as white noise in this case and a numerical approach should be used.

In summary of this section, we have developed a vector theory of degenerate FWM process inside optical fibers and have used it to study the impact of PMD on the performance of FOPAs and wavelength converters. We found that PMD not only changes the average value of the gain significantly but also introduces considerable signal fluctuations. For typical values of $D_p$ for modern fibers (around 0.05 ps/$\sqrt{\text{km}}$), fluctuations are in the 20–30% range over the flat region of the gain spectrum. The bandwidth of the FOPA gain spectrum may be limited by other factors related to fiber dispersion, but PMD is also likely to be a major limiting factor for modern FOPAs. As a rough guidance, the average differential group delay of the fiber ($D_p\sqrt{8L/3\pi}$) should be less than 50 fs to keep the PMD-induced signal fluctuations below 10% over the main portion of the gain spectrum.

## 11.3 Dual-Pump Configuration

The situation becomes even more complicated in the case of dual pumping because of the involvement of four interacting waves. The non-degenerate FWM is now governed by the following coupled equations obtained from Eq. (8.14):

$$\frac{d|A_l\rangle}{dz} = i\left[\beta_l + \frac{1}{2}\Delta\omega_p \boldsymbol{b}\cdot\boldsymbol{\sigma}\right]|A_l\rangle + i\gamma_e\left[\langle A_l|A_l\rangle + \langle A_h|A_h\rangle + |A_h\rangle\langle A_h|\right]|A_l\rangle, \tag{11.8}$$

$$\frac{d|A_h\rangle}{dz} = i\left[\beta_h - \frac{1}{2}\Delta\omega_p \boldsymbol{b}\cdot\boldsymbol{\sigma}\right]|A_h\rangle + i\gamma_e\left[\langle A_h|A_h\rangle + \langle A_l|A_l\rangle + |A_l\rangle\langle A_l|\right]|A_h\rangle, \tag{11.9}$$

$$\begin{aligned}\frac{d|A_s\rangle}{dz} &= i\left[\beta_s - \frac{1}{2}\Delta\omega \boldsymbol{b}\cdot\boldsymbol{\sigma}\right]|A_s\rangle + i\gamma_e\left[\langle A_l|A_l\rangle + \langle A_h|A_h\rangle + |A_l\rangle\langle A_l| + |A_h\rangle\langle A_h|\right]|A_s\rangle \\ &\quad + i\gamma_e\left[\langle A_i|A_l\rangle|A_h\rangle + \langle A_i|A_h\rangle\right]|A_l\rangle,\end{aligned} \tag{11.10}$$

$$\begin{aligned}\frac{d|A_i\rangle}{dz} &= i\left[\beta_i + \frac{1}{2}\Delta\omega \boldsymbol{b}\cdot\boldsymbol{\sigma}\right]|A_i\rangle + i\gamma_e\left[\langle A_l|A_l\rangle + \langle A_h|A_h\rangle + |A_l\rangle\langle A_l| + |A_h\rangle\langle A_h|\right]|A_i\rangle \\ &\quad + i\gamma_e\left[\langle A_s|A_l\rangle|A_h\rangle + \langle A_s|A_h\rangle\right]|A_l\rangle,\end{aligned} \tag{11.11}$$

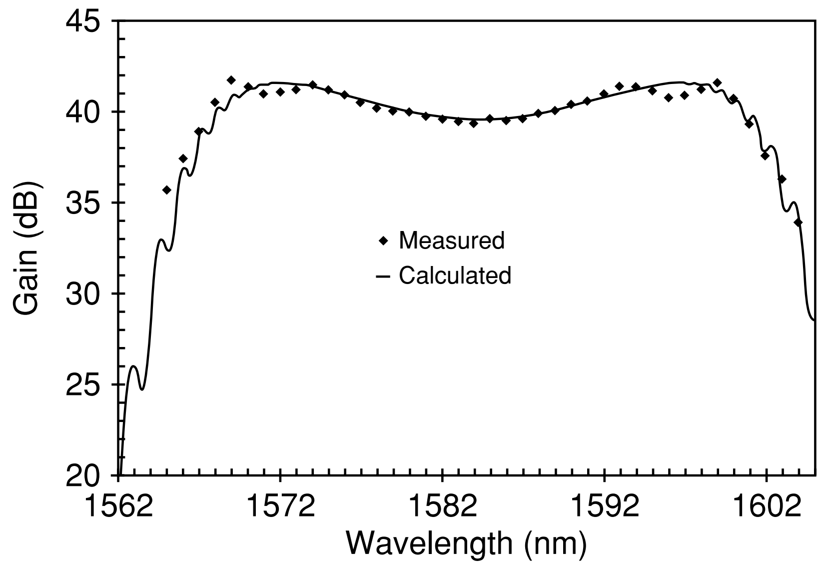


Figure 11.3: Measured and theoretical gain spectra for copolarizaed pump-signal launch states. The 1-km highly-nonlinear fiber, with a ZDWL of 1583.5 nm, $\gamma = 17/\mathrm{km/W}$, and PMD parameter of $D_p = 0.2\ \mathrm{ps}/\sqrt{\mathrm{km}}$, is pumped with two waves at 1559 and 1610 nm with powers of 600 and 200 mW, respectively. Theoretical fitting uses an effective fiber length of 600 m and $\beta_3 = 0.055\ \mathrm{ps}^3/\mathrm{km}$ and $\beta_4 = 2.35 \times 10^{-4}\ \mathrm{ps}^4/\mathrm{km}$ at ZDWL. Numerical simulations counts in all effects related to SRS and multiple coupled degenerate and non-degenerate FWM processes.

where we have set the carrier frequency in Eq. (8.14) at the center of the two pumps $\omega_0 = (\omega_l + \omega_h)/2$, $\Delta\omega_p = (\omega_h - \omega_l)/2$ is half of the frequency separation between the two pumps, and $\Delta\omega = \omega_s - \omega_0$ is the signal detuning from the pump center. Equations (11.8)-(11.11) show that not only the signal and idler, but the two pumps also rotate their SOPs around the pump center. This complexity causes the difficulty in finding an analytical description, and only the numerical simulations are possible [2].

However, some important results can be obtained by applying physical intuition into Eqs. (11.8)-(11.11), especially to the last two FWM terms in both Eqs. (11.10) and (11.11). First, similar to the single-pumping configuration in the previous section, compared with ideal isotropic fibers, random birefringence reduces FWM efficiency globally by a factor of $8/9$ because of reduction in the magnitude of the nonlinear parameter. Moreover, FWM efficiency in the orthogonal pumping configuration is half of that in the copolarized pumping configuration, rather than the one third found in the case of isotropic fibers (see Chapter 4). Second, in most cases of dual pumping, the signal and idler are sandwiched between the two pumps. As the PMD diffusion length is inversely proportional to the square of frequency separation: $L_d = 3/(D_p\Delta\omega)^2$, SOP diffusion is dominated by that between the two pumps if PMD is

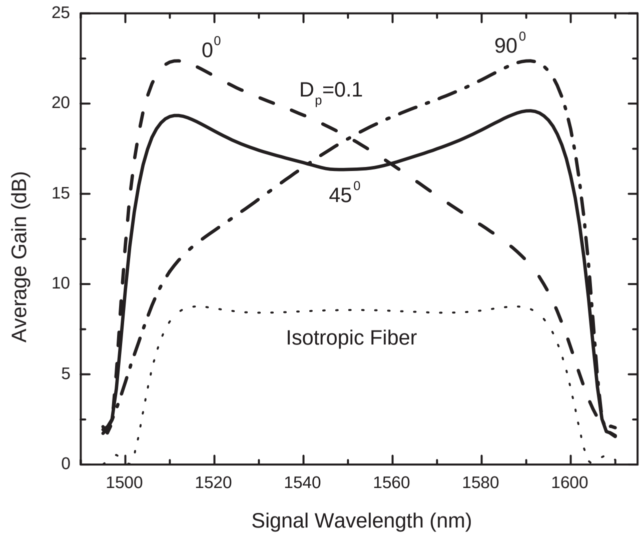


Figure 11.4: Average gain versus signal wavelength for three different initial linear SOP of the signal for $D_p = 0.1$ ps$/\sqrt{\text{km}}$; $\theta$ represents the angle in between the linear SOPs of signal and shorter-wavelength pump. The other pump is orthogonally polarized. the dotted curve shows, for comparison, the polarization-independent without birefringence, as discussed in Chapter 4. The fiber is assumed to have a ZDWL of 1550 nm, $\gamma = 10$ /km/W, $\beta_3 = 0.1$ ps$^3$/km, and $\beta_4 = 10^{-4}$ ps$^4$/km. It is pumped at 1502.6 nm and 1600.6 nm with powers each of 0.5 W. Only the non-degenerate FWM, as shown in Eqs. (11.8)-(11.11), is considered in the numerical simulations [2].

significant and if the pump spacing is much larger than the signal-idler spacing. Such random SOP diffusion for the two pumps causes the two pumps to become copolarized or orthogonally polarized equally probably along the fiber, leading to an average FWM efficiency of $(1+1/2)/2 = 3/4$ out of the maximum, which corresponds to $3/4 \times 8/9 = 2/3$ of the maximum in ideal isotropic fibers. This is indeed the case when we compared theory calculation with experimental results in Fig. 11.3, where we need to reduce the effective interaction length by about $2/3$ to fit the experimental measurement well [15].

On the other hand, the orthogonal pumping configuration becomes strongly polarization dependent, especially when signal wavelength is close to either one of the pump, as shown clearly in Fig. 11.4 [2]. This is so because the signal with a wavelength close to one pump remains aligned with that pump but decorrelates with the other pump rapidly because of a large frequency separation. Hence, the signal can see only the averaged effect of the farther pump but experiences the highest or smallest gain depending on if it started paralled or orthogonal to the closer pump. This also explains why for $\theta = 0^{\text{o}}$, gain peaks close to the shorter-wavelength pump but decreases as it gets closer to the other pump. This behavior agrees with experimental observation in Ref. [16]. Note that, when PMD is significant, such PMD-

| Pumping configuration | Ideal isotropic fiber | Effect of random birefringence | Effect of PMD |
|---|---|---|---|
| Copolarized | 1 | 8/9 | $<$ 8/9; 2/3 when PMD is large |
| Orthogonal | 1/3 | 8/9 $\times$ 1/2 = 4/9 | between 1/3 and 2/3 |

Table 11.1: Spin Selection rules for Non-Degenerate FWM

induced PDG is generally much lager than the fundamental one introduced by SRS and discussed in Chapter 4.

In summary of this section, we provide the FWM efficiencies in Table 11.3, normalized to the maximum value occurring in ideal isotropic fibers.

## 11.4 FWM-Based ZDWL Mapping

An accurate knowledge of dispersion variations along the fiber length is essential for modern WDM systems. The chromatic dispersion of any optical fiber, although designed to be norminally constant, varies along its length because of unavoidable variations in the core diameter. Several nondestructive measurement techniques make use of four-wave mixing (FWM) occurring inside optical fibers [17]-[21]. As FWM is sensitive to the local value of the zero-dispersion wavelength (ZDWL), or the chromatic dispersion (CD), it provides an efficient way to map ZDWL/CD variations along the fiber length. However, FWM is sensitive not only to the phase mismatch between the pump, signal, and idler waves but also to their relative polarization orientations [7]. Residual birefringence inside optical fibers induces polarization-mode dispersion (PMD) and randomizes the state of polarization (SOP) of any optical wave [22]. When the pump, signal, and idler waves propagate together along the fiber, PMD not only changes their SOPs randomly but also affects the phase matching of the FWM process. As a result, the random nature of PMD would induce fluctuations in the idler power generated through the FWM process. Such PMD-induced power fluctuation would affect the mapping of ZDWL or CD whenever FWM is used. In this section, we use the theory developed in the previous section to quantify the PMD effects on ZDWL mapping based on degenerate FWM. We show that PMD induces considerable fluctuations in the idler power during ZDWL/CD mapping and discuss its impact on the measurement accuracy.

In fiber dispersion mapping, generally the created idler (sometimes called the Stokes or anti-Stokes wave depending on whether it occurs on the red or blue side of the pump [18]) is recorded to obtain the dispersion information. The location of the three waves can be close to [19] or far from [18] the ZDWL depending on whether ZDWL or CD needs to be mapped. In this section, we choose them close to ZDWL and focus mainly on the ZDWL mapping. Eqs. (11.2)-(11.4) can be directly used. However, one thing different from FOPA is that the fiber under test is generally quite long in ZDWL mapping, and fiber loss is not negligible.

Analysis can be considerably simplified if we note that both the pump and signal powers are much larger than the idler power in practice. As a result, we can neglect pump depletion and signal amplification. Moreover, these two powers are either not large enough [17, 19, 21] or adjusted (signal power twice the copolarized pump power) such that the phase mismatch induced by self-phase and cross-phase modulations is cancelled automatically [18, 20]. For this reason, we neglect their effects in the following analysis. Under these conditions, the pump wave would only experience linear loss and phase variations with a propagation constant of $\beta_p$. Equations (11.3) and (11.4) now become

$$\frac{d|A_s\rangle}{dz} = -\frac{\alpha}{2}|A_s\rangle + i\left(\Delta\beta_s - \frac{1}{2}\Delta\omega \boldsymbol{b}\cdot\boldsymbol{\sigma}\right)|A_s\rangle, \tag{11.12}$$

$$\frac{d|A_i\rangle}{dz} = -\frac{\alpha}{2}|A_i\rangle + i\left(\Delta\beta_i + \frac{1}{2}\Delta\omega \boldsymbol{b}\cdot\boldsymbol{\sigma}\right)|A_i\rangle + i\gamma_e\langle A_s|A_p\rangle|A_p\rangle, \tag{11.13}$$

where $\alpha$ accounts for fiber losses. We assumed that both $\alpha$ and $\gamma_e$ are the same for the three waves because of relatively small frequency differences among them [7]).

In the absence of PMD, the FWM process is quite different for different pump polarizations due to the requirement of angular momentum conservation. However, in the presence of PMD, Equations (11.12) and (11.13) show that the FWM process depends on the inner product $\langle A_s|A_p\rangle$ [9]. As a result, the FWM process depends only on the relative orientation between the pump and signal SOPs.

What is important to know is the evolution of the idler power, $D_0 \equiv \langle A_i|A_i\rangle$, along the fiber, which is found, from Eqs. (11.12) and (11.13), to relate to the signal Stokes vector $\boldsymbol{S} \equiv \langle A_s|\boldsymbol{\sigma}|A_s\rangle$, signal power $S_0 = |\boldsymbol{S}|$, and two complex quantities $\rho \equiv i\langle A_s|A_i^*\rangle$ and $\boldsymbol{\Gamma} \equiv i\langle A_s|\boldsymbol{\sigma}|A_i^*\rangle$. After averaging the dynamic equation of $D_0$ over the birefringence fluctuations, we obtain the following coupled but deterministic equations in the case of a linearly polarized pump along the $x$ axis in the Stokes space [26]:

$$\frac{d\overline{D_0}}{dz} = -\alpha\overline{D_0} + \gamma_e P_0 Re(U), \tag{11.14}$$

$$\frac{dU}{dz} = -(\alpha + i\kappa + \eta/2)U + \gamma_e P_0\left(S_0 + \overline{S_x}\right), \tag{11.15}$$

$$\frac{d\overline{S_x}}{dz} = -(\alpha+\eta)\overline{S_x}, \tag{11.16}$$

where $U = \overline{\rho} + \overline{\Gamma_x}$, $\kappa = \beta_s + \beta_i - 2\beta_p$, $\eta = D_p^2(\Delta\omega)^2/3$, and $P_0(z)$ is the pump power. When the input signal is copolarized with the pump, the analytic solution is given by

$$\overline{D_0(z)} = 2\gamma_e^2 P_0^2(0) S_0(0) e^{-\alpha z}\int_0^z dz_1 e^{-(\alpha+\frac{\eta}{2})z_1}\int_0^{z_1} dz_2 \cosh\left(\frac{\eta z_2}{2}\right) e^{-\alpha z_2}\cos\left[\int_{z_2}^{z_1} dz_3\,\kappa(z_3)\right]. \tag{11.17}$$

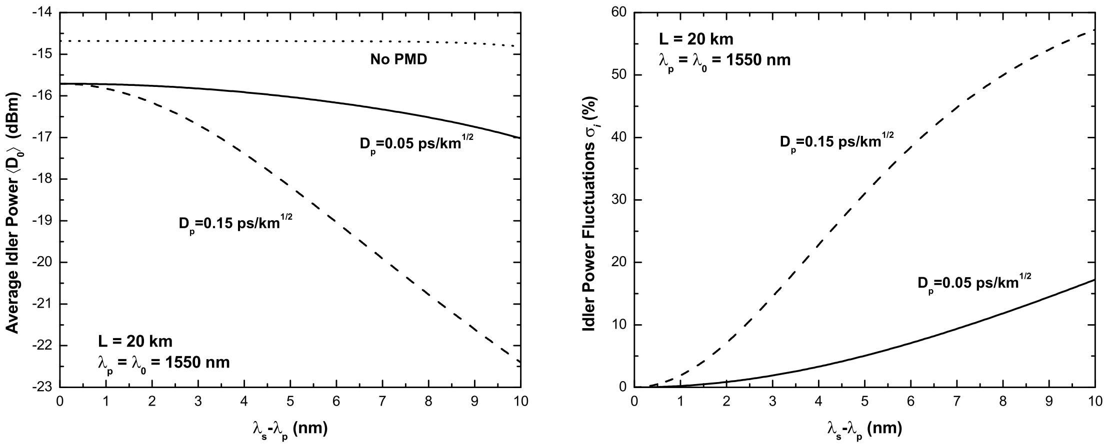


Figure 11.5: Average idler power (a) and its fluctuation levels (b) as a function of wavelength detuning between the signal and the pump for two values of the PMD parameter. The dotted line shows the no-PMD case. Other parameters are given in the text.

If the fiber has no PMD, $\eta = 0$ and $\gamma_e = \gamma$, then Eq. (11.17) returns to the deterministic case and coincides with the results of Ref. [19]. The same analytic solution holds when the input signal is orthogonally polarized to the pump except that the cosh function is replaced by a sinh function.

For the dispersion-measurement problem, we need to focus on the PMD-induced fluctuations in the idler power. The relative level of such fluctuations can be obtained from Eqs. (11.12) and (11.13) using

$$\sigma_i^2 = \frac{\left\langle D_0^2(L) \right\rangle - \left\langle D_0(L) \right\rangle^2}{\left\langle D_0(L) \right\rangle^2}. \tag{11.18}$$

The calculation of $\sigma_i^2$ requires the second-order moment $\left\langle D_0^2(L) \right\rangle$ of the idler, which is related to the second-order moments of $\vec{S}$, $D_0$, $\rho$, $\vec{\Gamma}$, and their combinations. Following the same procedure described earlier, we obtain the equations governing the evolution of these second-order moments and solve them numerically.

Figure 11.5(a) shows the average idler power as a function of wavelength detuning between the signal and the pump for two $D_p$ values when the input signal is copolarized with the pump. The pump wavelength $\lambda_p$ is located at the fixed ZDWL of $\lambda_0 = 1550$ nm so that the idler power is maximized and its spectrum is flat in a wide range of detuning in the case absent of PMD (dotted line). In general, $\lambda_p$ does not have to coincide with $\lambda_0$ but should be close to it to maintain a high FWM conversion efficiency [19]. We used $\gamma = 2$ W$^{-1}$/km, $L = 20$ km, $\beta_3 = 0.1$ ps$^3$/km, $\beta_4 = 1.0 \times 10^{-4}$ ps$^4$/km, $\alpha = 0.2$ dB/km, and $P_0(0) = S_0(0) = 5$ mW. When the signal wavelength is close to the pump, the idler power is proportional to $(8\gamma/9)^2$, and the PMD reduces the idler power by about $20\log_{10}(9/8) \approx 1$ dB. When the signal wavelength deviates considerably from the pump, the PMD effects increase, and the

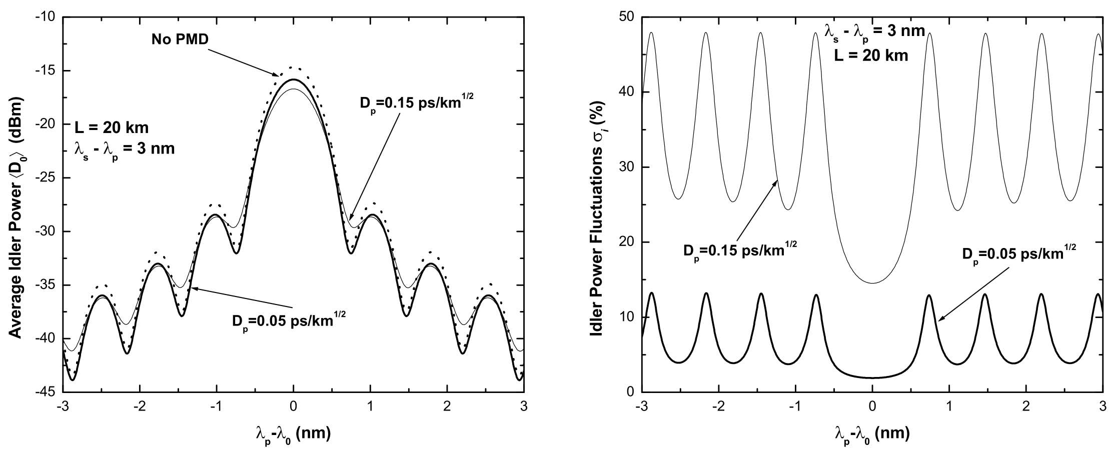


Figure 11.6: Average idler power (a) and its fluctuation level (b) as a function of pump wavelength detuning from the ZDWL for two values of the PMD parameter. The dotted line shows the no-PMD case. Other parameters are the same as in Fig. 11.5.

idler power decreases. The larger $D_p$, the larger the drop in the idler power.

Figure 11.5(b) shows the fluctuation level of idler power corresponding to the case of Fig. 11.5(a). Fluctuations increase quickly when the signal wavelength is detuned away from the pump. Idler fluctuations can be as large as 17 % when $\lambda_s - \lambda_p = 10$ nm even for $D_p = 0.05$ ps/$\sqrt{\text{km}}$. Fluctuations increase drastically with $D_p$. When $D_p = 0.15$ ps/$\sqrt{\text{km}}$, fluctuations become 57 % for the same detuning. The curves similar to those shown in Fig. 11.5 are obtained when $D_p$ changes because the PMD effects are determined by $D_p^2(\Delta\omega)^2$. When FWM is used for ZDWL mapping, the spatial resolution depends on the wavelength difference between the signal and the pump; the larger the difference, the higher the resolution [19]. However, as seen in Fig. 11.5, the PMD effects increase quickly with the wavelength difference and would reduce the accuracy of ZDWL mapping. One thus needs to be careful to balance the resolution and accuracy.

Figure 11.6 show the idler spectrum and its fluctuations when pump wavelength is varied. the detuning between the signal and the pump $\lambda_s - \lambda_p$ is fixed to 3 nm. Other parameters are the same as Fig. 11.5. The dotted line shows the case of no PMD; the thick and thin lines show the cases of $D_p = 0.05$ and 0.15 ps/$\sqrt{\text{km}}$, respectively. The PMD effects smooth the oscillation structure in the idler spectrum that is important to provide the information on ZDWL [19]. More importantly, large amount of fluctuations appear even for the small detuning of 3 nm. When $D_p = 0.15$ ps/$\sqrt{\text{km}}$, fluctuations in the range of 25 to 49 % are expected. The pump-scanned idler spectrum is commonly used in ZDWL mapping [17, 19, 21]. All the fine structure in the spectrum is interpreted as information associated with local variations of the ZDWL. Clearly, one should be careful when interpreting such spectra because large fluctuations induced by PMD might be included [19]. Since PMD effects changes with time, long-term repeated measurements may be required to obtain the average spectrum. Eq. (11.17) should be used to interpret the data.

Apart from the pump-scanned idler spectrum, the oscillation periods of the idler power along the fiber can be used to map the CD directly when the pump and signal work far away from the ZDWL [18, 20]. However, PMD would induce extra phase mismatch and thus change the local oscillation period randomly [27]. The whole theory presented above can also be applied to discuss the PMD effects on the CD measurements if one includes the effects of the finite pump and signal pulse widths and the Rayleigh backscattered nature of the idler.

In summary of this section, we have developed a general vector theory to include the PMD effects occurring inside optical fibers during the FWM process. We found that PMD changes the average idler power significantly and introduces a large amount of fluctuations because of random changes in the phase mismatch and in the relative angle between the pump, signal, and idler SOPs. The fluctuations induced by PMD can be quite large depending on the value of the PMD parameter. In measurements based on the pump-scanned idler spectrum or the spatial oscillation periods, PMD induces large fluctuations and would reduce the measurement accuracy. Long-term repeated measurement might be necessary for the dispersion mapping to reduce the PMD effects.

# References

[1] Q. Lin and G. P. Agrawal, Opt. Lett. **29**, 1114 (2004).

[2] F. Yaman, Q. Lin, and G. P. Agrawal, IEEE Photon. Technol. Lett. **16**, 431 (2004).

[3] Q. Lin and G. P. Agrawal, IEEE Photon. Technol. Lett. **15**, 1719 (2003).

[4] J. Hansryd, P. A. Andrekson, M. Westlund, J. Li, and P. O. Hedekvist, IEEE J. Sel. Top. Quan. Electron. **8**, 506 (2002).

[5] M. N. Islam and Ö. Boyraz, IEEE J. Sel. Top. Quan. Electron. **8**, 527 (2002).

[6] S. Radic, C. McKinstrie, and R. Jopson, Opt. Fiber Technol. **9**, 7 (2003).

[7] G. P. Agrawal, *Nonlinear Fiber Optics*, $3^{rd}$ ed. (Academic, New York, 2001).

[8] J. P. Gordon and H. Kogelnik, Proc. Natl. Acad. Sci. USA **97**, 4541 (2000).

[9] K. Inoue, IEEE J. Quan. Electron. **28**, 883 (1992).

[10] P. O. Hedekvist, M. Karlsson, and P. A. Andrekson, IEEE Photon. Technol. Lett. **8**, 776 (1996).

[11] O. Aso, S. Arai, T. Yagi, M. Tadakuma, Y. Suzuki, and S. Namiki, IEICE Trans. Electron. **E83-C**, 816 (2000).

[12] A. Galtarossa, L. Palmieri, M. Schiano, and T. Tambosso, Opt. Lett. **25**, 384 (2000); Opt. Lett. **26**, 962 (2001).

[13] P. K. A. Wai and C. R. Menyuk, J. Lightwave Technol. **14**, 148 (1996).

[14] Q. Lin and G. P. Agrawal, J. Opt. Soc. Am. B **20**, 1616 (2003).

[15] S. Radic, C. J. McKinstrie, R. M. Jopson, J. C. Centanni, Q. Lin, and G. P. Agrawal, IEE Electron. Lett. **39**, 838 (2003).

[16] S. Radic, C. Mckinstrie, R. Jopson, C. Jorgensen, K. Brar, C. Headley, Proc. OFC03, v.2, 508 (2003).

[17] H. Onaka, K. Otsuka, H. Miyata, and T. Chikama, IEEE Photon. Technol. Lett. **6**, 1454 (1994).

[18] L. F. Mollenauer, P. V. Mamyshev, and M. J. Neubelt, Opt. Lett. **21**, 1724 (1996).

[19] I. Brener, P. P. Mitra, D. D. Lee, and D. J. Thomson, Opt. Lett. **23**, 1520 (1998).

[20] J. Gripp and L. F. Mollenauer, Opt. Lett. **23**, 1603 (1998).

[21] M. González-Herráez, P. Corredera, M. L. Hernanz, and J. A. Méndez, Opt. Lett. **27**, 1546 (2002).

[22] H. Kogelnik, R. M. Jopson, and L. E. Nelson, in *Optical Fiber Telecommunications IV B*, I. P. Kaminow and T. Li Eds. (Academic, San Diego, 2002), Chap. 15.

[23] P. K. Wai, C. R. Menyuk, and H. H. Chen, Opt. Lett. **16**, 1231 (1991).

[24] S. G. Evangelides Jr., L. F. Mollenauer, J. P. Gordon, and N. S. Bergano, J. Lightwave Technol. **10**, 28 (1992).

[25] P. K. A. Wai and C. R. Menyuk, J. Lightwave Technol. **14**, 148 (1996).

[26] C. W. Gardiner, *Handbook of Stochastic Methods*, $2^{nd}$ Ed. (Springer, New York, 1985).

[27] C. Vinegoni, H. Chen, M. Leblanc, G. W. Schinn, M. Wegmuller, and N. Gisin, IEEE Photon. Technol. Lett. **15**, 739 (2003).

# 12 PMD and Self-Phase Modulation

In Chapters 9−11, we discussed the interaction of PMD with the nonlinear effects involving optical waves with different carrier frequencies. As the frequency separations among waves are generally much larger than the bandwidth of individual waves, the inter-channel PMD dominates the interactions. In this chapter, we focus on the other regime where only one intense pulse propagates inside a fiber and the nonlinear effect is dominated by self-phase modulation (SPM). In this case, PMD introduces differential-group delay (DGD) between the two polarization modes of the pulse and affects the nonlinear interaction between them. This situation turned out to be quite complicated as both the linear and nonlinear effects are time dependent and strongly coupled. In this chapter, we provide a simple approach to describe the propagation of optical solitons under such random perturbations.

## 12.1 Introduction

Optical solitons have been studied extensively because of their potential for high-speed long-haul optical communications [1]-[5]. As optical fibers exhibit PMD which introduces random differential group delay between the two polarization components of an optical pulse, optical solitons undergo random perturbations during their propagation inside a long-haul fiber link. Extensive studies have been carried out in the past decade to investigate the stability of optical solitons in the presence of PMD [6]-[17]. It turns out that optical solitons are fairly resistant to such PMD-induced perturbations and experience less DGD compared with linear pulses. Different theories have been developed to describe the interaction between solitons and PMD. However, all of them are quite complicated because of the complexity of the problem. In this chapter, we present a simple way to describe such effects, based on the particle nature of optical solitons. It turns out that the physical mechanism underlying such interaction is quite straightforward.

## 12.2 Particle Picture of Optical Solitons

Optical solitons form when SPM-induced chirp balances exactly the GVD-induced pulse broadening. Because of such a balance between the linear and nonlinear effects, solitons generally exhibit rather high degree of stability against external perturbations, and the whole pulse propagates along the fiber as an entity. As a result, we can treat the soliton as a particle and only focus on a few important degrees of freedom associated with the soliton evolution. We begin by defining the following macroscopic quantities

$$E \equiv \int_{-\infty}^{+\infty} \langle A|A\rangle d\tau, \qquad \boldsymbol{S} \equiv \frac{1}{E}\int_{-\infty}^{+\infty} \langle A|\boldsymbol{\sigma}|A\rangle d\tau, \tag{12.1}$$

$$\rho_0 \equiv \frac{1}{E}\int_{-\infty}^{+\infty} \tau\langle A|A\rangle d\tau, \qquad \boldsymbol{\rho} \equiv \frac{1}{E}\int_{-\infty}^{+\infty} \tau\langle A|\boldsymbol{\sigma}|A\rangle d\tau, \tag{12.2}$$

$$\omega_0 \equiv \frac{i}{2E}\int_{-\infty}^{+\infty} \langle A|\frac{\partial A}{\partial \tau}\rangle d\tau + c.c., \qquad \boldsymbol{\omega} \equiv \frac{i}{2E}\int_{-\infty}^{+\infty} \langle A|\boldsymbol{\sigma}|\frac{\partial A}{\partial \tau}\rangle d\tau + c.c., \tag{12.3}$$

$$\theta_0 \equiv \frac{i}{2E}\int_{-\infty}^{+\infty} \tau\langle A|\frac{\partial A}{\partial \tau}\rangle d\tau + c.c., \qquad \boldsymbol{\theta} \equiv \frac{i}{2E}\int_{-\infty}^{+\infty} \tau\langle A|\boldsymbol{\sigma}|\frac{\partial A}{\partial \tau}\rangle d\tau + c.c., \tag{12.4}$$

$$\kappa_0 \equiv \frac{1}{E}\int_{-\infty}^{+\infty} \langle\frac{\partial A}{\partial \tau}|\frac{\partial A}{\partial \tau}\rangle d\tau, \qquad \boldsymbol{\kappa} \equiv \frac{1}{E}\int_{-\infty}^{+\infty} \langle\frac{\partial A}{\partial \tau}|\boldsymbol{\sigma}|\frac{\partial A}{\partial \tau}\rangle d\tau, \tag{12.5}$$

$$\rho_2 \equiv \frac{1}{E}\int_{-\infty}^{+\infty} \tau^2\langle A|A\rangle d\tau, \tag{12.6}$$

where $|\frac{\partial A}{\partial \tau}\rangle$ and $\langle\frac{\partial A}{\partial \tau}|$ denote $\frac{\partial |A\rangle}{\partial \tau}$ and $\frac{\partial \langle A|}{\partial \tau}$, respectively. It is easy to recognize from these definitions that $E$ is the pulse energy and the vector $\boldsymbol{S}$ is the Stokes vector representing the global SOP of the pulse. $\rho_0$ is the pulse center ("mass" center), and $\rho_2$ is the second moment of the pulse. These two quantities together provide the root-mean square (RMS) pulse width $T$ as $T^2 = \rho_2 - \rho_0^2$.

It turns out that $\boldsymbol{\rho}$ is directly related to the first-order PMD vector. To see this, we transfer it into the spectral domain to obtain

$$\boldsymbol{\rho} = \frac{-i}{2\pi E}\int_{-\infty}^{+\infty} \langle\widetilde{A}|\boldsymbol{\sigma}|\frac{\partial \widetilde{A}}{\partial \omega}\rangle d\omega = \frac{-i}{2\pi E}\int_{-\infty}^{+\infty} \left[\widetilde{a}^*\frac{\partial \widetilde{a}}{\partial \omega}\langle s|\boldsymbol{\sigma}|s\rangle + |\widetilde{a}|^2\langle s|\boldsymbol{\sigma}|\frac{\partial s}{\partial \omega}\rangle\right] d\omega, \tag{12.7}$$

where we have used the field decomposition $|\widetilde{A}(z,\omega)\rangle = \widetilde{a}(z,\omega)|s(z,\omega)\rangle$, $\widetilde{a}(z,\omega)$ is the spectral amplitude, and $|s(z,\omega)\rangle$ is its normalized Jones vector with $\langle s(z,\omega)|s(z,\omega)\rangle = 1$. In particular, $\boldsymbol{\rho}$ is zero for any symmetric pulse with a constant SOP. In the linear propagation regime, the field amplitude evolves as $\widetilde{a}(z,\omega) = \widetilde{a}(0,\omega)e^{i\beta(\omega)z}$. As the first term of Eq. (12.7) is dominated by group delay, in general, it can be removed by a time transformation. The spectral evolution of polarization is related to the PMD vector as [20]

$$\frac{\partial |s(z,\omega)\rangle}{\partial \omega} = -\frac{i}{2}\boldsymbol{\Omega}(z,\omega)\cdot\boldsymbol{\sigma}|s(z,\omega)\rangle, \tag{12.8}$$

where $\boldsymbol{\Omega}$ is the conventionally defined PMD vector [20]. Substituting Eq. (12.8) into the second term of Eq. (12.7), we obtain

$$\boldsymbol{\rho} = \frac{-1}{4\pi E}\int_{-\infty}^{+\infty} \boldsymbol{\Omega}(z,\omega)\langle\widetilde{A}(z,\omega)|\widetilde{A}(z,\omega)\rangle d\omega. \tag{12.9}$$

This term is the average of the conventionally defined PMD vector over the pulse spectrum. In particular, if we assume $\boldsymbol{\Omega}$ is frequency independent, which amounts to considering only the first-order PMD, we obtain $\boldsymbol{\rho} \propto -\boldsymbol{\Omega}/2$: $\boldsymbol{\rho}$ is directly related to the first-order PMD vector but pointing in the opposite direction [pointing towards the slow principal state of polarization (PSP)].

The physical meaning of $\omega_0$ and $\boldsymbol{\omega}$ in Eq. (12.3) can be found in the spectral domain where they are given by

$$\omega_0 = \frac{1}{2\pi E}\int_{-\infty}^{+\infty} \omega \langle \widetilde{A}(z,\omega)|\widetilde{A}(z,\omega)\rangle d\omega, \tag{12.10}$$

$$\boldsymbol{\omega} = \frac{1}{2\pi E}\int_{-\infty}^{+\infty} \omega \langle \widetilde{A}(z,\omega)|\boldsymbol{\sigma}|\widetilde{A}(z,\omega)\rangle d\omega. \tag{12.11}$$

Clearly, $\omega_0$ is the carrier frequency (momentum) and $\boldsymbol{\omega}$ is the conjugate of $\boldsymbol{\rho}$ in the spectrum domain. We call it the *frequency vector* as it provides the carrier frequency difference between the two principal states of polarization. Applying the same procedure to $\kappa_0$ and $\boldsymbol{\kappa}$, we find

$$\kappa_0 = \frac{1}{2\pi E}\int_{-\infty}^{+\infty} \omega^2 \langle \widetilde{A}(z,\omega)|\widetilde{A}(z,\omega)\rangle d\omega, \tag{12.12}$$

$$\boldsymbol{\kappa} = \frac{1}{2\pi E}\int_{-\infty}^{+\infty} \omega^2 \langle \widetilde{A}(z,\omega)|\boldsymbol{\sigma}|\widetilde{A}(z,\omega)\rangle d\omega. \tag{12.13}$$

Therefore, $\kappa_0$ is the spectral width, and we call $\boldsymbol{\kappa}$ the *bandwidth vector*.

$\theta_0$ in Eq. (12.4) is related to pulse chirp, which can be observed by assuming a simple form of a scalar field as $A(\tau) = A_0(\tau)e^{i\phi(\tau)}$, where $A_0$ is the slowly varying field amplitude and is real. Substituting this into Eq. (12.4), we obtain

$$\theta_0 \approx \frac{-1}{E}\int_{-\infty}^{+\infty} |A_0|^2 \tau \frac{\partial \phi}{\partial \tau} d\tau, \tag{12.14}$$

where we have dropped the term related to $\partial A_0/\partial \tau$ by assuming its small magnitude. Expanding $\partial \phi/\partial \tau$ into a Taylor series, the lowest-order nonzero term of Eq. (12.14) corresponds to the pulse chirp. Similar to the bandwidth vector, we call $\boldsymbol{\theta}$ the *chirp vector*, which provides the differential chirp between the two PSPs. In the following section, we will use these parameters to describe the evolution dynamics of an optical soliton along a fiber.

## 12.3 Moment Theory of Vector Soliton Propagation

In general, the propagation of an optical pulse inside a fiber with random birefringence is governed by Eq. (8.14). Here we only consider optical pulses with relatively narrow bandwidth (corresponding to a temporal duration of a few picoseconds or longer) so that high-order effects, such as intrapulse Raman scattering, nonlinearity dispersion, and higher-order linear dispersion are all negligible. In this case, Eq. (8.14) reduces to

$$\frac{\partial|A\rangle}{\partial z}+\frac{i\beta_2}{2}\frac{\partial^2|A\rangle}{\partial\tau^2}=\frac{1}{2}\boldsymbol{b}\cdot\boldsymbol{\sigma}\frac{\partial|A\rangle}{\partial\tau}+i\gamma_e\langle A|A\rangle|A\rangle, \tag{12.15}$$

where $\gamma_e=8\gamma/9$, and we have made a temporal transformation as $\tau=t-\beta_1 z$ and a phase transformation as $|A(z,t)\rangle=|A(z,t)\rangle\exp(i\beta_0 z)$ to remove the trivial phase and pulse position evolution. Equation (12.15) is the so-called Manokov-PMD equation [22]-[24]. In the absence of PMD, Eq. (12.15) reduces to the Manakov equation [26] and supports Manakov solitons, which are indeed scalar solitons with constant SOP across their pulse profile: $|A(z,\tau)\rangle=a(z,\tau)|s\rangle$ where $|s\rangle$ is time independent and is determined by the input SOP.

Using Eqs. (12.1), (12.3), and (12.15), it is easy to show that the pulse energy and momentum are two conserved parameters:

$$\frac{dE}{dz}=0, \qquad\qquad \frac{d\omega_0}{dz}=0. \tag{12.16}$$

For convenience, we remove the carrier frequency of the pulse and set $\omega_0=0$. Using Eqs. (12.2), (12.4), (12.5), and (12.15), we obtain the dynamic equations governing the pulse parameters as:

$$\frac{d\rho_2}{dz}=-\boldsymbol{b}\cdot\boldsymbol{\rho}+2\beta_2\theta_0, \tag{12.17}$$

$$\frac{d\rho_0}{dz}=-\frac{1}{2}\boldsymbol{b}\cdot\boldsymbol{S}, \tag{12.18}$$

$$\frac{d\boldsymbol{S}}{dz}=\boldsymbol{b}\times\boldsymbol{\omega}, \tag{12.19}$$

$$\frac{d\boldsymbol{\rho}}{dz}=-\frac{1}{2}\boldsymbol{b}+\beta_2\boldsymbol{\omega}+\boldsymbol{b}\times\boldsymbol{\theta}, \tag{12.20}$$

$$\frac{d\boldsymbol{\omega}}{dz}=\boldsymbol{b}\times\boldsymbol{\kappa}-\frac{\gamma_e}{E}\int_{-\infty}^{+\infty}\boldsymbol{s}\frac{\partial s_0}{\partial\tau}d\tau, \tag{12.21}$$

where $s_0(z,\tau)\equiv\langle A(z,\tau)|A(z,\tau)\rangle$ is the power profile of the pulse and $\boldsymbol{s}(z,\tau)\equiv\langle A(z,\tau)|\boldsymbol{\sigma}|A(z,\tau)\rangle$ is the associated time-dependent Stokes vector. Similarly, we can find the dynamic equation for the chirp and bandwidth parameters $\theta_0$ and $\kappa_0$, and those for the associated chirp vector $\boldsymbol{\theta}$ and the bandwidth vector $\boldsymbol{\kappa}$.

Further analysis can be simplified considerably if we notice that, in the absence of PMD, the Manakov soliton not only maintains its profile and polarization during propagation, but is also free from chirp: $\boldsymbol{s}(z,\tau)=s_0(z,\tau)\boldsymbol{S}$ where $\boldsymbol{S}$ is constant. In this case, $\theta_0(z)=0$ and $\kappa_0(z)=\kappa_0(0)$, and Eqs. (12.4) and (12.13) show that $\boldsymbol{\theta}(z)=0$ and $\boldsymbol{\kappa}(z)=\kappa_0(0)\boldsymbol{S}$. The dominant effect of PMD is to introduce small temporal separation between the two polarization components of the pulse [18]-[20]. This leads to asymmetric XPM between them which in turn induces differential carrier frequency shift, represented by the nonlinear term of Eq. (12.21). Although such asymmetric XPM may also lead to some chirp and bandwidth changes on individual polarization components, it would be a higher-order effect and we can approximate $\theta_0 \approx 0$, $\boldsymbol{\theta} \approx 0$, and $\boldsymbol{\kappa}(z) \approx \kappa_0 \boldsymbol{S}(z)$. The nonlinear term in Eq. (12.21) vanishes for any pulse with a constant SOP across the profile, in particular, for the Manakov soliton without PMD. As PMD-induced DGD is small, the two polarization components mainly experience XPM from the intensity slope close to the center of Manakov soliton. Thus, we can expand in Eq. (12.21) the power profile in a Taylor series as

$$\frac{\partial s_0}{\partial \tau} \approx \left.\frac{\partial s_0}{\partial \tau}\right|_{\tau=0} + \left.\frac{\partial^2 s_0}{\partial \tau^2}\right|_{\tau=0} \tau + \cdots. \tag{12.22}$$

For Manakov soliton, $\left.\frac{\partial s_0}{\partial \tau}\right|_{\tau=0} = 0$ because of its symmetric shape, and the lowest-order nonzero term of Eq. (12.22) would be the term linearly dependent on $\tau$. Under these considerations, we obtain the following approximate coupled equations:

$$\frac{d\rho_2}{dz} \approx -\boldsymbol{b} \cdot \boldsymbol{\rho}, \tag{12.23}$$

$$\frac{d\boldsymbol{\rho}}{dz} \approx -\frac{1}{2}\boldsymbol{b} + \beta_2 \boldsymbol{\omega}, \tag{12.24}$$

$$\frac{d\boldsymbol{\omega}}{dz} \approx \boldsymbol{b} \times \kappa_0 \boldsymbol{S} - \gamma_e \xi \boldsymbol{\rho}, \tag{12.25}$$

where we have denoted $\xi \equiv \left.\frac{\partial^2 s_0}{\partial \tau^2}\right|_0$.

Equations (12.24) and (12.25) show clearly how solitons are resistant to external perturbations introduced by random PMD. In a small section of fiber, random PMD introduces a small DGD along a specific polarization [first term of Eq. (12.24)], which in turn causes asymmetric XPM on the two polarization states and thus introduces differential frequency shift between them [second term of Eq. (12.25)]. Because of group-velocity dispersion of the fiber, these two polarization components have different group velocities and thus introduce additional DGD to compensate the one by PMD [second term of Eq. (12.24)]. As a result, the total DGD is reduced. Optical solitons provide a trapping force like a potential well between its two polarization components to prevent them from separating apart.

Equations (12.23)-(12.25) together with Eqs. (12.18) and (12.19) consist of a complete set of dynamic equations governing the evolution of pulse parameters. Similar to Chapter 8, they should be treated in the Stratonovich sense [25]. In particular, as discussed in the previous section, the vector $\boldsymbol{\rho}$ is indeed the first-order PMD vector but with a half magnitude. Its magnitude provides a good quantification of the extent of the soliton stability. Therefore, by finding the statistics of $\boldsymbol{\rho}$, we can obtain the major dynamics of solition propagation. By use of the statistics of $\boldsymbol{b}$ in Eq. (8.16), performing averaging over random PMD as usual, we are able to obtain the dynamic equations governing the statistics of soliton evolution

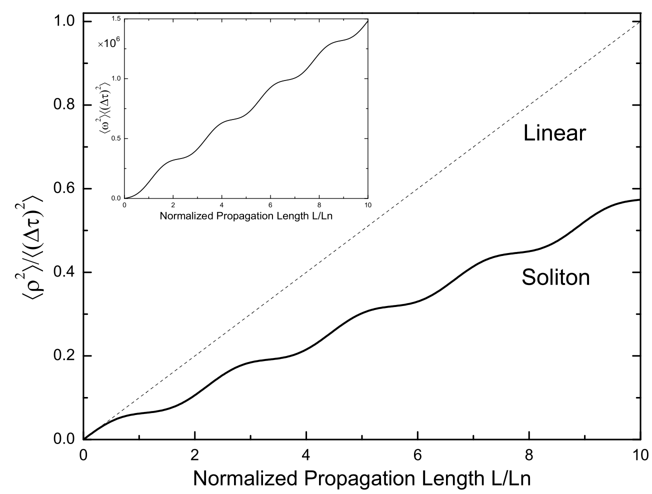


Figure 12.1: $\langle(\boldsymbol{\rho})^2\rangle$ as a function of propagation distance $L$. $\langle(\boldsymbol{\rho})^2\rangle$ is normalized by the mean square of linear DGD $\langle(\Delta\tau)^2\rangle = D_p^2 L$. The propagation distance is normalized by the nonlinear length $L_n$. The solid and dashed curves show DGD for solitons and linear pulses, respectively. The inset shows the corresponding normalized mean square of frequency vector: $\langle(\boldsymbol{\omega})^2\rangle\langle(\Delta\tau)^2\rangle$

as:

$$\frac{d\langle\boldsymbol{\rho}^2\rangle}{dz} = \frac{D_p^2}{4} + 2\beta_2\langle\boldsymbol{\rho}\cdot\boldsymbol{\omega}\rangle, \tag{12.26}$$

$$\frac{d\langle\boldsymbol{\rho}\cdot\boldsymbol{\omega}\rangle}{dz} = -\frac{k_0 D_p^2}{3}\langle\boldsymbol{\rho}\cdot\boldsymbol{\omega}\rangle + \beta_2\langle\boldsymbol{\omega}^2\rangle - \xi\langle\boldsymbol{\rho}^2\rangle, \tag{12.27}$$

$$\frac{d\langle\boldsymbol{\omega}^2\rangle}{dz} = -\frac{2k_0 D_p^2}{3}\left(\langle\boldsymbol{\omega}^2\rangle - k_0\langle\boldsymbol{S}^2\rangle\right) - 2\xi\langle\boldsymbol{\rho}\cdot\boldsymbol{\omega}\rangle, \tag{12.28}$$

$$\frac{d\langle\boldsymbol{S}^2\rangle}{dz} = -\frac{2D_p^2}{3}\left(k_0\langle\boldsymbol{S}^2\rangle - \langle\boldsymbol{\omega}^2\rangle\right). \tag{12.29}$$

These equations are linear and deterministic, and they can be easily solved to obtain the statistics of DGD of optical solitons. In the case of linear propagation, we neglect the effects of GVD and SPM, Eq. (12.26) then reduces to $d\langle\boldsymbol{\rho}^2\rangle/dz = D_p^2/4$, which provides a solution of $\langle\boldsymbol{\rho}^2(L)\rangle = D_p^2 L/4$, exactly the result of first-order linear PMD [18, 22, 27, 28] (note the magnitude of $\boldsymbol{\rho}$ is half of the conventional PMD vector). In the case of optical solitons, the trapping force induced by XPM between the two polarization components reduces the magnitude of $\boldsymbol{\rho}$ through fiber GVD [second term of Eq. (12.26)].

Figure 12.1 compares the magnitude of $\langle\boldsymbol{\rho}^2(L)\rangle$ in the cases of a linear pulse and an optical soliton, using the fiber parameters of $D_p = 0.1$ ps$/\sqrt{\text{km}}$ and $\beta_2 = -22$ ps$^2$/km at 1550 nm. The input soliton is assumed to be a Manakov soliton with a FWHM of 100 ps, corresponding to $T_0 = 56.7$ ps. The induced DGD for a soliton is less than 60% of that for linear pulses, indicating resistance of optical solitons to PMD. Moreover, Soliton DGD exhibits an oscillation with a period of about twice of the nonlinear length

$L_n = (\gamma_e P_0)^{-1} = L_D = T_0^2/|\beta_2|$, a length scale governing the SPM effect. The magnitude of frequency vector (inset of Fig. 12.1) exhibits an oscillation with a same period but is out of phase with the DGD oscillation because of the negative feedback mechanism induced by the combined effect of SPM and GVD, as discussed previously.

## 12.4 Conclusion

In conclusion, we have presented a simple moment theory to quantify the propagation of optical soliton in the presence of PMD, based on the particle nature of optical solitons. We show that an optical soliton exhibits considerable resistance to PMD-induced perturbations, and experiences a DGD less than 60% of that for linear pulses. Our theory provides a straightforward description of the underlying trapping mechanism.

## References

[1] H. A. Haus and W. S. Wong, Rev. Mod. Phys. **68**, 423 (1996).

[2] A. Hasegawa, Y. Kodama, A. Maruta, Opt. Fiber Technol. **3**, 197 (1997).

[3] A. Hasegawa, Chaos **10**, 475 (2000).

[4] L. F. Mollenauer, J. P. Gordon, and P. V. Manyshev, in *Optical Fiber Telecommunications III A*, I. P. Kaminow and T. L. Koch, eds. (Academic, San Diego, 1997), Chap. 12.

[5] C. R. Menyuk, G. M. Carter, W. L. Kath, and R. M. Mu, in *Optical Fiber Telecommunications IV B*, I. P. Kaminow and T. L. Koch, eds. (Academic, San Diego, 2002), Chap. 7.

[6] L. F. Mollenauer, K. Smith, J. P. Gordon, and C. R. Menyuk, Opt. Lett. **14**, 1219 (1989).

[7] P. K. A. Wai, C. R. Menyuk, and H. H. Chen, Opt. Lett. **16**, 1231 (1991).

[8] S. G. Evangelides, L. F. Mollenauer, J. P. Gordon, and N. S. Bergano, J. Lightwave Technol. **10**, 28 (1992).

[9] T. I. Lakoba and D. J. Kaup, Phys. Rev. E **56**, 6147 (1997).

[10] Y. Chen and H. A. Haus, Opt. Lett. **25**, 290 (2000); Chaos **10**, 529 (2000).

[11] M. Midrio, J. Opt. Soc. Am. B **17**, 169 (2000).

[12] C. Xie, M. Karlsson, H. Sunnerud, and P. A. Andrekson, Opt. Lett. **26**, 672 (2001).

[13] S. Boscolo, A. Pavan, and M. Midrio, J. Opt. Soc. Am. B **19**, 1 (2002).

[14] C. Xie, M. Karlsson, P. A. Andrekson, H. Sunnerud, and J. Li, IEEE J. Sel. Top. Quant. Electron. **8**, 575 (2002).

[15] T. P. Horikis and J. N. Elgin, Opt. Lett. **27**, 1516 (2002).

[16] A. Levent, S. G. Rajeev, F. Yaman, and G. P. Agrawal, Phys. Rev. Lett. **90**, 013902 (2003).

[17] Y. Chung, V. V. Lebedev, and S. S. Vergeles, Opt. Lett. **29**, 1245 (2004).

[18] C. D. Poole, in *Optical Fiber Telecommunications III A*, I. P. Kaminow and T. L. Koch, eds. (Academic, San Diego, 1997), Chap. 6.

[19] H. Kogelnik, R. Jopson, and L. Nelson, in *Optical Fiber Telecommunications IV B*, I. P. Kaminow and T. L. Koch, eds. (Academic, San Diego, 2002), Chap. 15.

[20] J. P. Gordon and H. Kogelnik, Proc. Natl. Acad. Sci. USA **97**, 4541 (2000).

[21] A. Galtarossa, L. Palmieri, M. Schiano, and T. Tambosso, Opt. Lett. **25**, 384 (2000); **26**, 962 (2001).

[22] P. K. A. Wai and C. R. Menyuk, J. Lightwave Technol. **14**, 148 (1996).

[23] D. Marcuse, C. R. Menyuk, and P. K. A. Wai, J. Lightwave Technol. **15**, 1735 (1997).

[24] C. R. Menyuk and B. S. Marks, J. Lightwave Technol. **24**, 2806 (2006).

[25] C. W. Gardiner, *Handbook of Stochastic Methods*, $2^{nd}$ Ed. (Springer, New York, 1985).

[26] G. P. Agrawal, *Nonlinear Fiber Optics*, $3^{rd}$ ed. (Academic, San Diego, CA, 2001).

[27] M. Karlsson and J. Brentel, Opt. Lett. **24**, 939 (1999).

[28] Q. Lin and G. P. Agrawal, J. Opt. Soc. Am. B **20**, 292 (2003).

# Appendix: List of Acronyms

All acronyms used in this thesis are listed here in alphabetical order.

| | |
|---|---|
| ASE | amplified spontaneous emission |
| ASRS | amplified spontaneous Raman scattering |
| CW | continuous wave |
| DGD | differential group delay |
| EDFA | erbium-doped fiber amplifier |
| FOPA | fiber-optic parametric amplifier |
| FOPO | fiber-optic parametric oscillator |
| FWHM | full width at half maximum |
| FWM | four-wave mixing |
| GVD | group-velocity dispersion |
| MI | modulation instability |
| GNLSE | generalized nonlinear Schrödinger equation |
| NRZ | nonreturn to zero |
| NF | noise figure |
| PCF | photonic crystal fiber |
| PMD | polarization-mode dispersion |
| RIFS | Raman-induced frequency shift |
| RMS | root mean square |
| SOP | state of polarization |
| SBS | stimulated Brillouin scattering |
| SOP | state of polarization |
| SPM | self-phase modulation |
| SpRS | spontaneous Raman scattering |
| SRS | stimulated Raman scattering |
| SVEA | slowly vary envelop approximation |

| | |
|---|---|
| SVPA | slowly vary polarization approximation |
| THG | third-harmonic generation |
| TOD | third-order dispersion |
| WDM | wavelength-division multiplexing |
| XPM | cross-phase modulation |
| ZDWL | zero-dispersion wavelength |